

*The National Nanotechnology Infrastructure Network  
Research Experience for Undergraduates Program*

**2004  
NNIN REU  
Research  
Accomplishments**

**NNIN**

Nanoscale Science,  
Engineering & Technology



**The 2004 National Nanotechnology Infrastructure Network  
Research Experience for Undergraduates Program Research Accomplishments**

**Table of Contents**

**National Nanotechnology  
Infrastructure Network (NNIN) ..... 4**

**2004 NNIN REU Introduction ..... 5**

**The 2004 NNIN REU Interns, by site ..... 6**

    Cornell University ..... 6

    Georgia Institute of Technology ..... 6

    Harvard University ..... 7

    Howard University ..... 7

    The Pennsylvania State University ..... 8

    Stanford University ..... 8

    University of California Santa Barbara ..... 9

    University of Michigan Ann Arbor ..... 9

    University of Minnesota Twin Cities ..... 10

    University of New Mexico ..... 10

    The University of Texas at Austin ..... 11

    University of Washington ..... 11

**The 2004 NNIN REU  
Research Accomplishments**

*in alpha order by intern's last name*

**Alley, R. Louis:**  
*Nanoelectromechanical Devices Based on  
Suspended Carbon Nanotube and Ge Nanowire  
Field Effect Transistors ..... 14*

**Anito, Mary:**  
*Fabrication of Microfluidic Devices with  
Integrated Transducers for Fluid Pumping ..... 16*

**Arias, Ana:**  
*The Media Coverage of Nanotechnology ..... 18*

**Bagga, Neha:**  
*Anion Exchange of GaAsSb/GaInAs Interfaces ..... 20*

**Bastianon, Nick:**  
*Fabricating Nano-Gap Metal Electrodes  
using Photolithography ..... 22*

**Bhatia, Priya:**  
*Selective Oxidative Patterning of Self-Assembled  
Organothiols Monolayers on Gold ..... 24*

**Brady, Kevin:**  
*Electrowetting for DNA Sequencing on Chip ..... 26*

**Burt, Nathaniel:**  
*Design and Fabrication of Tapered Waveguides  
in AlGaAs for Coupling Light in  
Nanoscale Optoelectronic Devices ..... 28*

**Carroll, Heather:**  
*Etch Resistance of Polymers used in  
Supercritical Carbon Dioxide Development ..... 30*

**Chalumo, Kovner:**  
*Design and Characterization of a  
Microcoil for Inter-Arterial Monitoring ..... 32*

**Cochran, Peter:**  
*Nanometer-Scale Lithography using an AFM ..... 34*

**DeRosa, Diana:**  
*Biomaterials in Microsystems: An Investigation  
of the Effect of Parent Ti Microstructure on the  
Morphology of Nanostructured Titania ..... 36*

**Dietz, Carl:**  
*Insulation of a Carbon Nanotube Interface  
for Retinal Prostheses ..... 38*

**Domenech Garcia, Maribella:**  
*Development of Devices for  
Nanofiltration of Biomolecules ..... 40*

**Fields, Diane:**  
*Comparison of Fabrication Methods  
for Tunnel Regions in a Biosensor ..... 42*

**Finger, Isaac:**  
*Effect of O<sub>2</sub> Plasma Treatment on the  
Leakage Current of Titanium Oxide  
Thin Films Formed via PMODTM ..... 44*

**Fraser, Eric:**  
*Characterization of AlGaN Material Quality for  
use in Deep-Ultraviolet Light Emitting Diodes ..... 46*

<b>Freeman, Elizabeth:</b> <i>Living Microorganisms Entrapped in Nano-Structured Latex Formulations Piezoelectrically Printed onto Bioelectronic Devices</i> .....	48	<b>Kung, Edward Chih Yuen:</b> <i>Optical Readout of MEMS-Based Infrared Detectors</i> .	76
<b>Froelich, Steven:</b> <i>New Materials and Applications of Nanoimprint Technology</i> .....	50	<b>Lee, William:</b> <i>Making Connections to Molecules for Molecular Electronics</i> .....	78
<b>Fu, Yenyun:</b> <i>Nanoscale Cantilevers for Ultrasonics and Nanoscale Folding</i> .....	52	<b>Miller, Nate:</b> <i>Ordered Nanostructures for Organic Photovoltaic Cells</i> .....	80
<b>Gainor, Danielle:</b> <i>Flow-Through Amperometric Enzymatic Biosensors Containing Glucose Oxidase</i> .....	54	<b>Moore, Eric:</b> <i>Reactive Electrospinning of Hydrogel Nanofibers</i> ...	82
<b>Gannon, John:</b> <i>Process Development for Novel Fibrous MEMS Structures</i> .....	56	<b>Moss, William:</b> <i>Micromagnetic Manipulation of Cardiac Tissue</i> .....	84
<b>Gantz, Jay:</b> <i>Diffusion of Electrolyte Solutions in Nanoporous Thin-Films</i> .....	58	<b>Newsome, Brad:</b> <i>Molecular Substrates for Nanobiotechnology</i> .....	86
<b>Gliem, Jill:</b> <i>Spreading of Cells on Supported Peptide Amphiphile Bilayer Membranes</i> .....	60	<b>Ng, Mai:</b> <i>Investigation of Novel Thermal Barrier Coating Materials by Minimum Thermal Conductivity</i> .....	88
<b>Goodfellow, Brian:</b> <i>Design and Application of a Fiber Pullout Test for Examining Controlled Interfaces in Fiber Reinforced Polymers</i> .....	62	<b>Ngandu, Kabongo:</b> <i>Resolution Enhancement Techniques for Optical Lithography</i> .....	90
<b>Hammond, William:</b> <i>Etching and Characterization Studies of Ag/n-Si Nanocomposite Films</i> .....	64	<b>Nguyen, Khiem:</b> <i>Fabrication and Characterization of a Nanonozzle</i> .	92
<b>Horgan, Briony:</b> <i>A 90 GHz, Corrugated, Compact Packing, Focal Plane Layout, Platelet Antenna Array</i> .....	66	<b>O'Day, Alexander:</b> <i>Fabrication of a Discriminating Gas Sensor</i> .....	94
<b>Hsu, Hsan-yin:</b> <i>Photochemical Synthesis of Gold Nanoparticles with Interesting Shapes</i> .....	68	<b>Olds, Nathan:</b> <i>Characterization and Optimization of ZEP520A Electron Beam Lithography Resist</i> .....	96
<b>Huang, Jessica:</b> <i>Manganese Doping of Germanium Nanowires Seeded from Gold Nanocrystals</i> .....	70	<b>Padgaonkar, Vaidehee:</b> <i>Thermal Effects in Silicon Based Resonant Cavity Devices</i> .....	98
<b>Karlsodt, Brandon:</b> <i>The Self Assembly of Microspheres in a Microchamber</i> .....	72	<b>Park, Heyjin:</b> <i>Nano-Excision of Thin Diamond Membranes for a High Brightness Electron Source</i> .....	100
<b>Krueger, Lisa:</b> <i>Hybrid Nano-Scale Pattern Formation Through Nanocrystal Self-Assembly</i> .....	74	<b>Philips, Peter:</b> <i>Simulations of Simplified Cell Membranes</i> .....	102
		<b>Pursel, Sean:</b> <i>Investigating the Formation of Polymeric Sculptured Thin Films as a Functional Template for Collagen Growth and Attachment</i> .....	104
		<b>Rudavsky, Rena:</b> <i>Mechanical Properties of Human Stratum Corneum: Influence of pH-Treatment</i> .....	106

<b>Saboktakin, Marjan:</b>	
<i>Ordered Growth on Nanostructured Glass Surfaces</i> .	108
<b>Salomon, Ludwig:</b>	
<i>Silicide Contacts to Ultra-Thin Silicon Films for Nano-Scale Devices</i> .....	110
<b>Sammy, Francis:</b>	
<i>The Growth of GaN Nanowires using Ni Nano Particles as Catalyst</i> .....	112
<b>Santangelo, Steven:</b>	
<i>Solution Phase Thermal Annealing Studies on the Activation Barrier to Ferromagnetism in Nanocrystalline Diluted Magnetic Semiconductor <math>\text{Co}^{2+}\text{TiO}_2</math></i> .....	114
<b>Sarik, John:</b>	
<i>Scaling Up Catalytic Nanomotors</i> .....	116
<b>Setlow, Cortland:</b>	
<i>Self-Assembly of Sub-Micron Channels for Nanofluidic Applications using Interferometric Lithography and Spin-Coating</i> .....	118
<b>Shaikh, Shahid:</b>	
<i>Reactive Ion Etching Process Development and Characterization</i> .....	120
<b>Silver, Marshall:</b>	
<i>The Novel Formation of Photodefinable Porosity to Fabricate Direct-Write Waveguides for Optoelectronic Applications</i> .....	122
<b>Slavik, Gregory:</b>	
<i>Applications of Nanofluidic Devices in Chemistry</i> ....	124
<b>Smith, Margo:</b>	
<i>Controlled Neuron Growth by Patterned Protein Gradients</i> .....	126
<b>Soumahoro, Tina:</b>	
<i>Surface-Enhanced Raman Scattering Substrates: Highly Sensitive Sensors for the Detection of Adsorbate Molecules</i> .....	128
<b>Staniszewski, Tabitha:</b>	
<i>MEMS Based Real-Time Non-Invasive Biological Cell Diagnostics</i> .....	130
<b>Staszkiwicz, Nicole:</b>	
<i>Synthesis and Characteristics of ZnO Nanowires</i> ...	132
<b>Stevens, Blake:</b>	
<i>Surface Functionalization of Barium Titanate Nanoparticles</i> .....	134
<b>Stolyarov, Alexander:</b>	
<i>Spectroscopic Imaging of Single-Walled Carbon Nanotubes by Resonant Raman Scattering</i> .....	136
<b>Tally, Lynette:</b>	
<i>Effect of Solution pH on the Retention and Flux of Aqueous Solutions of <math>\text{G}_3\text{-NH}_2</math> PAMAM Dendrimer by Regenerated Cellulose Ultrafiltration Membranes</i> ...	138
<b>Tillmann, Patricia:</b>	
<i>Stability of Silver Nanoparticles in Aqueous and Organic Media</i> .....	140
<b>Vallett, Paul:</b>	
<i>The Effect of Organic Compounds on the Synthesis of Nanophase Materials</i> .....	142
<b>Vaughan, Damian:</b>	
<i>Silicon Carbide Light Emitting Diode Fabrication and Characterization</i> .....	144
<b>Virost, Steven:</b>	
<i>Micro-Scale Two Phase Flow Device Fabrication</i> ....	146
<b>Whitlock Jr., Rogers:</b>	
<i>Quantum Computing via Single Charges in Self-Assembled Coupled Quantum Dots</i> .....	148
<b>Willett, James:</b>	
<i>Scanning Hall Probe Fabrication</i> .....	150
<b>Wu, Alyssa Xia:</b>	
<i>Miniaturizing DNA Sequencing Technology: Designing Microfluidic Channels for Performing Chemistry on Beads</i> .....	152
<b>Yang, Allen:</b>	
<i>Fabrication and Stabilization of Non-Spherical Colloids for Self-Assembly</i> .....	154
<b>Zheng, Yan:</b>	
<i>Biosensors on Surface Acoustic Wave Phononic Band Gap Structures</i> .....	156
<b>Index</b> .....	<b>159</b>

**The National Nanotechnology Infrastructure Network  
is made up of the following thirteen sites, and is supported by  
The National Science Foundation, the NNIN sites,  
our corporate sponsors and research users.**

**Cornell NanoScale Facility**

**Cornell University**  
250 Duffield Hall • Ithaca, NY 14853  
607-255-2329 • <http://www.cnf.cornell.edu>

**Microelectronics Research Center**

**Georgia Institute of Technology**  
791 Atlantic Dr NW • Atlanta, GA 30332  
404-894-5266 • <http://www.mirc.gatech.edu/>

**Center for Imaging & Mesoscale Structures**

**Harvard University**  
17 Oxford St Cruft 313 • Cambridge, MA 2138  
617-495-3161 • <http://www.cims.harvard.edu/index.html>

**Materials Science Research Center for Excellence**

**Howard University**  
2300 6th St NW • Washington, DC 20059  
202-806-6618 • [http://www.msrece.howard.edu/  
%7Eananet/NNUN.HTM](http://www.msrece.howard.edu/%7Eananet/NNUN.HTM)

**Triangle National Lithography Center  
North Carolina State University**

*(affiliate)*  
218A EGRC - Engineering Grad Res Ctr, Box 7911  
Raleigh, NC 27695-7920  
919-515-5153 • <http://www.tnnc.ncsu.edu/>

**Penn State Center for Nanotechnology  
Education and Utilization**

**The Pennsylvania State University**  
230 Innovation Blvd, 189 MRI Bldg  
University Park, PA 16802  
814-865-4931 • <http://www.nanofab.psu.edu/>

**Stanford Nanofabrication Facility  
Stanford University**

CIS 103 Via Ortega St, 420 Via Palou Mall  
Stanford, CA 94305-4085  
650-723-9508 • <http://snf.stanford.edu/>



[www.nnin.org](http://www.nnin.org)

**Nanotech at UCSB**

**University of California Santa Barbara**  
Electrical & Computer Engineering, 5153 Engineering I  
Santa Barbara, CA 93106-9560  
805-893-3244 • <http://www.nanotech.ucsb.edu/>

**Solid State Electronics Lab**

**University of Michigan, Ann Arbor**  
1301 Beal Ave • Ann Arbor, MI 48109-2122  
734-763-6650 • <http://www.eecs.umich.edu/ssel/>

**Nanofabrication Center**

**University of Minnesota**  
200 Union St, Rm 4-174 • Minneapolis, MN 55455  
612-625-6608 • <http://www.nfc.umn.edu/>

**Center for High Technology Materials**

**University of New Mexico**  
1313 Goddard SE, MSC04 2710  
Albuquerque, NM 87106  
505-272-7800 • <http://www.chtm.unm.edu/>

**Microelectronics Research Center**

**University of Texas at Austin**  
J.J. Pickle Center, 10100 Burnet Rd, MER 1.606B.  
Mailcode R9900 • Austin, TX 78758  
512-471-6730 • <http://www.mrc.utexas.edu/>

**Center for Nanotechnology**

**University of Washington**  
Box 351721 • Seattle, WA 98195-1721  
206-543-1776  
<http://www.nano.washington.edu/index.asp>

**REU Program Corporate Sponsors:**

Advanced Micro Devices • Agilent Technologies  
Analog Devices • Applied Materials  
Canon • Ebara Corporation  
Hewlett-Packard Company • Hitachi, Ltd  
IBM Corporation • Infineon  
Intel Corporation • LG Electronics, Inc.  
National Semiconductor Corporation  
Panasonic • Philips  
Renesas Technology Corporation • Robert Bosch Corp.  
Taiwan Semiconductor Manufacturing Company  
Texas Instruments, Incorporated • Toshiba

• • •

# The 2004 National Nanotechnology Infrastructure Network Research Experience for Undergraduates Program Research Accomplishments

## Introduction



*The 2004 NNIN REU interns at the network-wide convocation,  
held at The Pennsylvania State University, August 2004*

### **Welcome to the year 2004 Research Report of the National Nanotechnology Infrastructure Network's Research Experience for Undergraduate Program.**

Providing a focused experimental research experience in nanotechnology and its foundational subjects in a 10 week period is a challenging task; this report demonstrates that with effort from staff, faculty, graduate students, and the participating students, not only can it be successfully achieved, but also that it can lead to significant accomplishments by students who have just started on the path of technical education and getting their first experience with advanced hands-on research.

The NNIN national partnership, through our complementary strengths, cross-fertilization, multi-site education, and use of each other's resources, provides exciting projects and the means to achieve them in a reasonable time. Each student in the NNIN REU completes an independent research project selected for completion in 10 weeks with strong technical support and faculty supervision, undergoes strong hands-on training and education (also available through our web-site [www.nnin.org](http://www.nnin.org) in the multimedia section), and participates in a convocation at individual sites and at a common site to present their research efforts.

The focus on advanced research and knowledge, the strong mentoring and support, the strong exposure to a professional research environment, the strong expectations built into the research and presentations at convocations, the exposure to a wider variety of research conducted by peers and other users in diverse disciplines of science and engineering within the unifying facilities, and the strong scientific and social interactions across the network have been critical to the program's success. This year's participants also saw increased cross-site interactions through video-conferences and presentations, and hands-on experimentation.

NNIN came into existence in March of this year, and it is a real joy to see that this has allowed us to expand the number of participants to whom we can provide this unique chance.

I wish the participants the best wishes for future technical careers; NNIN hopes to see them build on this summer's experience, and my thanks to the staff, the graduate student mentors, and the faculty for their participation and involvement.

Sandip Tiwari  
Director, NNIN



**2004 NNIN REU Program at  
Cornell NanoScale Science &  
Technology Facility, Cornell University**

*Front row, left to right:*

- Ms. Ana Arias ..... page 18
- Ms. Maribella Domenech Garcia ..... page 40
- Ms. Vaidehee Padgaonkar ..... page 98
- Ms. Marjan Saboktakin ..... page 108
- Ms. Heather Carroll ..... page 30
- Ms. Diane Fields ..... page 42
- Ms. Melanie-Claire Mallison .... *site coordinator*

*Back row, left to right:*

- Mr. Allen Yang ..... page 154
- Mr. William Lee ..... page 78
- Ms. Yenyun Fu ..... page 52
- Mr. Ludwig Salomon ..... page 110
- Mr. John Gannon ..... page 56
- Mr. Steven Virost ..... page 146



**2004 NNIN REU Program at  
Microelectronics Research Center,  
Georgia Institute of Technology**

*Front row, left to right:*

- Mr. Yan Zheng ..... page 156
- Mr. Hsan-yin Hsu ..... page 68
- Mr. Khiem Nguyen ..... page 92

*Back row, left to right:*

- Mr. Nathan Olds ..... page 96
- Ms. Jennifer Tatham ..... *site coordinator*
- Mr. Marshall Silver ..... page 122
- Ms. Melissa Lowrimore .. *administrative assistant*
- Mr. Isaac Finger ..... page 44



**2004 NNIN REU Program at  
Center for Imaging & Mesoscale  
Structures, Harvard University**

*From left to right:*

- Mr. William Moss ..... page 84
- Mr. Alexander Stolyarov ..... page 136
- Mr. Shahid Shaikh ..... page 120



**2004 NNIN REU Program at  
Materials Science Research Center  
of Excellence, Howard University**

*Front row, left to right:*

- Mr. James Griffin ..... *program mentor*
- Ms. Patricia Tillmann ..... page 140
- Ms. Lynette Tally ..... page 138
- Mr. Damian Vaughan ..... page 144

*Back row, left to right:*

- Mr. Kovner Chalumo ..... page 32
- Mr. Francis Sammy ..... page 112
- Mr. William Hammond ..... page 64
- Dr. Gary Harris ..... *site director*



**2004 NNIN REU Program at  
Penn State Center for Nanotechnology  
Education and Utilization,  
The Pennsylvania State University**

*From left to right:*

- Mr. John Sarik ..... page 116
- Ms. Priya Bhatia ..... page 24
- Mr. Kabongo Ngandu ..... page 90
- Ms. Danielle Gainor ..... page 54
- Mr. Eric Moore ..... page 82
- Ms. Tabitha Staniszewski ..... page 130
- Mr. Sean Pursel ..... page 104
- Ms. Tina Soumahoro ..... page 128



**2004 NNIN REU Program at  
Stanford Nanofabrication Facility,  
Stanford University**

*Front row, left to right:*

- Mr. Kevin Brady ..... page 26
- Ms. Mary Anito ..... page 16
- Ms. Heyjin Park ..... page 100
- Mr. Nick Bastianon ..... page 22

*Second row, left to right:*

- Mr. Nate Miller ..... page 80
- Ms. Alyssa Xia Wu ..... page 152
- Mr. R. Louis Alley ..... page 14

*Third row, left to right:*

- Ms. Rena Rudavsky ..... page 106
- Ms. Jane Edwards ..... *site coordinator*
- Mr. Jay Gantz ..... page 58
- Mr. Carl Dietz ..... page 38

*Back row, left to right:*

- Mr. James Willett ..... page 150
- Dr. Michael Deal ..... *site coordinator*
- Mr. Nathaniel Burt ..... page 28



**2004 NNIN REU Program at  
Nanotech at UCSB, University  
of California Santa Barbara**

*Front row, left to right:*

- Ms. Angela Berenstein ..... *site coordinator*
- Ms. Mai Ng ..... page 88
- Ms. Diana DeRosa ..... page 36
- Ms. Jill Gliem ..... page 60

*Middle row, left to right:*

- Mr. Eric Fraser ..... page 46
- Mr. Peter Cochran ..... page 64
- Mr. Edward Chih Yuen Kung ..... page 76

*Back row, left to right:*

- Mr. Rogers Whitlock Jr. .... page 148
- Mr. Blake Stevens ..... page 134
- Mr. Peter Philips ..... page 102

*Not Pictured:*

- Ms. Briony Horgan ..... page 66



**2004 NNIN REU Program at  
Solid State Electronics Laboratory,  
University of Michigan, Ann Arbor**

*From left to right:*

- Mr. Steven Froelich..... page 50
- Ms. Nicole Staszkievicz ..... page 132
- Mr. Gregory Slavik ..... page 124



**2004 NNIN REU Program at  
Nanofabrication Center,  
University of Minnesota, Twin Cities**

*From left to right:*

- Ms. Elizabeth Freeman ..... page 48
- Mr. Alexander O'Day ..... page 94
- Ms. Margo Smith ..... page 126



**2004 NNIN REU Program at  
Center for High Technology Materials,  
University of New Mexico**

*From left to right:*

- Mr. Paul Vallett ..... page 142
- Mr. Cortland Setlow ..... page 118



**2004 NNIN REU Program at  
Microelectronics Research Center,  
The University of Texas at Austin**

*From left to right:*

- Ms. Neha Bagga ..... page 20
- Mr. Brian Goodfellow ..... page 62
- Ms. Jessica Huang ..... page 70



**2004 NNIN REU Program at  
Center for Nanotechnology,  
University of Washington**

*From left to right:*

- Mr. Brad Newsome ..... page 86
- Mr. Brandon Karlsgodt ..... page 72
- Mr. Steven Santangelo ..... page 114
- Ms. Lisa Krueger ..... page 74

National Nanotechnology  
Infrastructure Network

Research Experience  
for  
Undergraduates Program

**2004**  
**Research**  
**Accomplishments**

# Nanoelectromechanical Devices Based on Suspended Carbon Nanotube and Ge Nanowire Field Effect Transistors

Robert Louis Alley, Applied & Engineering Physics, Cornell University

NNIN REU Site: Stanford Nanofabrication Facility, Stanford University

Principal Investigator: Hongjie Dai, Department of Chemistry, Stanford University

Mentor: Qian Wang, Department of Chemistry, Stanford University

Contact: rla28@cornell.edu, hdai1@stanford.edu

## Abstract:

Semi-conducting carbon nanotubes (CNT) and germanium nanowires (GNWs) are desirable field-effect transistor (FET) elements because of their unique electrical properties and physical stability. Previous electromechanical measurements on CVD-grown suspended carbon nanotubes have shown that the band-gap of the tube can grow or shrink depending upon both the tube's chirality and on a tensile or perpendicular force from an AFM tip. Shorter and smaller diameter PECVD-grown tubes exhibit higher percentages of semi-conducting rather than metallic tubes. We are developing a process to suspend PECVD-grown nanotubes and germanium nanowires in FETs and to make similar measurements to determine the mechanical as well as electromechanical properties of nanotubes and nanowires. We will be investigating the compatibility of PECVD with previous techniques for measuring CVD-grown tubes by first fabricating and then measuring nanotube devices. In parallel, we will explore techniques to suspend nanowires in FETs, which has not yet been accomplished. AFM cantilever deflection and  $I-V_g$  curves will be used to obtain results.

## Introduction:

Carbon nanotubes are excellent one-dimensional elements for integrated circuitry (IC) because of their ability to ballistically transport electrons and because of their semiconducting properties. CNTs' ability to withstand high current densities makes them optimal components in nano-scale integrated circuitry. Previous experiments have shown that CNTs can be reliably grown across trenches and held in place on a substrate by Van der Waal's forces. Electrodes on either side of the trench can then be used to measure the tube's electrical properties while suspended and also while under mechanical strain. Similar suspended measurements have not yet been made on GNWs.

Until recently, there has not been a way to grow either semiconducting or metallic tube with high

selectivity. Li, et al., have developed a PECVD process which produces ~ 90% semiconducting tubes [1]. Controlling the chirality of tubes is very important in developing appropriate methods for their incorporation into conventional IC processes. A challenge related to using the current PECVD growth process is to create high-quality tubes with lengths similar to those produced by current CVD growth.

## Experiment:

A 1300-nanometer oxide layer was grown on heavily doped (I prime) silicon wafers. A thinner (~ 270 nm) layer of nitride was then grown on top of the oxide to assure undercutting later in the process. One- $\mu$ m-deep trenches were formed by patterning using the Karl Suss MA6/BA6 contact aligner with 3612 resist, dry etching, and wet etching. The wet-etch step is necessary to assure discontinuity in the metal deposition forming the electrodes. Electrodes were formed on either side of the trench through a lift-off process. A 600 nm spin-coat of PMMA was followed by a 1.6  $\mu$ m spin-coat of 3612. The 3612 resist was exposed and developed, and the exposed PMMA was dry etched. Deposition of 5Å of tungsten was followed by a 30 nm layer of platinum. The

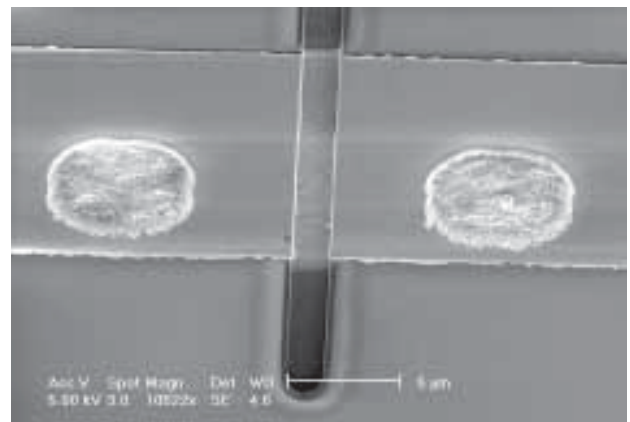


Figure 1: Scanning electron microscope image close-up of the trench, electrodes, and catalyst pads. The line outlining the trench shows the extent of the wet-etch undercut.

electrodes were patterned by an acetone lift-off. Catalyst pad windows were formed on either side of the trench through the same process.

The catalyst pads contained less than a monolayer of discrete 300-atom ferretin particles and were patterned with lift-off. Growth occurred at 600°C, with 80% CH<sub>4</sub> in argon flowing at a rate of 60 sccm. The plasma power was turned on for 3 minutes (RF power ~75 W) for PECVD growth. The gases and plasma were then switched off and the system was cooled to room temperature.

### Results and Conclusions:

Due to an error in an etching process, the first group of devices did not show significant response to changes in back-gate voltage. We were able to reproduce existing results to verify the quality of the second batch of fabricated devices. This included showing devices with very little hysteresis in the current vs gate voltage ( $I-V_g$ ) curve sweeping from -5 to 5 volts and back again. Preliminary data from PECVD tube growth shows a large amount of hysteresis compared with CVD growth, however,

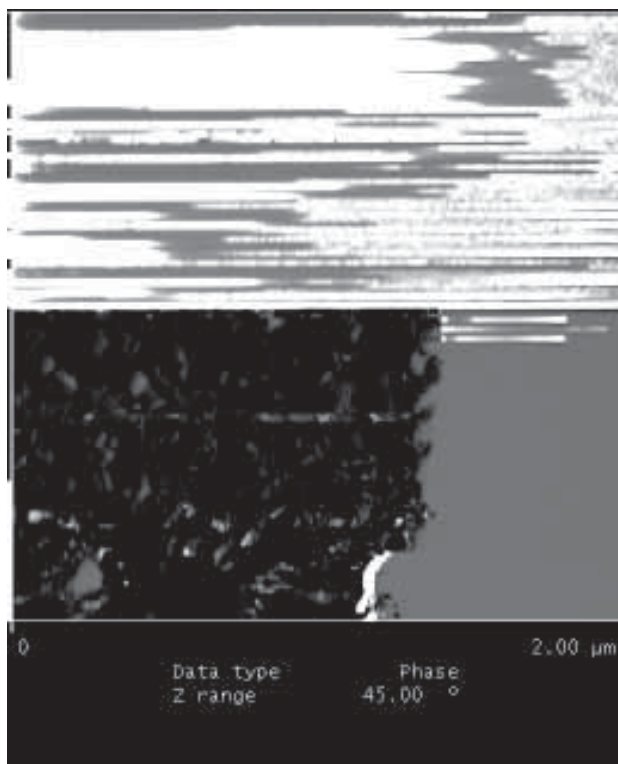


Figure 2: AFM showing the disruption of scanning due to a nanotube sticking to the atomic force microscope tip, ergo we were able to find and hit the tube.

these results will need to be verified through many more trials.

### Future Work:

Future studies will continue to focus upon PECVD tubes. Perhaps future studies will extend the study of electromechanical properties to silicon germanium and silicon nanowires. Other electromechanical measurements can be made on PECVD tubes and nanowires using a different type of suspended transistor device where the nanotube is not directly touched by the AFM tip.

### Acknowledgements:

I would like to thank Hongjie Dai and the Dai group, especially Qian Wang and Ali Javey, for teaching me about fabrication and device measurements. I greatly appreciate the funding from the National Science Foundation and the Center for Integrated Systems that has allowed me to stay and study at Stanford. I would like to thank Michael Deal, Jane Edwards, Marni Goldman, and Maureen Baran for their knowledge and assistance. I would like to thank Penn State for a wonderful convocation.

### References:

- [1] Li, et al. Preferential Growth of Single-Walled Carbon Nanotubes by a Plasma Enhanced CVD Method. *Nano Letters*, 4(2), 317-321 (2004).
- [2] Tomblor, et al. Reversible electromechanical characteristics of carbon nanotubes under local-probe manipulation. *Letters to Nature*, 405, 769-772 (2000).

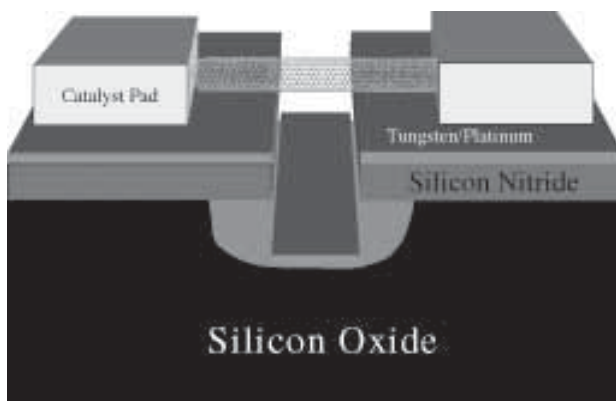


Figure 3: Conceptual representation of a suspended nanotube device.

# Fabrication of Microfluidic Devices with Integrated Transducers for Fluid Pumping

Mary E. Anito, Biomedical Engineering, Johns Hopkins University

NNIN REU Site: Stanford Nanofabrication Facility, Stanford University

Principal Investigator: Pierre Khuri-Yakub, Electrical Engineering, Stanford University

Mentor: Goksen Yaralioglu, Electrical Engineering, Stanford University

Contact: Mary2006@jhu.edu, khuri-yakub@stanford.edu

## Abstract:

The ability to fabricate miniaturized channels for the handling of biofluids helps to advance biomedical research. To further develop the use of these channels, we incorporate transducers to be used for the pumping of fluids throughout the system. We have etched the anisotropic channels into a double-side polished silicon wafer and at present the wafer is being bonded between two quartz wafers. Once this is completed, transducers will be added on top of the quartz wafer.

Transducers convert electrical energy into radiation pressure which is used to push the liquid in a desired direction. We are testing the use of sound radiation to facilitate the movement of fluids through the channels. Our group has already used transducers in such channels. To create a better device for pumping applications, we used a more complex geometric

layout. Once fabricated, we will be monitoring the movement of fluid in the channels by taking pictures with a charge coupled device camera. Through use of these developed channels and transducers, advancements in the field of microfluidics will be possible.

## Introduction:

Microfluidics is essentially the study of the movement of liquids in channels built on the micro or nano scale [1]. Advancements are being made in this field by testing the ability to move and direct liquids or certain particles as they move throughout the channel [2]. We need to detect the presence of certain materials and locate their positions in order to better understand the interactions of these microscopic substances.

This research group works to integrate transducers into microfluidic channels, and use ultrasound for detection and fluid actuation purposes [3, 4]. Our group's previous designs used single level channels, while our new design involves bi-level channels. Figure 1 shows the simpler one channel design next to our new more complex tri-channel design. While the previous research focused on using transducers for mixing liquids or switching channels to open or closed, our project is now testing the pumping capability of transducers.

Transducers work in the following way: the transducer is hooked up to a RF voltage source. This source excites the transducer, allowing it to emit sound wave propagation through the channel. The sound propagation has a corresponding radiation pressure, which actuates fluid in the channel. This pressure is used to move either the fluid or a specific particle in the stream. Figure 2 shows the positioning of the transducer in our design. We position the transducer so the pressure is applied precisely at the location and in the necessary direction to pump the liquid back up to the higher level, as shown in the picture of the complex bi-level design in Figure 2.

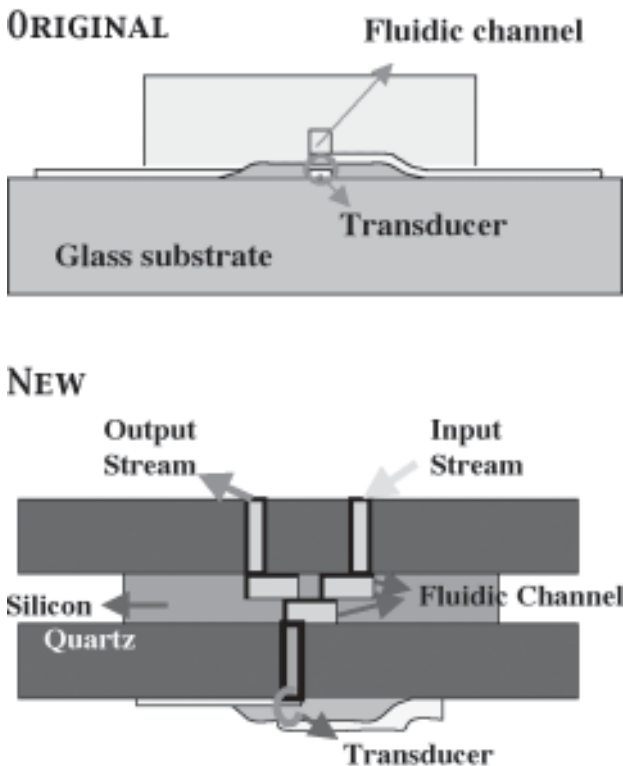


Figure 1: Comparison of old design with our new design.

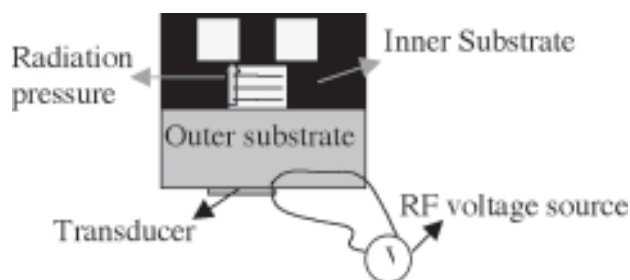


Figure 2: How the transducer works.

### The Fabrication Process:

We started out with a bare silicon double-side polished wafer and deposited 1500Å of oxide and 1500Å of silicon nitride on both sides. We then worked on the topside and spun 1.6 μm of photoresist atop the nitride, exposed a mask on the wafer and developed the wafer, making its design visible. Then we dry etched the nitride and oxide along the pattern exposed on the wafer and rinsed off the remaining photoresist with a Piranha mix of sulfuric acid and hydrogen peroxide. We then repeated the process of exposing and developing on the bottom side. After the final dry etch, the channels were anisotropically etched through the pure silicon with KOH. We then did a final rinse on the wafer with plasma to dissolve the remaining nitride, and with dilute hydrofluoric acid to dissolve the remaining oxide, leaving behind only the silicon wafer. Figure 3 shows a picture of our etched channel.

We are now bonding quartz wafers on each side of the silicon to create a platform on which to place the transducer. Once completed, we will deposit a layer of gold, covering an area we do not want dissolved with resist and then do a gold etch, leaving only a small area behind. On top of the gold, we will deposit a layer of zinc oxide and add the top electrode, successfully constructing a microfluidic device with an integrated transducer.

### Results:

Due to complications in bonding the quartz wafers, we have not yet been able to add the transducer. Once the transducer is added, testing will commence. Our test will consist of seeing if liquid can flow through the new design.

### Conclusions:

If liquid flows through our device, this research will have created a better device for pumping applications. Pumping is important to move liquids or particles into

desirable positions in order to monitor and better understand the movement and interactions of liquids on this scale. Pumping pushes the substances into a position beneath a microscope to be monitored. Better understanding of these substances can eventually lead to improvements in the field of medicine.

### Acknowledgements:

I would like to thank Goksen for all of his support throughout my research and the Khuri-Yakub group for welcoming me. I would like to also thank the Stanford Nanofabrication Facility and its staff for allowing me to do my research. Finally, thank you to the National Science Foundation for funding my project.

### References:

- [1] P. Gravesen, J. Branebjerg, and O.S. Jensen, "Microfluidics-a review", *Journal of Micromechanics and Microengineering*. Vol. 3, pp. 168-182, 1993.
- [2] S. Shoji, and M. Esashi, "Microflow devices and systems", *Journal of Micromechanics and Microengineering* Vol. 4 pp. 157-171, 1994.
- [3] Jagannathan, H.; Yaralioglu, G.G.; Ergun, A.S.; Degertekin, F.L.; Khuri-Yakub, B.T., "Micro-fluidic channels with integrated ultrasonic transducers", *Ultrasonics Symposium, 2001 IEEE*, Volume: 2, 7-10 Oct. 2001, Pages:859 - 862 vol.2.
- [4] Jagannathan, H.; Yaralioglu, G.G.; Ergun, A.S.; Khuri-Yakub, B.T., "Acoustic heating and thermometry in microfluidic channels" *MicroElectroMechanical Systems, 2003 Kyoto. IEEE 16th Annual International Conference on*, 19-23 Jan. 2003, Pages: 474 - 477.
- [5] Yaralioglu, G. G.; Wygant, I. O.; Marentis, T. C.; Khuri-Yakub, B. T., "Ultrasonic Mixing in Microfluidic Channels Using Integrated Transducers", *Anal. Chem.*; (Article); 2004; 76(13); 3694-3698.

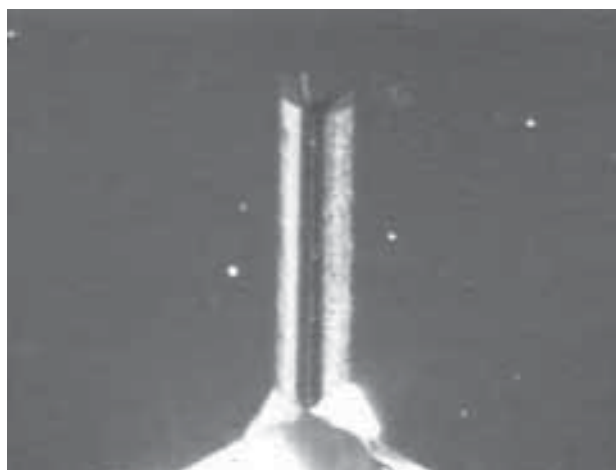


Figure 3: A channel in our device.

# The Media Coverage of Nanotechnology

Ana Isabel Arias, Computer Engineering & Business Economics,  
University of California, Santa Barbara

NNIN REU Site: Cornell NanoScale Science & Technology Facility, Cornell University

Principal Investigator & Mentor: Bruce Lewenstein, Communication Department  
and Science & Technology Studies, Cornell University

Contact: aarias@uemail.ucsb.edu, b.lewenstein@cornell.edu

## Introduction:

Work on the social and ethical issues surrounding the emerging field of nanotechnology has long been supported by the nano community. Some of the key issues discussed among this group are ethical, legal, economical, business-related, or political in nature.

A preliminary content analysis was completed last summer as a first effort at exploring the extent to which such social and ethical issues are reflected in the media and in public opinion. Articles relating to nanotechnology published between the dates of 1 January 1986 and 30 June 2003 in the New York Times, Washington Post, Wall Street Journal, and Associated Press were used in an analytical approach similar to a study done in Europe with the field of biotechnology.

The focus of this project is to update the existing preliminary analysis by coding articles published from the dates of 1 July 2003 to 30 June 2004 and to pursue the analysis in greater depth. The work involves identifying and retrieving media stories using computer databases, reading the stories and coding their content based on the prominence of themes, perspectives and positive or negative assessments, entering the data into a statistical database, and analyzing the results.

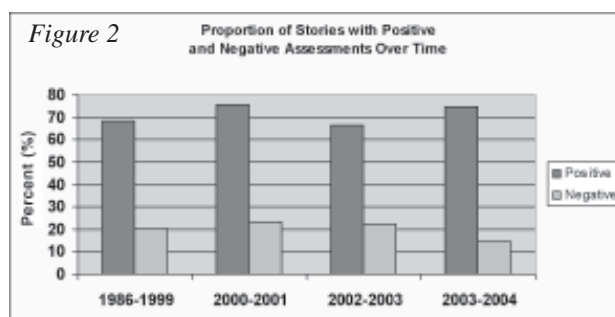
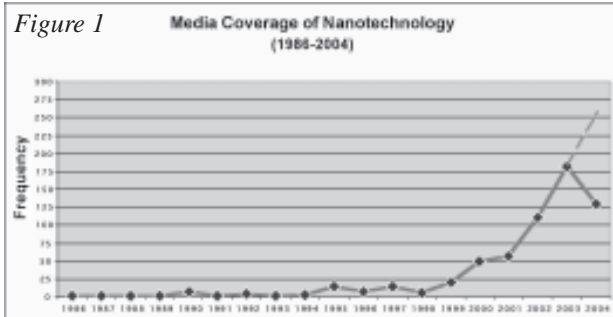
## Procedure:

The keyword “nanotechnology” was used to search online databases of newspaper articles published by the New York Times, Washington Post, Wall Street Journal, and the Associated Press dating from 1 July

2003 to 30 June 2004. A total of 245 articles containing the keyword were printed, read, and coded. The approach involved identifying key themes in the articles as well as frames, or perspectives. The main theme categories found in these articles were applications, policy, politics, financial, and safety/risks. The frames in these stories included progress, economic prospects and opportunities, ethical, Pandora’s box, runaway, public accountability, long way away, and confluence. For each theme and frame, either a zero (no mention), one (briefly mentioned), two (present), or three (dominant) was assigned depending on the prominence of the specified theme or frame in the article.

For instance, an example of Pandora’s box would be: “...studies have shown that nanoparticles can act as poisons in the environment and accumulate in animal organs” [1]. An example of the runaway frame: “...a swarm of millions of self-replicating microscopic robots, in a ravenous quest for fuel, would consume the entire biosphere until nothing remained but an immense, sludge like robotic mass” [2].

A rating was also given on the degree of positive and negative assessments of nanotechnology within the article. It is important to note than one article can have many different themes and frames as well as have both positive and negative assessments. After all articles were coded, the gathered data was entered into the Statistical Program for the Social Sciences in conjunction with the data from the existing preliminary analysis to achieve our results.



## Results and Conclusions:

Similar trends to the previous media analysis lead to the same general conclusions. Our results show that the media coverage of nanotechnology dramatically increased beginning in 1998, themes and frames found in the media coverage of nanotechnology roughly match those seen in early examples of emerging technology, such as biotechnology, and that both positive and negative aspects of nanotechnology are present in media coverage [3].

Figure 1 shows an almost nonexistent media coverage of nanotechnology up until 1998 when coverage dramatically increased at an almost exponential rate. The projected coverage through 2004 shows an even greater rate of coverage. Figure 2 shows a greater proportion of positive stories to negative ones in 2003-2004 compared to previous time periods. If we look at positive assessments by theme (Figure 3), we see that most of the positive comes from applications in nanotechnology as well as in financial opportunities. The possible applications of nano, in areas such as the environment and the medical field, are being widely discussed in these stories as well as the potential opportunity for investors to take part in what many consider to be the next revolution. Figure 4 shows that most of the negative assessments come from the risk and applications themes. There is great concern that nanoparticles could be potentially toxic and that such powerful technology can also be used for negative applications such as terrorism and environmental deterioration.

## Future Work:

Further research in this area would include updating the already existing media analysis on an annual basis to continue monitoring the media coverage of nanotechnology. By coding these articles into numerical representations of themes and frames, a big portion of the rhetoric, tone and overall content is lost. Therefore, expanding the project to include a more in-depth content analysis of the articles would be appropriate.

## Acknowledgements:

I would like to thank my principal investigator and mentor, Bruce Lewenstein, for his guidance and support throughout the whole summer. I would also like to thank the Cornell NanoScale Facility staff. Lastly, I would like to thank NNIN and the National Science foundation for the funding provided to make this research experience for undergraduates possible.

## References:

- [1] Weiss, Rick (2004). "Nanotech Poses Big Unknown to Science; As World Shrinks, Concerns Multiply." Washington Post, p.A1, 1 February.
- [2] Osborne, Lawrence (2003). "2003: The Third Annual Year in Ideas; The Gray-goo Problem." New York Times, p.73, 14 December.
- [3] Lewenstein, B.V., J.Radin, J.Diels. Nanotechnology in the Media: A Preliminary Analysis. Social and Ethical Issues in Nanotech; W.S. Bainbridge (2004).

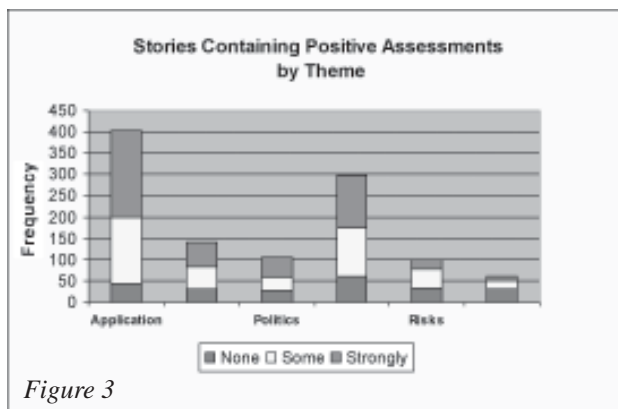


Figure 3

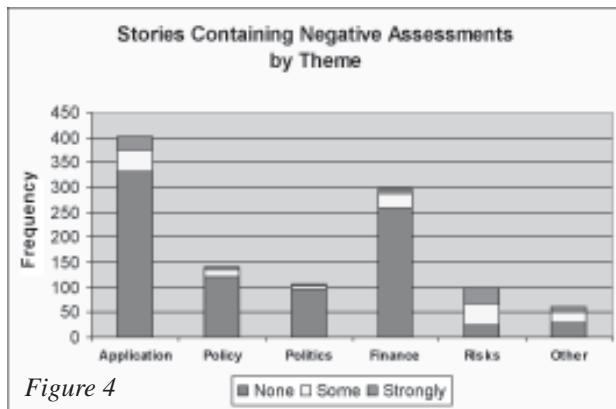


Figure 4

# Anion Exchange of GaAsSb/GaInAs Interfaces

Neha Bagga, Electrical Engineering, Oklahoma State University

NNIN REU Site: Microelectronics Research Center, University of Texas at Austin

Principal Investigator & Mentor: Archie L. Holmes, Jr., Electrical Engineering, University of Texas, Austin

Contact: neha0656@yahoo.com, holmes@ece.utexas.edu

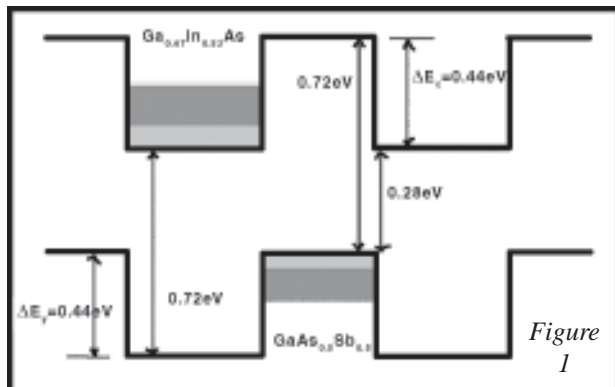
## Abstract:

The objective of this project is to investigate and study the anion exchange process at the interfaces of GaAsSb/GaInAs heterostructures. These superlattices were grown using Molecular Beam Epitaxy and characterized using High Resolution X-Ray Diffraction (HRXRD). GaInAs exposed to  $Sb_2$  flux, and GaAsSb exposed to  $Sb_2$  and  $As_2$  flux were studied in this work. The composition and thickness profiles of these grown samples were further determined using dynamical simulations. Comparisons between both studies were presented in order to better understand the As/Sb exchange process at the interfaces of GaAsSb/GaInAs.

## Introduction:

Bandgap engineering has been a prominent area of research during the past decade. Lately, several potential device applications in the mid-infrared region (2  $\mu m$ -5  $\mu m$ ) have generated much interest in arsenide and antimonide based photodetectors. Such devices have applications in chemical sensing, atmospheric sensing, gas monitoring, high speed IR-imaging and even medical diagnostics. These devices are physically realizable using type II multiple quantum well structures.

A type II quantum well structure has a staggered band alignment as shown in Figure 1. The electron transitions in such a structure are spatially indirect.



More and more interfaces are needed to maximize the number of electron transitions. Anion mixing at the interfaces can create traps in the mid-gap reducing the efficiency and sensitivity of the photodetector. Hence the structure of the interfaces is a very critical parameter as it has direct effects on the optical and electronic properties of the device.

The focus of this work is to characterize the anion exchange process at the interfaces of GaAsSb/GaInAs heterostructures. To achieve this goal, three different studies were performed.

- GaInAs exposed to  $Sb_2$  flux
- GaAsSb exposed to  $As_2$  flux
- GaAsSb exposed to  $Sb_2$  flux

Ten period superlattices were formed to introduce more interfaces to allow for an effective study of the properties.

## Procedure:

All samples for the study were grown in a customized Varian Gen II solid source MBE system. The growth chamber is equipped with group III effusion cells such as Ga, In, Al groups, and group V valved crackers for As, Sb and P. All samples were grown on InP substrate with a growth temperature was set to be 525-530°C. The exposure time was varied in the samples to change the exchange process.

The structure of the samples was analyzed by standard x-ray diffraction techniques. Dynamical simulations were conducted on the samples using RADS software to determine composition and thickness profiles.

## Results and Conclusion:

The first study was performed by exposing GaInAs to  $Sb_2$  flux to study the Sb-As exchange process. The exposure times were varied from 10 to 30s. Initially the interface layer was simulated as a single layer with a constant composition to model Sb exchange. Earlier work shows that Sb segregation is a common phenomenon in As based layers [1, 2]. Thus the

interface structure was optimized to include Sb segregation by adding another exponentially gradient interface layer where As composition decays by the following equation:

$$y = y_2 * e^{-t}$$

where  $y_2$  is the composition of As in the constant composition layer and  $t$  is the thickness of the segregation interface layer. X-ray scans for all three samples are shown in Figure 2. The satellite peaks are non-existent in the 10 second sample; some visible peaks can be seen in the 20 second sample whereas sharp satellite peaks are observed at the 30 second sample. The simulated results are shown in Table I.

$T_{\text{ex}}$	Sb Exchange			Sb segregation	
	$\text{Ga}_{0.47}\text{In}_{0.53}\text{As}$	$\text{GaInAs}(1-y)\text{Sb}(y)$	$y_{\text{ex}}$	$\text{GaInAs}(1-y)\text{Sb}(y)$	$y_{\text{ex}}$
10s	247.4Å	0.19 Å	0.2	0.10 Å	0.28
20s	250.9 Å	0.84 Å	0.2	0.50 Å	0.51
30s	246.7Å	2.07 Å	0.2	1.00 Å	0.71

The Sb exchange layer composition is virtually constant over the entire range of exposure times. The table also indicates that the thickness of the interface layer and the Sb segregation is directly proportional to the exposure time for a certain growth temperature. The x-ray scans for all three samples reveal sharp isolated peaks at either side of the substrate peak located at 6000 and -6000 relative seconds, approximately (Figure 2). This phenomenon was initially attributed to either Sb or In segregation but the modeling of the structures defied that assumption. Earlier work on similar material systems show no evidence of such an occurrence [1, 2]. At this stage these peaks could not be explained using dynamical theory alone. Other processes must be utilized to explore this phenomenon further.

The second structure was obtained by exposing GaAsSb to  $\text{Sb}_2$  flux for 30 seconds followed by the immediate overgrowth of GaAsSb layer. The x-ray simulations indicate minimal exchange at the interface layer (< 2.5%) (Figure 3a). Furthermore, the structure also shows some strain developing at the interface layer as the layers are 10% relaxed. The relaxation could be due to the quality of MBE growth.

The final structure was produced by  $\text{As}_2$  flux exposure to GaAsSb layer for 30 seconds (Figure 3b). Unfortunately x-ray simulations couldn't produce satisfactory models for the scans, thus the thickness and composition profiles for this sample could not be determined.

### Future Work:

Further research is needed to explain the As for Sb exchange process at the GaInAs on GaAsSb interface. The GaAsSb structure can be grown again under the same conditions to observe any reproducibility of results. The exposure times of  $\text{As}_2$  flux can be varied to study the effect of exposure times on the structure. Furthermore, XRD study can be supplemented with XSTM and PL to achieve proper results.

### Acknowledgments:

I would like to thank the following for their support and guidance: Dr. Archie Holmes, the MBE group, Amy Pinkston, Ms. Mallison, MER staff and NSF.

### References:

- [1] T. Brown, A. Brown, G. Mary, "Anion exchange at the interfaces of mixed anion III-V heterostructures grown by molecular beam epitaxy", Journal of Vacuum Science Technology, Vol. 20, No. 4, pp 1771-1776, July/August 2002.
- [2] J. Steinshnider, J. Harper, M. Weimer, C. Lin, S. Pei, D. Chow "Origin of Antimony segregation in GaInSb/InAs Strained -Layer Superlattices", Physical Review Letters, Vol. 85, No. 21, pp 4562- 4565, Nov 2002.

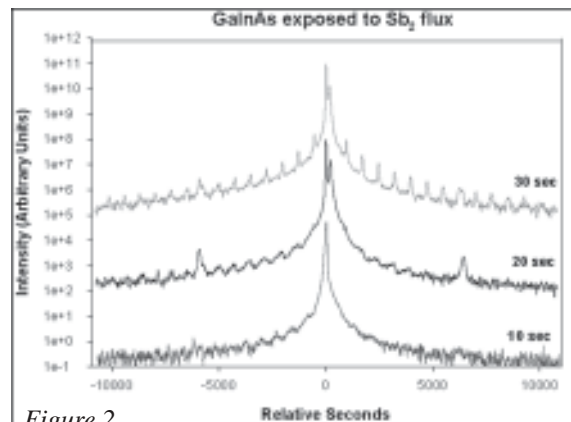


Figure 2

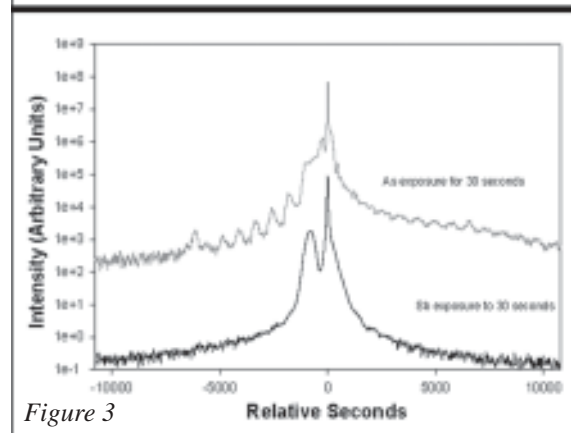


Figure 3

# Fabricating Nano-Gap Metal Electrodes using Photolithography

Nick Bastianon, Chemistry, University of California, Santa Barbara

NNIN REU Site: Stanford Nanofabrication Facility, Stanford University

Principal Investigator: Hongjie Dai, Department of Chemistry, Stanford University

Mentors: Ali Javey, Qian Wang, Department of Chemistry, Stanford University

Contact: nbastianon@umail.ucsb.edu, hdai1@stanford.edu

## Abstract:

The ability to measure the electrical properties of individual molecules is a crucial step en route to the possible use of molecules in transistors. Measuring the electronic properties is limited by difficulties encountered when trying to capture a single molecule and place it between two electrodes.

In this work, we are developing a new process to make such measurements possible. Using conventional photolithography, we are designing a procedure to fabricate nano-gap metal electrodes on a wafer scale. During fabrication, the source and drain are connected, and this connection is designed to have a weak spot, which can easily be broken with an applied voltage. By cooling the device to 4K using a liquid helium dewar and applying a voltage, we were able to break the shorted electrodes and create nm-scale gaps.

## Introduction:

Having the ability to trap an individual molecule between two electrodes is very desirable for several reasons, two of which are; being able to measure the electrical properties of a single molecule and being able to fabricate devices significantly smaller than previously thought possible. The first step in being able to achieve both of these goals is to have a device in which the gap between the two electrodes is small enough such that a single molecule will fit snugly between them. These devices can be made using electron-beam (e-beam) lithography [1, 2, 3] and photolithography. Both approaches are similar in that in each process, shorted devices are patterned then broken by applying a voltage yielding the desired gap.

The advantage of using e-beam lithography is that very small feature sizes can be patterned which, in turn, can be broken to give gaps on the range of 2-3 nm. Dai et al. and others [3] have already made these devices and the results are shown in Figure 1, showing that breakdown occurs at ~1.68 volts. The inset graph shows the tunneling current across the

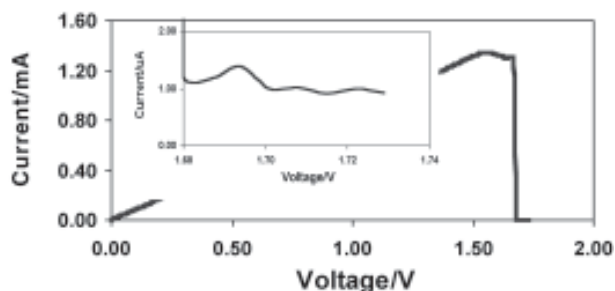


Figure 1: Electrical breakdown data for a device made by e-beam lithography.

newly formed gap, indicating a gap size of nm scale. The disadvantages to using e-beam are that it is very time consuming, expensive, and it cannot be mass-reproduced. In this work, our goal is to develop an inexpensive process using conventional photolithography that can make devices similar to those made using e-beam lithography but on a wafer scale.

## Procedure:

In order to obtain the desired gap size between the two electrodes, two separate masks were designed, one for the source electrode (half circle) and one for the drain electrode (small finger). The masks were designed to have various spacings between the electrodes with the hopes that any misalignment would still yield some functional devices. Starting with a p-type silicon substrate, a thin 10 nm gate oxide was grown. The source electrode was patterned using photolithography, and 0.5 nm Ti and 10 nm Au was deposited using e-beam evaporation. The drain electrode was patterned in the same manner, followed by evaporation of another 0.5 nm Ti and 10 nm Au. The unwanted metal and photoresist were removed by soaking the wafer in acetone for three hours. Upon closer inspection, it was determined that most of the devices had gaps between the two electrodes ranging from 100-250 nm (due to misalignment).

The approach we intended to use required a very small overlap of the two electrodes so we patterned the source electrode again. This time only 0.5 nm of

Ti and 7 nm Au were deposited, followed by soaking the wafer in acetone for three hours to remove the remaining photoresist and metal. The devices were then cooled to 4K using a liquid helium dewar followed by electrical breakdown.

### Results:

A completed device is shown in Figure 3 with the electrical breakdown data in Figure 2. The break occurred around 6.2 volts, which is a lot higher than we wanted. The e-beam devices broke at ~ 1.6 volts and there was a tunneling current left after the break; the devices we fabricated did not have any tunneling current after the break occurred. Figure 4 is a Scanning Electron Microscopy (SEM) image of a representative device made by photolithography after the break. From this image it can be seen that the breaks were not very clean, but in some regions, the gap is within the desired range. We feel the inconsistent gap ranges across the break are caused by excessive overlap, which requires higher voltage to break the devices resulting in a more violent break.

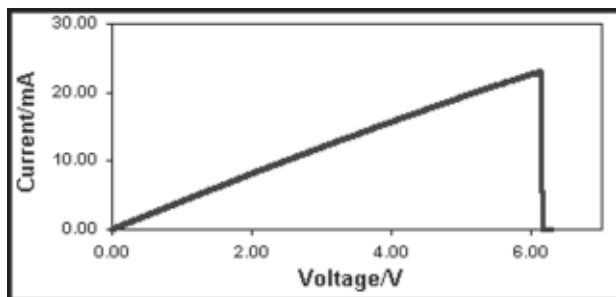


Figure 2: Electrical breakdown data for a device made by photolithography.

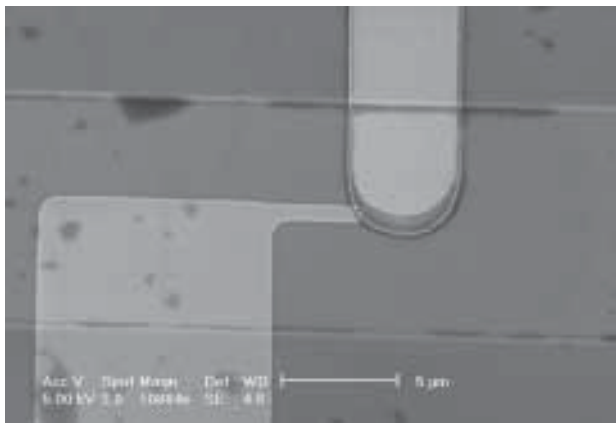


Figure 3: SEM image of completed device made by photolithography.

### Summary and Future Work:

In this work, we have developed a process to fabricate devices with nm scale gaps. The process still needs to be optimized but we feel that we are on the right track and can easily achieve our goal of making 2-3 nm gaps using photolithography.

Our plans include varying the thickness of both electrodes such that one is very thick and the other is very thin. Our hope is that this will allow us to form an even weaker spot, which can be broken at a very low voltage (< 1V). Once the process is optimized, we plan to deposit various molecules in the gaps and begin measuring their electrical properties and determine their possible use in transistors.

### Acknowledgements:

I would like to thank the Center for Integrated Systems, the National Science Foundation, and the National Nanotechnology Infrastructure Network for making this summer possible. I would also like to thank my P.I. Hongjie Dai, the SNF staff, along with the entire Dai group for taking the time to train and guide me through my work. Finally, I would like to give a very special thanks to my mentors Ali Javey and Qian Wang for all of their guidance and patience this summer.

### References:

- [1] Park, J. et al., "Coulomb blockade and the Kondo effect in single-atom transistors," Nature 417, 722-25 (2002).
- [2] Liang, W. et al., "Kondo resonance in a single molecule transistor," Nature 417, 725-729 (2002).
- [3] Park, H. et al., "Fabrication of metallic electrodes with nanometer separation by electromigration," Applied Physics Letters 59, 301-303 (1999).

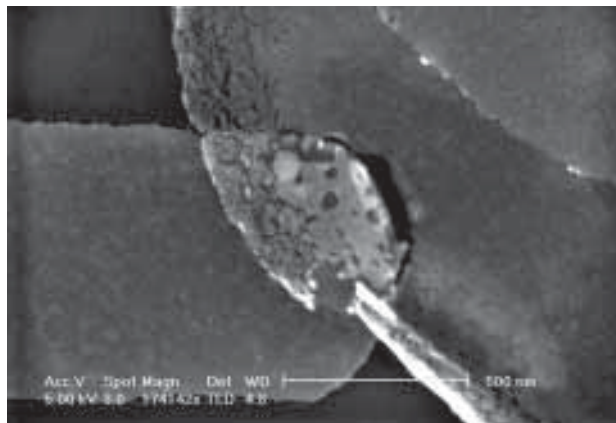


Figure 4: SEM image of a device made by photolithography after electrical breakdown.

# Selective Oxidative Patterning of Self-Assembled Organothiols on Gold

Priya Bhatia, Chemical Physics, Rice University

NNIN REU Site: Penn State Center for Nanotechnology Education and Utilization, Pennsylvania State University

Principal Investigator: Paul S. Weiss, Departments of Chemistry and Physics, Pennsylvania State University

Mentors: Adam Kurland and Amanda Moore, Chemistry, Pennsylvania State University

Contact: pbhatia@rice.edu, stm@psu.edu

## Abstract:

Ozone and ultraviolet light have been implicated in Self-Assembled Monolayer (SAM) oxidation. Although these agents have been successfully used to fabricate simple patterns of alternating oxidized and non-oxidized species at the micron scale, the full potential of oxidative patterning at the nanometer scale has yet to be explored. SAM oxidation chemistry is highly complex and the precise oxidation mechanisms are not yet fully understood.

Here, we report novel methods for: 1) elucidating the oxidation reaction dependence on oxidative agents and SAM functionality; and 2) fabricating oxidized surface-patterns. Our methods use commonly available tools, and afford ease and simplicity in comparison to conventional methods.

## Introduction:

The desire to develop simple techniques for the nanoscale patterning of SAMs has driven interest in understanding the complex processes of SAM oxidation. Although several research groups have used oxidative agents in conjunction with masks of various geometries to create oxidized patterns of SAMs [1], the specific nature of SAM oxidation remains unclear.

Researchers demonstrated that exposing SAMs to a broadband ultraviolet (UV) source in air results in SAM oxidation [2]. However, UV light of 185 nm in the presence of oxygen also generates ozone and it was uncertain whether 185 nm light directly oxidized SAMs by photo-oxidation or if the resulting ozone was the true oxidant. A few years later, it was found that ozone alone can induce SAM oxidation implying that ozonolysis is the responsible mechanism [3].

Most recently, however, researchers have demonstrated that a 254 nm ozone-free UV source can oxidize mercaptoundecanoic acid (MUDA), but not octadecanethiol (C18) [4]. These findings indicate that the terminal carboxylic acid functionality may play a role in another oxidation mechanism. Especially interesting is the possibility of selectively oxidizing different organothiols using various combinations of

oxidative agents.

Past studies used costly and laborious processes to research the effects of individual oxidants. We have developed a simple, readily available technique utilizing a UV clean instrument that can separate and manipulate oxidation variables. The UV clean instrument exposes samples to a broad-band UV source and generates ozone within a contained environment. Glass microscope slides, which block all UV irradiation, and quartz microscope slides which block deep UV but transmit 254 nm light, were used to mask the samples.

## Procedure:

Wafers of amorphous Au thermally evaporated onto silicon were submerged in 1 mM solutions of MUDA, mercaptohexadecanoic acid (MHDA) and C18 for 18 hrs to form ordered monolayers. A sample each of MHDA, MUDA and C18 was pressed against fresh quartz and glass slides and taped creating a "pocket" to minimize air infiltration. The covered samples were placed in a Boeckel 135500 instrument for 13 minutes, which was determined to be the ideal time span for exposure. Samples were removed and ellipsometric height was measured using a Gaertner Fixed Angle LSE Stokes Ellipsometer. Samples were then rinsed for one minute with 18 M $\Omega$  deionized water followed by a thirty second rinse in ethanol to remove any remaining oxidized species and ellipsometric measurements were retaken.

## Results and Conclusions:

**UV Clean/No Screen; Control:** Prior to UV clean, the MUDA monolayer measured approximately 18Å in height, 7Å higher than in previous experiments. The extra height may indicate the presence of interdigitated bilayers. After UV clean, the height dropped to 7Å followed by complete monolayer degradation after a water/ethanol wash (Figure 1). The monolayer removal after washing indicates that complete oxidation occurred during the UV clean and the 7Å visible before washing were likely the remnants

of oxidized species. We term the difference in height after UV clean but before washing as “volatile desorption.” The MHDA and C18 samples showed similar trends to MUDA; some degree of volatile desorption followed by complete monolayer removal after washing.

**No UV Clean/Glass Contact Screen:** A glass contact screen was placed on a sample each of MUDA, MHDA and C18 (without UV cleaning) to determine effects of the glass slide on monolayer thickness (Figure 2). The MUDA sample exhibited no change in height after removal of the glass contact screen but did exhibit a decrease in height after washing. This height decrease can likely be attributed to partial removal of the interdigitated bilayer during washing rather than any effects of the glass contact screen. The samples of MHDA and C18 showed no change in height before or after washing indicating that the presence of the glass microscope slide does not detectably influence monolayer height.

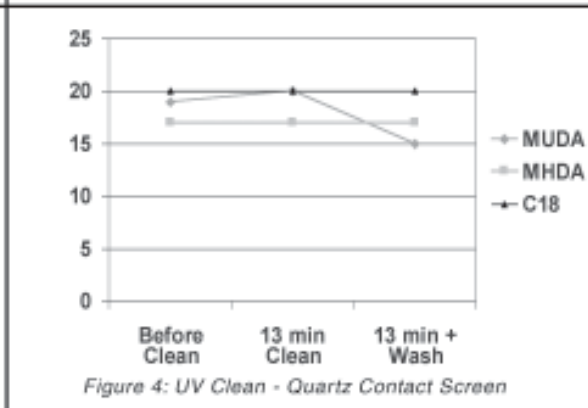
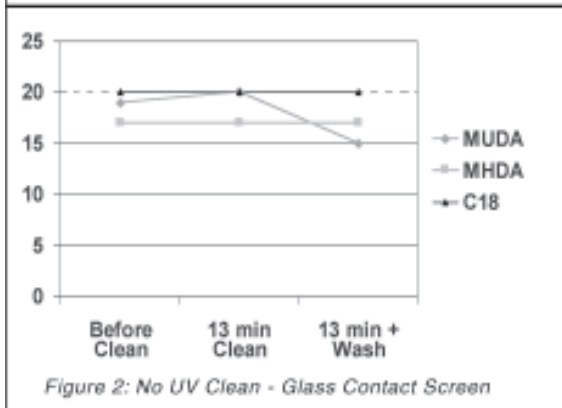
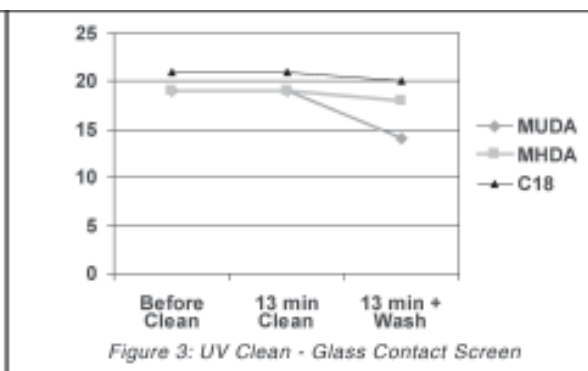
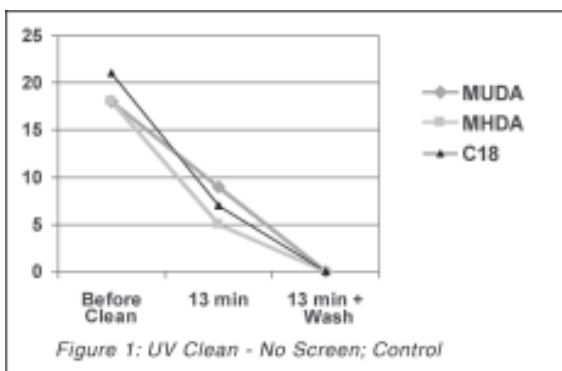
**UV Clean/Glass Contact Screen:** UV cleaned samples of MUDA, MHDA, and C18 with a glass screen displayed similar results to glass-screened samples which were not UV cleaned (Figure 3). This indicates that the glass contact screen protected the samples from UV and ozone exposure, preventing oxidation.

**UV Clean/Quartz Contact Screen:** After UV cleaning with a quartz contact screen, MUDA exhibited a 6Å loss in monolayer height and a further 7Å height loss after washing, indicating partial oxidation (Figure 4). These results are strikingly different from MUDA with a glass contact screen which exhibited no monolayer loss after UV cleaning. MHDA also exhibited a significant loss in monolayer height after UV cleaning whereas C18 demonstrated only minor height loss.

These results demonstrate clear differences in the oxidation of carboxylic-acid terminated SAMs (MUDA, MHDA) and alkyl-terminated SAMs (C18). The glass contact screen prevented the infiltration of UV light and ozone thereby preventing oxidation in all SAMs whereas in the case of the quartz screen which transmitted 254 nm light, partial oxidation was induced in MHDA and MUDA.

#### References:

- [1] Huang, J.; D.Dahlgren; J.Hemminger; Langmuir 1994, 10, 626-628.
- [2] Huang, J.; J.Hemminger; JAmChemSoc 1993, 115, 3342-3343.
- [3] Zhang, Y.; R.Terrill; T.Tanzer; P.Bohn; JAmChemSoc.; (Communication); 1998; 120(11); 2654-2655.
- [4] Brewer, N. J.; Rawsterne, R.E.; Kothari, S.; Leggett, G.J. J. Amer. Chem. Soc. 2001, 123, 4089 - 4090.



# Electrowetting for DNA Sequencing on Chip

Kevin Brady, Biomedical Engineering, Johns Hopkins University

NNIN REU Site: Stanford Nanofabrication Facility, Stanford University

Principal Investigator: Peter Griffin, Electrical Engineering, Stanford University

Mentor: Ali Agah, Electrical Engineering, Stanford University

Contact: brake2002@hotmail.com, griffin@plumb.stanford.edu

## Abstract:

Digital microfluidics is a technique that is based on controlled manipulation of unit-sized microdroplets. One of the methods for microdroplet actuation is electrowetting, which involves using an electric field to modify the wetting behavior of a nano-liter-sized liquid droplet in contact with an insulated electrode. Electrowetting allows for controlled dispensing, transport, mixing, and splitting of large numbers of these droplets across electrode arrays. We extend the use of the electrowetting device to DNA sequencing on a silicon wafer.

In our study, we designed and built arrays of electrodes, wired to a series of control pads programmed to run the reaction of pyrosequencing of DNA. Upon incorporation of a nucleotide, a pyrophosphate molecule is released, which will be converted to ATP and, in a cascade enzymatic reaction, produce visible light which will be detected at a site away from the reagents. By utilizing the electrowetting device to perform miniaturized pyrosequencing of DNA, the development of a more reliable, higher-automated sequencing technology is in sight.

## Introduction:

Electrowetting is the enabling technology behind miniaturized lab-on-chip systems, which is changing the way experimentation is being done today. Electrowetting involves using linear arrays of electrodes for manipulation of unit-sized liquid droplets. These microdroplets, which act as solution-phase reaction chambers, are transported, mixed, split, reacted, or analyzed in a discrete manner using a standard set of basic, programmable instructions [1, 2]. These basic instructions are used to create a lab-on-chip environment for miniaturized experimentation. In Figure 1, the two-plate electrowetting setup is shown.

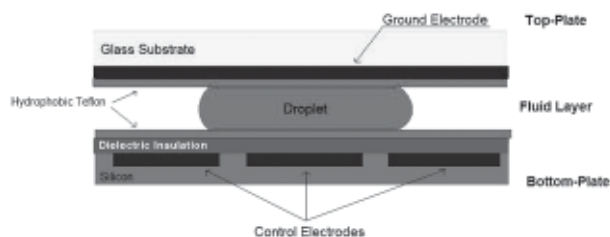


Figure 1: The electrowetting setup: A side view of digital microfluidics.

Electrowetting works much the same way as traditional analysis systems, only with much smaller volumes and much greater automation. Continuous fixed-flow microfluidics is a simpler alternative to electrowetting, but offer little in terms of reconfigurability and scalability [2]. Fixed flow channels also require large volumes of liquid for priming, which is not very cost-effective.

Work is being done to test the applications of electrowetting on wider ranges of established chemistries and protocols by scaling down to the nanoliter droplet format. In our study, we extend the use of electrowetting technology to pyrosequencing of DNA on a silicon wafer. Pyrosequencing is a DNA sequencing technique involving detection of released pyrophosphate and visible light resulting from DNA synthesis [3]. First, a single-stranded DNA template reacts with a nucleotide and DNA polymerase to produce pyrophosphate. In a cascade of enzymatic reactions, ATP is generated, which drives the reaction of luciferase with luciferin to produce visible light proportional to the amount of ATP present. Each nucleotide

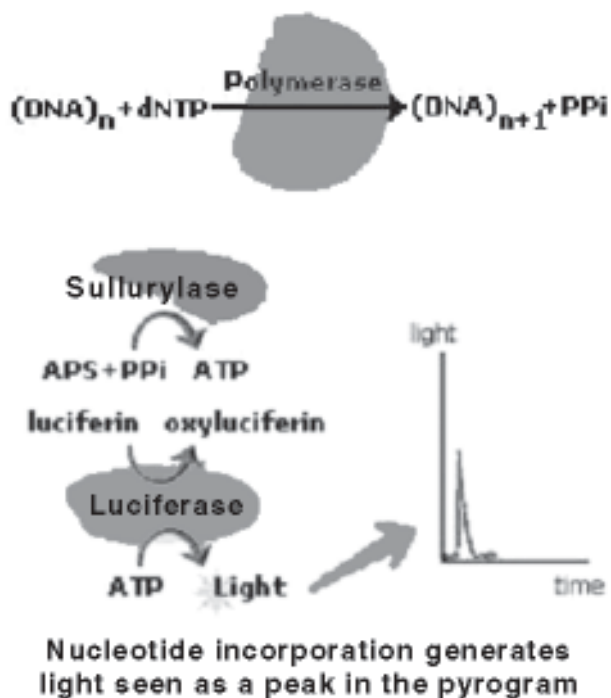


Figure 2: Cascade enzymatic reaction of pyrosequencing.

is added one at a time, and since the nucleotide added is known, the sequence of the DNA can be determined. This process shown in Figure 2, although it sounds simple, is quite expensive and cumbersome.

Our research group wishes to miniaturize the process, reducing the amount of sample and reagents needed. Miniaturization of pyrosequencing using electrowetting will reduce costs and increase automation, both crucial to large scale genetic testing.

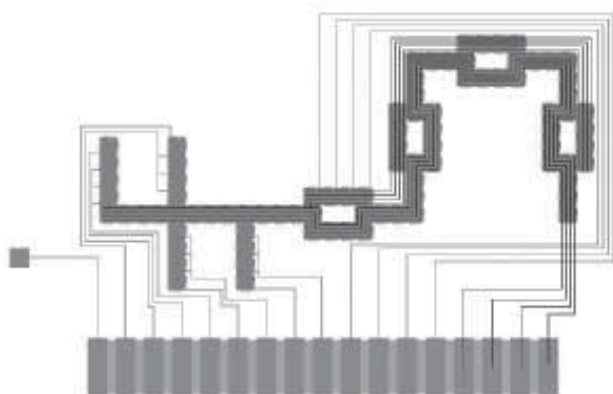


Figure 3: Our four-layered design of the electrowetting device.

#### Procedure:

Using the CAD program L-Edit, we designed our four-layered electrowetting device as shown in Figure 3. First a layer of oxide was grown on our silicon wafers. We then exposed and developed the buried wire layer on the surface of the oxide. After etching, we sputtered titanium metal on each wafer. We then baked in the oven at 650°C for 30 mins which created a titanium silicide layer and a titanium nitride layer.

After stripping the nitride layer, we deposited a thin layer of low temperature oxide. Next we exposed and developed the via-hole layer onto our wafers, etched holes down to the buried wire layer and sputtered aluminum metal on each wafer. We exposed and developed our electrode layer onto the surface of the aluminum and etched the surrounding aluminum away to form our patterned electrode arrays. We then deposited one more layer of LTO and etched holes down to our control pads. Finally we coated the wafer with a thin layer of Teflon®.

For the top plate, we coated a glass wafer with a thin layer of indium tin oxide, which we annealed to our substrate at 340°C for 10 minutes. Next we coated the wafer with Teflon®. Finally we brought the bottom plate and top plate together with spacers and tested the device for movement of droplets across the electrode arrays.

#### Results and Discussion:

We have completed the fabrication of the electrowetting chip. In Figure 4 is a TEM image of two interlocking electrodes from our completed wafer. We tested oscillation of droplets across electrodes, and we successfully moved liquid droplets across the four-phase transport hub. We believe this lab-on-chip for pyrosequencing of DNA using electrowetting shows great promise. Our study suggests that our device may help to miniaturize the process of DNA sequencing to lower costs and increase throughput and automation. We have yet to test the dispensing, splitting and merging structures on the chip, and our research group is still working on a means of detection of visible light. If a light signal can be detected when pyrosequencing reagents are reacted on our electrowetting chip, this will be the first step towards a successfully miniaturized pyrosequencer.

#### Acknowledgements:

NSF funding through the NNIN REU program at Stanford Nanofabrication Facility has made this study possible. I thank Professor Peter Griffin and Ali Agah for mentoring and guiding me this summer, and Mike Deal and the rest of the staff at SNF for coordinating the REU program at Stanford.

#### References:

- [1] Duke University, <http://www.ee.duke.edu/Research/microfluidics/>.
- [2] Vijay Srivivasan, Vamsee K. Pamula and R.B. Fair, An integrated digital microfluidic lab-on-a-chip for clinical diagnostics on human physiological fluids, *Lab on a Chip*, 2004, 4, 1-11.
- [3] Mostafa Ronaghi, Pyrosequencing sheds light on DNA sequencing. *Genome Research*, 2001, 11, 3-11.
- [4] Graphic adapted from [www.pyrosequencing.com/pages/technology.html](http://www.pyrosequencing.com/pages/technology.html).

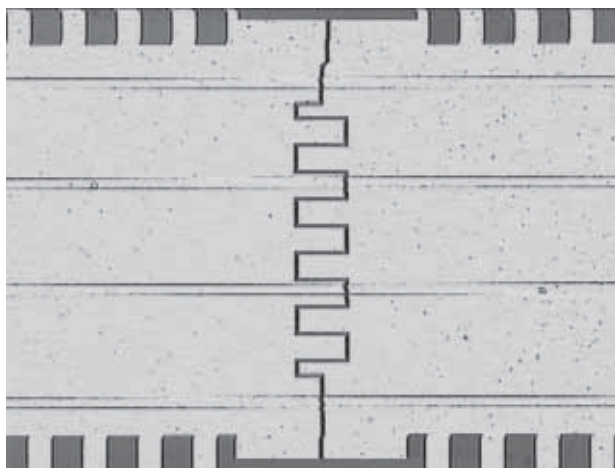


Figure 4: TEM image of two interlocking electrodes.

# Design and Fabrication of Tapered Waveguides in AlGaAs for Coupling Light in Nanoscale Optoelectronic Devices

Nathaniel Burt, Electrical Engineering, Kansas State University

NNIN REU Site: Stanford Nanofabrication Facility, Stanford University

Principal Investigator: James S. Harris, Electrical Engineering, Stanford University

Mentor: Luigi Scaccabarozzi, Applied Physics, Stanford University

Contact: nburt@ksu.edu, harris@snowmass.stanford.edu

## Abstract:

While typical frequency-conversion devices in use today require that optical signals be transformed by slow and power-consuming electrical circuitry, all-optical devices would be an appealing alternative, eliminating the need for electric conversion. Our work is concerned with improving the coupling efficiency in existing submicron-scale AlGaAs waveguides having an embedded microcavity. This can be achieved by adding a tapered structure at each end, which greatly increases coupling at both the input and the output facets. We have optimized parameters of two taper geometries through simulations. Measurements of relevant optical characteristics are presented.

## Introduction:

The aim of this project is to design and fabricate a structure capable of coupling more light into an existing nanoscale all-optical frequency conversion device [1]. Because the device has sub-wavelength cross-sectional dimensions, a significant size mismatch exists between its tightly confined propagating mode and the field propagating in free space. The coupling efficiency is determined by the overlap integral between the fields on either side of the interface, so the mode size must be transformed toward the ends of the device to closely match the free-space field. A well-documented, highly effective solution involves adding a tapered section to each end of an optical device.

## Preliminary Investigations:

Researchers have achieved modal expansion within optical devices using many types of waveguide tapers [2]. Two general types exist—tightly confining waveguides flaring outward at the ends and loosely confining waveguides with inward tapers at the ends. We have investigated the two laterally tapered structures shown in Figure 1.

We simulated and optimized both end facet geometries using a semi-vectorial finite difference

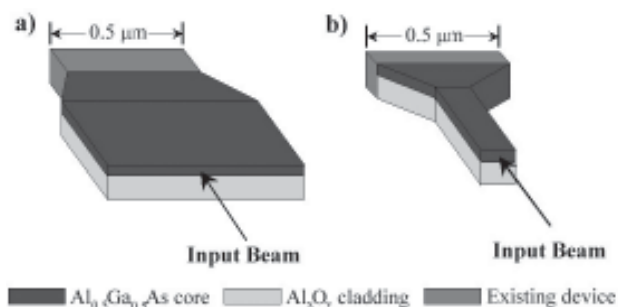


Figure 1: Laterally tapered waveguides.  
a) conventional taper and b) inverse taper.

frequency domain scheme [3]. All structures were assumed to have a 200 nm thick  $\text{Al}_{0.5}\text{Ga}_{0.5}\text{As}$  ( $n=3.3$ ) core above a completely oxidized, 2.5  $\mu\text{m}$  thick  $\text{Al}_{0.97}\text{Ga}_{0.03}\text{As}$  ( $n=1.61$ ) lower cladding, as these are inflexible parameters of the existing microcavity waveguide. The incident energy was approximated as a Gaussian beam having a  $1/e^2$  radius of 2  $\mu\text{m}$ .

The first structure of interest, a conventionally tapered waveguide, is similar to the existing device in that its upper cladding is air. It is attractive because it would require few changes in the fabrication process. The high index of refraction contrast between the core and air cover (3.3 to 1) causes the propagating mode to be tightly confined within the core. The structure flares laterally outward at both end facets, allowing horizontal expansion of the mode toward the ends of the device. Our simulations indicated that this conventionally tapered waveguide would yield a modest coupling efficiency of 32% at an optimum width of 4  $\mu\text{m}$ .

While flaring the waveguide outward allows the mode to expand laterally, the mode must also expand in the vertical direction in order to closely match the Gaussian intensity distribution of the incident light. A waveguide having a very small core area at the end facets effectively squeezes the mode out of the waveguide, allowing for significant horizontal and vertical expansion of the mode. Our simulations indicated that a waveguide inversely tapered to

approximately 170 nm in width would yield a coupling efficiency of just over 90%. It is logical that the most efficient end facet has a nearly square core given that the desired mode profile is circularly symmetric.

#### Device Fabrication:

The fabrication process begins with growth of a heterostructure by molecular beam epitaxy. A 2.5  $\mu\text{m}$  thick  $\text{Al}_{0.97}\text{Ga}_{0.03}\text{As}$  layer to be used as the lower waveguide cladding is deposited onto a GaAs substrate, followed by a 200 nm thick  $\text{Al}_{0.5}\text{Ga}_{0.5}\text{As}$  layer that later forms the waveguide core. Next, the positive electron-beam photoresist PMMA (950K, 2%) is spun onto the wafer to a thickness of approximately 80 nm. A Raith150 electron-beam lithography system is then used to transfer the waveguide patterns to the PMMA. A solution of MIBK:isopropanol=1:3 is used to develop the PMMA.

The next step is the definition of waveguide sidewalls to a depth of approximately 1  $\mu\text{m}$ . Because PMMA is a poor dry etch mask, a 20 nm thick chromium film is deposited via electron-beam evaporation and selectively removed during the standard liftoff procedure. The chromium acts as a highly effective mask during the subsequent chlorine-based dry etching process, which defines the waveguide sidewalls.

After the chromium mask is removed, the refractive index of the  $\text{Al}_{0.97}\text{Ga}_{0.03}\text{As}$  layer below the core is changed from 3.3 to 1.61 by oxidation in a 420°C furnace having a 100 sccm flow of water vapor and nitrogen. The oxidation rate was observed to be constant at roughly 130 nm/min. Successfully fabricated conventionally tapered waveguides are shown in Figure 2.

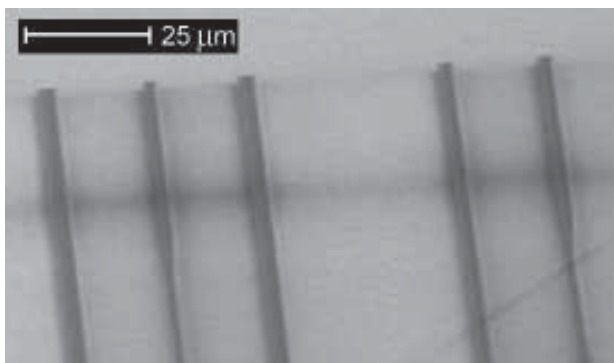


Figure 2: SEM micrograph of conventionally tapered waveguides.

#### Results and Conclusions:

We have fabricated conventionally tapered waveguides and characterized their relevant optical properties. Although simulations predicted that these waveguides would have relatively low coupling efficiencies, they are easily fabricated and therefore offer a simple means of validating numerical simulations. As shown in Figure 3, measured coupling efficiencies of conventionally tapered devices agree well with simulations.

#### Future Work:

We are refining the fabrication of inversely tapered waveguides. Once inversely tapered waveguides of satisfactory quality have been produced, we will characterize their optical properties. We will also numerically analyze the misalignment tolerances of our most promising devices.

#### Acknowledgements:

I would like to thank my mentor, Luigi Scaccabarozzi, for his guidance and patience, Katrin Cox for her many simulations, Michael Deal, Jane Edwards, Maureen Baran, Melanie-Claire Mallison, the SNF staff, CIS partners, and the NSF.

#### References:

- [1] L. Scaccabarozzi, Z. Wang, X. Yu, W.T. Lau, M.F. Yanik, S. Fan, M.M. Fejer, J.S. Harris, Jr., Proc. SPIE, vol. 5355, pp. 111-119 (2004).
- [2] I. Moerman, P. P. Van Daele, and P.M. Demeester, IEEE J. Sel. Topics Quantum Electron., vol. 3, pp. 1308-1320 (1997).
- [3] M.S. Stern, IEE Proceedings J (Optoelectronics), vol. 135, no. 1, pp. 56-63 (1988).

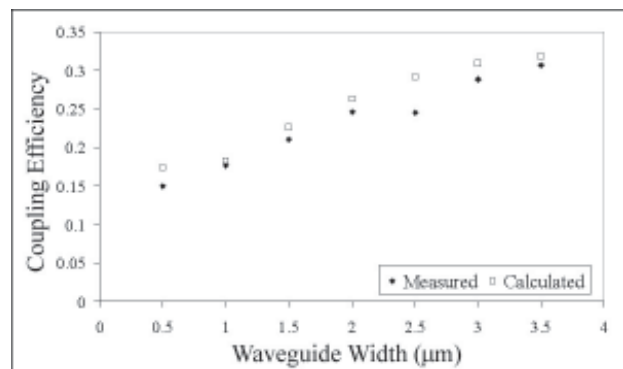


Figure 3: Comparison of measured and simulated coupling efficiencies for conventionally tapered waveguides.

# Etch Resistance of Polymers used in Supercritical Carbon Dioxide Development

Heather Carroll, Chemical Engr. and World Literature, North Carolina State University

NNIN REU Site: Cornell NanoScale Science & Technology Facility, Cornell University  
Principal Investigator: Dr. Christopher Ober, Materials Science and Engineering, Cornell University  
Mentor: Nelson Felix, Chemical and Biomolecular Engineering, Cornell University  
Contact: hmcarrol@ncsu.edu, cober@ccmr.cornell.edu

## Abstract:

Photoresists are commonly developed in such corrosives as tetra-methyl ammonium hydroxide. Supercritical carbon dioxide (SCCO<sub>2</sub>) development offers a more environmentally-friendly alternative, as it is readily available for use and very easy to recycle or discard. Reactive Ion Etch testing, using oxygen and trifluoromethane gases, is being performed on photoresists that become soluble or insoluble in SCCO<sub>2</sub> upon ultraviolet exposure. The photoresists being analyzed include positive-tone fluorinated resists containing perfluorooctyl methacrylate groups, negative-tone silicon-containing polystyrene-based resists and positive-tone polysilsequiazane resists.

Current research yields data that shows the fluorinated photoresists have the least etch resistance of the three sets previously mentioned. The silicon-containing polystyrene-based photoresists etch at about half the speed of the fluorinated resists, most likely due to their lack of fluorine and negative-tone behavior. This etch data is currently being used to further the characterization of these photoresists for their use in development in SCCO<sub>2</sub>.

## Introduction:

Research of SCCO<sub>2</sub> as a developer is dependent upon the photoresists used in the development process. The purpose of this research project is to investigate one of the

fundamental process characteristics of photoresists used in development with SCCO<sub>2</sub>. The specific photoresists discussed include those found to be soluble in SCCO<sub>2</sub>—a set of fluorinated resists shown in Figure 1, a polystyrene-derived silicon resist and a polysilsequiazane resist.

## Procedure:

Photo Acid Generators (PAG) and resist were dissolved in a 10% PAG to resist ratio in roughly 1 ml of solvent (methyl isobutyl ketone for silicon resists or trifluorotoluene for fluorinated resists). Wafers (150 mm) were primed with HMDS for fluorinated resists, left clean for silicon resists. Photoresists were spun on a table-top spinner at 2000 or 2500 rpm. The wafers were post-baked at 115°C for one minute. Flood exposures of varying lengths (to ensure good exposure) were then performed on half of the wafers, generally at 235-260 nm for the fluorinated photoresists and 405 nm for the silicon photoresists. The film thickness of the photoresist was then measured with a profilometer. The silicon wafers were then placed into an RIE plasma etcher and etched for 1:30 (fluorinated resists) minutes or 3 minutes (silicon resists) at a time with a CHF<sub>3</sub> and O<sub>2</sub> etch (40 sccm). The film thickness on the silicon wafer was then re-measured.

## Results and Conclusions:

By dividing the difference in thickness by the time etched, we determined the etch rates of these photoresists.

P1, also known as 2-(4-ethylphenyl)-2-propyl adamantoate with perfluorooctyl methacrylate groups, the first fluorinated photoresist, had average etch rates between 15 nm/min (unexposed) and 19 nm/min (exposed).

P2, also known as 2-(4-ethylphenyl)-2-propanol with perfluorooctyl methacrylate groups, had etch rates of anywhere from 0.5 nm/min to 33 nm/min. The reason for the large variation is that we did three trial runs of P2 using different percentages of perfluorooctyl groups on the main chain polymer. The first, V5, which was 80% fluorinated, gave etch rates of 8.5 nm/min to 33 nm/min. The second, V7, which was 35% fluorinated, gave etch rates of 0.5 nm/min to 15 nm/min. The last, V11, which was 65% fluorinated, surprisingly gave etch rates of 12 nm/min to 29 nm/min. When averaged and graphed, we get a graph like that of Figure 2. While there does not seem to be a correlation from the data, there is a possibility that the %

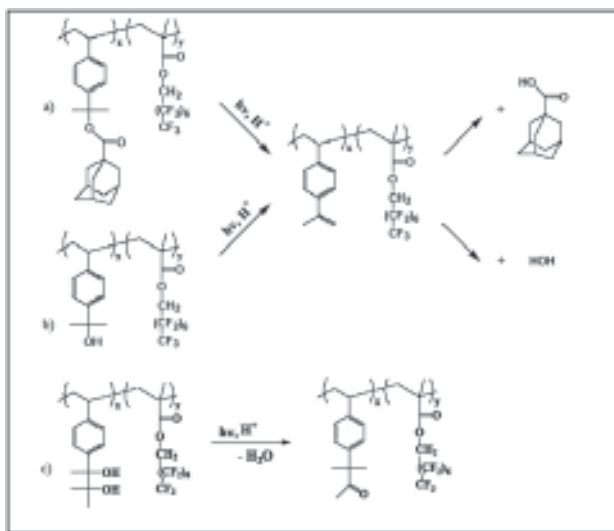


Figure 1: a) P1, b) P2 and c) P3 and their solubility switches.

fluorine has a direct relationship with the etch rate, as you can tell from the error bars present. From this, it could be possible that the more perfluorooctyl groups in the resist, the faster it etches.

P3, also known as 2-(4-ethenylphenyl)-3-methylbutyl-1,2 diol with perfluorooctyl methacrylate groups, had etch rates slower than the other two groups of fluorinated resists, most likely because it was only 35% fluorinated. P3 had etch rates between 5.5 nm/min and 11 nm/min.

S1, also known as poly(chloromethylstyrene-co-trimethylsilylstyrene), had etch rates that were generally slower than those of the fluorinated resists, between 3.5 nm/min and 18 nm/min. We performed three trials using different molecular weights of S1, 11,000 g/mol, 22,000 g/mol and 100,000 g/mol. The 11k trial gave exposed etch rates of 2.8 nm/min to 9.2 nm/min. The 22k trial gave exposed etch rates of 2.4 nm/min to 10 nm/min. The 100k trial gave exposed etch rates of 2.3 nm/min to 8.2 nm/min. Graphing the etch rates versus the molecular weights of S1, we get Figure 3. It is hard to define a relationship between the etch rate and molecular weight of S1, but within the error bars, it could be suggested that as the molecular weight increases, the etch rate decreases.

S2, a polysilsequiazane, had etch rates between 10 nm/min and 16 nm/min.

The graph comparing the discussed etch rates to the control Shipley 1813 resist is shown in Figure 4.

**Future Work:**

More research should be pointed at determining the relationships between % fluorine and etch rates presented in the fluorinated resists found in this research. Research should also be performed on the relationship between molecular weight of S1 and etch rate of S1.

**Acknowledgements:**

H. Carroll thanks Dr. Christopher Ober, Nelson Felix and the research team at Cornell University for all their help. Carroll also thanks NNIN, NSF and CNF for their support of the research.

**References:**

- [1] Allen, Robert D., Sharon K. Obendorf and Christopher K. Ober, et al. "Supercritical CO<sub>2</sub> Processing for Submicron Imaging of Fluoropolymers." Chem. Mater., 12, 41-48 (2000).
- [2] Ober, Christopher K. and Gina L. Weibel. "An overview of supercritical CO<sub>2</sub> applications in microelectronics processing." Microelectronic Engineering, January 2003, vol. 65, issue 1, 145-152.
- [3] Pham, Victor. Ph.D. Thesis, Cornell University, 2004. Chapters 4, 5.

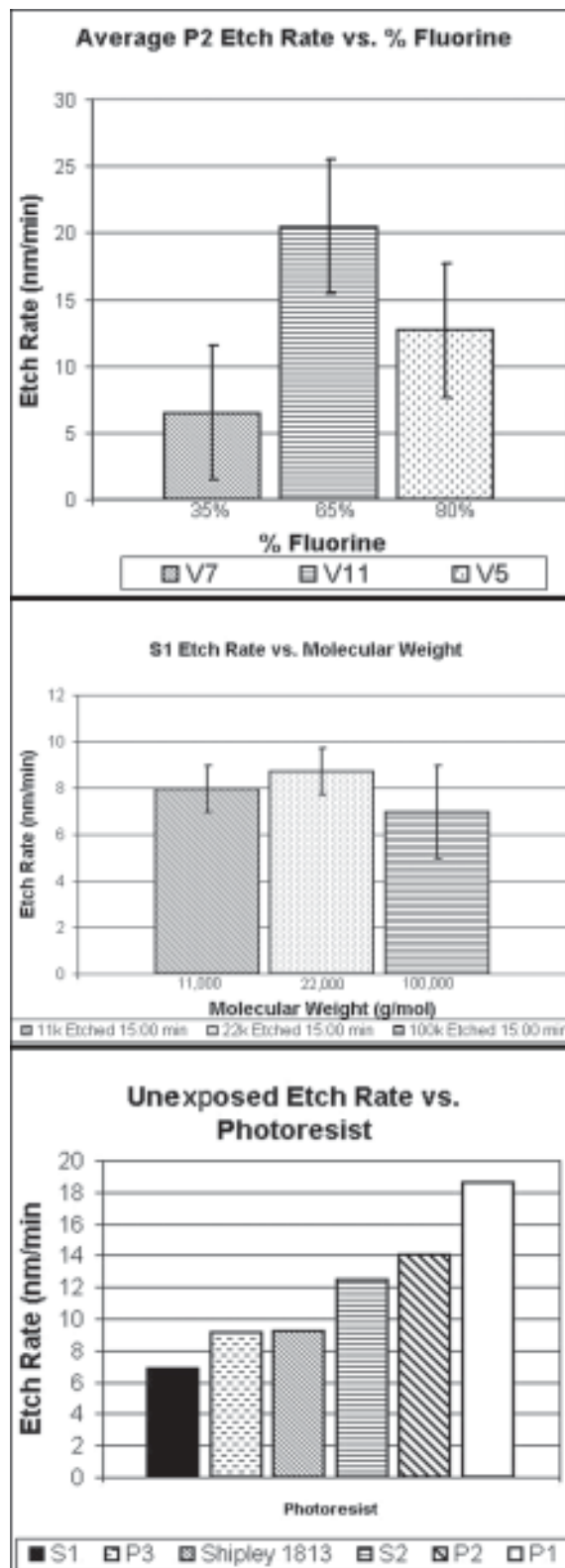


Figure 2, top: Average P2 etch rate vs. % Fluorine in trials V5, V7 and V11.

Figure 3, middle: S1 Etch Rate vs. Molecular Weight.  
Figure 4, bottom: Unexposed Etch Rate vs. Photoresist.

# Design and Characterization of a Microcoil for Inter-Arterial Monitoring

Kovner Chalumo, Physics, Howard University

NNIN REU Site: Materials Science Research Center of Excellence, Howard University

Principal Investigator: Gary L. Harris, Ph.D., P.E., Professor and Associate Director, MSRCE, Howard University

Mentor: Abhishek Motayed, MSRCE, Howard University

Contact: kchalumo@howard.edu, GHarris@msrce.howard.edu

## Abstract:

This paper focuses on the design and characterization of a micro-implantable telemetric system used for monitoring inter-arterial blood pressure, and monitoring parameters (physical dimensions, inductance, capacitance, resistance) of the device that effectively modify the efficient transmission of power.

Evaluation and characterization of an implantable telemetric unit is of utter importance because of parasitic electric effects that take effect during transmission of electromagnetic waves at high alternating current frequencies. These electrical parasitic effects are responsible for signal degradations as well as other hindering phenomena. There are requirements that this system must fulfill; it must be powered remotely, ergo, doing so efficiently, consume little to no power (ideally), and present little if any effect on the human body. Silicon carbide technology offers interesting perspectives for inter-arterial, inter-cranial, and inter-ocular sensor development.

## Introduction:

Telemetry involves the transmission of information/data from a fixed point to a remote receiving system. The information/data that is sent telemetrically can, for example, be the response of a capacitive unit implanted in a human artery. Proliferations of this example are used frequently in medical applications.

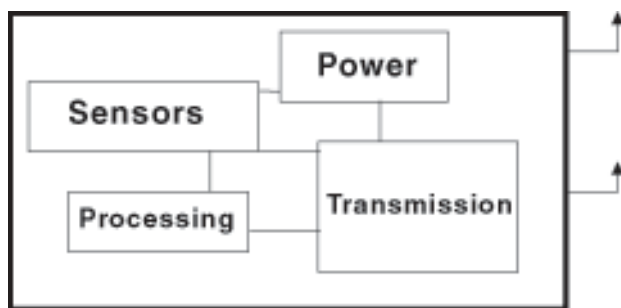


Figure 1: A simplified telemetric unit for monitoring purposes: sensors, processing circuitry, transmission circuitry, power circuitry, and housing case.

Implantable medical devices are not limited to, but include, monitoring inter-arterial, inter-cranial, and inter-ocular measurements.

Implantable telemetric units can be implemented in micromechanical technologies using silicon as a building block. Other means have proven themselves difficult and inefficient. So using micromachining and silicon, there is a greater feasibility that telemetric systems can be made economically efficient.

## Telemetric System Configuration:

A simplified rendition of a telemetric unit can be seen in Figure 1. Telemetric monitoring operates on the principal of continuous measurement of certain parameters, with transmission of these data to a remote system. Figure 1 displays the crucial components necessary for a minimal telemetric unit: the power controller, signal circuitry, transmission circuitry, and sensor device, without compromise to the housing case. An ideal microtelemetric system for implantation consumes little power, is powered remotely and is capable of transcutaneous transmission.

Figure 1 implies various implementations. The power source can be either a battery or an inductively coupled power link. The latter implementation is the main focus of this paper. The device in Figure 1 essentially works as a transceiver, capable of functioning remotely, void of any battery power. So, inductive coupling participates heavily, if not most heavily, in sound transfer of power from the remote to the host implanted system. The sensor device can be configured using piezoresistive, capacitive, or resonant sensors. We have decided to utilize a capacitive sensor because monitoring blood pressure requires measuring stress variations in blood level. The other sensors are incapable of this function.

## Theory:

The objective of this research is a preliminary task which involves characterizing a planar microcoil for use in an implantable microsystem. The task is

preliminary because it is part of a process which includes designing, characterizing, and fabricating a telemetric device for inter-arterial blood pressure monitoring. This paper focuses on the design and characterization of a planar microcoil so that transmission of power from a remote system to host is maximized and efficient.

Below is a list of physical phenomena that participate in effectively reducing/increasing efficient power transfer:

**Self-Inductance:** Self-inductance is defined as the magnetic flux per unit current in a coil. Simply, self-inductance is two times the energy stored in the magnetic field divided by the square of the current through the coil. We have focused on the self-inductance of various coils that operate on low-frequencies and have no skin effect.

**Series Resistance:** The series resistance of a planar microcoil can be divided into two. One which is dependent of frequency and one which is not. The frequency dependent resistance is a result of the strong time-varying magnetic fields produced by the alternating current in the circuit. The dependent resistance is a result of the wire materials resistivity, which varies for different materials. This series resistance can be deduced using Ohm's law.

**Parallel Resistance:** The parallel resistance is caused by the finite resistance of the insulating layer in which the coil is placed. The influence of parallel resistance is negligible; therefore, we will disregard it in our endeavors.

**Parasitic Capacitance:** The parasitic capacitance of the microcoil is composed of 3 individual capacitances; the capacitance between the turns and substrate, the coil's turns and the capacitance between the pads and substrate.

**Mutual Inductance:** The mutual inductance between two coils depends on the self-inductance of the receiver coil and a special parameter, which is a measure of the coupling, and depends on the relative positioning of both the coils.

**Q-Factor:** The Quality-factor of a receiver is a measure of efficiency. The q-factor of a coil is directly proportional to the transmitted energy the coil receives, yet indirectly proportional to the energy of heat dissipated by that receiver. Another way to express the efficiency of a coil is in terms of the coil's impedance or output voltage with respect to the frequency at which the coil operates. Hence, the greater the quality factor the better the transmission.

## Results and Conclusions:

As the outer/inner ratio of the coil increases,  $z$  (Figure 2), the resistance and capacitance of the coil decreases. We realized a indirect relationship between the two. In contrast, the intrinsic resonance frequency and Q-factor increase with the outer/inner ratio. If the frequency of the transmitter remains constant, the preceding statement fails to hold any validity. The Q-factor reaches a maximum when the outer/ratio of the coil is about 0.3. As the intrinsic resonance frequency increases, the amount of energy for collection increases. The Q-factor of a microcoil can be maximized by three main factors; 1. decreasing the series resistance of the microcoil, 2. decreasing the parasitic capacitance, and 3. increasing the self-inductance of the microcoil.

## Acknowledgements:

Gary L. Harris, Ph.D., P.E. Professor and Associate Director, and Abhishek Motayed, both of MSRCE, Howard University.

## References:

- [1] C.R. Neagu, Characterization of a planar microcoil for implantable Microsystems, Sensors and Actuators A62 (1997), pp. 599 - 611.
- [2] R. Puers, Linking sensors with telemetry: impact on the system design, Tech. digest 8th Int. Conf. Solid State Sensors and Actuators. Stockholm, Sweden, June 25 - 29 June, 1995, pp. 47 - 50.
- [3] F.E. Terman, Radio Engineers Handbook, McGraw-Hill, London. 1943.

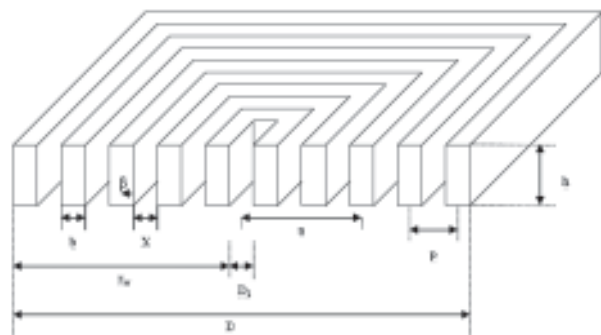


Figure 2: Cross-section of a planar microcoil displaying geometric parameters and the relations between them.  $z = D_i/D$ ,  $p = x_1 + b$ ,  $r_w = (D_i - D)/2 = D(1 - z)/2$ ,  $a = (D_i + D)/4 = D(1 + z)/4$ ,  $s = D_i + r_w = D(1 + a)/2$ ,  $N = R_w/p = D(1 - a)/2$ ; where  $D =$  diameter of coil,  $r_w =$  winding depth,  $b =$  width of wire,  $h =$  height of wire,  $a =$  mean radius of coil,  $D_i =$  internal diameter,  $\beta =$  current depth penetration,  $x_1 =$  distance between adjacent turns.

# Nanometer-Scale Lithography using an Atomic Force Microscope

Peter Cochran, Mechanical Engr. and Applied Mechanics, University of Pennsylvania

NNIN REU Site: Nanotech at UCSB, University of California Santa Barbara

Principal Investigator: Dr. Evelyn Hu, Electrical & Computer Engineering, University of California Santa Barbara

Mentor: Dr. Brian Thibeault, Electrical & Computer Engineering, University of California Santa Barbara

Contact: cochran@seas.upenn.edu, hu@ece.ucsb.edu

## Abstract:

With the current development of nanoscale mechanisms, the necessity to create  $< 50$  nm features on surfaces is becoming an important ability for researchers to have. Current lithography tools are either too inadequate or too expensive, e.g. optical and electron-beam lithography, for modest researchers to employ, which has led to the development of Atomic Force Microscope (AFM) Lithography. AFM lithography is an emerging technology praised for its cost-efficient potential to create  $< 50$  nm (as low as 10 nm) features on silicon and other substrates. However reproducibility issues have plagued researchers in reaching this tool's potential. During our research we have discovered key methods to resolve these issues to make AFM lithography a robust tool.

These methods include using non-contact mode microscopy during oxidation to reduce AFM tip wear and increase control of oxide size. Controlling variables such as tip voltage, scan height, scan speed and humidity enable the user to systematically calibrate the size of the oxide written. Through these methods, we were able to consistently produce oxide lines 50 nm in width, 1 nm in height and several microns in length, and were able to reproduce these lines over 30 times without sign of tip decay.

## Introduction:

AFM lithography uses anodic oxidation to create features on the target surface using electrically conductive tips. Due to atmospheric humidity, an ambient layer of water exists on the surface of the substrate which provides the oxygen species necessary for oxidation. A meniscus forms between the tip and sample due to the small distance (around 5 nm) between them. A voltage bias is applied to the tip to generate a strong electric field on the order of  $10^9$  V/m, which causes hydroxide-ion diffusion and drives hydroxide ions from the water meniscus to the surface.

From our studies, it can be seen that using non-contact mode during oxidation promotes long tip life

and reproducible data. Feature width (and height) is primarily linked to voltage bias. Width can also be varied with scan speed, average tip height, and humidity. We have also found that surface conditions play a key role in the reproducibility of data. It was found that using a hydrophilic tip and a hydrophobic substrate produced the best results.

We have also found that the thinnest features can be produced by oxidizing a series of dots, rather than lines, on the surface. This can be done by positioning the tip close to the surface to form a water bridge between the tip and surface. This water bridge can be stretched to confine hydroxide-ion diffusion thus resulting in smaller features [1].

## Procedure:

Each AFM tip was imaged using the FEI Sirion SEM before and after oxidation to examine the effect of tip wear during oxidation. The tip is then placed on the microscope and engaged on the surface (usually silicon). We used the Digital Instruments Nanoscope IV for every experiment. After we realized contact lithography was too erratic, we conducted every experiment thereafter in non-contact mode. We oxidized the surface by drawing a series of lines. This is done by scanning the tip across the surface at a steady height and steady speed, with a voltage bias always on.

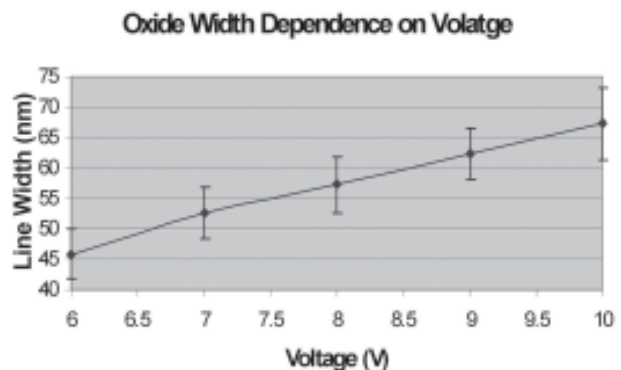


Figure 1

We experimented systematically with various parameters, mainly tip voltage bias, scan speed, and amplitude set point (AS). The latter determined the amount of damping the oscillating tip underwent when engaged. From later experiments, we could derive a relationship between AS and average distance from surface (AS increases as z-distance increases). We also experimented systematically with surface conditions of tip and substrate, i.e. hydrophilic nature.

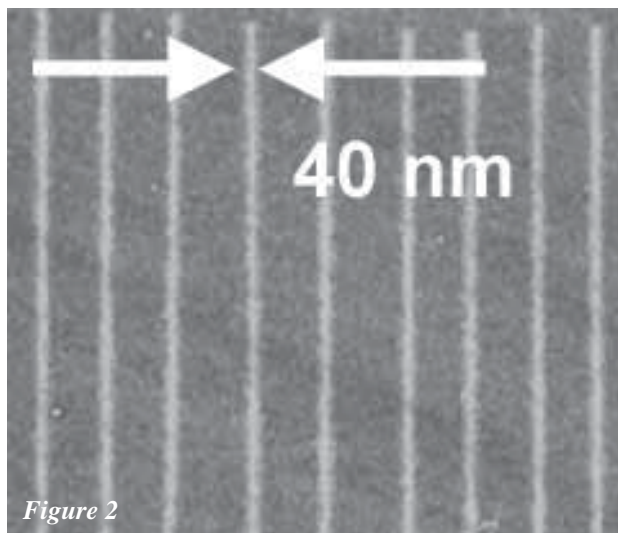


Figure 2

### Results and Conclusions:

Of the three main parameters, we found that voltage bias was a first-order parameter; oxide height and size were primarily linked to voltage (Figure 1). Higher voltage bias produced taller and wider oxides. For our tests, we ranged the voltage from -6V to -12V, scan speed about 0.1  $\mu\text{m/s}$ , and average z-distance roughly 7-8 nm. Each tip was calibrated using these parameters to achieve best results. We could consistently reproduce lines 1 nm high and 50 nm wide, and as small as 30 nm wide (Figure 2). Also, we found that because non-contact mode was used, virtually no tip was broken or worn unless mistreated.

For this type of non-contact lithography, a.k.a. line drawing, we found best results with hydrophobic surfaces. This is because as the probe moves across the surface, the water meniscus between the tip and sample must always exist for oxidation to occur. Because the surface is hydrophobic, the meniscus can easily slide across the surface, as opposed to a hydrophilic surface, where the meniscus is attracted to the surface. If the meniscus is attracted to the surface, there will be too much tension on the meniscus and it will break, causing irregularities.

Likewise, best results arise when the tip is hydrophilic because the meniscus tends to follow the tip. Also, due to contact angles, the shape of the meniscus will be smaller with a hydrophilic tip, resulting in a narrower oxide (Figure 3).

For future experiments, we found it promising that instead of “drawing lines”, smaller oxide widths can be achieved by connecting series of small dots. We will use a hydrophilic surface, because we are no longer “dragging” the tip along the surface, but rather positioning the tip above the surface, applying a voltage to oxidize, and repeating. In other words, voltages will be pulsed as opposed to being continuous. Because of this, we can use a hydrophilic surface to achieve the smallest possible meniscus width, again due to contact angles (Figure 4).

### Acknowledgements:

I would like to thank Brian Thibeault, Bill Mitchell, and Evelyn Hu for their help and mentoring abilities, and also the NSF and the CNSI for their support.

### References:

- [1] Calleja, Garcia, Roher, Appl.Phys. 86, 1899, 1999.
- [2] Keller, Franke, Surf. Sci., 294, 409, 1993.

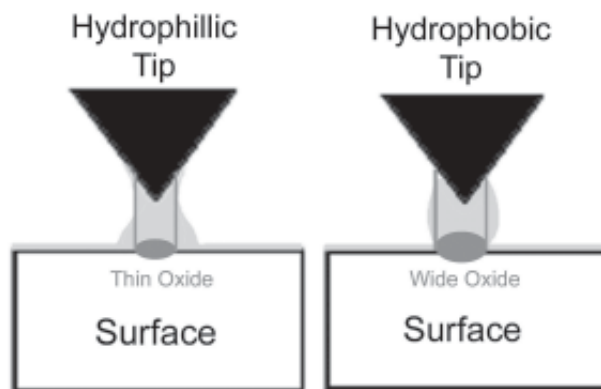


Figure 3

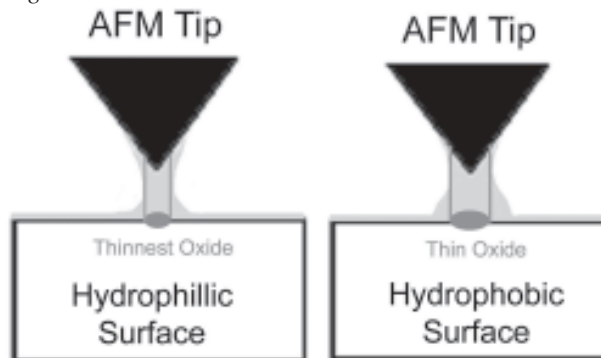


Figure 4

# Biomaterials in Microsystems: An Investigation of the Effect of Parent Ti Microstructure on the Morphology of Nanostructured Titania

Diana DeRosa, Biosystems Engr., Biochem. & Molecular Biophysics, University of Arizona

NNIN REU Site: Nanotech at UCSB, University of California Santa Barbara

Principal Investigator: Dr. Noel MacDonald, Materials Department, University of California Santa Barbara

Mentor: Zuruzi Abu Samah, Materials Department, University of California Santa Barbara

Contact: dianad1@email.arizona.edu, nmacd@engineering.ucsb.edu

## Abstract:

Nano-structured titania (ns-TiO<sub>2</sub>) has many desirable properties for integration into biological systems and nano/micro electrical mechanical systems (N/MEMS). Ns-TiO<sub>2</sub> is being considered for applications ranging from catalyst for organic decontamination, cell scaffolds for implantable devices and sensing elements for detection of gases and biological macromolecules.

One promising route for implementing ns-titania into N/MEMS devices is by reacting titanium films with aqueous hydrogen peroxide (H<sub>2</sub>O<sub>2</sub>) solution. Hence the effect of parent Ti microstructure and H<sub>2</sub>O<sub>2</sub> solution on the morphology ns-titania produced needs to be understood. This work investigates the kinetics of the above reaction using an electro-oxidation method. The effect of parent Ti film thickness, deposition rate of Ti films, H<sub>2</sub>O<sub>2</sub> concentration and temperature on the reaction kinetics was investigated.

## Introduction:

There are two main objectives for researching the reaction of ultra-thin titanium metal films (< 0.5 μm) with H<sub>2</sub>O<sub>2</sub> solution to form nano-structured titania (TiO<sub>2</sub>). The first is to understand the kinetics of the reaction and to determine the rate-limiting step. The second is to evaluate the morphology of the ns-titania as related to the reaction conditions and the microstructure of the parent Ti films.

We found two reaction kinetics depending on thickness of the parent Ti film. For films less than 50 nm thick, the kinetics are interface-reaction controlled. For thicker films, the reaction is controlled by the diffusion of Ti through an intermediate gel layer. The titania gel layer has a porous sponge-like morphology and is amorphous. Upon annealing at 300°C, the gel crystallizes into anatase nano-crystals about 5-25 nm in diameter. The ns-titania layer was evaluated using UV-Vis, XRD, AFM, and SEM.

## Procedure:

The main method that evaluates the progress of the reaction is electro-oxidation. A thin film of Ti is

evaporated onto a glass substrate in the form of a circuit. The circuit is closed using a Digital Multimeter to record resistance changes as the reaction takes place. The circuit on the glass slide is then partially submerged into a beaker of 180 ml of 10% H<sub>2</sub>O<sub>2</sub> that has been heated to 80°C. A lid with a slit cut out for the glass slide covers the beaker, and PDMS is used to seal the remaining incongruities between the slit and the slide. Figure 1 shows a diagram of this setup.

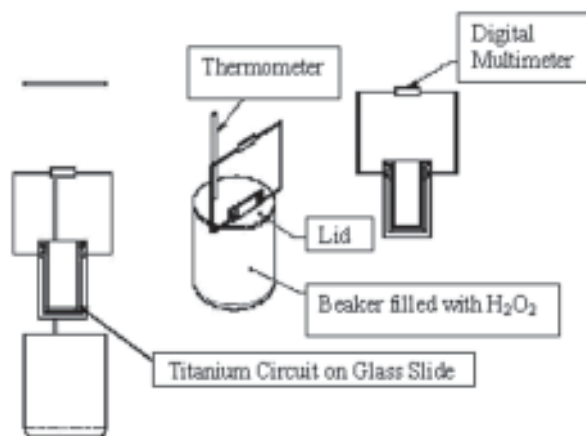


Figure 1: Diagram of the Electro-Oxidation Method.

Using the electro-oxidation method, the reaction is evaluated as a function of time, temperature, parent Ti film thickness, H<sub>2</sub>O<sub>2</sub> concentration, and deposition rate of the Ti film.

Scanning Electron Microscopy (SEM), Atomic Force Microscopy (AFM), X-Ray Diffraction (XRD) and UV-Visible Spectroscopy are implemented to evaluate the morphology of the ns-titania.

## Results and Conclusions:

For the electro-oxidation data, refer to the table of graphs in Figure 2. The thicker Ti films (> 0.5 μm) proceed by a diffusion-limited reaction kinetic, and the thinner Ti films (< 0.5 μm) proceed by an interface-limited reaction kinetic (Figure 2A). The lower concentrations of H<sub>2</sub>O<sub>2</sub> (5% for 50 nm and 5, 10% for 200 nm) proceed by the diffusion-limited kinetic, and the higher concentrations proceed by the interface-

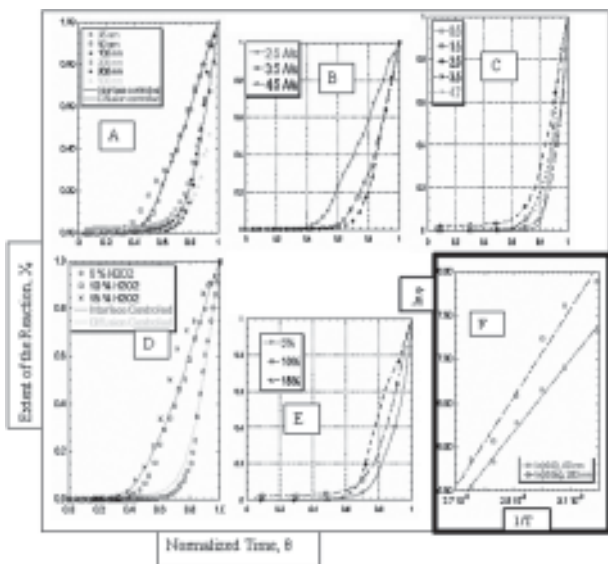


Figure 2: Table of Graphs.

limited reaction kinetic. Figure 2D is the graph for the 50 nm samples and 2E is the graph for the 200 nm samples. For the slower deposition rates of the 50 nm samples, the reaction proceeds by the interface reaction kinetic (Figure 2B). All of the 200 nm samples proceed by the diffusion-limited reaction kinetic when varying the deposition rate (Figure 2C). The normalization method for the electro-oxidation data is explained in Figure 3.

Normalization	Activation Energy Analysis
At $\frac{dR}{dt} = 0$ , $t = t_{\infty}$ and $R(t_{\infty}) = R_{\infty}$	$\varphi = \varphi_0 e^{-\frac{E_a}{kT}}$
Extent of the reaction, $X = \frac{R(t) - R(0)}{R(t_{\infty}) - R(0)}$	$\ln \varphi = \frac{E_a}{kT} + \varphi_0$
Normalized Time, $\theta = \frac{t}{t_{\infty}}$	Figure 3: Calculations.

As the Ti ions and the  $H_2O_2$  react, they form an amorphous gel layer through which the molecules must diffuse for the reaction to take place. Which molecule diffuses is unknown. At the thinner films, the gel layer is so thin that the rate-limiting step is the actual binding of the  $H_2O_2$  molecules to the Ti (IV) ion, or the interface control. At thicker films, the diffusion of the molecules through the gel layer is the rate-limiting step, or the diffusion control.

By varying the temperature, it is possible to find the activation energy required for the reaction to occur (Figure 2F). In Figure 3, the way the activation energy graph is plotted is explained. The activation energy for the interface controlled reaction kinetic is exactly double what Sever theorized the activation energy of one  $H_2O_2$  molecule to bind to one Ti (IV) ion [1]. Samuni postulated that the reaction mechanism might

take place between a Ti (IV) ion and more than one molecule of  $H_2O_2$  [2]. It is likely that the mechanism for the interface-controlled reaction occurs with the binding of two  $H_2O_2$  molecules to one Ti (IV) ion.

The XRD and UV-Vis data is only used to verify that the samples we are creating actually are titania, and that upon annealing the amorphous  $TiO_2$  at  $300^\circ C$ , we were forming an anatase crystal structure. The SEM and AFM photos were used to evaluate the morphology of the ns-titania, as formed, as a function of the thickness of the parent Ti film.

In Figure 4, it is evident that for thicker Ti films, the ns-titania has a porous, sponge-like morphology. For thinner Ti films, the ns-titania has a porous, grain-like morphology.

### Future Work:

The future work for this project includes optimizing the process conditions to implement ns-titania into actual devices. In this work unpatterned ns-titania films are formed. However, implementation of ns-titania into practical devices requires the use of patterning of ns-titania films. Hence further work should study the feasibility of different materials such as silicon nitride and silicon dioxide as masks. Also, the effect pore size of the ns-titania needs to be quantified using gas-adsorption techniques. This is critical for application of ns-titania as 'active' components in devices for macromolecular separation.

### Acknowledgments:

NSF; DARPA; NNIN REU; Angela Berenstein, Director; Zuruzi Abu Samah, Mentor; Dr. Noel MacDonald, P.I.

### References:

- [1] R. Sever, T. Root, J. Phys. Chem. B. 2003, 107, 4090.
- [2] A. Samuni, J. Phys. Chem. 1972, 76, 634.

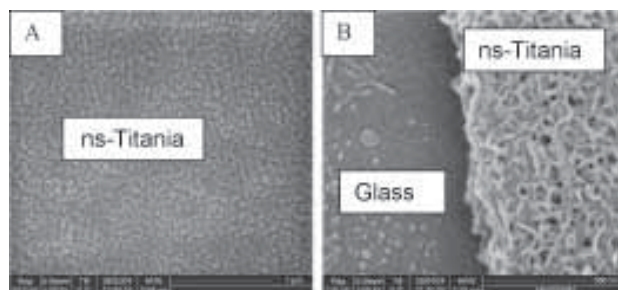


Figure 4: SEM: A, 100 nm parent Ti film; B, 500 nm parent Ti film.

# Insulation of a Carbon Nanotube Interface for Retinal Prostheses

Carl Dietz, Applied Physics, Yale University

NNIN REU Site: Stanford Nanofabrication Facility, Stanford University  
Principal Investigator: James Harris, Applied Physics, Stanford University  
Mentor: Ke Wang, Applied Physics, Stanford University  
Contact: carl.dietz@yale.edu, harris@snowmass.stanford.edu

## Abstract:

Retinal prostheses are a novel attempt at restoring human vision. We have designed a novel prosthetic device using carbon nanotubes, and attempted to design a passivation layer for the device. We were successful in fabricating a passivation layer using silicon dioxide and silicon nitride films.

## Introduction:

Human vision is the result of an electrical signal generated in the retina. Two of the leading causes of blindness, age-related macular degeneration and retinitis pigmentosa, damage the cells responsible for generating this signal, but leave intact the system of cells which delivers the signal to the brain [1]. Retinal prostheses would, in theory, deliver a signal from an imaging device to the nerve system and restore sight.

Instead of using traditional planar electrodes to deliver a signal, our device uses an array of carbon nanotube pillars which would give greater proximity to the retinal nerve system, thus requiring less power and delivering a higher quality signal. To limit the signal at only the desired target neurons, the substrate and the sidewalls of the array must be passivated. Various coatings were tested on the device for passivation, and methods of exposure for signal delivery were attempted.

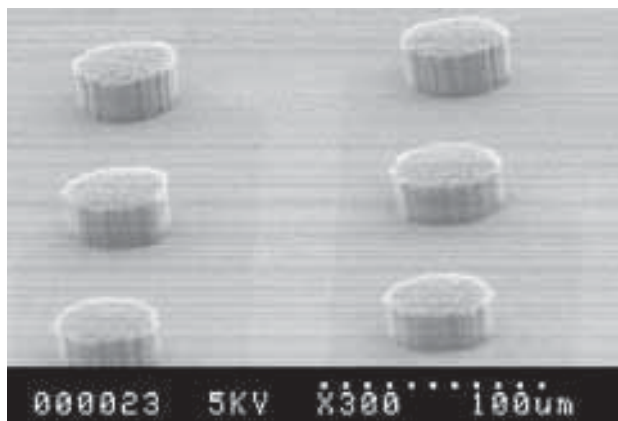


Figure 1: An array of uncoated nanotube pillars.

## Fabrication and Experimental Method:

Our prototype device was fabricated on a silicon substrate, covered with 5000Å of SiO<sub>2</sub>. A 6 x 6 array of electrodes was deposited on the substrate, consisting of a thin film of polysilicon, an adhesion layer of titanium, and platinum. A lead seed was deposited at the tip of each electrode, and nanotube pillars were grown on the electrodes using a CVD process. The growth conditions were in an environment of 99.8% ethylene at 700°C for 15-30 minutes [2].

Two different types of passivation layers were tested: spin-coated polymers, and PECVD deposited silicon oxide and nitride films. In each instance, the material was deposited and the device contacts were exposed. The arrays were then examined using scanning electron microscopy. We tested the arrays for leakage current by soaking each device in a

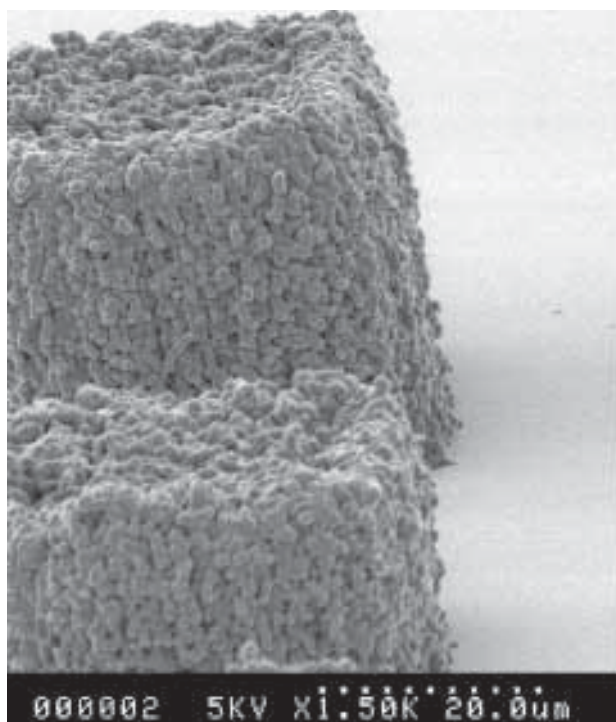


Figure 2: Nanotube pillars coated with 1000Å oxide, 2000Å nitride.

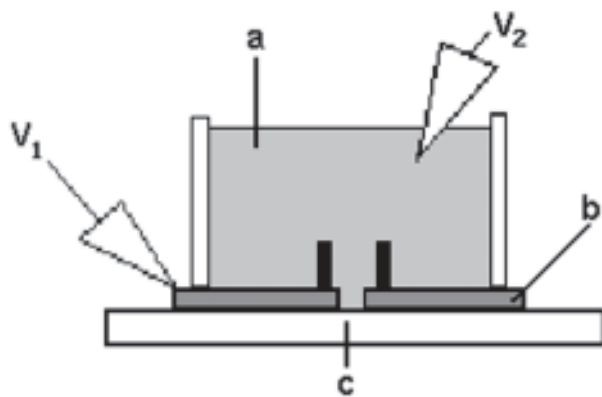


Figure 3: Leakage current testing. (a) Saline solution. (b) Pt electrodes with carbon growths. (c) Silicon substrate.

phosphor-buffered saline solution, and placing a probe on a contact and a Pt counter electrode submerged in solution. Current versus voltage was then measured from zero volts to two volts bias.

An appropriate passivation layer for our purposes must reduce the leakage current emitted by the array by at least two orders of magnitude. Additionally, the layer must be biocompatible, biostable, and hermetic to be compatible with its environment in the retina.

### Experimental Results and Discussion:

A number of spin coated polymers were tested on the arrays to test the nanotube pillars' ability to withstand a spin coating. Shipley 3612 and Microchem SU-8 2007 were deposited, as well as HD Microsystems PI 2556 polyimide. Low viscosity polymers coated the arrays well, while higher viscosity ones ripped the pillars off. Both 3612 and SU-8 successfully coated the arrays; however, neither is biocompatible. The polyimide solution had a higher viscosity and destroyed the device in spin coating.

Two thicknesses of oxide/nitride coatings were tested. The first was 1000Å of oxide capped by 2000Å nitride; the second was 1300Å oxide, followed by 5400Å nitride, followed by another 1300Å oxide. The conditions for deposition of the oxide were a plasma of SiH<sub>4</sub> and NO<sub>2</sub> at 350°C; the conditions for deposition of the nitride were a plasma of SiH<sub>4</sub> and NH<sub>3</sub> at 350°C. Since the deposition is done at a moderately high temperature, there is concern of thermal stress build-up between layers which expand at different rates. The thicknesses of the triple coating are intended to minimize the stress between layers and avoid cracking.

Leakage currents were tested for each coating for biases between zero and two volts, and compared to

leakage currents for uncoated nanotube arrays. The 1000Å oxide / 2000Å nitride coating reduced leakage current by approximately two orders of magnitude; the 1300Å oxide / 5400Å nitride / 1300Å oxide coating reduced leakage current by almost three orders of magnitude.

### Summary and Conclusions:

Carbon nanotube arrays for retinal prostheses were fabricated, and were tested with various passivating coatings. We have concluded that a sandwich layer of silicon oxide and nitride is appropriate to meet the demands of the device and its intended environment. The thicknesses of the oxide and nitride films were optimized so as to minimize stress within the device surface. A coherent method now needs to be developed so that the tips of the nanotube pillars can be exposed from the passivation layer in order to deliver an electrical signal to the retina.

### Acknowledgements:

I would like to thank the Center for Integrated Systems at Stanford and the National Science foundation for their support. I would also like to thank Ke Wang, Jim Harris, and Hongjie Dai for their assistance with this project.

### References:

- [1] Malini Narayanan Nadig et al. "Development of a silicon retinal implant," *Clinical Neurophysiology*, 1999, 1545-1553.
- [2] Shoushan Fan et al. "Self-Oriented Regular Arrays of Carbon Nanotubes and Their Field Emission Properties," *Science*, 1999, 283 (5401): 512.

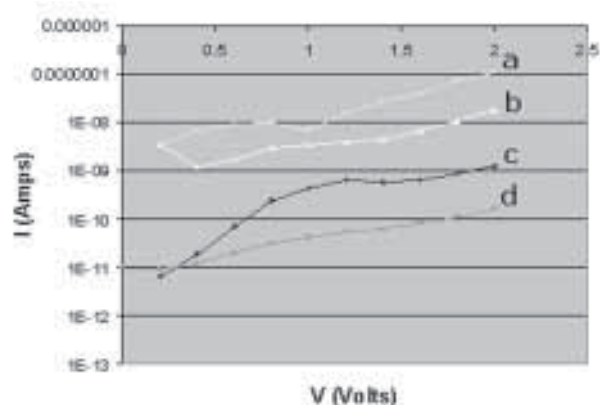


Figure 4: Leakage current data. (a) Uncoated array. (b) 1000/2000Å coating. (c) 1300/5400/1300Å coating. (d) No electrodes (noise).

# Development of Devices for Nanofiltration of Biomolecules

Maribella Domenech Garcia, Industrial Biotech., University of Puerto Rico-Mayaguez

NNIN REU Site: Cornell NanoScale Science & Technology Facility, Cornell University

Principal Investigator: Dr. Michael Spencer, Electrical and Computer Engineering, Cornell University

Mentor: Lori Lepak, Chemistry, Cornell University

Contact: mara600@coqui.net, spencer@ece.cornell.edu

## Abstract:

The genetic testing of samples derived from whole blood requires the separation of DNA (1.5-3 nm in diameter, negatively charged) from hemoglobin (5.5 nm, pH dependent charge). Our goal is to fabricate a biocompatible porous membrane device that can be compatible with nano- and microscale devices, for molecular sieving and dialysis applications.

While even e-beam lithography cannot reliably generate features smaller than 20 nm laterally, metal films thinner than 10 nm can routinely be deposited and later wet-etched away as a sacrificial layer to leave behind channels which may measure several microns laterally, yet be thin enough to exclude by size alone biomolecules larger than the initial film thickness. The project consisted of three parts: fabrication of channels, SU-8 molding of PDMS chambers, and flow tests.

The development of the constrictions consisted of depositing alternate layers of metals and oxide over a thin silicon wafer (100-200  $\mu\text{m}$ ) using photolithography techniques. In general, we deposited alternate layers of  $\text{SiO}_2$  to make the floor of the channel hydrophilic and prevent the electrodes from shorting out, and used Al as the sacrificial layer because it can be removed selectively vs. Si,  $\text{SiO}_2$ , and Au. The constricted channels were as small as 4 nm wide, which means that hemoglobin should not be able to pass through them. The PDMS chambers act as reservoirs for the molecules. Presently our research is directed toward the addition and improvement of electrical gates (Au) above the channels to allow passage through the constriction by charge modulation as well as size.

## Introduction:

The genetic testing of samples derived from whole blood requires the separation of DNA from hemoglobin. Currently it takes a few days to receive the results of such a test. With the use of photolithography techniques and other applications,

filters can be developed with sieves thin enough to separate specific proteins with sizes ranging between 5-15 nm, in a shorter time.

Applying metal evaporation and etching techniques, metal films thinner than 10 nm can be deposited and later wet-etched away as a sacrificial layer to leave behind channels which may measure several microns wide, producing a constriction thin enough for size exclusion separation. By the addition of electrical gates above the channels, the passage through the channels of molecules with a definite charge such as DNA can be modulated by charge as well as size.

The overall goal of the project is to fabricate a biocompatible porous membrane device that could be used to separate DNA from hemoglobin. The device will be compatible with nano- and micro-scale devices, and used for dialysis applications, newborn screening tests for congenital diseases and PCR enhancement. It also could be incorporated in DNA chips for quick medical analysis using small amounts of sample.

## Procedure:

The procedure used to fabricate the constrictions is illustrated on Figure 1.

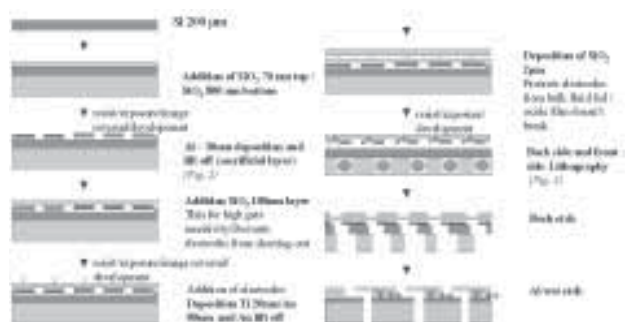


Figure 1: Fabrication of Constrictions.

## Results and Conclusion:

We were trying to add a pair of electrodes over the pattern. As you can see in Figures 2 and 4, the old

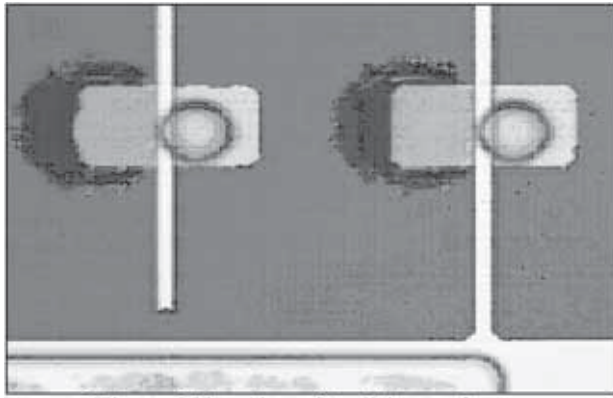


Figure 2 Top view after lithography

design contained only a 4  $\mu\text{m}$  electrode that did not allow us to modulate efficiently the electric field through the passage. In the new design, we have two electrodes 2  $\mu\text{m}$  wide each with a separation of 3  $\mu\text{m}$  between. In figure 4, we can see that this design allows us to create an electric gradient where one electrode is less positive than the other one. Unfortunately, due to limited resolution of the pattern in the EV620 contact aligner, the new electrode design could not be fabricated. Although, due to the shortage of time, the device could not be finished and tested, work will continue during the next semester.

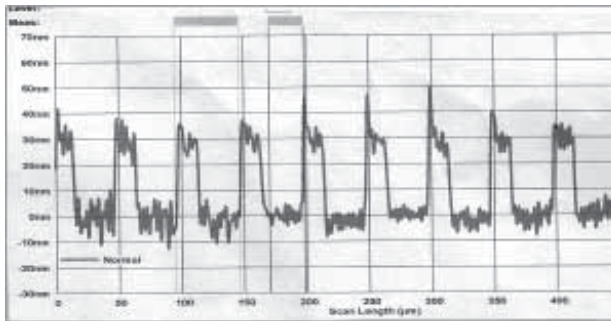


Figure 3. Al rectangles 30nm flat within noise levels of instrument.

### Future Work:

Future work for this project will be the improvement of electrical gates in order to perform the resolution in the exposure process. The mask for the electrodes should be redesigned with the electrodes over the pattern larger than 2  $\mu\text{m}$  in order to be developed correctly.

### Acknowledgements:

Professor Michael Spencer, Lori Lepak, Diego Rey, Rachel Gabor, Cornell NanoScale Facility, Wadsworth Center, Nanobiotechnology Center and National Science Foundation.

### References:

- [1] Campbell, Stephen A. "The Science and Engineering of Microelectronics Fabrication", Oxford University Press. 1996.p.182-275.
- [2] Zant, Peter Vant. "Microchip Fabrication", 3rd ed. McGraw-Hill. 1997.p. 99-399.



Electrical Field



Electrical Field Gradient

Figure 4: Placement of electrodes.

# Comparison of Fabrication Methods for Tunnel Regions in a Biosensor

Diane Fields, Materials Science and Engineering, Virginia Polytechnic Institute

NNIN REU Site: Cornell NanoScale Science & Technology Facility, Cornell University

Principal Investigator: Professor Michael Spencer, Electrical and Computer Engineering, Cornell University

Mentor: Tadahiro Kaburaki, Electrical and Computer Engineering, Cornell University

dmfields@vt.edu, spencer@ece.cornell.edu

## Abstract:

Recently, biosensor devices have become a major area of interest in nanotechnology. Many of these devices require microfluidic systems that include tunnel regions. The focus of this project is to fabricate tunnel regions using various methods in order to compare the clarity and characteristics of the tunnel regions. The first two methods use a sacrificial aluminum layer to form the tunnel. With this process, tunnels as small as 200 nm in height were achieved. Other methods studied include patterning channels in SU-8, polyimide, and PDMS.

## Introduction:

Currently, there is high interest in using biosensors for the detection of water and air contamination. The basic components of a biosensor include biological recognition interfaced with a signal transducer. Some biosensor designs also require microfluidic channels in order to transport ion currents that are transduced into measurable currents and voltages [1].

The goal of the research reported here was to fabricate tunnel regions for the microfluidic system of a biosensor. As seen in Figure 1, the biosensor design in consideration requires tunnels to separate an artificial cell membrane from reservoir areas. The reservoirs are used to easily fill the microfluidic channels which sit below the artificial cell membrane.

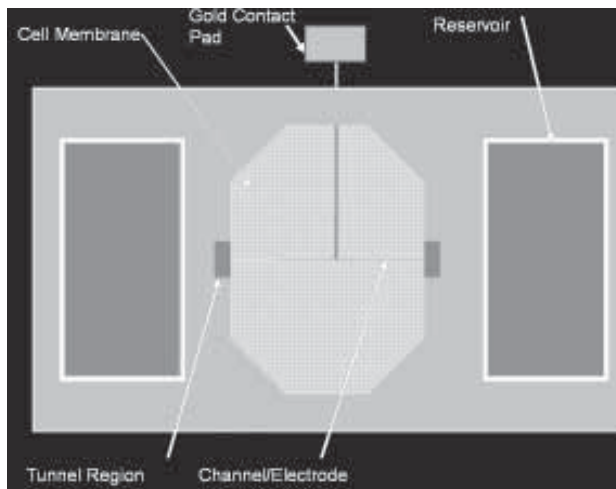


Figure 1: Biosensor layout.

When fabricating the tunnel regions, there are two main concerns. First, there must be complete isolation between the reservoirs and cell membrane area. Second, the tunnels must be clear and allow for careful filling of the channels from the reservoir. The methods explored include: (1) using a sacrificial aluminum layer; (2) patterning channels into SU-8; and (3) making a SU-8 mold to pattern the tunnels in PDMS.

## Procedure:

**Sacrificial Aluminum Layer:** The first method, shown in Figure 2, used a sacrificial aluminum layer to create the tunnel regions. In order to create these regions, first a mask including the biosensor's channels, tunnel regions, and reservoirs (Figure 1) was created using the Mann 3600 pattern generator. The mask pattern was transferred to glass wafers using the EV 620 contact aligner. After exposure and development the pattern was etched down into the wafer approximately 1  $\mu\text{m}$  using the Plasma Therm 72 Reactive Ion Etcher.

Following etching, lift off resist and Shipley 1827 were spun on the wafers and the contact aligner was used to expose only the tunnel regions. After development, 10 nm of Chrome and then 200 nm of Aluminum were deposited by electron beam evaporation. Lift off using 1165 remover was then performed, so that the aluminum remained only at the tunnel regions.

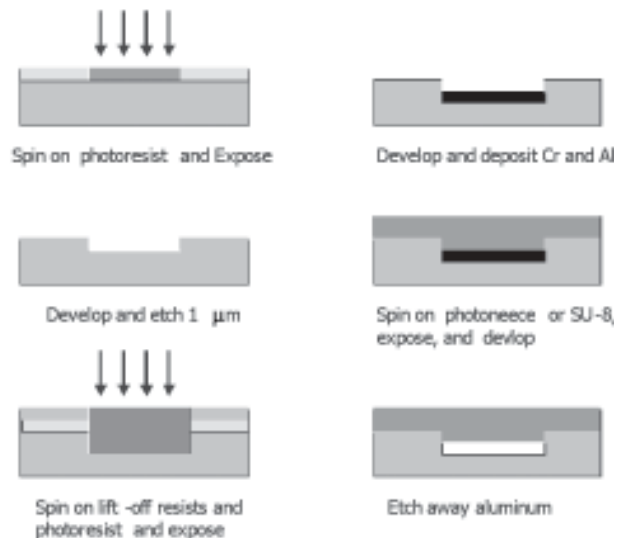


Figure 2: Sacrificial aluminum layer process.

Next, the cover layer was spun on and developed. This layer formed the border between the cell membrane and the reservoirs. Two cover layer materials experimented with were photoneece and SU8-50. Photoneece is an electrically insulating photosensitive polyimide which uses the same development procedures as normal Shipley resists; the only difference in processing is that photoneece requires a 6 hour cure after development [2]. SU-8 is a negative epoxy-based photoresist capable of producing high aspect ratio features. It requires a lengthy soft bake (15 to 90 minutes) and development in SU-8 developer [3]. Once the cover layer was finished, the aluminum in the tunnel regions was etched out using a wet aluminum etch.

**SU-8 and Photoneece Tunnels:** The second method explored to make tunnels involved creating channels in SU-8 or photoneece and then making a cover layer out of PDMS. To test this method a pattern using a range of channels from 5  $\mu\text{m}$  to 100  $\mu\text{m}$  was used as a mask. The same development steps used to create the SU-8 and photoneece cover layers in the sacrificial aluminum layer method were used to create the channels. The cover layer material used, PDMS (polydimethyl-siloxane), is a durable silicon elastomer.

**SU-8 Mold:** The final tunnel fabrication method studied involved creating a mold out of SU-8, which was then used to form the channels of the tunnel regions in PDMS. In order to create a mold, similar SU-8 tunnel method were implemented. However, in the mold the regions which before were trenches were the raised regions, and vice-versa. Once the mold was finished, it was cast with PDMS. The PDMS was then degassed to remove air bubbles and cured for 3 hours. After curing, the PDMS layer was manually peeled off the SU-8 mold. PDMS was also used as the cover layer in this method.

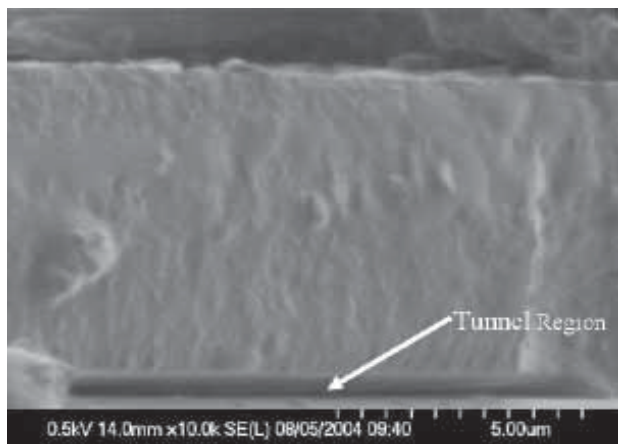


Figure 3: SEM image of tunnel formed by sacrificial aluminum layer method.

## Results and Conclusions:

The sacrificial aluminum layer process produced clear etch through regions as small as 200 nm in height. A cross section of a tunnel region with a photoneece cover layer is shown in the SEM image of Figure 3. These channels would be ideal for controlled fluid flow in the biosensor and for channels using capillary action to transport fluid.

The photoneece channels were 5  $\mu\text{m}$  high, and they resulted in clear pathways for channel widths as small as 5  $\mu\text{m}$ . The recipe used for the SU-8 tunnels produced 100  $\mu\text{m}$  high walls, but they did not produce clear channels for widths smaller than 50  $\mu\text{m}$ . However, the SU-8 mold was clearly defined, which resulted in clear PDMS channels for widths down to 5  $\mu\text{m}$ . Figure 4 shows images of the mold and the resulting channels.

## Acknowledgements:

I thank Dr. Michael Spencer and my mentor, Tadahiro Kaburaki, of Cornell University's Electrical & Computer Engineering Department for their support and guidance in this project. I also thank the staff at CNF for their support and NSF for making this opportunity possible.

## References:

- [1] Mehrvar, Mehrab, "Fiber-Optic Biosensors - Trends and Advances," *Analy.Sciences*, V16, pp 677-693, July 2000.
- [2] Toray Group, "Photoneece Photosensitive Polyimide Coating," <http://torayusa.com/tomac/products/photo.htm>, May 23, 2001.
- [3] Microchem, Nano SU-8, [http://www.microchem.com/products/pdf/SU8\\_50-100.pdf](http://www.microchem.com/products/pdf/SU8_50-100.pdf), February, 2002.

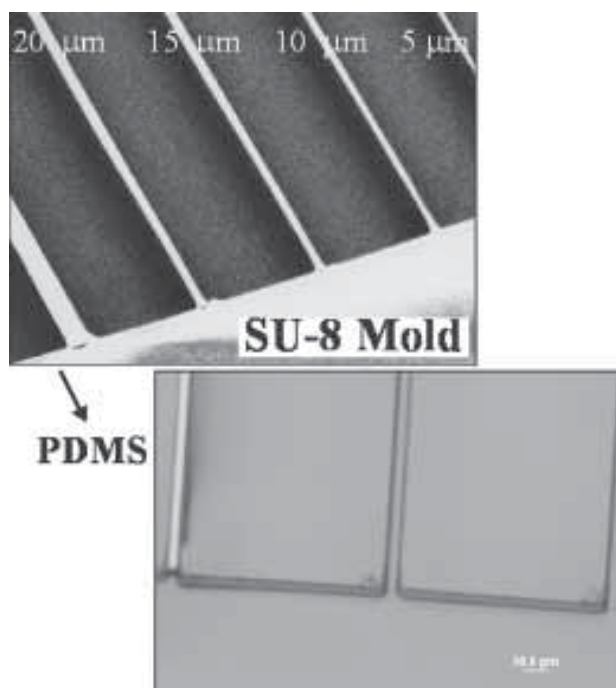


Figure 4: SU-8 mold and subsequent PDMS channels.

# Effect of O<sub>2</sub> Plasma Treatment on the Leakage Current of Titanium Oxide Thin Films Formed via PMODTM

Isaac Finger, Chemical Engineering, University of Florida

NNIN REU Site: Microelectronics Research Center, Georgia Institute of Technology

Principal Investigator: Clifford Henderson, Chemical & Biomolecular Engineering, Georgia Institute of Technology

Mentor: Ashwini Sinha, Chemical & Biomolecular Engineering, Georgia Institute of Technology

Contact: ickfin@ufl.edu, cliff.henderson@che.gatech.edu, ashwini.sinha@chbe.gatech.edu

## Abstract:

Photochemical Metal Organic Deposition or PMODTM is a recently reported method for the formation of metal oxide thin films. The present work describes a preliminary investigation into the effect of O<sub>2</sub> plasma annealing on the leakage current of titanium oxide thin films formed by the aforementioned method.

Titanium oxide films resulting from PMODTM were treated with O<sub>2</sub> plasma. The treated films were incorporated into parallel plate test capacitors which were then used to measure the leakage current of the dielectric material.

## Introduction:

Due to their characteristic high dielectric constant ( $k$ ), metal oxides with perovskite structure have been utilized in many current microelectronics technologies. Examples of such technologies are high-density dynamic random access memory (DRAM), microwave tuning devices, and embedded capacitors for electronic packaging. Recent development of procedures for the deposition of these materials as thin films has made such technologies feasible [1-5]. Some applications, such as those using polymeric substrates, require these films to be deposited at low temperature and produced at low cost.

Photochemical metal-organic deposition was first investigated by Hill, et al. [6, 7]. More recently Henderson, et al. have investigated the application of this process for photo-patterning as well as hydrothermal treatment of the products [8]. These studies have yielded a methodology for low temperature, cost effective photo-patternable deposition of titanium oxide and its conversion to the perovskite structure. Investigations into the optimization of each step as well as addition of other treatments to the processing scheme are being carried out to look into the full potential and flexibility of this methodology.

Titanium oxide PMOD forms an amorphous, nanoporous material which can be further processed to direct changes in its structural configuration and electrical properties. This work describes a preliminary investigation into the effect of plasma annealing on the leakage current of these thin films.

## Procedure:

**Spin-Coating and Photo-Conversion:** The PMOD precursor formulation was spin coated on an appropriate substrate using a CEE 100CB spin coater [8]. The coated substrate was then irradiated for 30 min using an OAI Model 500 DUV contact aligner.

**Thermal Annealing:** The photoconverted films were annealed on a hot plate in air at 300°C for 15 min.

**O<sub>2</sub> Plasma Annealing:** Samples of the annealed film were treated with O<sub>2</sub> plasma in a Plasma-Therm RIE. Treatments were carried out at 30°C, 200 mTorr and 400 W. Treatment times were varied from 5 to 35 min.

**Leakage Current Measurements:** The leakage currents of the plasma treated samples were determined by applying a voltage across parallel plate capacitor structures and measuring the resultant current. MIM (metal-insulator-metal) capacitors were fabricated by depositing a blanket film of PMOD metal oxide on a sputtered platinum coated silicon wafer and depositing sputtered gold top electrodes.

The top electrodes were circles of different sizes (100 μm to 500 μm in diameter). Test probes were contacted to two adjacent top electrodes forming a circuit of two MIM capacitors in series. Current was measured from 0 to 30 V at 100 mV increments using an HP-4156 Precision Semiconductor Parameter Analyzer.

## Results and Discussion:

**Data Normalization:** The circuits tested were effectively made up of a voltage source connected to two identical capacitors in series. Consequently, the

data collected from the experiment was normalized to reflect the behavior of one of the capacitors in the series. The current is uniform throughout the circuit and does not need any manipulation. The voltage applied across two capacitors in series is twice that applied to either of them individually. Thus, the data is normalized by dividing the applied voltage of the circuit by 2. The data shown in Figure 1 reflects this normalization.

The leakage current of a capacitor at any applied voltage is directly proportional to the surface area of the capacitor electrode. To compare the leakage currents of different samples the surface area of the capacitors compared was held constant. All data shown herein was collected from capacitors with diameter 300  $\mu\text{m}$ .

The leakage currents of the capacitors tested the experimental increase as a function of the applied voltage. At low voltages the resulting current seems linear and remains close to zero. At some critical point, the current begins increasing rapidly and behaves more like a parabolic or exponential function of applied voltage. Such behavior is an indication that the capacitor is nearing failure. In this investigation, it was found that the voltage where the critical point occurred, in a particular sample, was related to the time of exposure to  $\text{O}_2$  plasma. From Figure 1 we see that this critical point occurs at a different voltage for each corresponding treatment time.

The critical point for the samples treated for 5 and 35 minutes occur at lower voltages than that of the sample treated for 15 minutes. This suggests that there is a treatment time between 5 and 35 minutes that would correspond to a maximum critical point voltage.

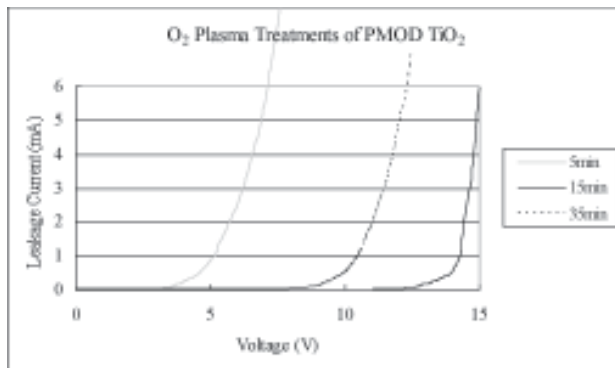


Figure 1: Leakage Current vs. Applied Voltage of PMOD  $\text{TiO}_2$  samples treated with  $\text{O}_2$  Plasma. Treatment times included are 5, 15 and 35 min.

### Future Work:

We do not have a very good understanding of how the  $\text{O}_2$  plasma treatment physically changes the titanium oxide film in this procedure. Research to further elucidate the dynamics behind this relationship, as well as find the optimal processing parameters, is currently under way. A better understanding of this treatment will aid in its integration in a larger processing scheme.

### Acknowledgements:

The authors would like to acknowledge the staff of the Microelectronics Research Center at the Georgia Institute of Technology for their attentiveness and technical support.

### References:

- [1] J. Scott, Annual Rev of Mats Science 28, 79 (1998).
- [2] R. Wallace & G. Wilk, MRS Bulletin 27(3), 192 (2002).
- [3] J.Prymak, S.Bhattacharya and K.Paik, in Fundamentals of Microsystems Packaging, R. Tummala, Editor, p. 420, McGraw Hill, New York (2001).
- [4] P. Wise, I. Reaney and W.E. Lee, J. Mater. Res. 17(8), 2033 (2002).
- [5] R.Ulrich, D. Nelms, L.Schaper and D. Parkerson, High Density Interconnects 1(4), 40 (1998).
- [6] R. Hill, et al., Materials Chemistry and Physics 43, 233 (1996).
- [7] S. Goetting, B. Palmer, M. Gao and R. Hill, J. Mater. Sci. 29, 6147 (1994).
- [8] S.Mukherjee, et al., Electrochem. Soc. 28, 263-275 (2003).

# Characterization of AlGaIn Material Quality for use in Deep-Ultraviolet Light Emitting Diodes

Eric M. Fraser, Physics, Pomona College

NNIN REU Site: Nanotech at UCSB, University of California Santa Barbara

Principal Investigator: Dr. Shuji Nakamura, Materials, University of California at Santa Barbara

Mentor: John Kaeding, Materials, University of California at Santa Barbara

Contact: eric.fraser@pomona.edu, shuji@engineering.ucsb.edu

## Abstract:

High-power deep-UV light emitting diodes and laser diodes can be used in a variety of applications, including the detection of anthrax and other biological agents, water purification, and high-density optical storage. Deep-UV LEDs are composed of an AlN template layer and AlGaIn active device layers grown epitaxially by metal-organic chemical vapor deposition on c-plane sapphire. To achieve efficient LEDs with reasonable lifetimes and light output, the material must be high quality. The project focuses on characterizing the crystal quality and surface morphology of the AlN and AlGaIn using X-ray diffraction, atomic force microscopy, and other methods, and relating these qualities to device performance. Additionally, we seek to determine the relationship between AlN layer quality and AlGaIn layer quality. Plan-view transmission electron microscopy data suggest that current dislocation densities in the AlN template layers range from  $5 \times 10^9 \text{ cm}^{-2}$  to greater than  $1 \times 10^{10} \text{ cm}^{-2}$ , which will propagate into subsequent layers and affect device performance.

Finally, we are designing a procedure using x-ray rocking curve analysis to determine the dislocation density in the AlGaIn layers as a function of growth parameters, including growth temperature, pressure, and composition, as well as AlN template quality.

## Introduction:

Compared to other light sources, optimized LEDs use little power, are extremely compact, generate little heat, are inexpensive, and offer very long lifetimes. Deep-UV LEDs and LDs have the potential to detect and decontaminate biological agents including anthrax, purify water, allow for non-line-of-sight communications, dramatically increase the storage capacity of optical storage, and provide efficient sources of white light. Current technology allows for near-UV LEDs to the mid-300 nm range. The target wavelength is 280 nm. To achieve the listed advances,

however, the LEDs and LDs must be of sufficiently high quality.

## Procedure:

The thin films were grown epitaxially on two-inch diameter (001) sapphire by metalorganic chemical vapor deposition (MOCVD). The wafer was heated to  $\sim 1000^\circ\text{C}$ . Trimethylaluminum and trimethylgallium were injected in nitrogen or hydrogen carrier gas with gaseous ammonia into the MOCVD reactor. The precursors decomposed in the hot zone to deposit on the sapphire wafer, forming single-crystal AlN, AlGaIn, or GaN layers.

We used several different characterization techniques to determine the quality of the layers. The two most common techniques were optical microscopy and x-ray diffraction (XRD). Optical microscopy gives qualitative data about the surface of the material. XRD gives quantitative data about the crystal structure quality, in particular the density of edge and screw dislocations. We took rocking curve (w-scans) XRD data of the (002) plane and (201) plane to find the density of screw- and edge-type dislocations, respectively [1].

Ideal films would be transparent, free of surface defects, and exhibit narrow XRD rocking curve peak widths.

Since the AlN layer is merely a template layer for the actual AlGaIn device layers, we wanted to

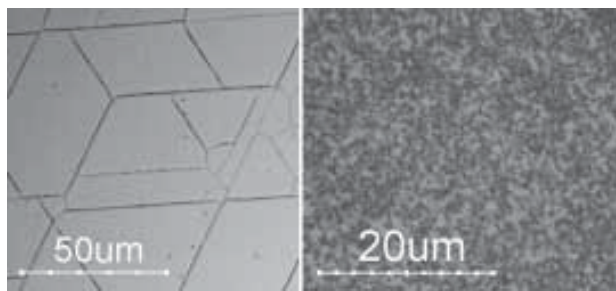


Figure 1, left: Optical image of cracking on surface of AlN template. Figure 2, right: Optical image of impurity deposits on AlGaIn (dark spots).

determine a method for taking quantitative measurements of AlGa<sub>N</sub> layer quality relative to the AlN template layer. The on-axis (002) measurement is trivial to take, since the AlN and AlGa<sub>N</sub> peaks are separated by a few degrees. The off-axis peaks, however, proved to be much more difficult, since the correct angles were not known. By comparing the relative positions of the (002) peaks of AlN and AlGa<sub>N</sub>, we could determine the relative composition. Using this data, we could then determine the correct diffraction angles for any specified plane by interpolating between AlN and AlGa<sub>N</sub> parameters. We attempted scans of the (102), (201), and (204) directions. Non-reproducibility issues related to AlN template growths precluded experiments to investigate AlGa<sub>N</sub> device layers.

We explored several sets of conditions to improve reproducibility. Temperature and pressure were changed routinely. Additional modifications were made to the reactor design to eliminate pre-reactions between the gases.

### Results and Analysis:

Optical microscopy showed material with a variety of defects, including cracking (Figure 1) and impurity deposits (Figure 2). High-quality material should be homogeneous and optically smooth.

(002) rocking curves of AlN templates yielded significant differences in material quality, as illustrated in Figure 3. The FWHM increased an order of magnitude between samples. To a rough approximation, the threading dislocation density is proportional to the square of the XRD rocking curve FWHM, indicating a significant degradation in material quality. The cause of this increase is still unknown.

The attempt to characterize the AlGa<sub>N</sub> quality indicated that the quality must improve before we can take quantitative data. The AlN and AlGa<sub>N</sub> peaks were so broad and close together in the (102), (201), and (204) scans that we were not able to reliably separate them (see Figure 4). If the material quality improves, the peaks should narrow, allowing the two peaks to be distinguishable and allowing for quantitative analysis on each.

### Future Work:

Prior deposits on reactor quartzware may affect subsequent material growth. To investigate the source of this variability, the quartzware will go through a

high-temperature HCl bake to remove deposits from the surface. Clean quartzware will be tested against dirty quartzware for any effects on material quality, and to determine the length of time for stable growth. Early tests indicate there is similar variation in the (201) XRD FWHM.

### Acknowledgments:

John Kaeding and Dr. Nakamura have provided excellent support and instruction throughout this project. As the old adage goes, one can learn more in failure than in success. I find that particularly true here, for I have learned not only the difficulties of semiconductor fabrication, but also of the very process of scientific research. This work was completed with support from DARPA and NSF.

### References:

- [1] B. Heying, X. Wu, S. Keller, Y. Li, D. Kapolnek, B. Keller, S. DenBaars, J. Speck. Appl. Phys. Lett. 68 (5), 29 Jan 1996. 643-545.

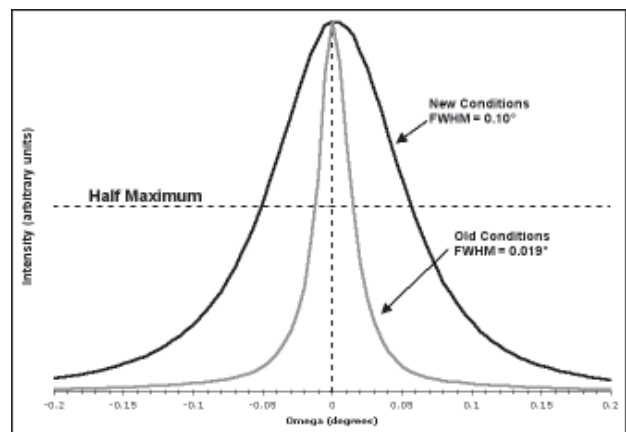
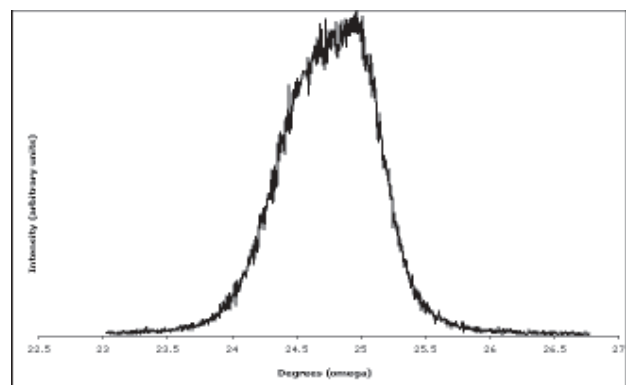


Figure 3, above: (002) XRD data of AlN Templates. Narrow peaks indicate better material quality.

Figure 4, below: (102) XRD data of AlN/AlGa<sub>N</sub> layers. This peak is likely actually composed of two peaks.



# Living Microorganisms Entrapped in Nano-Structured Latex Formulations Piezoelectrically Printed onto Bioelectronic Devices

Elizabeth (Za) Freeman, Biochemistry, Lawrence University

NNIN REU Site: Nanofabrication Center, University of Minnesota, Twin Cities

Principal Investigator & Mentor: Dr. Michael C. Flickinger, Biochemistry, Molecular Biology, and Biophysics, Biotechnology Institute, University of Minnesota, Twin Cities

freemane@lawrence.edu, mflick@cbs.umn.edu

## Abstract:

Using piezoelectric deposition, living microorganisms in a latex formulation can be printed onto bioelectric devices for mercury ( $Hg^{+2}$ ) detection. When *Escherichia coli* HB101 containing the *mer-lux* plasmid pRB28 is entrapped in a nano-porous latex ink, it survives piezoelectric printing, drying, rehydrating, and being induced with  $Hg^{+2}$  to luminescence through Lux synthesis. The reactivity of *E. coli mer-lux* when printed in dot arrays with two piezo tips (opening: 25  $\mu m$  and 50  $\mu m$ ) was examined by inducing with 1 to 10,000 nM  $Hg^{+2}$ . The necessity of forming nano-pores in the dried latex ink and the ability of *E. coli* to survive piezoelectric deposition were investigated. Reactive microbial inks have many potential applications such as detecting mercury in the environment, in fish, or in metal recovery.

## Introduction:

Organic mercury is a biologically active form of mercury that enters the environment as inorganic mercury through natural (volcanoes) and human (industrial plants) sources. Inorganic mercury easily

oxidizes in the atmosphere and travels, as organic (methyl mercury) and ionic mercury ( $Hg^{+2}$ ), through rainwater, through sediments, and through fish consumption, bringing it in contact with humans. When consumed, organic (methyl mercury) and ionic mercury ( $Hg^{+2}$ ) can cause loss of nerve cells which leads to numbness, difficulty in speech, along with loss of coordination, sight, and hearing.

*Escherichia coli* HB101 pRB28 *mer-lux* is capable of detecting biologically available  $Hg^{+2}$  and reacting through luminescence [1, 2]. *E. coli* is tough and can survive piezoelectric printing, drying, rehydrating, and being induced with  $Hg^{+2}$  and still express new gene products. The  $Hg^{+2}$  acts as a signal to the *E. coli* and the *E. coli* respond by luminescence, which can be detected by a scintillation counter. The *E. coli* are entrapped within a nano-structured material (Figure 1). Nano-pores are the spaces between the partially coalesced polymer particles. Nano-pores serve as a pathway for  $Hg^{+2}$  to get to the entrapped *E. coli*.

The *E. coli* latex polymer mixture which is reactive to  $Hg^{+2}$  when dried (printed) and rehydrated will be referred to as “smart” ink. “Smart” ink is similar to ink-jet ink because they both contain four basic properties: solvent, dye/pigment, binder, and additive. The piezoelectric printer (Nano Plotter GeSIM) is a highly accurate printer with the ability to print 10 x 10 dot arrays, with varying pitches and number of droplets per dot, with two different tips openings (nano = 50  $\mu m$  and pico = 25  $\mu m$ ). Ultimately the piezoelectric printer could be used to print “smart” ink onto a bioluminescent bioreporter integrated circuit (BBIC)

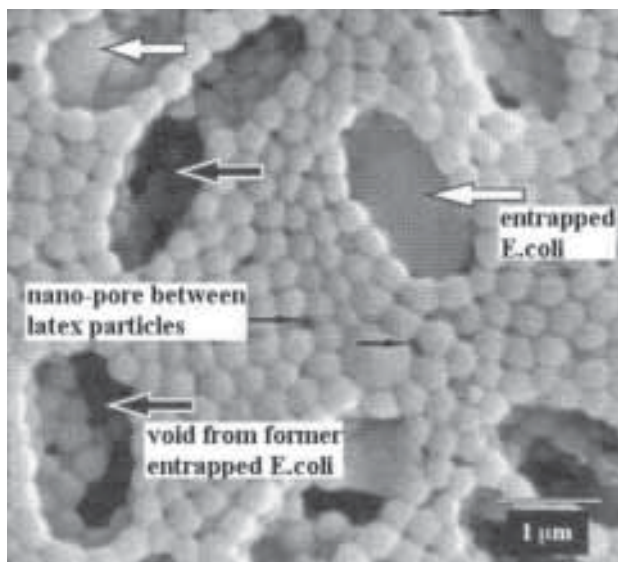


Figure 1: Nano-structured *E. coli* embedded acrylate/vinyl acetate latex composite.

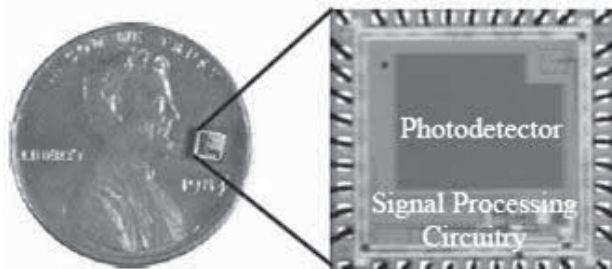


Figure 2: BBIC is 2 x 2 mm.

(Figure 2) [3]. This would allow the BBIC to detect  $Hg^{+2}$  through the luminescence of the *E. coli* entrapped in the nano-structured latex formulation.

This project had three goals. The first goal was to determine if the “smart” ink would be reactive to various  $Hg^{+2}$  concentrations when piezoelectrically printed with the two different tip openings. The second was to determine if nano-pores were a necessary component within the dried “smart” ink. Finally, the third goal was to determine the reactivity change, if any, between a manually pipetted macrodot (not printed, not subjected to strong shear stress) of similar volume to a piezoelectrically printed array of “smart” ink.

### Procedure:

Grow an overnight *E. coli mer-lux* culture. The following morning, start a new culture at an  $OD_{600}=0.1$  and let it grow until  $OD_{600}=1.0$ . Centrifuge and re-suspend the *E. coli* multiple times. Obtain the weight of the wet cell pellet. Prepare the “smart” ink recipe following Lyngberg et al. [4] but with a dilution with water to 25% of the original concentration. Glycerol and sucrose were only used when nano-pores were needed in the “smart” ink [1]. Print the “smart” ink with the piezoelectric printer (Nano Plotter GeSIM) in 10 x 10 dot array with five drops/dot with either the nano (50  $\mu m$  opening) or pico (25  $\mu m$  opening) tip onto polyester. When making macrodots, an estimated volume was used for the 10 x 10 piezoelectrically printed array. Pipette 250 nl (nano tip array) and 100 nl (pico tip array) onto polyester and let dry for an hour. Rehydrate and induce the arrays or macrodots with  $Hg^{+2}$  concentrations of 0 nM, 1 nM, 10 nM, 100 nM, 1,000 nM, and 10,000 nM. Place into a liquid scintillation counter and record the luminescence for 720 minutes.

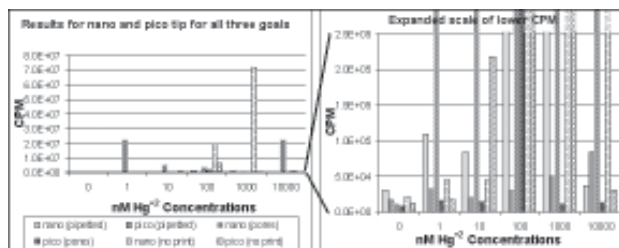


Figure 3: All *E. coli mer-lux*  $Hg^{+2}$  induction results.

### Results (Figure 3):

Goal 1: “Smart” ink can be piezoelectrically printed through the nano and pico tips and still be able to

react when induced with  $Hg^{+2}$ . Goal 2: When nano-pores are created by the addition of glycerol and sucrose strong luminescence does occur from the nano and pico tips. There is an average of over 200-fold increase, with a maximum of 2000-fold increase, when there are nano-pores versus when there are not nano-pores. Goal 3: Some vitality is lost when the “smart” ink is piezoelectrically printed versus manually pipetted in a macrodot.

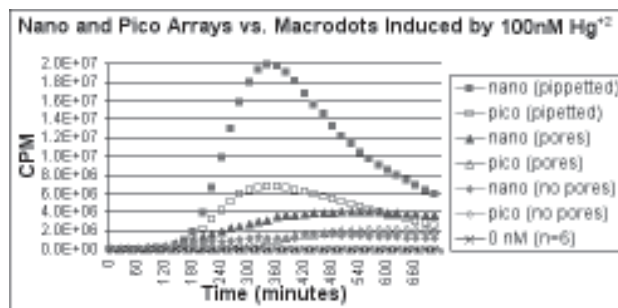


Figure 4: All *E. coli mer-lux* induction results at 100 nM  $Hg^{+2}$ .

### Conclusions (Figure 4):

The “smart” ink can be printed with the nano and pico tips and still detectably react to  $Hg^{+2}$ . Nano-pores are necessary for detectable luminescence. *E. coli* suffer a lose of vitality but are still reactive when piezoelectrically printed as an array versus pipetted by hand as a macrodot.

### Future Work:

Manipulate the “smart” ink recipe to get smaller dot and pitch size as well as to detect lower  $Hg^{+2}$  concentrations. Determine an improved “smart” ink recipe to increase *E. coli* vitality and reactivity when piezoelectrically printed.

### Acknowledgments:

Thank you, Dr. Michael C. Flickinger and Matt Laudon, for your help and support this summer.

Figure 1 and 2: Courtesy of Professor M. C. Flickinger, University of Minnesota, Nanotechnology Day, May 2004.

### References:

- [1] Lyngberg, O.K. et al. *Biotechnol. Bioeng.* 62: 44-55 (1999).
- [2] Lyngberg, O.K. et al. *J.Ind. Microbiol. Biotechnol.* 23: 668-676 (1999).
- [3] Nivens, D.E. et al. *Journal of Applied Microbiology.* 96: 33-46 (2004).
- [4] Lyngberg, O.K. et al. *Biotechnol. Prog.* 17: 1169-79 (2001).

# New Materials and Applications of Nanoimprint Technology

Steven Froelich, Chemical Engineering, Villanova University

NNIN REU Site: Solid State Electronics Laboratory, University of Michigan, Ann Arbor

Principal Investigator: L. Jay Guo, Electrical Engineering, University of Michigan

Mentor: Philip Choi, Electrical Engineering, University of Michigan

Contact: steven.froelich@villanova.edu, guo@eecs.umich.edu

## Introduction:

Nanoimprinting is a type of lithographic process that provides a simple and efficient way of patterning nanostructures. The primary motivation for accurate and efficient nanolithography is the ability to create smaller functional device structures, such as those found in nanoscale transistors. Key to the commercial success of these smaller device structures is low cost and high throughput manufacturing capabilities.

In nanoimprint lithography, a rigid mold containing nanoscale features is embossed into a polymer material that has been cast on a wafer substrate. The polymer layer thickness is such that under prescribed temperature and pressure, a thin viscous polymer fluid will form between the mold's protrusions and the substrate surface. This acts as a 'soft cushion' which protects the nanofeatures on the mold. However, as a result, the existence of a residual resist layer is present in the recessed regions of the mold. This must be removed by a separate plasma-based anisotropic etching step before pattern definition can be completed.

Nanoimprint lithography presents new challenges for further optimization of the technology. There is a demand for new materials with properties more appropriate for the particular requirements of nanoimprinting. One critical requirement is to provide mold releasing properties during the de-molding process while not compromising the adhesion of the mold to the substrate. When imprinting high density patterns, the imprinted polymer tends to adhere to the mold, creating pattern defects that are not acceptable for many applications. Therefore, a material with low surface energy is desirable. Another critical property of nanoimprint resist materials is that they must have high etching resistance to allow pattern definition to be completed.

The focus of this project is to analyze a new graft copolymer material. By investigating the spin coating rate, the plasma-based anisotropic etching characteristics, and the imprinting conditions, the

material was tested for properties suitable for the imprint application. Comparing these results with other industry standard thermoplastics, this material offers some unique properties for high-throughput patterning of nanostructures.

## Procedure:

A Polydimethylsiloxane (PDMS) based graft copolymer was obtained from Dow Corning. A 10% weight solution of the graft copolymer was prepared by dissolving 10 grams of the graft copolymer in 90 grams (92.88 mL) of 2-[1-methoxy]propyl acetate (PGMEA) an organic solvent. The solution was filtered using a 2  $\mu\text{m}$  porous capillary filter. The solution was kept in a sealed glass container and stored in a dark cabinet. Once synthesis of the solution was completed, the spin coating pattern was characterized.

The spin pattern was determined by first applying a thin layer of solution to a silicon wafer. Then the wafer was spun at a speed between 1 and 5 thousand rpm for 30 seconds. While spinning, the solvent would quickly evaporate and a thin uniform film would form on the silicon wafer. Subsequently, the sample would then be placed on a hot plate at 80°C for 2 minutes so that any remain solvent would evaporate.

Next, the thickness of the polymer film was measured using ellipsometry. The thickness of the polymer film layer was found to decrease with an increase of the speed of the spin-coating (Figure 1).

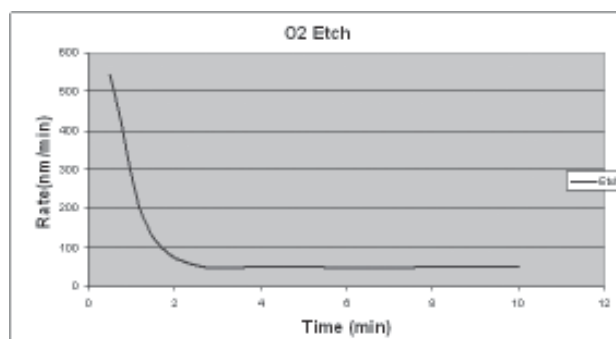


Figure 1

After the spin pattern was characterized, the graft copolymer could be tested for imprint-ability. First, the mold was treated with a perfluorosilane surfactant to form networks of covalent siloxane bonds, which make the surfactant coating layer chemically and thermally stable. This reduces the tendency of adhesion of the imprinted polymer to the mold. Then, a silicon wafer was prepared by first spin coating a thin layer of Hexamethyldisiloxane (HMDS) to increase adhesion between the polymer layer and the substrate. Next a 500 nm thick layer of the graft copolymer was prepared. After baking on a hot plate at 80°C for 2 minutes, the sample was ready to be imprinted.

The first objective was to characterize how effective the imprinting process is under different temperatures. Based on the glass transition temperature, a range between 150°C and 90°C was selected. Then samples were imprinted at 10°C intervals at 600 psi for 5 minutes, then allowed to cool below the glass transition temperature. These samples were then examined for mold separation, resolution and pattern transfer. The material imprinted optimally at 130°C (see Figure 2).

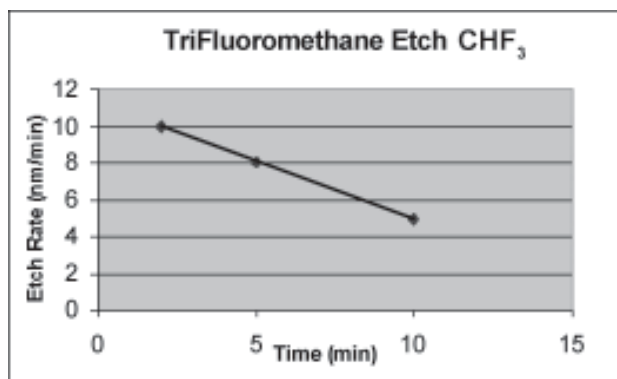


Figure 2

Finally, the plasma-based anisotropic etching character of the graft copolymer was studied. First, a sample was prepared by spin coating a selected thickness. The sample was then etched under prescribed conditions. The first objective was to separately determine the etching character of Oxygen and CHF<sub>3</sub> TriFluoromethane etching. The power was set to 100 Watts and the pressure was set to 200 mT. The Oxygen flow rate was set to 32 sccm and the TriFluoromethane flow rate was 25 sccm. It was found that the Oxygen etch rate stayed approximately 50 nm/min at etch times above 2 minutes (Figure 2).

The TriFluoromethane etch rate was found to linearly decrease with time (see Figure 3).

Once the etching characters of both Oxygen and TriFluoromethane were found, both were used with proportional flow rates according to their etch rates. This combination optimized etching of both components while maintaining the fidelity of the pattern. However, later etches were conducted under a pressure of 20 mT in order to better preserve the pattern transfer.

**Conclusions:**

Imprint lithography duplicates the surface relief patterns by mechanical embossing. Based on this principle, nanoimprint techniques can achieve pattern resolutions beyond the limitations of other conventional techniques. The focus of this experiment was to analyze a new graft copolymer material. Graft copolymer materials have dual surface properties through microphase segregation that can be exploited. This graft copolymer’s low imprint temperature and pressure, high resolution, high etching resistance, and low surface energy, offer some unique properties for high-throughput patterning of nanostructures.

**Acknowledgments:**

I would like to thank L. Jay Guo and Phil Choi for their expertise and help in conducting this research.

**References:**

[1] L. J. Guo, “Topical Review: Recent progress in nanoimprint technology and its applications,” J. Phys. D: Appl. Phys, Vol. 37 (11), pp. R123-R141, 2004.

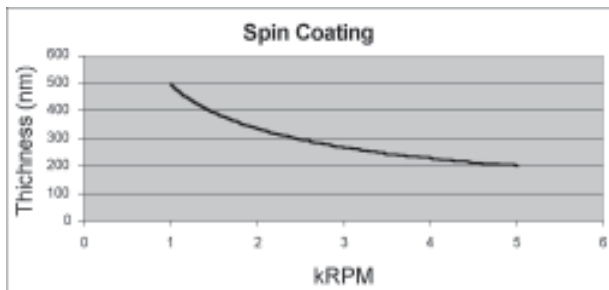


Figure 3

# Nanoscale Cantilevers for Ultrasonics and Nanoscale Folding

Yenyun Fu, Electrical Engineering, University of California, Santa Barbara

NNIN REU Site: Cornell NanoScale Science & Technology Facility, Cornell University

Principal Investigator: Amit Lal, Electrical & Computer Engineering, Cornell University

Mentor: Serhan Ardanuc, Electrical & Computer Engineering, Cornell University

Contact: alexiafu@umail.ucsb.edu, al274@cornell.edu, sma34@cornell.edu

## Abstract:

This project utilizes the charge storing property of oxide-nitride dielectric to fabricate cantilevers for actuation. We propose to achieve this by depositing charge on oxide-nitride cantilever, then releasing the cantilever thus freeing it to bend with electrostatic force. Charge deposition was attempted with both Atomic Force Microscopy (AFM) and exposure of samples to radioactive sources. Lift-mode was verified with AFM to detect long range magnetic and electric forces. The release of thin oxide-nitride layers was also demonstrated by wet etch in TMAH.

## Introduction:

Memory devices such as EEPROM/NROM utilize oxide-nitride and oxide-nitride-oxide dielectrics to store bits.  $\text{Si}_3\text{N}_4$  contains a large number of traps thus providing a low-potential site for storing charge [1]. In this paper, we explore the usage of charge storage capability of oxide-nitride for cantilever actuation. With 10-40 nm of oxide/nitride, the electric-field between AFM tip and sample should be adequate to exceed the breakdown voltage of dielectric layers and deposit charge.

## Procedure:

To test charge writing/reading with AFM, a single mask process was used to fabricate oxide-nitride-oxide samples. First oxide layer was ~10 nm, nitride was Si-rich LPCVD ~6-20 nm, final oxide layer was thermal oxidation of nitride at 900°C. We were unable to obtain

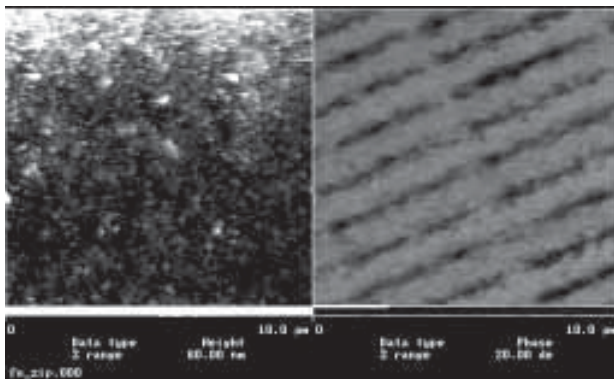


Figure 1: AFM scan of 250 MB zip disk.

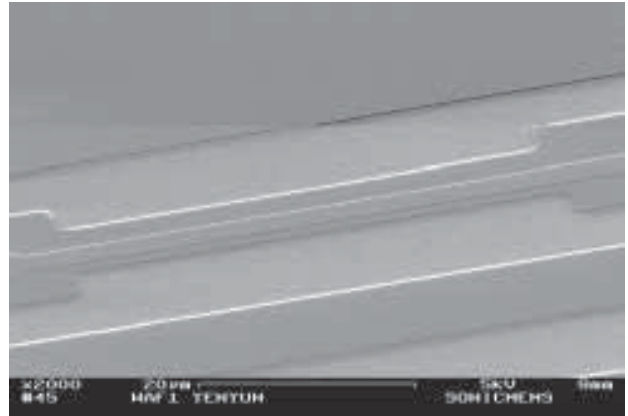


Figure 2: Cantilevers with thinner folding region ~ 2  $\mu\text{m}$ .

a good thickness measurement of the third oxide layer.

MikroMasch NSC36/Ti-Pt tips were used in tapping/contact mode on a JSPM-4210 AFM/STM. Conduction was verified between the Ti-Pt tip and silicon samples by ramping I-V characteristics. However, by applying a sample bias 10-100V in AC/contact modes, charge was not detected. At large biases, the tip becomes damaged and cannot be used for charge detection after being used for charge writing. Charge deposition possibly failed due to low retention time of Si-rich nitride or the final oxidation removed most of the nitride.

Charge writing was attempted on our final oxide-nitride-poly-nitride cantilever with Dimension 3100 in tapping/contact modes. Bias was applied by connecting an external voltage source to the sample. Tip scan rates were varied from 0.02-1  $\mu\text{m/s}$  while scanning a 50 nm x 50 nm region and applying a voltage of 10-100V. Electric force microscopy (EFM) was performed by applying a 3-5V bias and lifting the tip by 10-150 nm while scanning. However, no contrast in phase signal was observed at the region of interest. The experiment was repeated on a 10 nm  $\text{SiO}_2$  sample to decrease the breakdown field, however no phase contrast was observed for biases up to 70V in contact mode. During charge writes with Dimension AFM, tip damage was less of an issue at high biases.

We then tried charge-reading by exposing samples to radioactive Ni-63/Po-210 beta/alpha source to eliminate

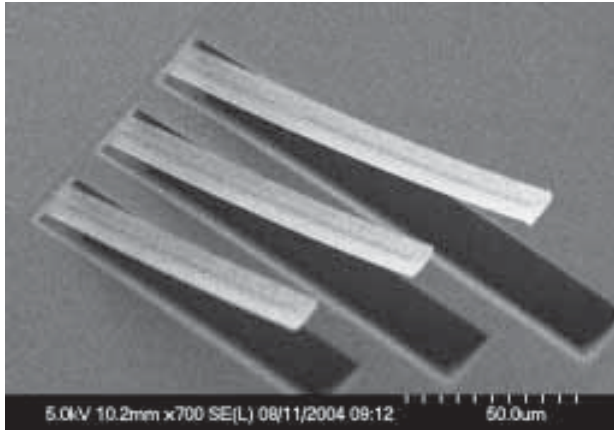


Figure 3: 2  $\mu\text{m}$  wide cantilever.

the factor of charge not being deposited. However, changes in the conductivity/topography of samples after exposure were undetected. This is because high energy electrons were accelerated through oxide-nitride-oxide instead of being retained.

To verify the ability of AFM to detect long-range forces, we imaged magnetic media with magnetic tips. MikroMasch NSC36/Co-Cr tips and Dimension 3100 were used. To detect long-range forces instead of atomic forces as in normal AFM operation, the tip is displaced 10-100 nm from samples. We were able to image magnetic patterns on a 250 MB zip disk at 10 nm lift height. In Figure 1, the left image is the topography of the zip disk; the right image is magnetic patterns of stored data.

Next, we proceeded to cantilever fabrication. The first layer was low-stress LPCVD nitride of 50 nm which served as protection for cantilever release. 50 nm of polysilicon was then deposited for conduction. Finally, oxide-nitride dielectrics were grown at 6/55 nm respectively.

The last task was to release cantilevers from the silicon substrate so that they could bend freely. TMAH was chosen over KOH due to selectivity over  $\text{Si}_3\text{N}_4$  and  $\text{SiO}_2$ . Etch rate of LPCVD nitride  $< 20 \text{ \AA/hr}$  and thermal oxide  $< 100 \text{ \AA/hr}$  while the etch rate of silicon is  $\sim 1\text{-}40 \text{ \mu m/hr}$  depending on crystal orientation [2]. Since increased undercutting is desired in releasing cantilevers, cantilever structures were oriented  $45^\circ$  on silicon substrate because TMAH etch rate is greater in (100) than (111) plane [2]. From etch characterization on a sample without metal, we found that optimal etch time is approximately 1 hr for  $70^\circ$  20% wt. TMAH. However, when we etched our final sample for 1 hr with  $70^\circ$  20% wt. TMAH, all of the structures were underetched. It may be that the final sample had Au/Cr-contacts that reacted with TMAH solution causing final etch time to be  $> 1\text{hr}$ . In Figures 3 and 4, we see 2  $\mu\text{m}$  cantilevers

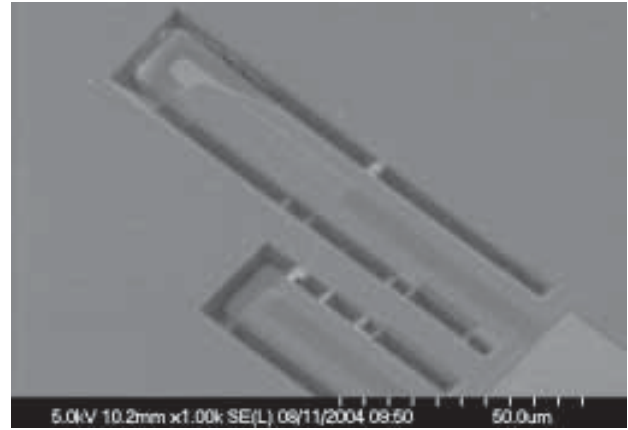


Figure 4: 10  $\mu\text{m}$  cantilever - under-etched.

that are fully released and thicker 10  $\mu\text{m}$  cantilevers that are underetched.

### Results and Conclusions:

Fabrication of the cantilevers was successful; the minimum resolved features were 2  $\mu\text{m}$  with stepper lithography. E-beam lithography is ideal to resolve smaller features and to fabricate smaller cantilevers that bend easier with electrostatic force. The process to release cantilevers worked well however etch rates need to be re-characterized with samples containing metal and for cantilevers of particular thicknesses.

We successfully verified the ability of AFM to detect long-range forces by detecting magnetic forces. It is more likely that charge is not being written rather than not detecting charge. During charge writes in contact mode, setpoint was increased to decrease potential tip damage. However in the future, setpoint should be decreased to increase contact with sample and decreasing tip scan speed.

Although EFM could be performed without applying bias, it is ideal to increase resolution of phase signal. Applying biases of opposite sign and observing phase signal can verify that the pattern is due to electric forces.

### Acknowledgements:

Serhan Ardanuc, Prof Amit Lal, CNF staff, and Melanie-Claire Mallison.

### References:

- [1] H. Bachhofer, "Transient conduction in multidielctric silicon-oxide-nitride-oxide semiconductor structures," *Journal of Applied Physics*, vol. 89, pp. 2791-2800, Mar. 2001.
- [2] A. Merlos, "TMAH/IPA Anisotropic etching Characteristics," *Sensors and Actuators*, vol. 37-38 pp. 737-743, 1993.

# Flow-Through Amperometric Enzymatic Biosensors Containing Glucose Oxidase

Danielle Gainor, Biology, Duquesne University

NNIN REU Site: Penn State Center for Nanotechnology Education and Utilization, Pennsylvania State University

Principal Investigators: Dr. Gregory McCarty, Engineering Science and Mechanics;

Dr. Joseph Irudayaraj, Agricultural and Biological Engineering; The Pennsylvania State University

Mentor: Peter Waldrab, Electrical Engineering, Pennsylvania State University

Contact: gainor848@duq.edu, gmccarty@enr.psu.edu, josephi@psu.edu

## Abstract:

Amperometric biosensors are commonly used in clinical diagnostics. In this work, a flow through amperometric biosensor platform for the detection of biologically important species is microfabricated and tested.

The sensor was created by bonding PDMS microchannels to a glass wafer containing platinum electrodes. Using common surface chemistry techniques, enzymes were immobilized onto the platinum electrodes. Varying the enzyme used enables the sensor to be tailored for detection of a particular species. In this case the enzyme localized on the electrode is glucose oxidase, enabling the system to detect glucose concentration. Glucose oxidase catalyzes a reaction that oxidizes glucose and ultimately produces electrons. The electrons are then detected by a platinum electrode and converted into interpretable results. This electron flow is proportional to the number of glucose molecules or the glucose concentration in the sample.

The objective of this project is to examine how different ionic concentrations influence the detection of glucose concentration at a constant voltage.

## Introduction:

Biosensors promise low-cost, rapid, and simple-to-operate analytical tools. Amperometric biosensors have found their place in many fields of analytical chemistry

and are of great interest in clinical, food, and environmental analysis. Biosensors are commonly linked with blood glucose monitoring and are therefore extremely important for the health of diabetic patients. Other biosensor applications include detection of pathogenic organisms in food supplies, sugar measurement in drink products, and several other uses. Enzymatic amperometric biosensors work well in these areas because of their specificity, speed, simplicity, and reusability. Microfluidic analytical systems are especially helpful because they offer reduced reagent consumption, smaller analysis volumes, and better throughput than macroscopic systems.

There are many factors that influence the performance of the sensor. Some factors that affect electron detection by the electrode include pH, temperature, and ionic concentration. In this project, we chose to concentrate on the effects of increasing ionic concentration in solution. To test the different solutions, we fabricated a device using several techniques including chemical deposition, photolithography, reactive ion etching, and plasma bonding.

## Procedure:

The fabrication of the bioanalytical device consists of two main parts; creating a glass wafer with platinum electrodes and synthesizing a PDMS cast containing microchannels. The PDMS microchannels are made by pouring a solution of PDMS over a patterned silicone wafer. To create the patterned wafer for PDMS casting, we placed a 25  $\mu\text{m}$  layer of SU8-25 onto a silicone wafer (refer to Figure 1A and 1B). To do this, we performed a dehydration bake at 250°C followed by an application of HDMS. The wafer was spun dry at 4,000 rpms. We then static applied SU8-25 and slowly increased the speed to 1500 rpm for 35 seconds. A pre-exposure bake was performed before exposing the wafer to UV light on vacuum contact for 20 seconds. We then allowed a short post-exposure bake and developed the wafer in SU-8 developer for 2 minutes. Figure 1C shows the wafer after the photolithography process.

The PDMS solution consists of a 10:1 ratio of PDMS to activator Sylgred184. The solution was degassed in a vacuum chamber at 30 mtorr for 1 hour and then poured over the patterned silicone wafer and baked overnight (Figure 1D). The PDMS solution hardened and was then peeled off of the patterned wafer leaving an impression of

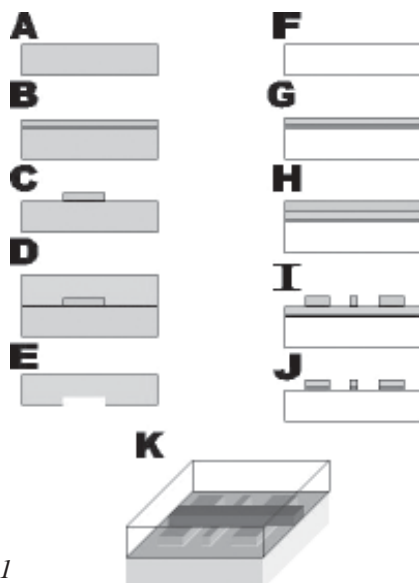


Figure 1

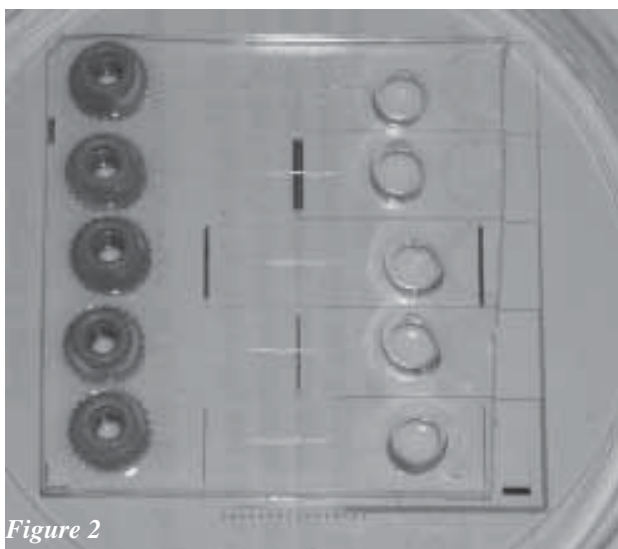


Figure 2

microchannels on the surface as shown in Figure 1E.

To create the electrodes, we evaporated 10 nm Cr and 100 nm Pt onto a 3" glass wafer in the Kurt J Lesker Evaporator (see Figure 1F and 1G). We then applied a layer of photoresist (Figure 1H) by doing an evaporation bake at 110°C for 5 minutes. We then static applied NFR-012 and spun at 300 rpm/s until we reached 4000 rpms. A pre-exposure bake followed by a 4 second exposure on vacuum contact was performed. We then completed a post exposure bake and developed the wafer in a 1:1 ratio of MF-312 developer and water for 60 seconds. Figure 1I shows the results after development.

The glass wafer was then placed in a PlasmaTherm and a 10 minute Platinum and 30 second Chrome etch was applied. We then performed a wet etch with a 2:1 solution of H<sub>2</sub>O and Cr etch. Afterwards, a 4 minute photoresist etch was applied to clear all photoresist off the wafer. Figure 1J diagrams the finished glass wafer with electrodes.

To bond the PDMS cast to the glass wafer with electrodes, we placed both in an oxygen plasma at 120 mtorr for 20 seconds. The device was baked at 90°C for 24 hours to assure adhesion (see Figure 1K). Figure 2 shows a photo of the finished microfluidic amperometric biosensor.

After the biosensor is completely fabricated, we immobilized glucose oxidase onto the platinum electrode using common surface chemistry techniques. The sensor was then tested using phosphate buffer solutions containing different ionic concentrations. A constant voltage was applied and the resulting current was monitored.

## Results and Conclusions:

We were able to successfully fabricate a microfluidic amperometric enzymatic biosensor containing five microchannels and platinum electrodes. When testing the device using increasing substrate concentrations, we found that the chemical detection at the electrode also increased (see Figure 3). Therefore, increasing the amount of substrate in solution causes more reactions to take place on the electrode.

We also tested the device by flowing a 3 mM and 30 mM phosphate buffer solution containing 100 μM glucose through the microchannels. As shown in Figure 4, an increase in ionic concentration results in an increase in current and therefore better detection at the electrode.

## Future Goals:

Future work includes experimenting with different pH solutions, and also varying temperatures to examine how they influence the reaction and the detection of the electrode.

## Acknowledgements:

Special thanks to Dr. Gregory McCarty, Dr. Joseph Irudayaraj, Peter Waldrab, and the rest of the PSU staff for their guidance and support. I would also like to thank the NNIN REU program and the NSF for making this experience possible.

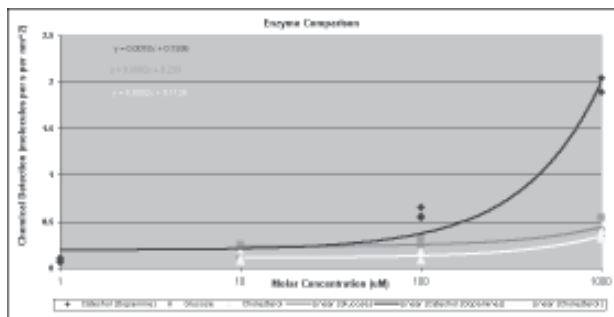
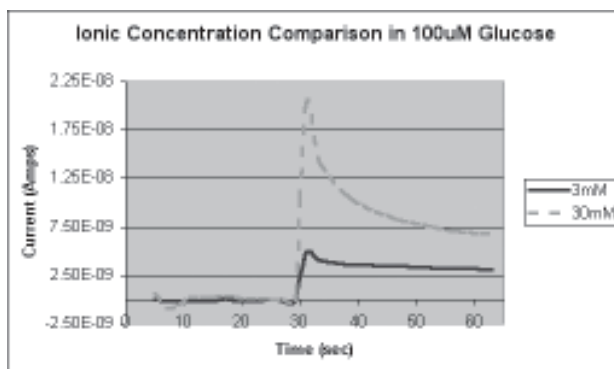


Figure 3, above. Figure 4, below.



# Process Development for Novel Fibrous MEMS Structures

John Gannon, Mechanical Engineering, University of California at Santa Barbara

NNIN REU Site: Cornell NanoScale Science & Technology Facility, Cornell University

Principal Investigator: Michael Thompson, Materials Science and Engineering, Cornell University

Mentor: Shahyaan Desai, Materials Science and Engineering, Cornell University

Contact: johnnygannon@umail.ucsb.edu, mot1@cornell.edu

## Abstract:

Micro Electronic Mechanical Systems (MEMS) have been developed primarily using isotropic materials such as silicon, and are processed using traditional semiconductor fabrication techniques. It is of importance to investigate other materials which exhibit anisotropic material properties that allow for the design and development of application specific tailored micro-mechanical structures.

Fibrous materials display a broad range of anisotropic behavior depending on the type of material of which they are composed. This project focused on the development of a simple fabrication process to incorporate fibrous materials into MEMS structures. Since cantilevers are the most basic of MEMS structures, a fabrication process was developed to make graphitic fibers based cantilevers on silicon wafers using conventional photolithography, wet and dry etching techniques.

## Introduction:

This project was motivated by the fact that materials selection for MEMS is severely limited to traditional semiconductor fabrication materials, which lack basic mechanical property flexibility, preventing the development of structures designed for specific types of deformation and actuation modes. Therefore anisotropic materials must be investigated for specific MEMS devices.

Many fibrous anisotropic materials have strong mechanical properties. The choice of graphite fibers was made because they provide high strength with

good strain characteristics and their deposition process is well characterized. Graphite fibers were used to fabricate aluminum tipped cantilever beams. The aluminum tip would act as a mirror to reflect light from a laser that could be gathered and processed to develop a position verses time characterization data plot.

The goal of the project was to develop a fabrication process for aluminum tipped graphite fiber cantilever beams and begin elementary testing and characterization of the graphite cantilever beam.

## Method:

The process consisted of starting with a four inch silicon wafer. Low stress silicon nitride was grown onto the wafer using a Low Pressure Chemical Vapor Deposition (LPCVD). The silicon nitride thickness was in the range of 500-750 Å. Then the back side of the wafer was coated with 1 µm of Shipley 1813 photolithography resist. The wafer was exposed to ultra violet light with a backside mask made of 1 mm squares. Next the wafer was developed using MIF 300. The backside of the wafer was left with photo resist covering all but 1 mm squares. The exposed silicon nitride squares were etched using a Plasma Thermal 72 (PT72) etcher. The gas used to etch the silicon nitride was CF<sub>4</sub> which etched the nitride at about 300-350 Å/min. The wafer was left with silicon exposed squares. Then the wafer was dipped in KOH and the silicon squares were etched all the way thru the silicon wafer. KOH does not react with silicon nitride, and once all the silicon was removed, only silicon nitride membranes covering the square aperture were left. (See Figure 1.)

Then the front side of the wafer was patterned, exposed and developed using photolithography. This step patterned the nitride membranes for an aluminum deposition. 1000 Å of aluminum was deposited using a thermal evaporator under vacuum. The wafer was set into acetone and lift off was induced. The lift off procedure only left aluminum where the resist had

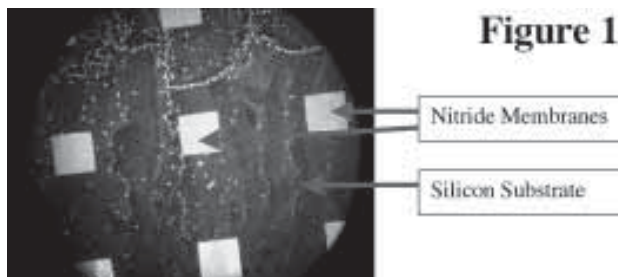
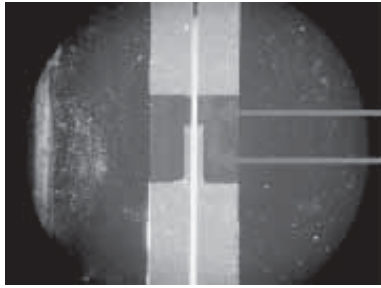


Figure 1



**Figure 2**

Nitride Membrane  
Aluminum Strip

been exposed. The wafer had an aluminum strip on each of the silicon nitride membranes. (See Figure 2.)

With the aluminum attached to the membrane, the graphite fibers were deposited onto the wafer. (See Figure 3.) To keep the fibers anchored to the wafer, Shipley 1075 photo resist was used. Shipley 1075 served as a glue to bond the fibers to the aluminum tips and also to hold the fiber onto the wafer. The silicon nitride membranes were etched away using the PT72. The photo resist held the aluminum to the bottom of the fiber beam. (See Figure 4.)

The last step of the cantilever beam fabrication process was releasing the beam. This step was accomplished by using a laser to cut the graphite fiber at a desired location. Depending on the location of the laser cut, different lengths of cantilevers could be tested for characterization. Once the cantilever was released, the wafer could be cut and the devices could be tested. The devices were tested by attaching the wafer chip to a piezoelectric material and providing an oscillating voltage. The piezoelectric material would create an oscillation force applied to the cantilever and this oscillation frequency of the cantilever was directly proportional to the applied voltage to the piezoelectric material.



**Figure 3**

Aluminum strip  
Nitride membrane  
Graphite Fibers

**Discussion and Conclusion:**

Problems with the silicon nitride membranes stability arose at the beginning of the research. This was solved by making sure the low stress silicon nitride was grown with the right process conditions and with proper spacing of devices on the wafer. Another challenge that was faced happened to be with the aluminum strip not staying in place after the silicon nitride etch. The process was modified by laying the graphite fibers onto the aluminum and then securing the tip of the aluminum strip to the fibers using photo resist.

Elementary device characterization was very promising, with a natural frequency of around 25 kilohertz. However, further device and material characterization is needed to produce feasible devices for the application proposed.

**Acknowledgments:**

This research would not have been possible without the help from the Cornell NanoScale Facility staff, Michael Thompson and most of all, Shahyaan Desai.

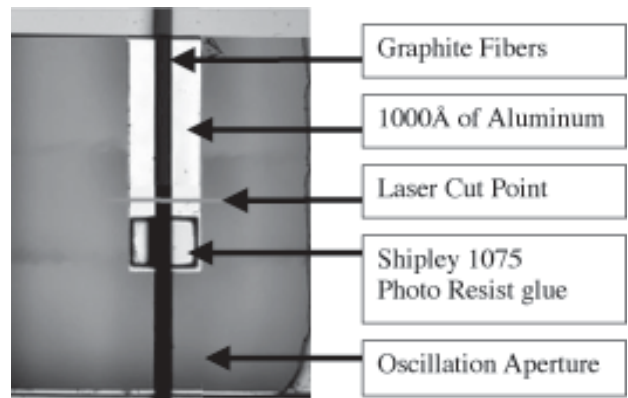


**Figure 4**

# Diffusion of Electrolyte Solutions in Nanoporous Thin-Films

Jay Gantz, Mechanical Engineering, F.W. Olin College of Engineering

NNIN REU Site: Stanford Nanofabrication Facility, Stanford University

Principal Investigator: Reinhold H. Dauskardt, Materials Science Engineering, Stanford University

Mentor: Eric P. Guyer, Materials Science Engineering, Stanford University

Contact: jay.gantz@students.olin.edu, dauskardt@stanford.edu

## Abstract:

A number of next generation nano-scale devices require hybrid organic-inorganic nanoporous thin-film glasses for advanced functionality. Though such materials are currently available, the chemically active solutions the films encounter during fabrication can instigate subcritical crack growth which can potentially limit the reliability of a device. It is important to know if reactive aqueous solutions encountered over the lifetime of a product can diffuse into porous methylsilsequioxane (MSSQ), affecting subcritical crack growth. It has been demonstrated that diffusion of the solutions into a porous film can alter the films' stress state, which ultimately affects the rate of crack growth [1]. The MSSQ selected for this study is highly hydrophobic (contact angle with water is  $\sim 90^\circ$ ) and aqueous diffusion into the material is thought to be highly unlikely.

Here we show that various aqueous solution chemistries do in fact diffuse into the films and the rate of diffusion is influenced by salient solution parameters such as pH, ionic strength and organics.

## Introduction:

Nanoporous MSSQ is a promising new material being considered in the semiconductor, biosensor, optical and pharmaceutical industries. With porosity levels often approaching  $\sim 10$ -50 vol% the films are incredibly fragile and the Si-O-Si backbone of this glass renders the films susceptible to stress corrosion cracking in reactive environments. These factors have limited integration and long term reliability of the films. Understanding how chemically active solutions effect cracking is essential for these materials to be considered viable candidates in these technologies.

In this study, we examine how aqueous solutions diffuse into nanoporous MSSQ films, a behavior believed to affect the long term reliability of the films [1]. We begin by examining the effects of solution pH and observe that with increasing pH, diffusion rates increase dramatically. The ionic strength of the solutions is also demonstrated to affect the rate of diffusion at a fixed pH. Furthermore, it is shown that the presence of organics dramatically affects the diffusion behavior. This study reveals the complex interplay between solution chemistry and diffusion and identifies the need for further study.

## Procedure:

The films used in this study were 400 nm thick,  $\sim 40$  vol% porous MSSQ with pore diameters of  $\sim 4$  nm. We examine the diffusion of aqueous solutions into these films using a previously described technique [2] in which the film is capped with optically transparent silicon nitride using plasma enhanced chemical vapor deposition. A schematic of the Si nitride capped MSSQ can be seen in Figure 1.

The capped MSSQ is then cleaved into wafer sections approximately one-half inch square. The wafer sections are then submerged, exposing the freshly cleaved edges to solution. The diffusion front is observed and recorded using an optical microscope. As the solution diffuses into the MSSQ, the refractive index of the composite changes and the film color changes as seen in the photomicrograph shown in Figure 1. All samples referenced in this paper are LKD-6103 (JSR Corporation, Japan) porous MSSQ. Three samples were run in each test condition. Error bars in all figures are  $\pm 1$  standard deviation.

## Results and Conclusions:

The MSSQ was initially exposed to a number of buffered solutions with pH values ranging from 1 to 11 and water (pH 6) as shown in Figure 2. These tests demonstrate that aqueous diffusion does indeed take place in MSSQ despite

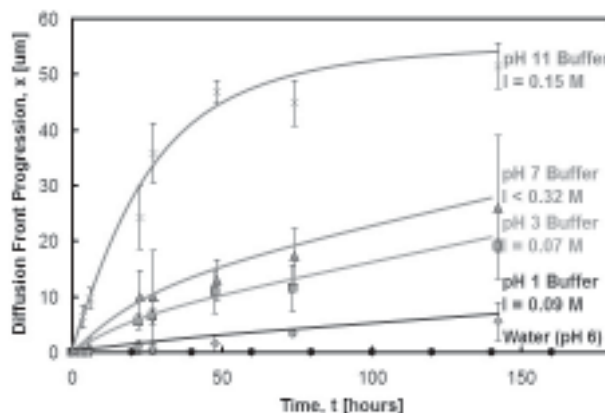


Figure 1: The diagram at the left shows the observation method of capped MSSQ with solution diffusion from the cleaved edge. The photomicrograph at the right is a top down view of the cleaved edge submerged in pH 11 buffer; note the diffusion front that has progressed nearly 100  $\mu\text{m}$ .

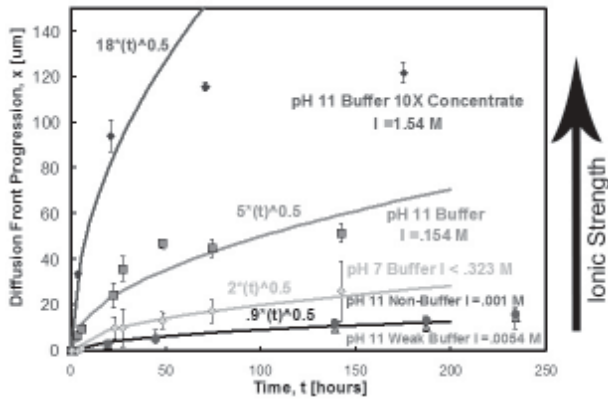


Figure 2: The above diffusion front vs. time graph shows the diffusion behavior of MSSQ in a range of pH buffer solutions and water. In the buffered solutions, higher pH levels increase the rate of diffusion. Note that water does not diffuse.

the inherently hydrophobic nature of the material. With increasing pH in the buffered solutions, the rate of diffusion increases dramatically. The solid lines represent a classic diffusion relationship derived from Fick's laws: diffusion distance goes as the square root of diffusivity multiplied by time. The data is consistent with the model, however, water is an interesting anomaly to this trend as no diffusion is apparent.

To further elucidate the diffusion behavior, we varied the ionic strength (and consequently the activity of the solution) at a fixed pH, as shown in Figure 3. With increasing ionic strength the diffusion rate increases. Note, however, that the pH 7 buffer diffuses faster than some of the lower ionic concentration pH 11 buffers. We believe that this phenomenon is due to the presence of organic species in the buffered solution and as their concentration increased, the solutions diffused faster.

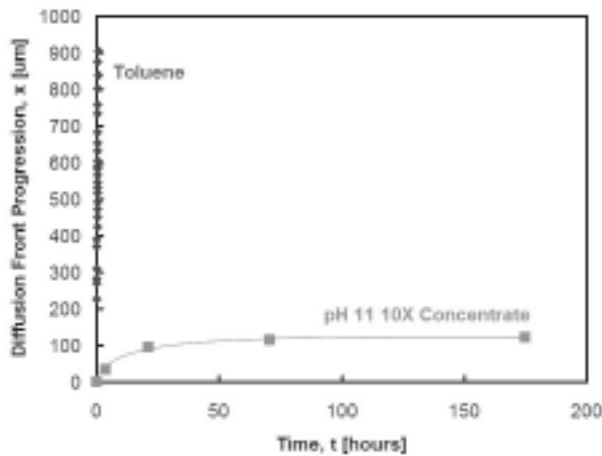


Figure 3: This graph shows the differing diffusion behaviors of pH 11 solutions with different chemistries. Note the deviation from the diffusion behavior predicted by Fick's laws in the pH 11 buffer 10X concentrate.

To investigate the effect of organics, we tested toluene (Figure 4). The startling behavior of toluene confirmed our suspicion. A higher concentration of organics increases the rate of diffusion; in toluene the entire specimen was saturated in under 40 minutes.

Overall, this work has shown that aqueous diffusion does take place in porous MSSQ. Our data reveals a very complex interplay between diffusion and solution chemistry; diffusion behavior is affected interdependently by ionic concentration (solution activity), pH and organic species concentration.

#### Future Work:

We are currently investigating the diffusion behavior of thin-films with lower porosities. We would like to isolate individual buffer constituents to see if they have an effect on diffusion behavior alone. In order to further investigate the effects of pH and ionic concentration, we would like to formulate our own solutions at specific pH levels and ionic concentrations (solution activity). Lastly, we would like to investigate the apparent deviation from Fick's law behavior at high ionic concentrations.

#### Acknowledgements:

I would like to thank the National Science Foundation for funding this research. I would also like to thank Professor Reinhold H. Dauskardt and Eric P. Guyer, Materials Science and Engineering, Stanford University, CA; Dr. Michael Deal and the entire staff at the Stanford Nanofabrication Facility, Stanford University; and the National Nanotechnology Infrastructure Network Research Experience for Undergraduates Program.

#### References:

- [1] E. P. Guyer, M. Patz, R. H. Dauskardt. Effect of Porosity on the Fracture of Nanoporous Thin-Films. To be submitted to Advanced Materials.
- [2] M. A. Worsley, et. al., Detection of Open or Closed Porosity in Low-k Dielectrics by Solvent Diffusion. To be submitted to the Journal of Materials Research. 2004.



Figure 4: In this graph the diffusion rate of toluene is many orders of magnitude more rapid than pH 11 concentrated buffer solution, saturating the entire sample in less than 40 minutes. Error bars are too small to be visible at this scale.

# Spreading of Cells on Supported Peptide Amphiphile Bilayer Membranes

Jill L. Gliem, Chemical Engineering, Lehigh University

NNIN REU Site: Nanotech at UCSB, University of California Santa Barbara

Principal Investigator: Matthew Tirrell, Chemical Engineering, University of California, Santa Barbara

Mentor: Dimitris Stroumpoulis, Chemical Engineering, University of California, Santa Barbara

Contact: jgliem@gmail.com, tirrell@engineering.ucsb.edu

## Abstract:

Peptide amphiphile bilayer membranes may lead to the design of better biomaterials, which will have a variety of uses in medical research. A couple of these areas include in vitro tissue formation and cell specific drug delivery. Currently, work is being done to determine a composition of lipid and peptide amphiphile that will best facilitate cell adhesion and spreading. Vesicle solutions of naturally derived lipids and peptide amphiphiles are prepared. These vesicles are allowed to form a bilayer on a hydrophilic glass substrate. Mouse fibroblast cells are introduced to the bilayer environment and allowed to interact for three hours. Fluorescence and optical microscopy were used to visualize the bilayer and the cells. To quantify cell spreading, imaging software is used to determine the shape factor of the cells.

## Introduction:

Cell adhesion to synthetic surfaces is a topic that has undergone much research in the past fifteen years. In an effort to contribute to the understanding of this topic, our primary goal is to identify important parameters for cell adhesion. The synthetic surfaces that are used in this study are supported bilayer membranes. A bilayer is the result of the self-assembly of amphiphiles, molecules that have a hydrophilic head group and a hydrophobic tail group. In solution, the amphiphiles arrange with the tails inward and the heads exposed to the water/bilayer interface. It is imperative that these membranes are not exposed to air; if that occurs, the membrane would be irreparably damaged. Figure 1 shows a simple bilayer membrane.

A class of amphiphiles contains a hydrophilic peptide head group, a spacer, and hydrophobic tails. These molecules are called peptide amphiphiles (PA). In this study, the peptide head group contains the peptide sequence known as RGD, which has been shown to promote adhesion with many types of cell integrins, molecules on the cell surface that are integral to adhesion [1].

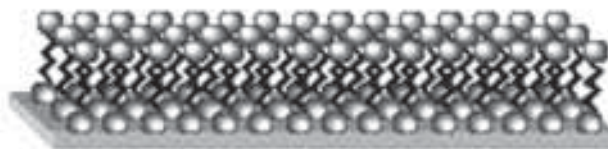


Figure 1: Phospholipid bilayer membrane.

This study focuses on how two different peptide amphiphiles facilitate cell adhesion. The only difference between the two is the size of the spacer group present. For naming purposes, the peptide amphiphiles will be called by their spacer group name, C2 and PEO (polyethylene oxide).

## Procedures:

Vesicle solution of ten percent PA, eighty-five percent egg phosphatidylcholine (egg PC), and five percent Texas Red (fluorescence marker) was prepared and dried under nitrogen to a thin film. The film was then hydrated for an hour and extruded to form vesicles with a diameter of roughly 100 nm. An additional solution of Texas Red and egg PC was prepared using the same techniques.

Bilayers were formed on hydrophilic glass substrates that were cleaned via plasma oxidation. The substrates were affixed to the bottom of a sterile petri dish and a drop of sodium chloride solution was pipetted onto the substrate followed by the vesicle solution. Sodium chloride acted as an agent to increase the pressure on the vesicles and thus, rupture them. As the vesicles ruptured, a continuous, supported bilayer was formed on the substrate. The petri dish was filled with deionized water to insure that the bilayer would not be exposed to air.

To prepare the environment for the addition of cells, some of the water was removed and replaced with Dulbecco's cell medium. Mouse fibroblast cells were introduced to the bilayer environment and incubated for three hours. A similar, more detailed procedure can be seen in a study done by Kam and Boxer [2].

After the cells were allowed to adhere to the surface, optical microscopy was used to visualize their morphologies. Digital pictures of the bilayers were taken and imported into Scion Imaging to determine the shape factor. The shape factor is represented by the equation:

$$4\pi(a)(p)^{-2}$$

Shape factor values range between 0 and 1, with 1 representing a perfect circle. It should be noted that shape factor alone does not indicate adhesion; rather, one sample's shape factor in relation to another sample gives a quantitative idea of how much spreading actually occurred.

### Results:

The bilayers composed of egg PC and 10% C2 PA showed no cell adhesion, with average shape factors of 0.85 and 0.84, respectively. Bilayers composed of 10% PEO PA showed evidence of cell adhesion with an average shape factor of 0.76, or 9.5% cell spreading from the original round morphology.

### Discussion:

The results obtained in this study could be explained by the different lengths of the spacer groups. It is believed that the longer spacer makes the RGD peptide more accessible to integrins; however, this hypothesis must undergo further experimental work.

### Future Work:

The current way of preparing bilayers allows for only one composition of PA to be present on the substrate. It is desired to have one substrate with many corrals of bilayers, each containing a different composition. As shown in Figure 2, there would be an array of bilayers separated by protein barriers.

This would give researchers a versatile tool that allows individual corral study or observation of how the entire concentration gradient affects cell adhesion. To achieve such a gradient, two solutions, one of pure

lipid and one of lipid/PA would be exposed to the substrate via a microfluidic device. Much work is being done to design such a device; however, there are many obstacles to overcome, for example; the fluid mechanics and fabrication of such a small apparatus.

### Acknowledgements:

I would like to thank Professor Matt Tirrell, Dimitris Stroumpoulis, Angela Berenstein, and the Tirrell lab group for their help and support this summer. I would also like to acknowledge the National Science Foundation and the National Institutes of Health for their financial support.

### References:

- [1] Ruoslahti E. RGD and other recognition sequences for integrins. *Ann.Rev.Cell Dev. Biol.* 1996; 12: 697-715
- [2] Kam L, Boxer SG. Cell adhesion to protein-micropatterned-supported lipid bilayer membranes. *Journal of Biomedical Materials Research* 2001; 55:487-495.

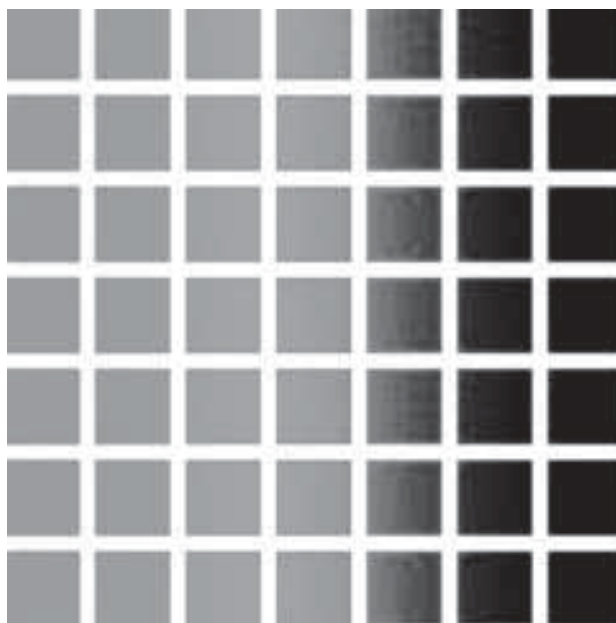


Figure 2: Sample concentration gradient.

# Design and Application of a Fiber Pullout Test for Examining Controlled Interfaces in Fiber Reinforced Polymers

Brian Goodfellow, Materials Science and Engineering, Cornell University

NNIN REU Site: Microelectronics Research Center, University of Texas at Austin

Principal Investigator & Mentor: Dr. Kenneth M. Liechti, Aerospace Engineering and Engineering Mechanics, University of Texas at Austin

Contact: bwg6@cornell.edu, kml@mail.utexas.edu

## Abstract:

A fiber pullout test for examining controlled interfaces in fiber reinforced polymers has been designed and demonstrated. This test has been utilized in determining interfacial fracture toughness for sapphire/epoxy single fiber composite specimens. Some of these specimens incorporated a self-assembled monolayer at the sapphire/epoxy interface as a means of adhesion control—thus altering its interfacial fracture toughness. The application of self-assembled monolayers as controlled interfaces has a wide variety of applications in composite materials—predominantly in MEMS applications where near-frictionless interfaces are desired. The understanding and characterization of these self-assembled monolayers as fiber/polymer interface adhesion control is crucial to their potential in future applications.

## Introduction:

Between components of a composite material, there exists an interface region on the order of several nanometers thick. The properties of this interface region can differ greatly from those of the bulk materials. Furthermore, the performance of the interface can significantly affect the overall performance of the materials system. Thus, by controlling the interface, one should be able to control the performance of the composite material.

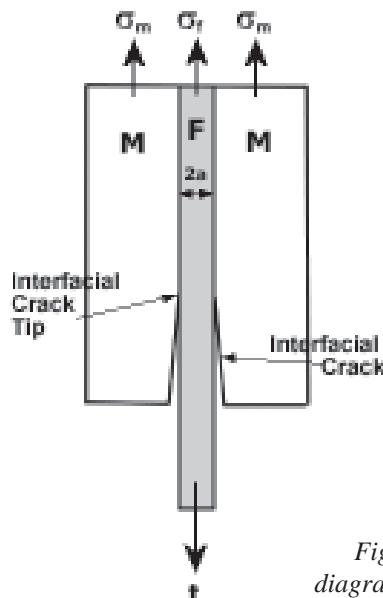


Figure 1: Schematic diagram of fiber composite.

The use of self-assembled monolayers (SAMs) as a means of controlling interface fracture has been proposed [1]. Potential uses of this idea include increasing or decreasing the interface fracture toughness as well as controlling the way in which the material fails. Examples of useful SAMs for this application are octadecyltrichlorosilane (OTS), BrUTS, and DTS. In theory, specifically chosen SAMs applied to an interface can lead to control over various materials fracture properties.

This research is devoted to the design and implementation of a fiber pullout test for the examination and characterization of these SAM interfaces. The theory for the test comes from fracture mechanics—specifically the calculation of the strain energy release rate  $G$ . From Figure 1, it is straight-forward to derive the strain energy release rate as

$$G = \frac{at^2}{4E_f} \left[ \frac{\Sigma}{\Sigma + \frac{f}{1-f}} \right]$$

where  $a$  is the fiber radius,  $\Sigma = E_m/E_f$  (ratio of Young's moduli), and  $f$  is the fiber volume fraction. Further manipulation of this equation leads to an expression for the critical load,  $P_c$ , at which point interface crack propagation begins:

$$P_c = 2\pi \sqrt{a^3 G_c E_f \left[ 1 + \frac{f}{\Sigma(1-f)} \right]}$$

where  $G_c$  is the critical strain energy release rate and the object of this test. Thus, when a single fiber composite test specimen is put in uniaxial tension, crack propagation should occur at  $P_c$ . From this data,  $G_c$  can be obtained.

## Experimental Procedures:

The first stage of the test design was the design of the specimen. A sapphire fiber (~125  $\mu\text{m}$  diameter) and an araldite epoxy matrix were chosen. To introduce a crack into the fiber/matrix interface, a small non-masked section of the fiber was coated with a thin coat of Teflon® before being embedded in the matrix. A dogbone shape was chosen as the specimen geometry because molds for this shape were available from previous experiments and only needed a few modifications. One side of the specimen was left

unchanged while the other was modified in order to effectively grip the sapphire fiber in the tensile machine. It is noteworthy to point out that the cross-section for this specimen is rectangular. While the equations mentioned earlier are derived for circular cross-sectioned specimens, this difference is essentially negligible for the interested range of specimen dimensions. The epoxy was cured for 2 hours at 60°C and allowed to cool overnight in order to lower residual stresses on the interface.

The second stage of the test design was the testing setup. Basically, a standard uniaxial tension test with a constant rate of displacement was used. The tension machine consisted of a stepper motor, a set of linear bearings positioned on vertical rods, and a 100 lb load cell. Also, a microscope and camera were mounted in order to observe and record the propagation of the interface crack. The specimen was to be pulled in uniaxial tension through several propagations until the fiber became totally debonded.

Lastly, some of the fibers were to be coated with OTS. The outline for the procedure used for this is as follows: 1) organic cleaning, 2) hydroxylate the surface, 3) remove excess water from the surface using oven, 4) deposit OTS (in dry box), 5) organic cleaning. These specimens were made and tested in the same ways as above with the exception that no Teflon® was used to introduce an interface crack.

### Results and Discussion:

After much development, this experiment succeeded in obtaining a  $G_c$  value for the specimens. However, there were unexpected characteristics in the data which will be discussed later. Various stages of the crack propagation can be seen in Figure 2. For the specimens without the SAM interface, an average value of 147 J/m<sup>2</sup> for  $G_c$  was obtained from the data (SD: 77). This is a reasonable value for this materials system and thus was the first success of this research. The specimens with an OTS interface had an average value of 75 J/m<sup>2</sup> for  $G_c$  (SD: 41). This is almost half as large as the specimens without an OTS interface.

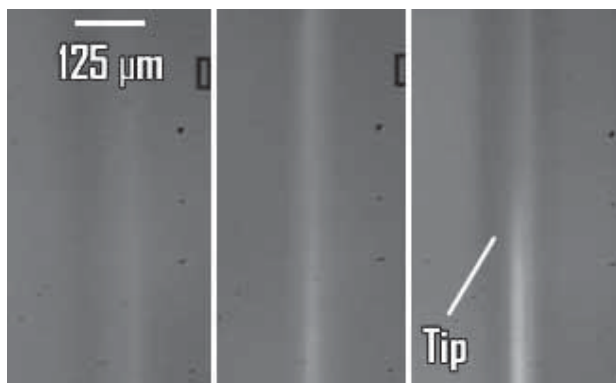


Figure 2: Region of fiber before crack propagation (left), after (middle), and crack tip (right).

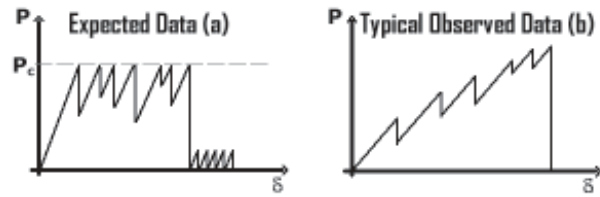


Figure 3: Discrepancy between (a) expected and (b) observed data.

Since it was expected that the OTS would lower the fracture toughness of the materials system, this is taken as the second success of this research.

Figure 3 shows the discrepancies between the expected and observed data. Specifically, in the observed data, the crack propagation peaks increase in height and there is fiber fracture instead of total debonding. Possible reasons for the increase in crack propagation peaks are; 1) residual stresses were present due to the curing process, and 2) crack initiation via Teflon® spray produced a non-uniform interface. To correct this, future research could involve curing the epoxy at room temperature for one week to greatly reduce residual stresses and finding a better way to initiate a crack at the fiber/epoxy interface to eliminate non-uniform effects of Teflon® spray.

Using fracture mechanics, it was found that, given the stress state, dimensions, and properties of the fiber, the fiber should have fractured when it did. To correct this, future research could involve increasing the fiber diameter or by coating the exposed fiber with silicone or a similar material.

### Acknowledgments:

I would like to thank Dr. Kenneth Liechti for all the guidance he provided throughout this project, the technical staff at UT-Austin ASE&EM, Ms. Melanie-Claire Mallison and the NNIN REU Program, and the NNIN and NSF for funding.

### References:

- [1] Mello, A. W. and Liechti, K. M. (2002), "Controlling mixed-mode interfacial fracture toughness with self-assembled monolayers". *Journal of Applied Mechanics*, to appear.

# Etching and Characterization Studies of Ag/n-Si Nanocomposite Films

William Hammond, Physics, College of William and Mary

NNIN REU Site: Materials Science Research Center of Excellence, Howard University

Principal Investigator: Clayton W. Bates, Jr., MSRCE, Howard University

Mentor: Juan White, MSRCE, Howard University

Contact: wthamm@wm.edu, bates@msrce.howard.edu

## Abstract:

Studies were done on 3  $\mu\text{m}$  thick Ag/n-Si composite films prepared by magnetron co-sputtering. This material is being investigated for use as a photodetector for detecting radiation in the 8-14  $\mu\text{m}$  wavelength range. During sputtering, some Ag particles coalesce and create a segregated layer on the surface. In order to use the optoelectronically sensitive composite layer in a device, this segregated layer must be removed. Both an HF wet-etch and a  $\text{Cl}_2$  RIE dry-etch were employed. Resistivity measurements were taken to determine when, during the etching process, the segregated layer was removed; SEM imaging was used to confirm these conclusions. It was found that the wet etch altered the structure of the composite, while the dry etch left behind an involatile film of AgCl.

## Introduction:

The goal of this research is to design a material that will be incorporated into a device that will detect infrared radiation. This photodetector will absorb wavelengths of 8-14  $\mu\text{m}$ , which is a strong part of the blackbody emission for 300K. The material being studied contains Ag nano-sized particles uniformly distributed throughout a semiconductor matrix of n-Si. Photons in the 8-14  $\mu\text{m}$  wavelength range are absorbed by the Ag nano-sized particles. They produce photoexcited electrons that tunnel through the metal-semiconductor interface and give rise to a signal current in an external circuit.

Previous studies by this group have produced and characterized Ag/n-Si composites that absorb radiation in the desired range [1]. This has been achieved by co-sputtering 4:1 n-Si:Ag onto Si (111) substrates maintained at 400°C throughout deposition. At this sputtering temperature, the n-silicon remains amorphous within the composite. In order to achieve greater efficiency in our device, we want to sputter at a temperature high enough to crystallize the n-Si. However, higher sputtering temperature yields larger Ag particles and more dark current.

Although pure silicon crystallizes at 600-650°C, we prepared a fully crystalline matrix by sputtering at 550°C. This is due to metal-mediated crystallization, in which the silver particles act as crystallization sites for the n-Si [2]. We chose a sputtering ratio of 4:1 Si:Ag because at 20 at%

Ag there are enough Schottky junctions to proliferate a photocurrent while still minimizing dark current. This is because at 20 at% Ag, the composite is at half its percolation threshold, which is the point at which continuous paths of Ag are produced throughout the Si matrix.

Silver particles within the composite tend to rise to the surface and form a segregated layer. This phenomenon occurs because Ag particles achieve lower energy by avoiding contact with silicon. This segregating effect actually occurs at all deposition temperatures but increases with temperature. Sputtering at 400-550°C creates a layer of Ag particles equal in thickness to approximately 5-10% of the 3  $\mu\text{m}$  composite film. It is important to note that below this segregated layer, uniformly embedded Ag particles still remain throughout the Si matrix. The segregated layer must be etched away so we can incorporate this composite into a device.

## Procedure:

Cleaved 1  $\text{cm}^2$  portions of 550°C sputtered wafers were etched using a wet etch as well as a dry etch. The material was periodically removed from etching and the resistivity of the film was measured using a four-point probe. Etching was discontinued after the resistivity increased to resemble

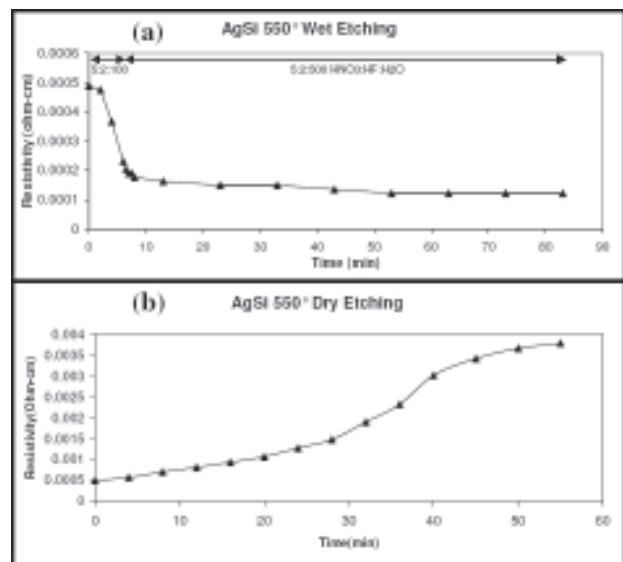


Figure 1. Resistivity vs. etching time: (a) wet etching, (b) dry etching.

that of our n-Si, which ranges from 0.005 to 0.011  $\Omega$ -cm. To confirm the removal of the segregated layer, the sample was cleaved, mounted perpendicularly, and cross-sectionally imaged with an SEM.

The wet etch technique first employed consisted of an etching solution of 2:5:100 HF:HNO<sub>3</sub>:H<sub>2</sub>O. The sample was submerged in solution and agitated with an ultrasonic bath at one minute intervals for 7 mins. The solution was then diluted to 2:5:500 and the sample was submerged for ten minute intervals for another 80 minutes.

The dry etch technique was a reactive ion etch of Cl<sub>2</sub>. We etched in 4-5 minute intervals for 55 minutes.

### Results and Conclusions:

In previous studies of composites sputtered at 400°, the chemical etch uniformly reduced the material without changing the structure of the composite layer. For the composites sputtered at 550°, however, this was not the case. Etching these samples only decreased the resistivity of the material from its initial value of  $5 \times 10^{-4}$   $\Omega$ -cm to more closely resemble the resistivity of metallic silver (Figure 1a). SEM cross-sectional images of the material before and after the etching process appear in Figures 2a and 2b, respectively. From these images, it is apparent that the etching process altered the physical structure of the composite. While the structure originally appears solid, it appears porous after etching. This analysis suggests that the chemical etch selectively etches silicon, leaving behind a composite of higher atomic % silver. These results were confirmed by Rutherford backscattering analysis of the etched films.

In contrast, the dry etch technique did not alter the structure of the composite. As shown in Figure 1b, the resistivity increased during the etching to closely resemble the value of the n-Si. This suggested that we were successful in exposing the composite. However, SEM imaging showed that the etching left an involatile product, AgCl, on the surface (Figure 2c).

In conclusion, we found that the differing properties of crystalline and amorphous Ag/n-Si composites greatly influenced our etching results. The same etch that left intact an amorphous matrix of silicon deformed the physical structure of a crystalline matrix.

### Future Work:

An efficient procedure for removing the segregated layer from these materials will be pursued further. Once this is completed, Hall measurements can assess the transport properties of the composite, and absorption data can test its optical properties.

### Acknowledgements:

I would like to acknowledge Dr. Clayton Bates, Dr. Juan White, and the MSRCE faculty for their generous support and guidance as well as the NSF and NNIN for funding.

### References:

- [1] C.W. Bates, Jr., unpublished results.
- [2] T.J. Konno, R. Sinclair, *Phil. Mag.*, B71 (1995) 163.

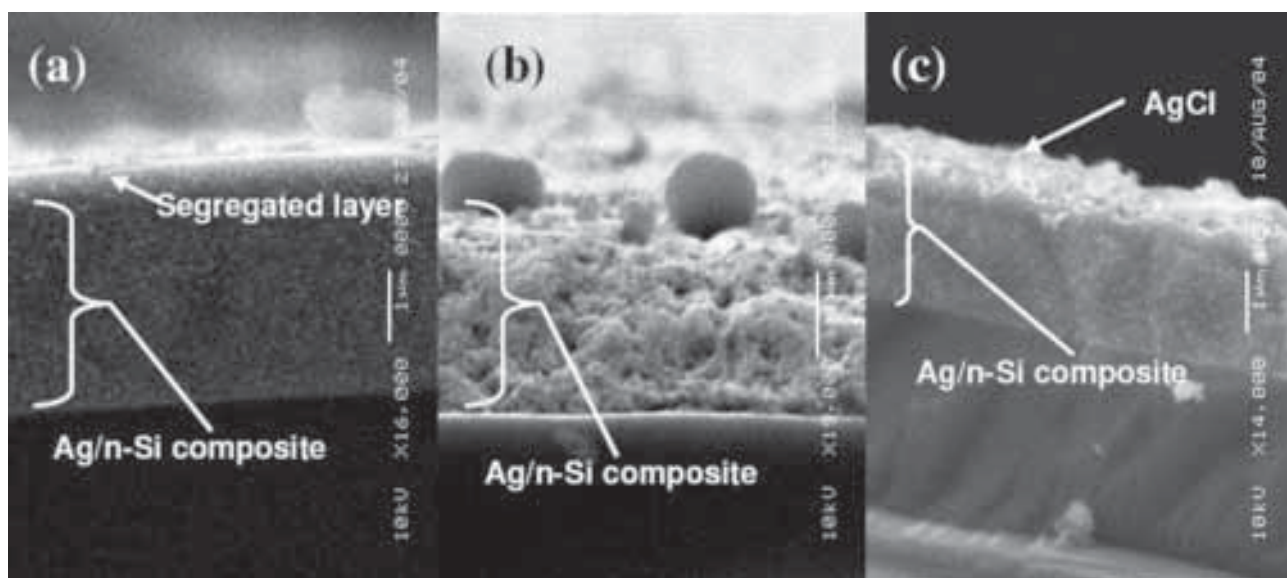


Figure 2: SEM cross-sectional: (a) before etching, (b) after wet-etch, (c) after dry-etch.

# A 90 GHz, Corrugated, Compact Packing, Focal Plane Layout, Platelet Antenna Array

Briony Horgan, Physics, Oregon State University

NNIN REU Site: Nanotech at UCSB, University of California Santa Barbara

Principal Investigator: Dr. Philip Lubin, Experimental Cosmology, University of California Santa Barbara

Mentor: Dr. Miikka Kangas, Experimental Cosmology, University of California Santa Barbara

Contact: briony@orst.edu, lubin@cfi.ucsb.edu

## Abstract:

Corrugated feed horns channel light from free space into waveguides while reducing noise and interference; however, they are expensive to fabricate using current methods. The platelet fabrication methods presented in this paper are straightforward and inexpensive, allowing efficient development of large arrays of corrugated horns. The focal-plane horn array improves upon our previous scalar designs by allowing the array to focus on one point, such as the primary mirror in a telescope.

Unfortunately, tests conducted on the compact-packing array suggest that reflections within the horn skew the beam pattern results. We have concluded that curving the horn near the aperture interferes with optimal operation.

## Introduction:

One of the broadest goals of astrophysics is to gain an understanding of the evolution of the universe. General relativity allows for several different evolutionary models, all differing by what values they assign unknown cosmological constants. By examining disturbances in remnant thermal radiation from the big bang—known as the cosmic microwave background (CMB)—astrophysicists can describe the distribution and composition of the early universe, which in turn helps to determine the most accurate model.

The Lubin Experimental Cosmology group employs arrays of thermally sensitive detectors in their satellite and balloon-borne CMB telescopes. The impedance mismatch between free space and the inside of the detector waveguide can cause reflections at the aperture. To overcome this effect, a type of waveguide known as a horn is used. As shown in Figure 1a, a horn resembles a funnel, and acts in a similar way. By gradually increasing the impedance of the waveguide from that of free space, the horn “funnels” the incoming light into the waveguide.

Ideal metal is infinitely conducting and does not interact with electromagnetic waves. As the metal in the walls of the waveguide is not ideal, it will produce reflections. Cutting grooves into the wall of the horn with a depth of  $1/4$  of a wavelength counteracts this effect. When the component of a wave that is perpendicular to the surface reflects back, it will destructively interfere with itself at the entrance of the groove, effectively eliminating all light contacting the surface. This method also allows the horn to be “tuned” to a specific frequency. Unfortunately, the grooves make molding the horns difficult, which is why we have pursued the development of platelet arrays [1].

Previously, we have tested platelet arrays composed of straight, unfocused horns. Focusing the array on the “source,” as shown in Figure 1b, improves the array’s resolution. Although straight and focused horns would be optimal, this would not allow us to use the same detector array as for the unfocused horn array. Our solution is to curve the horns so that the aperture is directly over the exit waveguide, as shown in Figure 2a.

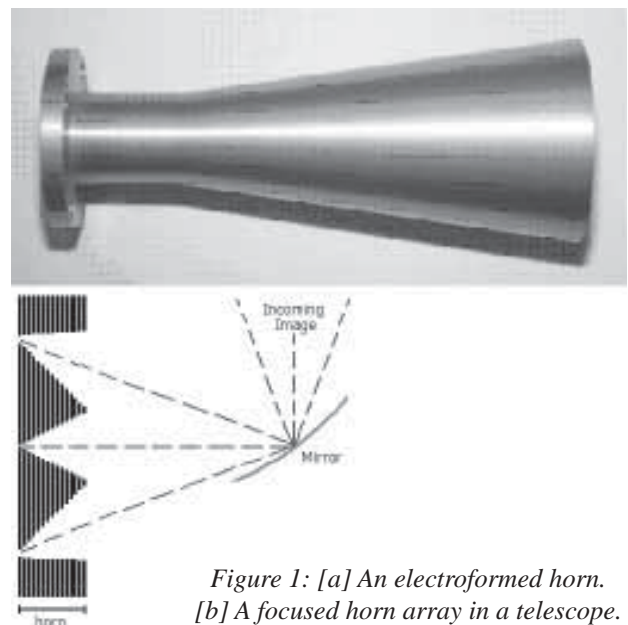


Figure 1: [a] An electroformed horn.  
[b] A focused horn array in a telescope.

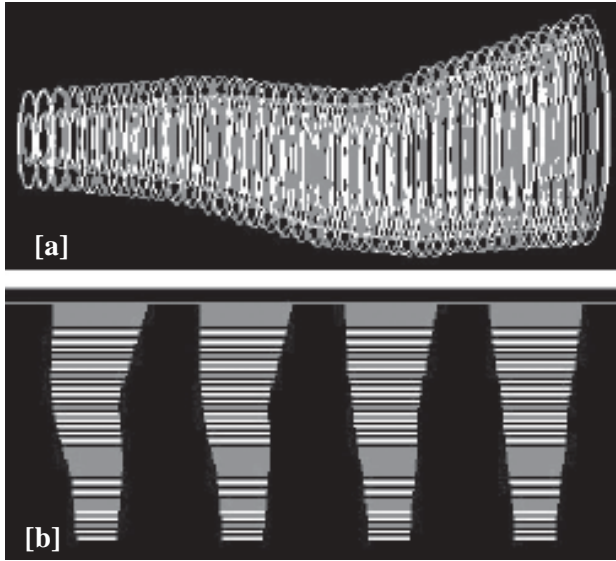


Figure 2: [a] A compact-packing horn.  
[b] A 4-pixel horn array.

**Procedure:**

We designed our horn arrays using the LISP scripting language and AutoCAD. We can now generate designs for straight, focused, and curved arrays at any size and frequency, quickly and easily.

For our prototype, we chose to build a small, 90 GHz, 4-horn array, with aperture tilts of 0°, 5°, 10°, and 15° (Figure 2b). Made entirely with brass stock and brass shim stock, the array consisted of 75 plates ranging from 3 to 40 mils in thickness. Although the 0.5-inch base plate with waveguide sockets was fabricated using machine shop quality mills, the array plates themselves were machined using MasterCAM and a MaxNC tabletop CNC mill.

After aligning and assembling the plates, the array was exposed to a Gaussian, W-band source that spanned over 40° at full-width, half-max. The array was mounted on a stepper motor, and the output of each horn was recorded every 40 arcminutes between -60° and +60° in both azimuth and elevation. After passing the co-polar and cross-polar outputs for both the E and H-planes through multiple optical amplifiers, a whisker diode and a lock-in amplifier, we produced the intensity graph shown in Figure 3b using IDL data processing software and in-house algorithms.

**Results and Conclusions:**

We have previously shown that using the scalar horn results in a gain of 20 dB and side lobes attenuated from the main lobe by at least 22 dB, which satisfies requirements for use in CMB observations [2]. Tests

conducted on the curved prototype indicate that it has a high gain, but lacks the resolution of the scalar horns because of multiple main lobes and unwanted cross-polar signal amplification.

Figure 3a shows an intensity map for the co-polar source-detector orientation for our straight horn prototype. Figure 3b shows the same map, albeit less finely tuned, for our curved horn prototype with maximum slant (15°). The central lobe is as expected; however, the secondary lobe on the right should not be present. We have attributed its presence to internal reflections within the curved, outer section of the horn.

**Future Work:**

The group is currently developing a horn design that should eliminate both the problem of the internal reflection inside the curved horn and the need for the aperture of the horn to be directly over the waveguide. Instead of curving the horn near the aperture, the first 75 plates are linearly slanted. To align the aperture, another 75 plates will be added with the corrugated waveguide slanting in the opposite direction.

**Acknowledgments:**

I would like to thank Dr. Miikka Kangas, Dr. Phil Lubin, the Lubin research group, and the UCSB Physics Machine Shop staff for all their support and assistance. I would also like to thank our sponsors: NNIN, NSF, California Space Grant, and California Space Institute.

**References:**

- [1] R.W. Haas, et al., "A submillimeter wave platelet horn array: fabrication and performance," 5th Int. Conf. on Space and Terahertz Tech., 1994, pp.674-681.
- [2] M.M. Kangas, et al., "A Modular 90-GHz High-Gain Scalar Corrugated Platelet Antenna Array," IEEE Trans. Antennas Propagat., in progress.

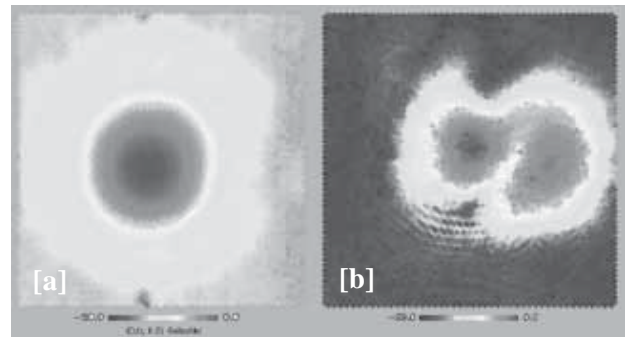


Figure 3: Co-polar intensity-dB plots for [a] straight and [b] 15°-slant compact-packing horns.

# Photochemical Synthesis of Gold Nanoparticles with Interesting Shapes

Hsan-yin Hsu, Electrical Engineering, Purdue University

NNIN REU Site: Microelectronics Research Center, Georgia Institute of Technology

Principal Investigator: Mostafa El-Sayed, Laser Dynamics Lab, School of Chemistry & Biology, Georgia Tech

Mentor: Susie Eustis, Laser Dynamics Laboratory, School of Chemistry & Biology, Georgia Institute of Technology

Contact: hsu@purdue.edu, mostafa.el-sayed@chemistry.gatech.edu

## Abstract:

Our research focused on gold nanoparticle synthesis using UV irradiation to form interesting shapes. Xenon lamp irradiation with a band pass filter selecting wavelengths 250 nm to 350 nm was used to excite the gold precursor, hydrogen tetrachloroaurate(III) trihydrate ( $\text{HAuCl}_4(3\text{H}_2\text{O})$ ) in ethylene glycol (EG). The excited gold precursor is then reduced to gold metal atoms by the solvent, ethylene glycol (EG) and through disproportionation. Polymer polyvinylpyrrolidone (PVP) was used as the surfactant. Optical spectroscopy and transmission electron microscopy were used to characterize the particles. Particle sizes with triangular, pentagonal, and hexagonal shapes were fabricated with various sizes.

It was demonstrated that this convenient method is versatile to fabricate gold nanoparticles with controlled size and shape.

## Introduction:

Nano-scaled materials are of great interest due to their optical and catalytic properties varying with their sizes and shapes [1, 2]. This dependence comes from the spatial confinement of the electrons. In gold metal nanoparticles, strong light absorption in the visible region is shown. The strong absorption results from nanoparticles' coherent oscillation of the free electrons on the particle surface called the surface plasmon resonance. The surface plasmon resonance of gold nanoparticles has broad application and has drawn great attention in recent years [1, 2]. Herein, we report a photochemical gold nanoparticle synthesis method.

In the reaction, the gold salt,  $\text{HAuCl}_4$  absorbs the UV light to generate an excited electronic state, and then reacts with ethylene glycol (EG), which serves as both the solvent and the reducing agent. The gold salt is gradually reduced to  $\text{Au}^0$ .  $\text{Au}^0$  then disproportionates to form gold atoms. The gold atoms serve as nucleation sites for further growth of nanoparticles. The surface regulating polymers (PVP) are expected to bind on the gold surface, insulate the particles from

gold ions and further aggregation, therefore stopping growth and stabilizing the particles. Further, PVP is believed to have selective interaction between different planes of the gold crystal, thus enhancing the growth along one direction while reducing the growth along another direction [3]. Therefore, with different PVP and gold salt concentrations, we can control the shapes and sizes of the particles.

## Results and Discussion:

The effects of altering gold salt concentration, PVP/Au ratio and light intensity on the particles formed were studied. In gold concentration studies, samples were prepared by adding different gold salt volumes, while maintaining constant PVP/Au molecular ratio. Based on TEM images, higher gold salt concentration, lower PVP concentration and lower irradiation power produce larger particles. These images are shown in Figure 1 (a)-(d) with; (a) low gold salt concentration, (b) high gold concentration, (c) high PVP concentration, and (d) low PVP concentration. This trend was also observed in the optical spectra as a red shift of the plasmon resonance absorbance peak around 540 nm and an increase in the infrared absorption

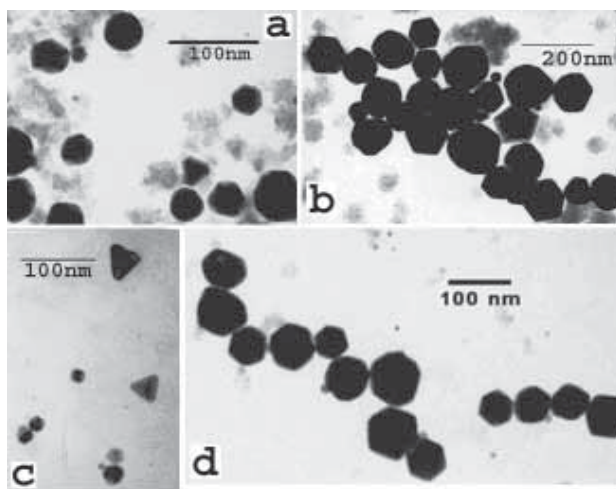


Figure 1: TEM images of gold nanoparticles generated with different parameters.

region. Typical optical absorption spectra are shown in Figure 2.

In typical samples, hexagonal shapes presented about 30% of the particles. Triangles, pentagons represented about 10% and 5% respectively, and the other 50% were spheres and random shapes. For hexagons, the highest yield of 50% can be achieved by using 54  $\mu\text{l}$  PVP, 70  $\mu\text{l}$  gold salt, and 2.7 ml EG with 8 aluminum screening layers. The statistics were obtained from TEM images. Generally, the triangular particles percentage was higher in the samples with smaller particles. Reactions have been carried out both with and without stirring. It was found that particles exhibit better uniformity in size and better yield of interesting shapes without stirring.

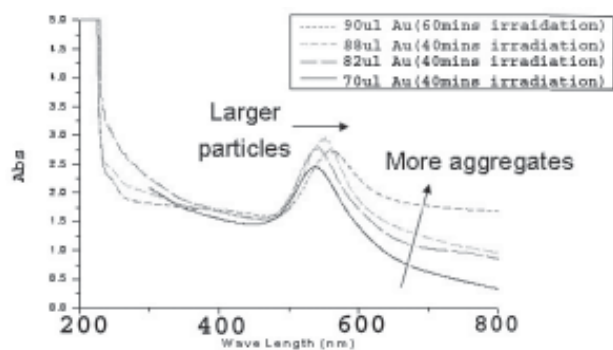


Figure 2: Optical spectra with samples generated with different gold salt concentration.

### Experimental Procedure:

Solutions of 0.375M PVP, 0.083M  $\text{HAuCl}_4$  were prepared in ethylene glycol for use in all experiments. Samples with different combinations of EG, PVP, and  $\text{HAuCl}_4$  were placed in a 1 centimeter path length quartz cuvette for irradiation. A typical sample consisted of a homogenized solution of 2.7 ml EG, 68  $\mu\text{l}$  PVP, and 70  $\mu\text{l}$   $\text{HAuCl}_4$ . Samples were fixed and not stirred. An 88 watts xenon lamp was used for irradiation with a band pass filter selecting wavelengths 230 nm to 380 nm, with layers of closely packed aluminum screening used to adjust the irradiation power. The setup is illustrated in Figure 3. Absorption spectra were measured on a Shimadzu UV-3103-PC spectrophotometer. For the TEM sample preparation, a drop of sample was placed on a carbon coated copper grid, left overnight in the dark, and dried

with a heat gun. Alternatively, a drop of sample solution was attached on one side of the copper grid, which then was gently placed on filter paper with the opposite site facing down. The grids were washed with small volume of water to remove excess PVP prior to viewing in the TEM.

### Future Works:

Future work should be focused on further optimizing the yield. Some possible parameters are to provide uniform UV-irradiation across the sample, to use other surfactants, and to use narrower bandwidth filters.

### Acknowledgements:

I would like to thank my principal investigator Professor El-Sayed, and my mentor Susie Eustis for the research guidance. I would like to thank all the researchers in the laser dynamic laboratory for the valuable discussion and meetings.

I would also like to thank Jennifer Tatham and the Microelectronic Research Center staff at Georgia Institute of Technology for the assistance. Finally, I want to thank NSF and NNIN for the funding to make the research possible.

### References:

- [1] Link, S.; El-Sayed, M, "Shape and size dependence of radiative, non-radiative and photothermal properties of gold nanocrystals," Int. Reviews IN Phys. Chem., 2000, Vol. 19, No. 3, 409-453.
- [2] El-Sayed, M., "Some Interesting Properties of Metals Confined in Time and Nanometer Space of Different Shapes," Accounts of Chemical Research, Vol. 34, No. 4, April 2003.
- [3] F. Kim; S. Connor; H. Song; T. Kuykendall; and P. Yang, "Platonic Gold Nanocrystals," Angew. Chem., 2004, 116, 3759-3763.

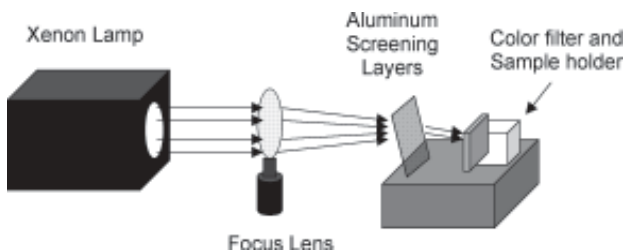


Figure 3: Diagram of the experimental set-up

# Manganese Doping of Germanium Nanowires Seeded from Gold Nanocrystals

Jessica Huang, Chemistry, Harvard University

NNIN REU Site: Microelectronics Research Center, University of Texas at Austin

Principal Investigators: Tobias Hanrath, Doh C. Lee, Brian A. Korgel, Department of Chemical Engineering, Texas Materials Institute, and Center for Nano and Molecular Science and Technology, University of Texas at Austin  
Contact: [jhuang@fas.harvard.edu](mailto:jhuang@fas.harvard.edu), [korgel@che.utexas.edu](mailto:korgel@che.utexas.edu)

## Abstract:

Reports of ferromagnetism in the semiconductor  $\text{Mn}_x\text{Ge}_{1-x}$  motivated the exploration of Mn doping of Ge nanowires grown by colloidal methods. The combination of semiconducting properties with ferromagnetism in these nanostructures would provide an ideal experimental system for fundamental studies of spin-dependent electron transport as well as a potential “building block” for new technological opportunities in information storage and computing.

The Ge nanowires were synthesized using the supercritical fluid-liquid-solid (SFLS) approach, in which Ge nanowire growth via thermal degradation of an organogermane precursor is seeded by alkanethiol-capped Au seed nanocrystals. Following nanowire synthesis, the nanowires were exposed to an Mn source, such as an organomanganese precursor, in the supercritical reactor. After Mn exposure, the Ge nanowires were characterized using HRSEM and TEM, EELS and EDS to determine the doping level in the nanowires.

## Introduction:

The development of semiconductor nanowires has stemmed much research into the future miniaturization of electronic devices through higher device density [1]. Moreover, a new dimension has been added into these studies by the possibility of doping semiconductor nanowires with magnetic impurity atoms to yield ferromagnetism. At the bulk scale, successful synthesis of Mn doped Ge demonstrating ferromagnetism has already been reported [2, 3].

Synthesis of magnetic semiconductor nanowires would further benefit fundamental studies of their magnetic properties and point toward future applications in spin-dependent semiconductor technologies.

This paper reports attempts at the controlled synthesis of  $\text{Mn}_x\text{Ge}_{1-x} \cdot (\text{Cp}^*)_2\text{Mn}$  (manganocene) was used as the Mn source and reacted with Ge nanowires under different reaction parameters. Using this

approach, only trace amounts of Mn:Ge doping were achieved.

## Procedure:

Ge nanowires were synthesized by Au nanocrystal-seeded growth in supercritical solvent, in a SFLS process developed at the University of Texas by Hanrath et al. [4].

The reaction injection precursor was prepared under inert atmosphere and consisted of 30  $\mu\text{l}$  of 0.1M diphenylgermane (DPG,  $(\text{C}_6\text{H}_5)_2\text{H}_2\text{Ge}$ , Gelest, 95%) and 21  $\mu\text{l}$  of size mono-disperse alkanethiol-coated Au nanocrystals (Ge:Au ratio 1000:1) in 2 ml hexane solvent. A second solution of 56 mg of  $\text{Cp}^*\text{Mn}$  dispersed in 2 ml hexane served as the Mn precursor for doping (Ge:Mn ratio 500:1).

A flow-through reactor was created using a 1 ml titanium reactor cell connected to high-pressure tubing via LM-6 HIP reducers (High-Pressure Equipment Co.). A 4 x 10 mm silicon wafer was placed inside the titanium cell. The reactor cell and tubing was connected to a high-pressure liquid chromatography (HPLC) pump (Alcott) and enclosed in insulation and a heating block. A digital pressure gauge (Sensotech) monitored system pressure. Oxygen was purged by flowing deoxygenated, anhydrous hexane through the system several times. The system was heated to 385°C, and system pressure ramped to 500 psi by increasing hexane flow.

After rinsing the injection loop with hexane, the injection solution was loaded into a 350  $\mu\text{l}$  sample loop and delivered at a pressure of 1200 psi. The reaction was allowed to run approximately 10 minutes while the system cooled and pressure decreased. The loop was again rinsed with hexane, and the Mn precursor solution was then injected and delivered by repressurizing to 1200 psi.

The reactor was cooled and depressurized by ejecting the excess liquid reaction mixture. The sample was then rinsed with more hexane at a low flow rate to minimize impurities.

Nanowires were characterized by high-resolution scanning electron microscopy (HR-SEM, LEO 1530 at 10kV). High-resolution Transmission Electron Microscopy (HRTEM) samples were prepared by drop-casting a dilute solution of nanowires in hexane on carbon-coated 200 mesh Cu grids (Electron Microscope Sciences).

### Results and Conclusions:

HRSEM images showed that the reaction product consisted of a dense mesh of long tangled nanowires (Figure 1). TEM images also revealed that nanowires were relatively clean and free of crystalline defects (Figure 2). The average nanowire diameter was ~ 20 nm and reached lengths of tens of micrometers. Although Ge nanowire growth was abundant, EDS revealed very little Mn present in nanowires. Mn doping was not effective using the approach of post-synthesis exposure and annealing in the presence of an organomanganese precursor. We speculate that the low, or in some cases nonexistent, doping results from poor Mn diffusivity from the nanowire surface into the nanowire core. The addition of the organomanganese precursor during the nanowire synthesis may provide one route to effective Mn doping.

Preliminary results from Hanrath et al. have shown promise with substantial doping. The anticipated challenges with this method relate to the competitive decomposition of the Ge and Mn precursors with dissolution in the Au seed particles, which potentially could quench nanowire formation altogether.

In conclusion, Mn doping of Ge nanowires is anticipated to be possible based on previous research of bulk semiconductors, however, appropriate reaction conditions and doping strategy must be developed to achieve these goals. It appears that post-synthesis exposure of the nanowires to the dopant—at least in the solution-phase—and subsequent annealing may not prove to be an effective method.

### Future Work:

Future efforts will focus on increasing the amount of Mn doping. With substantial doping, the Ge nanowires will then be used for fundamental studies of magnetism in nanowires. Magnetic properties may be measured using a superconducting quantum interference device (SQUID).

### Acknowledgements:

Many thanks to Dr. Brian Korgel and members of

his research group for opening up their lab space and allowing this research opportunity. Special thanks to graduate researchers Doh Lee and Tobias Hanrath for their direction and support, as well as to the NNIN REU program and the National Science Foundation.

### References:

- [1] A. Singh, V. Kumar, and Y. Kawazoe, *Physical Review* 69 233406 (2004).
- [2] S. Cho, S. Choi, S. Hong, Y. Kim, J. Ketterson, B.J. Kim, Y.C. Kim, and J. Jung, *Physical Review* 66 033303 (2002).
- [3] F. Tsui, L. He, L. Ma, A. Tkachuk, Y.S. Chu, K. Nakajima, and T.Chikyow, *Physical Review Letters* 91 177203-1 (2003).
- [4] T. Hanrath and B. Korgel, *J. Am. Chem. Soc. Articles* 124 1424 (2001).

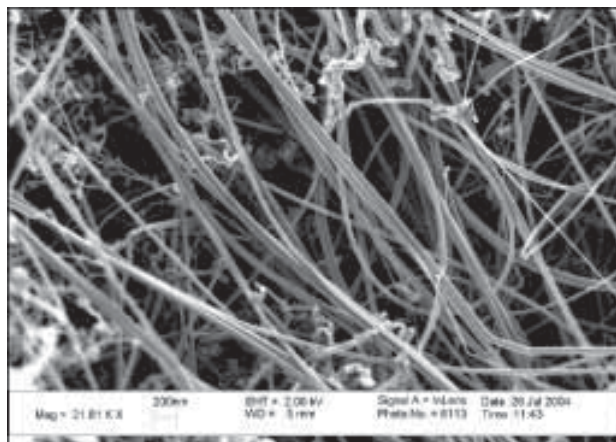
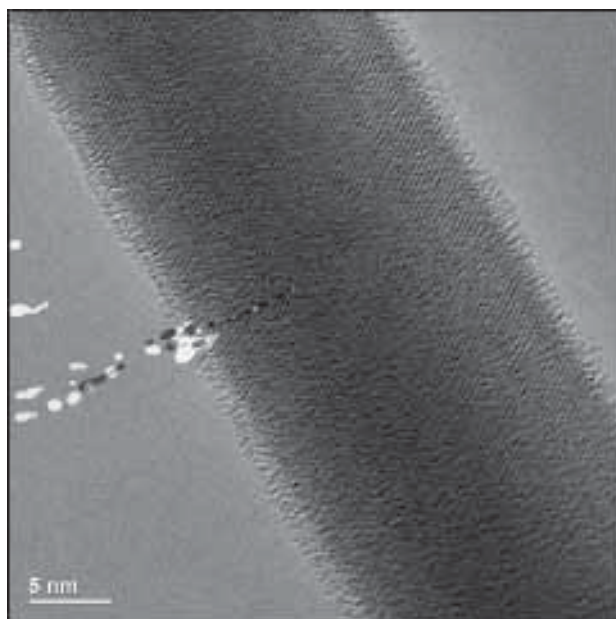


Figure 1, above: SEM image of Ge nanowire.

Figure 2, below: TEM image of Ge nanowire.



# The Self Assembly of Microspheres in a Microchamber

Brandon E. Karlsgodt, Electrical Engineering, Dordt College

NNIN REU Site: Center for Nanotechnology, University of Washington

Principal Investigator: Dr. Deirdre Meldrum, Electrical Engineering, University of Washington

Mentor: Dr. Joseph Chao, Electrical Engineering, University of Washington

Contact: brndnkrl@dordt.edu, deedee@ee.washington.edu

## Abstract:

Frequently, applications of microspheres require a methodology for selectively placing the spheres. This paper discusses the creation of a methodology for placing a near monolayer of microspheres and nanospheres inside of microchambers (ranging in size from approximately 100  $\mu\text{m}$  to approximately 3 mm) attached to two channels (20  $\mu\text{m}$  in diameter). Uniform sphere distribution is prohibited by two internal flow pattern effects: evaporation and capillary effect.

Capillary forces cause the spheres to be pulled toward the edge of the microchamber and into the two channels. In addition, uneven evaporation causes an outward flow pattern that causes the spheres to form a ring upon drying, a ring that is commonly referred to as a “coffee ring.” To overcome these difficulties, a polydimethyl siloxane (PDMS) mask allows a selected area of the microchamber to be treated with oxygen plasma, creating an interface between the treated area of the microchamber and the non-treated area of the channels. This causes the water containing the spheres to stay out of the channels, thereby reducing the capillary force that draws the beads to the edge of the chamber. Heating the sphere-containing droplet altered the flow pattern of the spheres in the droplet, and, consequently, the “coffee ring” was less pronounced.

Further experimentation with this method could lead to a more uniform monolayer of spheres.

## Introduction:

The Microscale Life Sciences Center is a collaboration of 10 investigators from various departments at the University of Washington and the Fred Hutchinson Cancer Research Center. “The goal of the Microscale Life Sciences Center at the University of Washington is to apply microsystem-based devices for the multiplexed, real-time, multiparameter analysis of individual cells” [1]. This desire to measure multiple cellular parameters necessitates the creation of a system for capturing

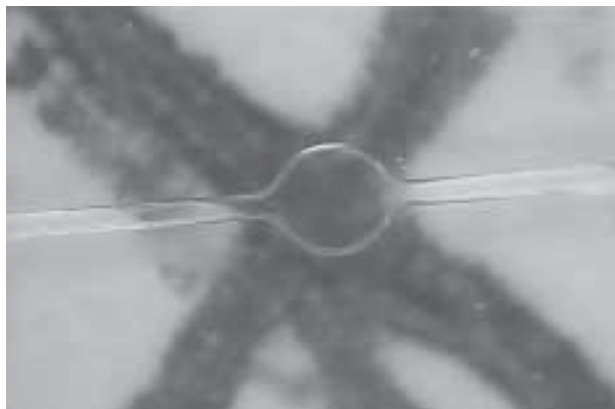


Figure 1: The geometry of the microchamber.

single cells and observing, in real time, various parameters of the cell and its surrounding environment.

The system currently being developed is attempting to utilize microchambers with a geometric structure similar to the microchamber shown in Figure 1. Once a cell is trapped inside of the chamber, another subsystem is needed to monitor parameters of the cell and its surrounding area, namely that of the microchamber. Microspheres and nanospheres, with chemically modified shell layers, have been shown to be effective in a variety of bio-sensing applications [2].

Effective utilization of microspheres as biosensors requires a methodology for the selective placement of the microspheres inside of the microchamber. This paper describes the creation of a methodology that leaves a near monolayer of 1  $\mu\text{m}$  beads inside of a microchamber.

## Materials:

The microbeads primarily used were 1, 4.5, and 10  $\mu\text{m}$  polystyrene beads from Polysciences, Inc. Sphere-containing water droplets were placed on both flat, glass substrates and etched glass substrates. A polydimethyl siloxane (PDMS) mask was used to selectively treat various areas of the glass substrates with oxygen plasma.

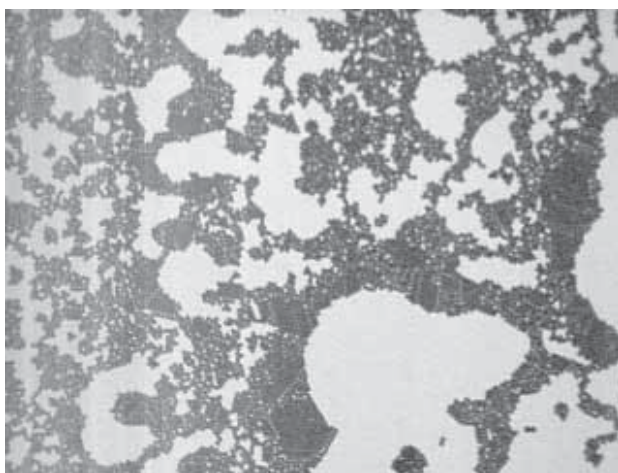


Figure 2: Inner portion of a dried droplet.

### Results and Discussion:

Figure 2 demonstrates the sphere distribution in the inner portion of the droplet without any treatment, where the 10 microliter drops containing 10  $\mu\text{m}$  beads were placed on a glass substrate and allowed to dry. The spheres in the inner portion of the droplet are very disordered. In addition, there is a thick ring of microspheres around the edge of the dried droplet. This ring is not pictured, but it resembles the rings that form when one spills a droplet of coffee on a flat surface and allows the droplet to dry unmolested.

Both the disorder of the dried beads and the formation of the “coffee ring” are undesirous and are caused by the flow pattern of the droplet’s fluid as the droplet dries. As the liquid at the edge of the droplet evaporates, fluid flows from the inside of the droplet to the contact line on the outside of the droplet. Thus, a fluid-flow pattern from the center of the droplet to the outside of the droplet is established. A summary of this phenomenon is discussed in [2]. The inside to outside flow pattern pushes the majority of the microspheres to the edge of the droplet leaving a “coffee ring” at the edge of the dried droplet and a disorderly scattering of microspheres in the center of the dried droplet. This inside to outside flow pattern is undesirous because neither a ring nor a disorderly scattering of microspheres is conducive to placing a uniform monolayer.

In order to change the flow pattern, the droplets were placed on the substrate, and the substrate was heated on a hot plate. The new flow pattern caused the microspheres to move to the center of the droplet. Placing the microchamber in the center of the droplet and using the hot plate to move the microspheres to

the center of the droplet was a method of placing microspheres in the microchamber.

The second problem was due to the capillary forces and the geometry of the chamber. The capillary forces would pull the spheres towards the microchannels and edges of the microchamber. This problem was countered by creating a hydrophobic-hydrophilic interface at the point where the microchannel entered the microchamber. This interface was created by using a PDMS mask to cover only the microchannels while leaving the microchamber exposed and treating the exposed microchamber and only the exposed microchamber with oxygen plasma. The treatment rendered the microchamber hydrophilic relative to the microchannels. The hydrophobic-hydrophilic interface acted as a blockade and reduced the effect of the capillary forces.

Figure 3 shows the results without the interface and the results with the interface. Further experimentation with the methods of changing the flow pattern and methods of plasma treatment should lead to even better results.

### Acknowledgements:

Dr. Joseph Chao, Sarah McQuaide, and Dr. Mark Holl.

### References:

- [1] Lindstrom and Meldrum. “Life-on-a-chip.” [www.nature.com/reviews/micro](http://www.nature.com/reviews/micro). November 2003. Volume 1. pp 158-164.
- [2] Goody and McDevitt. “Multishell Microsensors...”. J. AM. Chem. Soc. Vol 125, No. 10, 2003.
- [3] Deegan, et al. “Capillary Flow...” Nature. Vol. 389. 23 Oct. 1997.

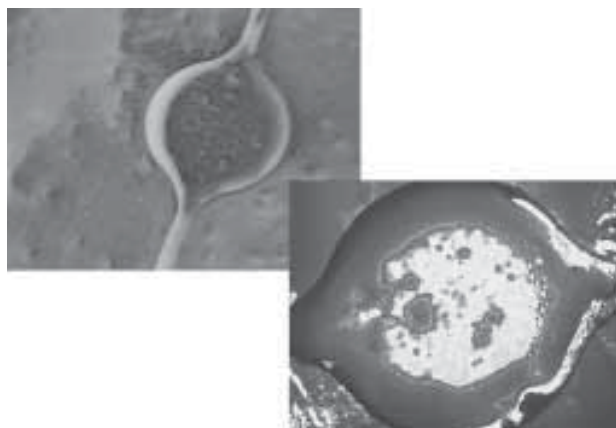


Figure 3: Chamber without interface on top and with interface on bottom.

# Hybrid Nano-Scale Pattern Formation Through Nanocrystal Self-Assembly

Lisa Krueger, Chemistry / Electrical Engr., California State University, Channel Islands

NNIN REU Site: Center for Nanotechnology, University of Washington

Principal Investigator: Prof. Babak Parviz, Electrical Engineering, University of Washington

Mentor: Lisa LaFleur, Electrical Engineering, University of Washington

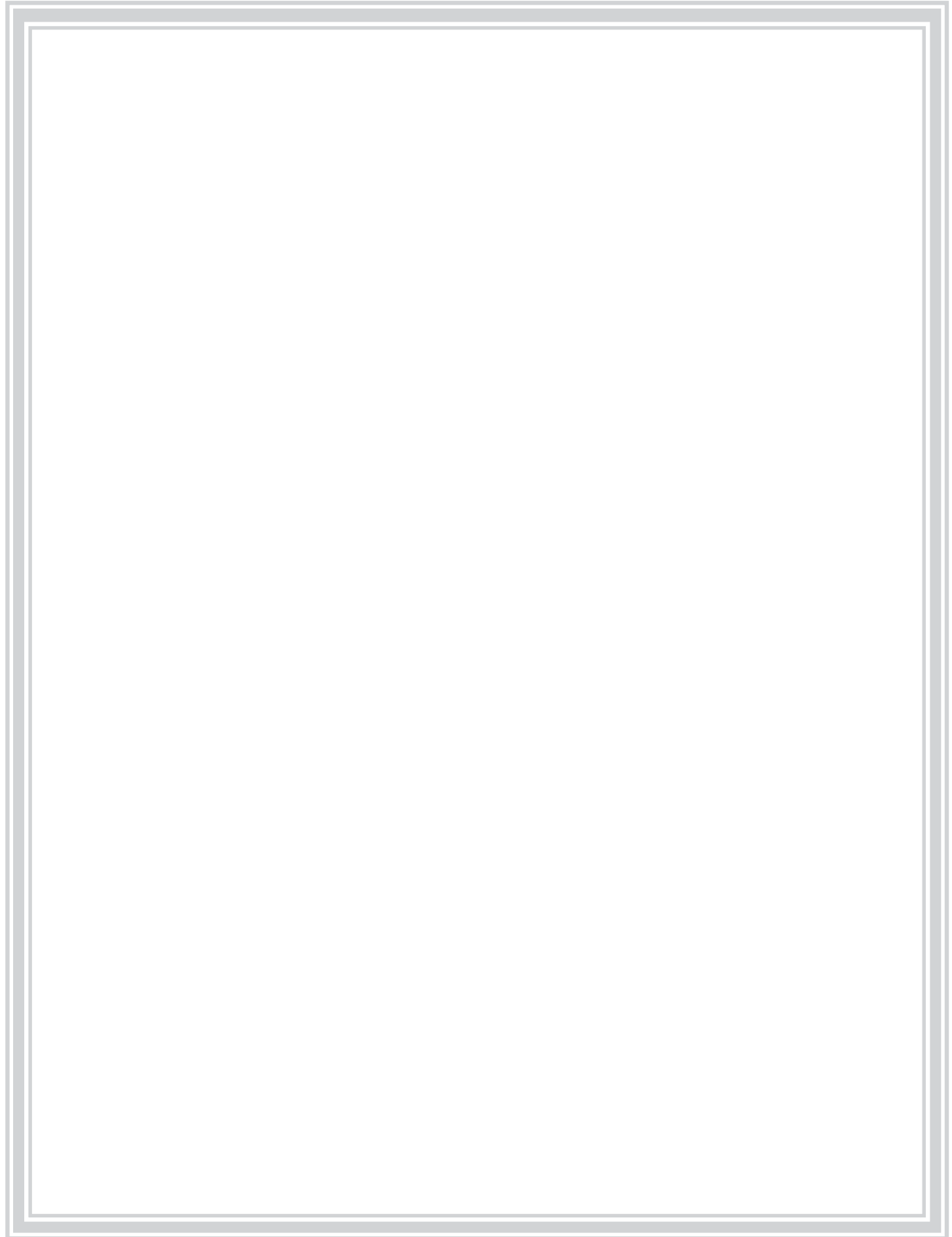
Contact: babak@ee.washington.edu

## **Abstract:**

This project aims to create ordered arrays of semiconducting nanocrystals (NC) on silicon and silicon dioxide surfaces by taking advantage of template-assisted self-assembly. The ability to integrate optically-active materials with nano-scale precision onto silicon substrates in a cost-effective fashion is one of the key technologies necessary to build hybrid electronic-photonics integrated circuits.

In our approach, a nano-scale template is fabricated via electron-beam lithography. This template contains recessions on the surface that form arrays of dots and lines. By dispensing a solution containing semiconducting nanocrystals, we aim to show that the NC's self-assemble onto the template due to tuned capillary and electrostatic interactions. We have made the templates by electron-beam lithography with 100 nm features in poly(methyl methacrylate) PMMA.

We transferred the patterns made in PMMA to silicon or silicon dioxide surface via reactive ion etching. We have used two types of core/shell CdSe/ZnS nanocrystals for the self-assembly experiments. In order, they were 8 nm (dispersed in toluene) and 45 nm (dispersed in water) in diameter with peak photoluminescence emission at 680 nm.



# Optical Readout of MEMS-Based Infrared Detectors

Edward Kung, Engr. Physics / Mathematics, University of Illinois Urbana Champaign

NNIN REU Site: Nanotech at UCSB, University of California Santa Barbara

Principal Investigator: Dr. John Bowers, Electrical & Computer Engineering, University of California Santa Barbara

Mentor: Mr. Raja Jindal, Materials Science, University of California Santa Barbara

Contact: bowers@ece.ucsb.edu

## Abstract:

In this project, we construct and characterize a simple optical readout system for a bimorph micro-electromechanical system (MEMS)-based infrared detector array. In our project, a bimorph MEMS is a heat absorbing pixel attached to a bimorph beam consisting of two different materials, each with different coefficients of thermal expansion (CTE). The difference in CTE causes the beam to deform when exposed to IR radiation, and the angular deflection may be measured optically using a laser and a beam position detector.

## Introduction:

The imager we are attempting to build consists of an array of bimorph MEMS beams with a heat absorbing pixel attached to each beam. The pixel absorbs incoming IR radiation, and the heat spreads to the beam, causing the beam to bend and hence the pixel to deflect. The angular deflection in the pixel is proportional to the change in temperature  $\Delta T$ , and can be measured by reflecting a laser off the pixel's surface and into a detector. The laser can be made to scan across the array of pixels, giving a  $\Delta T$  measurement for each pixel. The measurements can then be constructed into an image.

The specific focus of my internship on this project was to develop and analyze a rudimentary model of the optical readout system. In my model, illustrated in Figure 1, a collimated laser beam with  $\lambda = 670$  nm is focused using a lens onto the MEMS array plane. The beam is then reflected into a second lens which focuses the beam into a differential detector.

## Analysis of Differential Detector:

The differential detector is a quad photodiode which is configured to output a voltage proportional to the difference in current generated by the left and right halves, given by Eq.1, Eq.2, and Eq.3.  $R$  is the responsivity of the detector,  $P$  is the incident power,  $d$  is the horizontal distance from the beam center to

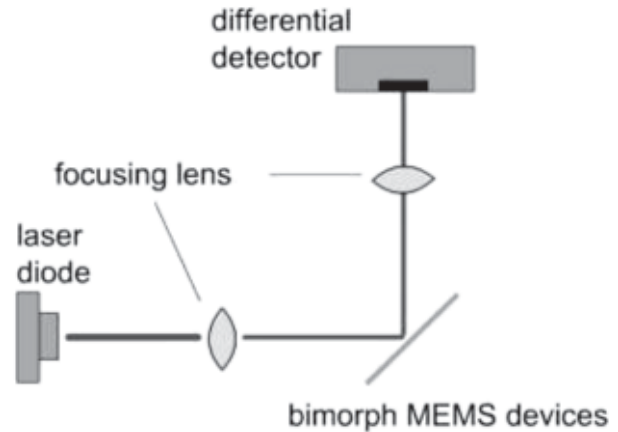


Figure 1: Optical readout system.

the center of the differential detector,  $w$  is the radius of the beam incident on the detector,  $G$  is the length of the detector quad, and  $g$  is the width of the gap between the detector cells. If the focal length of the second lens is  $f_2$ , then  $d$  can easily be converted to  $\Phi$ , the angular deflection of the reflecting surface, using Eq.4.

The integrals in Eq.2 and Eq.3 are difficult to solve analytically, but one notes that they are simply Gaussian distribution functions with mean  $\mu = d$  and

$$V_{out} = (I_R - I_L) \cdot 10^4 \text{ volts} = \Delta I \cdot 10^4 \text{ volts} \quad \text{Eq.1}$$

$$I_R = \Re P \frac{\int_{-g/2}^{G/2} \exp\left[-2\left(\frac{x-d}{w}\right)^2\right] dx}{\int_{-\infty}^{\infty} \exp\left[-2\left(\frac{x-d}{w}\right)^2\right] dx} \quad \text{Eq.2}$$

$$I_L = \Re P \frac{\int_{-g/2}^{g/2} \exp\left[-2\left(\frac{x-d}{w}\right)^2\right] dx}{\int_{-\infty}^{\infty} \exp\left[-2\left(\frac{x-d}{w}\right)^2\right] dx} \quad \text{Eq.3}$$

$$d = 2f_2\phi \quad \text{Eq.4}$$

$$i_{shot} = \sqrt{2e\Delta f(I_R + I_L)} \quad \text{Eq.5}$$

standard deviation  $\sigma = w/2$ . Using values relevant to our setup, and varying between three different values for beam radius, we obtain the plot of voltage response to angular deflection given in Figure 2. In the region near zero, the voltage response is approximately linear. As the angle increases, the sensitivity of the detector decreases. It is important to note that after a particular angle, the detector is no longer sensitive to changes. This implies that in my particular readout system there is a maximum detectable angle, and hence, temperature change. If the incident beam radius is made smaller, the sensitivity near zero increases (higher  $dV/d\Phi$ ) but the maximum detectable angle decreases as well.

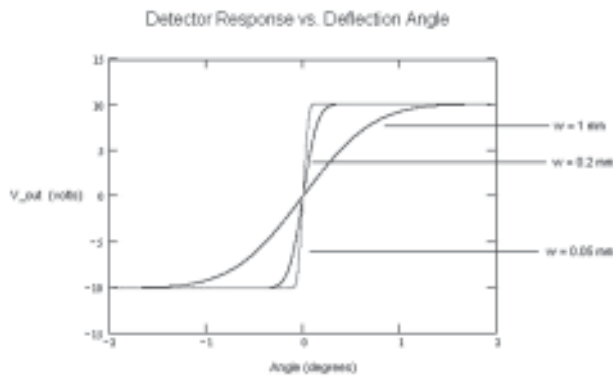


Figure 2: Differential detector response.

### Noise Limited Sensitivity:

The output current  $\Delta I$  and the shot noise  $i_{\text{shot}}$  in the differential detector are both functions of the angular deflection  $\Phi$  in the bimorph devices, which is in turn a function of the temperature change of the device  $\Delta T$ . The exact relation is beyond the scope of this paper; for these purposes, it is sufficient to know that the relation is linear. The minimum detectable temperature change,  $\Delta T_{\text{min}}$ , is the change in temperature for which the output current equals the shot noise. The shot noise is given by Eq.5 where  $e$  is the charge of an electron and  $\Delta f$  is the bandwidth of the detector, here assumed to be 30 Hz.  $\Delta I$  and  $i_{\text{shot}}$  are plotted for various beam radii on Figure 3. The points of intersection are  $\Delta T_{\text{min}}$ .

As expected, a smaller beam radius yields a higher sensitivity (lower  $\Delta T_{\text{min}}$ ). It is apparent, however, that regardless of the beam radius,  $\Delta T_{\text{min}}$  is very small, on the order of  $\mu\text{K}$ , well within our sensitivity requirements. This analysis on  $\Delta T_{\text{min}}$  is valid only when shot noise is dominant over all other noise effects. At the

time of writing, such was not the case. We detect noise levels of about 1 mK due to unknown causes.

### Conclusion and Future Work:

The analysis above shows how the system we constructed behaves according to the angular deflections on the MEMS plane. We have also showed that there are limits to the range of detectable temperature changes, based on the radius of the beam incident on the differential detector. Future work on this project will focus primarily on reducing noise. Possible sources for noise include vibrations in the ground, pressure waves in the air, and thermal leakage from the devices. As of yet we have not fabricated a detectably working MEMS device. When we have done so, we can characterize its response to heat and answer certain important questions as: how fast does the beam bend in response to heat, and how does the source temperature correspond to change in device temperature? When we have a full model for the behavior of a particular system we may begin working on automating the readout system for a full implementation of the imager.

### Acknowledgements:

I would like to thank my mentor Raja Jindal and my principal investigator Dr. John Bowers for their patience and support for this project. I would also especially like to thank all the members of Dr. Bowers' research group for making me feel welcome and for helping me with all the questions I've had.

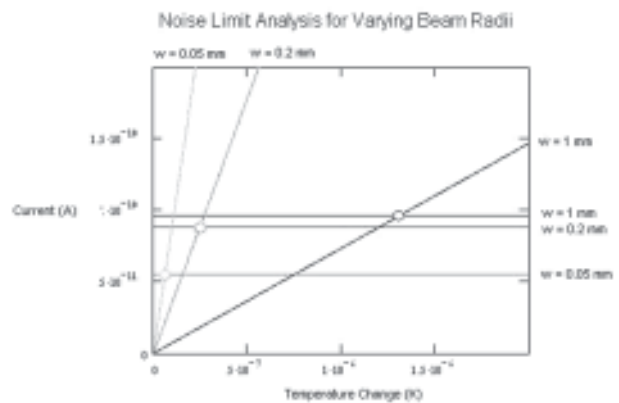


Figure 3: Noise limit sensitivity analysis.

# Making Connections to Molecules for Molecular Electronics

William Lee, Electrical Engineering, Virginia Polytechnic Institute and State University

NNIN REU Site: Cornell NanoScale Science & Technology Facility, Cornell University

Principal Investigator: James R. Engstrom, Chemical and Biomolecular Engineering, Cornell University

Mentors: Abhishek Dube and Manish Sharma, Chemical and Biomolecular Engineering, Cornell University

Contact: wlee@vt.edu, jre7@cornell.edu

## Abstract:

Cross-bar molecular electronic devices can be used for both memory and logic purposes. Our project's ultimate goal was to fabricate a cross-bar array to characterize molecule-based electronic junctions using a self-assembling monolayer (SAM) to form the molecular layer. The immediate objectives were to optimize SAM growth on blanket films and to develop a process for patterning the bottom electrodes into a substrate. To study SAM growth, blanket platinum films were evaporated on silicon substrates. The usefulness of chemical-mechanical polishing (CMP) the platinum substrates was also investigated. Using atomic force microscopy (AFM), the CMP and non-CMP samples were characterized for roughness. Octadecanethiol was used to form the SAMs. The SAMs formed were then characterized using AFM, contact angle measurements, and ellipsometry. It was seen that the SAMs were more uniform on the polished substrates. The electrode patterning was done using standard fabrication techniques.

## Introduction:

The motivation for developing molecular electronic devices is the ability to fabricate denser circuits. Traditional devices can take up large amounts of space, but in working with molecular layers, the basic unit of measurement can be brought down from the  $\mu\text{m}$  scale to the molecular scale.

The design of our molecular electronic device is a cross-bar array where a single molecular layer is

sandwiched between two sets of parallel electrodes perpendicular to each other. Before actual fabrication of the device, research had to be done to learn how to produce a uniform layer of single molecules standing up vertically from the surface of the substrate; the process flow for patterning the electrodes also had to be developed. An octadecanethiol self-assembling monolayer (SAM) was used to form the molecular layer. A uniform molecular layer is critical to the device performance because any deformities in the layer, such as separation of molecules due to too much tilt or holes in the layer, could cause undesirable short circuits to form between the electrodes in later fabrication processes.

Using nano-imprint lithography, H-P Labs were able to fabricate a similar device where each cross point was able to be used as an active memory cell. By simultaneously applying different voltages to the electrodes, the resistance at each cross point could be reversibly switched. In doing so, an electric current could be switched on and off creating rewritable, nonvolatile memory, and in other settings could be used for demultiplexing and multiplexing [1].

## Procedure:

Research began by using e-gun evaporation to evaporate 1400 Å blanket platinum films with 100 Å titanium adhesion layers onto silicon wafers with a native oxide layer. Some of these samples were then chemical-mechanical polished (CMP). In performing the CMP, a platinum slurry wasn't commercially available so the slurry normally used for  $\text{SiO}_2$ , which

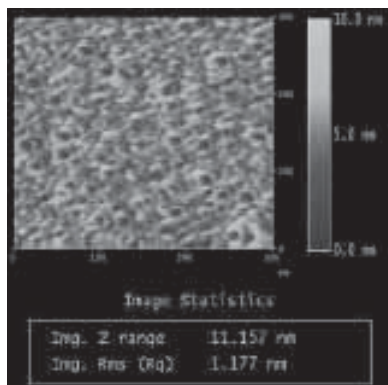


Figure 1: SAM growth on non-CMP sample.

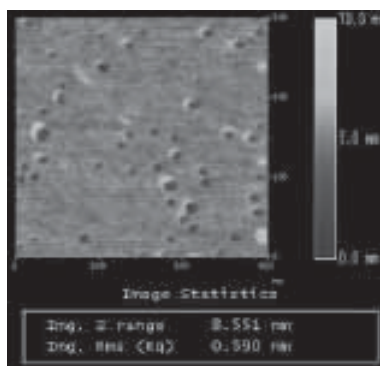


Figure 2: SAM growth on CMP sample.

is the least chemically aggressive, was used. Using the atomic force microscope (AFM), the surface roughness of all the samples was analyzed. The surface roughness is important because a more uniform SAM forms on a flatter surface. It was seen with the AFM that the non-CMP samples had a RMS roughness of about 6-8 Å, while the CMP samples had a RMS roughness of 3-4 Å.

Next a 24-hour liquid phase deposition process was used to grow the octadecanethiol SAM on the substrate surfaces. The AFM was used again to examine the growth of the monolayer. Figure 1 and Figure 2 show the SAM growth on the non-CMP and CMP samples, respectively.

The design of the electrodes called for a set of eight parallel platinum strips, 15 μm wide and 1000 μm in pitch, which fanned out to 200 μm by 200 μm macroscopically accessible contact pads. To perform the patterning of the bottom electrodes, a silicon wafer with 6000 Å of thermal oxide was started with. Soft contact photolithography was used to transfer the design from the mask to the resist. A reactive ion etch was used to etch down 1500 Å into the unprotected thermal oxide. Again, e-gun evaporation was used to evaporate a 1400 Å platinum film with a 100 Å titanium adhesion layer onto the substrate. Lift-off was then carried out. The electrodes were made ideally flush with the surface to prevent complications in the CMP and SAM growth. Again, some of the patterned samples were then CMP. The next steps were to grow SAMs on the samples and form the top electrodes. The top electrodes were to be formed by evaporating through a silicon nitride shadow mask of the same dimensions. This work was performed by an REU intern from the Cornell Center for Materials Research who was also on this project.

### Results and Conclusions:

As shown in Figure 1, there's a denser amount of holes in the monolayer on the non-CMP sample. Whereas in Figure 2, it shows that greater defect-free areas are covered on the CMP sample. In the lower left, there's an ~100 nm by 100 nm area of a perfectly

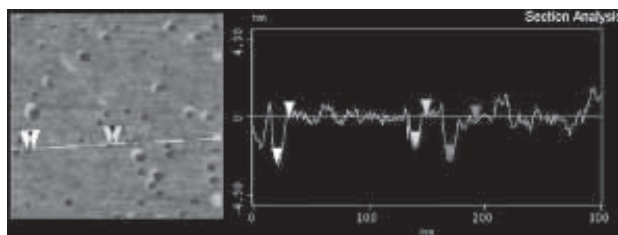


Figure 3: Line scan of SAM on CMP sample.

uniform monolayer. Looking at the profile of the non-CMP sample with a line scan showed that there were many islands of about 23 Å in height, the theoretical length of the octadecanethiol molecule. Figure 3 shows a line scan of the monolayer on the CMP sample in Figure 2. The left part of the graph shows a relatively flat section which corresponds to a uniform layer of densely packed molecules standing vertically. The pits in this scan are again about 23 Å deep, showing where there are holes in the monolayer. From this analysis, it's clearly concluded that the SAMs grow more uniformly on CMP platinum films than on non-CMP ones.

To begin the fabrication of the device, a process to pattern the bottom electrodes into the substrate was developed. The result of this process can be seen in Figure 4, a scanning electron microscope (SEM) image of the patterned wafer.

### Future Work:

The next steps in the project are to finish the fabrication of the device for the testing and characterization of molecular electronics. The next area of challenging research is how to integrate molecular electronic devices with existing electronics, such as CMOS [1].

### Acknowledgements:

Principal Investigator: James R. Engstrom. Mentors: Abhishek Dube and Manish Sharma. CCMR REU: Mark Dreibelbis. CNF faculty and staff. Inorganic-Organic Interfaces. NNIN and NSF.

### References:

- [1] Chen Y, Jung G, Ohlberg D, Li X, Stewart D, Jeppesen J, Nielsen K, Fraser Stoddart J, Stanley Williams R. Nanoscale molecular-switch crossbar circuits. IOP Electronic Journals [online] 2003; Issue 4 April 2003. Available: <http://www.iop.org/EJ/abstract/0957-4484/14/4/311/> via the INTERNET. Accessed 2004 June 16.

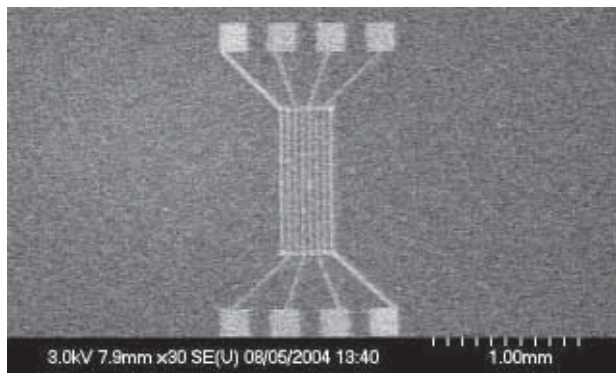


Figure 4: SEM image of bottom electrodes.

# Ordered Nanostructures for Organic Photovoltaic Cells

Nate Miller, Materials Science and Engineering, Case Western Reserve University

NNIN REU Site: Stanford Nanofabrication Facility, Stanford University  
Principal Investigator: Michael McGehee, Materials Science, Stanford University  
Mentor: Vignesh Gowrishankar, Materials Science, Stanford University  
Contact: natemiller@case.edu, mmcgehee@stanford.edu

## Abstract:

Though potentially a source of clean, renewable energy at a cost even lower than conventional power, organic solar cells are at present far too inefficient. The leading strategy for making efficient organic cells is to create nanoscale ordered bulk heterojunctions.

In this work, we used Nanosphere Lithography and Block Copolymer Lithography as methods to pattern Cr nano-dots on Si for use as masks during reactive ion etching (RIE). With these techniques we were able to produce arrays of Si pillars on the order of 120 nm tall and 20 nm wide, which are very close to the ideal length scale. Devices employing these nanostructured substrates have not yet been tested, but exciton splitting, charge collection and overall cell efficiency are expected to be improved.

## Background:

Due to their high cost of production, the use of inorganic solar cells has been relatively limited. Organic semiconductor devices are inherently much less expensive to manufacture, but less efficient due to low charge mobility in the polymer. The most common strategy for making more efficient organic photovoltaics is to use a bulk heterojunction in which

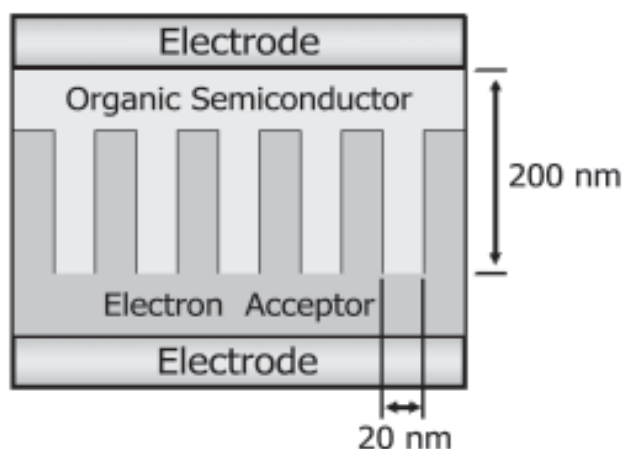


Figure 1: Schematic cross section of the ideal nanostructured heterojunction showing nanoscale interpenetration of the two semiconductor materials.

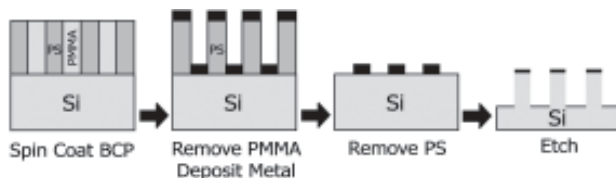


Figure 2: Schematic cross-sectional view of the Block Copolymer Lithography process.

excitons (coupled electron-hole pairs) are split at an interface between two semiconductors with offset energy levels [1, 2]. Since excitons only diffuse 4-20 nm in most organic semiconductors, the interface must be patterned at this scale.

An ideal bulk heterojunction consists of a 100-300 nm thick film of one semiconductor with arrays of 10-20 nm wide pores filled with the other semiconductor, shown schematically in Figure 1 [3]. The electron acceptor material could be any semi-conductor with the right energy levels, and is typically inorganic. Ideally this would be something inexpensive such as titania, but for the purposes of proving the concept of the nanostructured interface, we chose to try to obtain the ideal structure in silicon, which has better understood properties and processing techniques.

We used nanosphere lithography and block copolymer lithography along with reactive ion etching to produce pillars of Si that could be infiltrated with organic semiconductor to create photovoltaic cells.

## Nanosphere Lithography:

With this technique, a monolayer of polystyrene nanospheres ~ 34 nm in diameter were spin cast from aqueous suspension onto Si substrates. Next, an electron beam evaporator was used to deposit ~ 5 nm of Cr onto the samples. Because the particles are spherical, even when perfectly packed, there are spaces between them which allows metal to be deposited directly onto the Si surface, but only in small islands.

We then removed the spheres by dissolving them away in toluene, which left only the small islands of metal on the surface. By choosing a plasma highly

selective to Si (NF<sub>3</sub>), the metal islands acted as a mask during RIE leaving behind pillars of Si.

### Block Copolymer Lithography:

With this technique, thin films of PS-PMMA (polystyrene-poly methyl methacrylate) block copolymer were spin cast from toluene solution onto Si substrates during which the polymer phase-separated into a periodic array of 25 nm PMMA cylinders in a matrix of PS. Ultraviolet light was used to selectively degrade and remove the PMMA cylinders leaving an array of pores, allowing Cr to deposit directly onto the Si surface at the bottom of the pores during subsequent e-beam evaporation. The PS was then removed leaving a periodic array of 25 nm Cr nano-dots on the Si surface. This process is shown schematically in Figure 2.

### Results and Discussion:

The Si pillars created using both lithography techniques were characterized using ultra high resolution scanning electron microscopy (UHR SEM). In Figure 3, which shows the best results obtained with the nanosphere lithography technique, we see that the spatially irregular pillars are ~ 130 nm tall, ~ 25 nm wide, and ~ 25 nm apart.

In Figure 4, which shows the best results obtained with the block copolymer lithography technique, we see that the pillars are ~ 120 nm tall, ~ 20 nm wide, and ~ 15 nm apart, and much more geometrically homogeneous than the results of the nanosphere technique. These structures are very close to the ideal nanostructure that we are trying to create. Ideally we would like the pillars to be somewhat taller, but in terms of width and separation these structures are

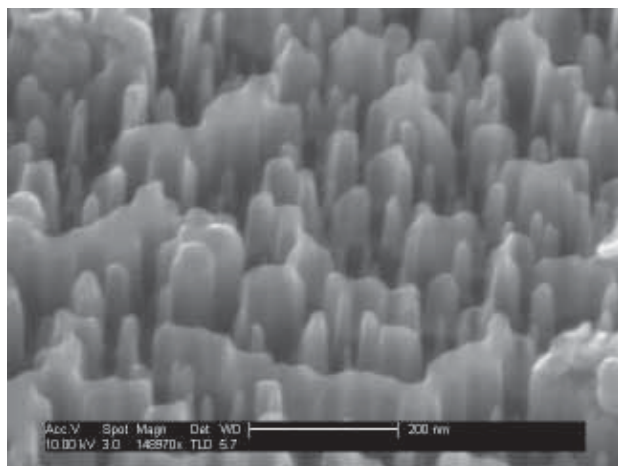


Figure 3: UHR SEM image of structure made using Nanosphere Lithography showing ~ 130 nm tall Si pillars

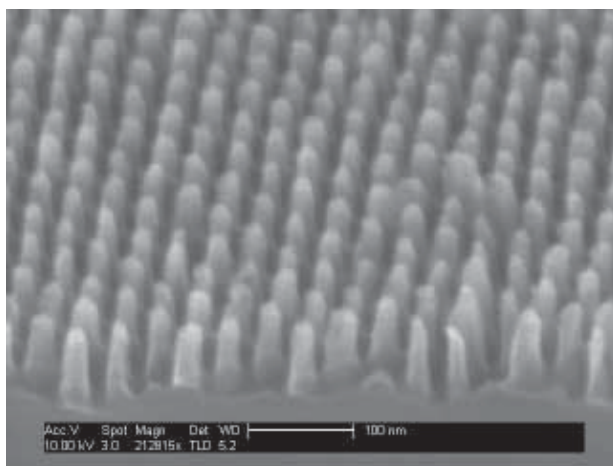


Figure 4: UHR SEM image of structure made using Block Copolymer Lithography showing ~ 120 nm tall Si pillars.

nearly perfect. Additionally, these pillars have relatively straight sides, which would allow for greater ordering and better transport characteristics in the infiltrated organic semiconductor.

The nanosphere technique is an easier process and has so far produced slightly taller pillars, but the block copolymer technique produces a much more ordered structure. Furthermore, this technique has the advantage that it lends itself to greater geometric control since it is relatively trivial to change the molecular weight of the block polymers, which directly affects the size and spacing of the resulting pillars.

### Summary and Future Work:

We have created highly ordered nanostructures in Si, which are very close to the desired size and shape. In the near future, devices utilizing these structures in the heterojunction will be made and tested. Additionally, the entire process of making the pillars and devices should be optimized to maximize efficiency. Ultimately, this knowledge and technology may need to be transferred to some material other than Si, such as titania.

### Acknowledgements:

Vignesh Gowrishankar, Prof. Mike McGehee and the McGehee Research Group, the SNF and the Center for Integrated Systems, the National Nanotechnology Infrastructure Network, and the National Science Foundation.

### References:

- [1] Tang, CW. Appl. Phys. Lett., 48, p183, 1986.
- [2] Heeger et al. Science, 270, p1789, 1995.
- [3] Coakley, KM et al., Adv. Func. Mats., 13, p301, 2003.

# Reactive Electrospinning of Hydrogel Nanofibers

Eric Moore, Chemistry, Drexel University

NNIN REU Site: Penn State Center for Nanotechnology Education and Utilization, Pennsylvania State University

Principal Investigator: Seong H. Kim, Chemical Engineering, Pennsylvania State University

Mentor: Sae-Hoon Kim, Ceramics Engineering, Kangnung National University

Contact: ewm@drexel.edu, shkim@engr.psu.edu, moelkim@yahoo.co.kr

## Abstract:

Electrospinning has been used to produce networks of hydrogel nanofibers. These fibers were spun from a mixture of monomer, cross-linker and photoinitiator, pre-polymerized to achieve the necessary viscosity. UV irradiation of the fibers in flight allows polymerization and cross-linking of the nanofibers prior to collection.

Using this technique, fibers of sub-micron diameter have been produced. The fibers have been characterized by optical microscopy and SEM. Effects of applied voltage, flow rate and needle-substrate spacing have been investigated. In aqueous solution, the swollen fiber network allows efficient mass transport of ions and other dissolved species, as well as serving as a support structure; these properties make hydrogel nanofibers a good candidate for biomedical applications.

## Introduction:

Hydrogels are hydrophilic polymer networks swollen with water; the polymer network may be held together via bonding or intermolecular forces. Hydrogels have found wide use with the biomedical field for use in drug delivery, cell and enzyme immobilization, tissue engineering, and optical lenses [1, 2]. One, particular hydrogel, poly(2-hydroxyethyl methacrylate), first proposed for biomedical use in 1960, has seen use in all of these areas [2].

Diffusion through the hydrogel matrix is of particular importance for biological applications [3]. Cells require a supply of nutrients, and a mechanism to remove waste products and enzymes cannot catalyze reactions without a supply of substrate. By increasing the surface area to volume ratio of the matrix, the rate of diffusion can be increased. One method to increase this ratio when working with fibers is to decrease the diameter; hence nanofibers have a higher surface area to volume ratio than a microfiber.

Nanofibers can be produced by several methods; drawing, template synthesis, self-assembly, or electrospinning. Of these methods, only electrospinning offers a clear path to industrial scale up. Electrospinning uses a high potential, in the kilovolt range, to eject a jet of viscous fluid from a capillary. Traditionally this jet has been a polymer solution or melt which solidifies via solvent evaporation or cooling in flight, resulting in a continuous fiber non-woven mat on the collector [4].

Traditionally, hydrogel structures have been formed in templates or via machining of the polymer in the dry state. Neither of these methods are viable for the production of nanofibers. Electrospinning allows the production of continuous hydrogel nanofibers by spinning a jet of polymer precursor under UV irradiation. The jet consists of monomer, cross-linker and photoinitiator which polymerizes and cross-links in flight. This process uses a chemical reaction during the electrospinning process, hence the term reactive electrospinning.

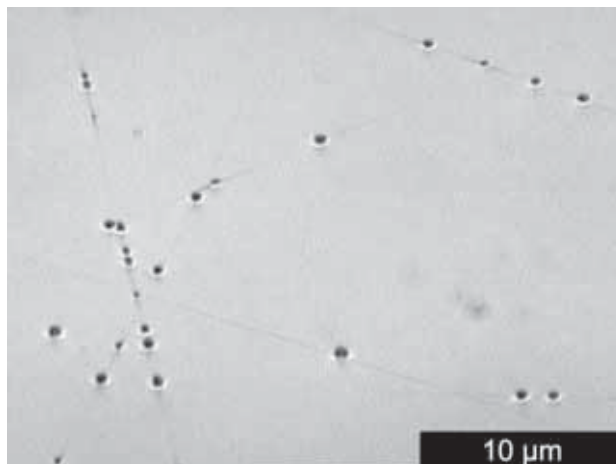
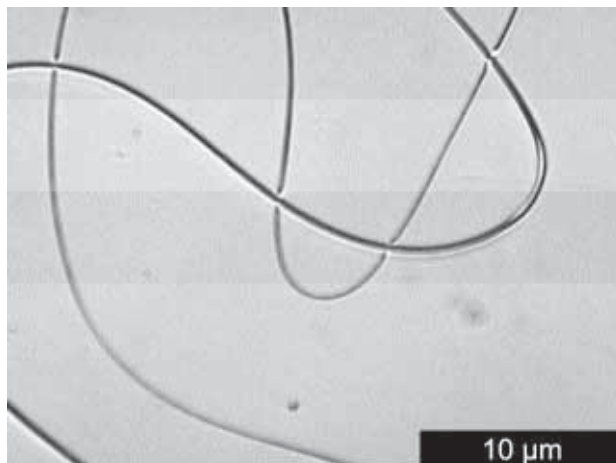


Figure 1, above: 2000x optical image of low viscosity 0% MAA sample (7 kV, 18 cm, 0.0005 mL/min).

Figure 2, below: 2000x optical image of high viscosity 0% MAA sample (7 kV, 18 cm, 0.0010 mL/min).



### Experimental Procedure:

2-hydroxyethyl methacrylate (HEMA) and methacrylic acid (MAA) were used as monomers, cross-linked by ethylene glycol dimethacrylate. 2,2'-azobisisobutyronitrile (AIBN) was used for thermal initiated radical polymerization. HEMA, MAA, EGDMA and AIBN were obtained from Aldrich. Final polymerization used Dorocur-1173, a commercial photoinitiator from Ciba Chemical.

Two mixtures were used: HEMA, MAA 0 mol% or 8 mol%; EGDMA 0.3 mol%; AIBN 0.25 mol%; and Dorocur-1173, 4 mol%. These precursor mixtures were heated in a water bath at 78-82°C for four to six minutes. Following removal from the water bath, polymerization was quenched in cold water for approximately two minutes.

A three mL slip tip syringe (Becton-Dickson) with a 30 gauge 1/2 inch needle (Becton-Dickson) was filled to 1.5-2 mL using the previously pre-polymerized mixture. The syringe was placed into a syringe pump (Harvard, PHD 2000) and infused at a rate of 0.0003-0.0007 mL/min. A positive high voltage of ~6-10 kV was applied to the needle tip; the grounded collector was placed 10-25 cm from the needle. UV irradiated during electrospinning and for the 5 minute post-spin cure was supplied by a 200 W UV lamp (Oriol).

### Discussion:

A range of fiber diameters are produced ranging from sub-micron to several microns. The large fibers are easily visible under optical microscopy, as shown in Figures 1 and 2.

Electrospinning has a large parameter space. Within this space, some parameters can be easily controlled and their effects qualified, such as applied potential, others such as humidity are more difficult.

In investigating this parameter space, three parameters were varied systematically: applied potential (6-10 kV), tip-to-collector distance (10, 18, 25 cm), and infuse rate (0.0003, 0.0005, 0.0007 mL/min). Unlike infuse rate and applied potential, tip-to-collector distance was always optimized to a single value, 18 cm. 10 cm does not allow sufficient time for polymerization during flight, and 25 cm is too far away to easily attract the fibers. Observed trends were similar to those reported in the literature [5].

Of all of the parameters effecting fiber morphology, the most crucial, yet difficult to control parameter, is viscosity. Viscosity control, using the water bath, is coarse and has poor reproducibility, due to the rapidly changing viscosity as the degree of polymerization increases. Considering two samples, one of low viscosity and one of high viscosity, can demonstrate the importance of this parameter. Figures 1 and 2 show optical micrographs of low and high viscosity samples, respectively. Lower viscosity produces finer

beaded fibers, while higher viscosity produces thicker, smoother fibers.

SEM characterization of the produced fibers reveals that fibers were produced with a minimum diameter of 193 nm, shown in Figure 4. This demonstrates that true nanofibers can be produced using reactive electrospinning.

### Acknowledgements:

Dr. Seong Kim, Dr. Sae-Hoon Kim, Sujith Nair, the Kim Group, PSU, and NSF.

### References:

- [1] Hoffman, A.S. *Adv. Drug Deliv. Rev.* 2002, 43, 3.
- [2] Montheard, J.-P.; Chatzopoulos, M.; Chappard, D. *MacromolSciRev MacromolChemPhys*, C32, 1, 1992.
- [3] Amsden, B. *Macromolecules* 1998, 31, 8382.
- [4] Huang, Z.-M.; Zhang, Y.-Z.; Kotaki, M.; Ramakrishna, S. *Composites Sci. Technol.* 2003, 63, 2223.
- [5] Fong, H.; Chun, I.; Reneker, D.H. *Polymer* 1999, 40, 4585.

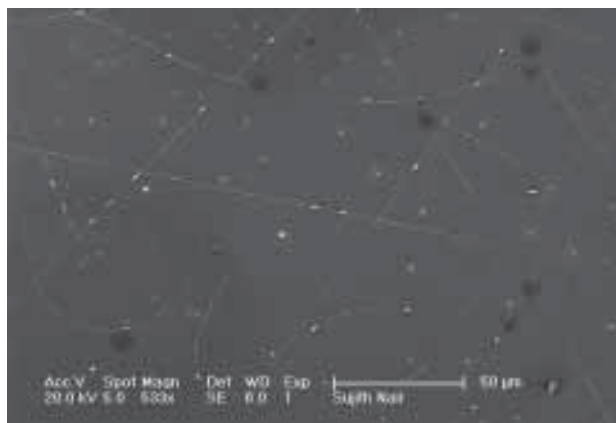
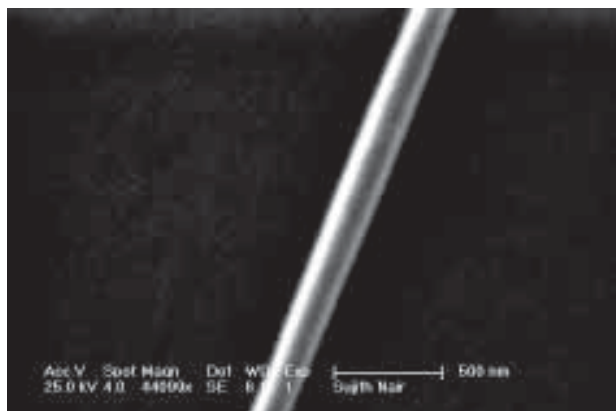


Figure 3, above: SEM of wide view of produced fibers.

Figure 4, below: SEM of smallest produced fiber, 193 nm.



# Micromagnetic Manipulation of Cardiac Tissue

William Moss, Physics and Computer Science, Haverford College

NNIN REU Site: Center for Imaging & Mesoscale Structures, Harvard University

Principal Investigator: Robert Westervelt, Division of Engineering and Applied Science, Harvard University

Mentor: Tom Hunt, Division of Engineering and Applied Science, Harvard University

Contact: wmos@deas.harvard.edu, westervelt@deas.harvard.edu

## Abstract:

Studies of failing heart tissue have shown numerous changes in the cellular microenvironment. More specifically, changes in the cell shape, alignment, and gap junction distribution suggest that stresses and strains within the cell have caused both structural and electrical changes.

The focus of this project is to fabricate a device capable of stressing and straining cells in patterns that mirror the experimental findings. We hope to elucidate how these changes in the cellular microenvironment can affect the electrophysiological functioning of the cell and perhaps precipitate arrhythmias.

We attach matrix-protein coated magnetic beads to specific receptors on the cell membrane, and then, by running currents through nanoscale gold wires below the cells, we are able to create highly localized magnetic field gradients. The resulting magnetic field is highly controllable and capable of exerting forces on the membranes of the cells via the beads.

## Introduction:

Research on failed heart tissue has shown changes in the intercellular environment, suggesting that mechanical stress can contribute to ventricular arrhythmias [1]. The most common method for testing the mechano-electrical properties of cardiac tissues is through the inflation of a balloon within the heart. The action potentials across the cardiac surface can be measured and correlated with the magnitude of the strain on the heart tissue.

The problem with this method is that it is not specific to individual molecules or even cells; thus it is not only not known which cell proteins are responsible for the impulse that causes these changes within the heart, but it is not even clear which cells are responsible.

In our experiment, we are looking to explore the influence of specific integrin proteins on the functioning of the cell. By attaching specific matrix-proteins to the surface of magnetic beads, we are able

to select specific proteins on the cell surface for binding. Once the protein has bound to the cell surface, we can manipulate the beads by generating controlled magnetic fields.

To generate these highly controllable magnetic fields, we used a series of twenty microwires, each connected to a computer-controlled current source. By placing the beaded cells above these wires, we are able to exert forces on the beads by running currents through the wires, generating a magnetic field gradient above the wires.

Our specific aims for this setup are threefold: to test if mechanical strains exerted on the integrin proteins will alter the action potential propagation; to test whether the changes in the  $Ca^{++}$  metabolism of the cell due to micromechanical stimulation contribute to arrhythmias; and to test whether some integrin proteins are more efficient transducers of mechano-electrical coupling.

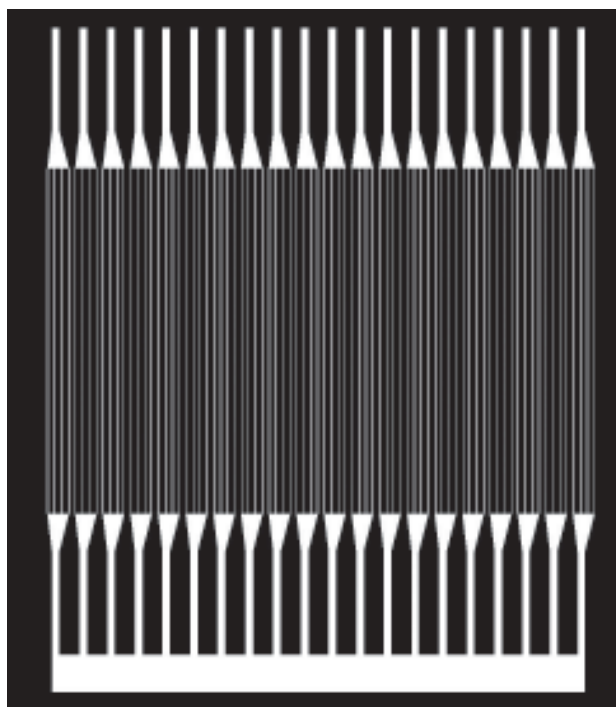


Figure 1: The pattern of wires printed onto our samples.

### Procedure:

Our samples were fabricated using a standard photolithography process. We started with a 2.5 cm diameter sapphire window. We then spun on a layer of Lift-off Resist (Microchem Corp.) followed by a layer of Shipley 1813. We followed that by exposing the photoresist through a chrome mask (Figure 1), in an AB-M UV aligner for 2.6 seconds. The sample was then developed in Shipley CD-26 developer for 60 seconds, with gentle agitation, followed by a wash in DI water, and nitrogen drying. Finally the sample was placed in a Sharon Thermal Evaporator, where 75 Å of titanium and 500 Å of gold were evaporated onto the sample. The remaining resist was then removed using Remover PG (Microchem Corp.).

The sample was then electroplated for four hours in Oromerse BR (Technic Inc.) at 0.2 mA, plating on approximately 2.5 μm of gold onto the exposed regions. Finally the sample was coated with a 9 μm layer of SU-8 (Microchem Corp.), forming a protective biocompatible coating over the wires.

### Result and Conclusions:

We were able to generate magnetic fields capable of exerting forces on the 4.5 μm magnetic beads, attracting beads suspended in water to a current carrying wire. Nevertheless, the forces generated were not of the magnitude we were aiming for. To that end, a redesign of the chip will be necessary to facilitate an increase in the forces generated. Since the magnetic field is proportional both to the current running through the wire and the distance from the wire, proposed designs will bring the wires closer together as well as making the wires larger, to allow for a lower resistance and therefore an increase in the allowable currents.

Also, due to constraints imposed by the optical mapping setup, the entire device must be translucent. This, unfortunately, requires that copper or other metals not be used as a heat sink. The wires, however, generate enough heat that temperature control is necessary, mandating a new design. Current plans

include using a water chamber in contact with the bottom of the wires, allowing for temperature controlled water to be run below the wires, dissipating excess heat and allowing the device to be held at a fixed temperature.

### Acknowledgments:

I would like to thank Benjamin Diop-Frimpong, a fellow REU student, for working with me this summer, as well as Tom Hunt, my mentor, for guiding Ben and I through the summer and teaching me an enormous amount not only about MEMS technology, but about research in general. I would also like to thank Professor Robert M. Westervelt, my principal investigator, as well as Hakho Lee, another member of the Westervelt group, for helping us with the micromagnetics. I, as well, would like to thank Professor Kevin Kit Parker and the rest of the disease biophysics group, for bringing us into their studies of cardiac tissue. Finally, I would like to thank the NSF for funding the NNIN REU program, which provided me with this wonderful opportunity.

### References:

- [1] Hansen DE. Mechanoelectrical feedback effects of altering preload, afterload, and ventricular shorting. *Am J Physiol.* 11993 264(2 Pt 2):H4234-32.

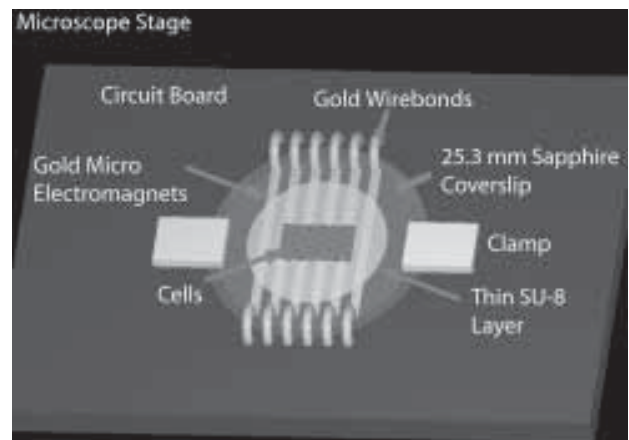


Figure 2: Schematic diagram of our experimental setup.

# Molecular Substrates for Nanobiotechnology

Brad Newsome, Biochemistry, Asbury College

NNIN REU Site: Center for Nanotechnology, University of Washington

Principal Investigator: Mehmet Sarikaya, Materials Science & Engineering, University of Washington

Mentor: Deniz Sahin, Molecular Biology and Genetics, Istanbul Technical University (visiting graduate student)

Contact: bradley.newsome@asbury.edu, sarikaya@u.washington.edu

## Abstract:

For nearly two decades, phage display has been used as an extraordinarily powerful tool for many biotechnological and biological applications. It is a very effective tool for isolation of specific peptides from very high numbers of diverse peptides and proteins. DNA sequences of interest are inserted into the phage genome and the encoded protein is displayed on the surface of the phage as a fusion product to one of the phage coat proteins. This serves as a tool for linking phenotypes of phage displayed peptide or protein with the genotypes encoding that molecule.

Whereas phage display usually involves protein-protein interactions, the focus of this research is using inorganics as a substrate to isolate polypeptides capable of binding inorganic material with high affinity. Single-crystal quartz pieces (001 plane) were used as the substrate for the selection of quartz-specific 12-amino acid peptides from a PhD-12 phage display library. Five biopanning rounds were carried out to obtain DNA sequences and the binding properties of 001 plane quartz were compared to that of 100 plane quartz. The amino acid sequences are compared to search for trends or convergence to a specific sequence.

## Introduction:

Molecular Biomimetics is the marriage of materials science engineering and molecular biology for development of functional hybrid systems, composed of inorganics and inorganic-binding proteins [1]. The new approach takes advantage of DNA-based design, recognition, and self-assembly characteristics of biomolecules. (See Figure 1.)

Phage display is a technique developed by George Smith in which proteins or peptides are displayed on the surface of a bacteriophage [2]. Phage display serves as a selection method in which a peptide or protein is expressed as a fusion with a coat protein of a bacteriophage. This results in the display of the fused

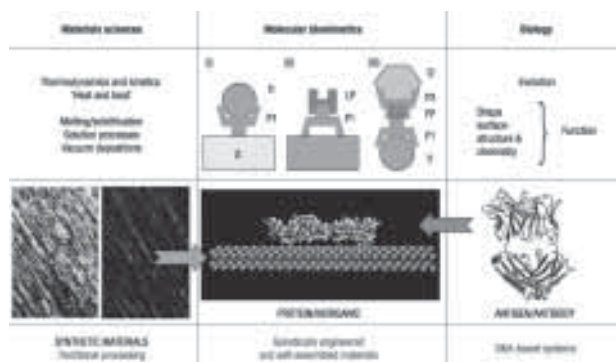


Figure 1: Molecular biomimetics.

protein on the surface of the phage while the DNA encoding the fusion resides within the phage.

A large part of phage display lies in linking the phenotype of a phage displayed peptide with the genotype encoding that molecule, packaged within the same virion. This allows for the selection and amplification of specific clones of phage, as well as the rapid determination of the amino acid sequence of the protein or peptide using DNA sequencing.

Although phage display has typically been used to study protein-protein interactions, this experiment studies protein-inorganic interactions in binding. Because of this, the conditions must be optimized according to that for inorganics. (001) surface plane quartz was used in this experiment to study binding. Comparison with different surface planes of quartz tested previously will provide information about binding characteristics of certain polypeptides on the surface.

The purpose of this research is then to provide the binding characteristics of the different surface planes of quartz for the eventual self-assembly by genetically engineered polypeptides for inorganics (GEPs).

## Procedure:

**Substrate Preparation:** (001) surface plane quartz was washed with ethanol, water, and buffer using sonication. 0.1% detergent containing PC buffer (pH 7.5) was then applied to the substrate and the phage library was added onto the surface.

**Peptide Selection:** PhD-12 library was exposed to the single crystal quartz wafer substrate in PC buffer (pH 7.5) containing 0.1% detergent solution to reduce phage-phage interactions on the surface. After a 30 min rotation, the surface was washed with 0.1% detergent-containing PC buffer (pH 7.5) to eliminate the nonspecific bindings. These washing cycles were repeated ten times for each biopanning round, with a total of 5 rounds. The detergent concentration was increased gradually up to 0.5%. The phage were eluted from the surface by addition of elution buffers for 15 minutes, and the eluted phage were transferred to a fresh tube and neutralized with Tris-HCl. The eluted phage after each round were mixed with *Eschericia coli* ER2738 host cell and plated on LB plates containing Xgal and IPTG. Single plaques were picked and ssDNA was isolated from these plates and sequenced.

**Sequencing:** QIAprep®SpinM13 Kit was then used to isolate single stranded DNA of phage M13 picked up from the XGal/IPTG plates. Then the isolated DNA was isolated by PCR in the presence of dye-labeled terminators. For the purification of the PCR product, Sephadex G-50 was used. DNA samples were then sequenced using automated cycle sequencing. -96 gIII primer, 5'-CCC TCA TAG TTA GCG TAA CG-3', was used for the amplification of ssDNA.

**Results and Conclusions:**

The amino acid sequences obtained to date show some convergence, but it is necessary to have more sequences before analysis is beneficial. The similar sequences seen in Figure 2 show that the phage is specifically binding to the quartz surface. At this point, the sequences for the fourth and fifth rounds are pending, as well as more sequences for the first and third rounds.

Although more experimentation is necessary to determine if the peptides are binding specifically and strongly on the surface of the quartz, this research shows with confidence that this process is effective at isolating peptides that bind to the surface of inorganics. This will pave the way for further research in self-assembly by GEPIs.

**Future Work:**

Sequencing will be continued and the amino acid sequences will be further compared to search for trends or convergence to a specific sequence. Fluorescence microscopy will be used to determine binding affinities of the sequences. Multiple sequence alignment method will be used to analyze the similarities of phage display selected sequences inside and also between the silica binding sequences.

**Acknowledgements:**

I would like to thank Mehmet Sarikaya, Dong Qin, Ethan Allen, and Deniz Sahin for their leadership roles and education in this field I would also like to thank the NSF for financial support and NNIN for this research opportunity.

**References:**

- [1] Sarikaya, M., Tamerler, C., Jen, A., Schulten, K. & Baneyx, F. Molecular biomimetics: nanotechnology through biology. Nature Materials 2, 577 (2003).
- [2] Smith, G. Phage-Display Vectors and Libraries Based on Filamentous Phage Strain fd-tet. Science 228, 1315 (1985).

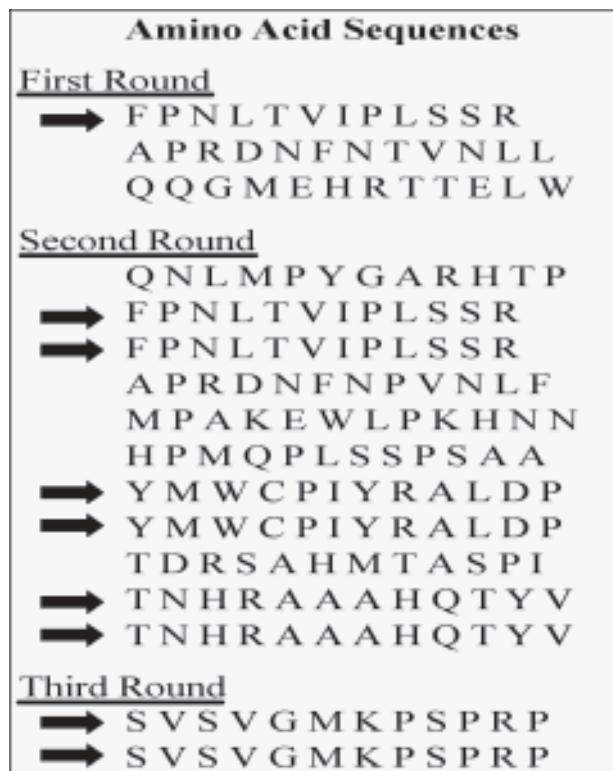


Figure 2: Results.

# Investigation of Novel Thermal Barrier Coating Materials by Minimum Thermal Conductivity

Mai Ng, Materials Science and Engineering, University of Washington

NNIN REU Site: Nanotech at UCSB, University of California Santa Barbara

Principal Investigator: David Clarke, Materials Department, University of California Santa Barbara

Mentor: Michael Winter, Materials Department, University of California Santa Barbara

Contact: spork@u.washington.edu, clarke@engineering.ucsb.edu

## Abstract:

Thermal barrier coatings are used to increase the efficiency of gas turbine engines. The current thermal barrier coating is yttria-stabilized zirconia, however, other material systems with superior properties are being sought for the next generation of turbine engines. This study examines the effect of ion exchange, zirconia with hafnia, on intrinsic thermal conductivity. To achieve this goal, thermal diffusivity of the ceramic mixtures is measured with the Flashline 3000. The effects of ion combinations on the thermal diffusivity are then examined in an attempt to search for potential new thermal barrier coatings.

## Introduction:

With technology rapidly advancing, there exists a growing need for materials that are applicable at elevated temperatures. Rising efficiency of gas engines and higher power-to-weight ratios mean operating temperatures are also expected to climb. Standard coatings, such as yttria-stabilized zirconia, will no longer be suitable. Thus materials with lower thermal conductivity must be sought.

Thermal barrier coatings have low thermal conductivity, which enables the minimal transfer of heat from the exterior to the superalloy's surface, significantly lowering the operating temperature. This prevents temperature related damage incurring upon the engine. As illustrated in Figure 1, the thermal barrier coating is bonded to the superalloy via bond coat. These interactions between layers create a complex system, however, in this study, only the thermal barrier coating is considered.

The significance of a thermal barrier coating lies in its ability to vastly lower initial contact temperature (operating temperature) that a superalloy undergoes. This is represented by the quantified measure of thermal conductivity, which relates to the transfer of energy within a material. The experimentally measurable property of thermal diffusivity describes propagation of heat by conduction during time

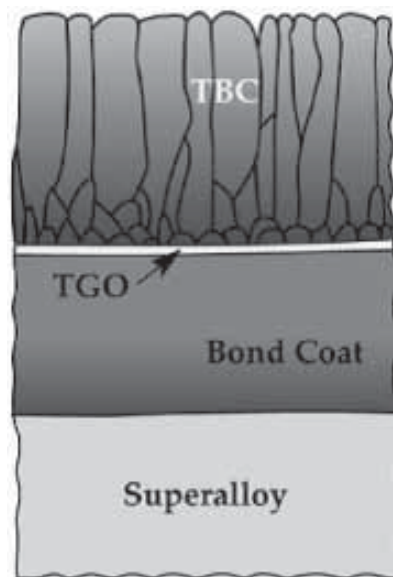


Figure 1: Schematic of a thermal barrier coating, thermally grown oxide, bond coat and superalloy.

dependant temperature changes. A higher thermal diffusivity value indicates more rapid heat propagation, whereas thermal conductivity describes the quantity of heat that passes through the unit area (of a plate) in unit time with a temperature gradient present.

In the high temperature setting typical for thermal barrier coating operation, heat, which can be considered vibrational energy or a phonon, may be scattered by obstacles such as pores or lattice stains. Materials allowing heat to easily travel through possess high conductivity, whereas materials with low conductivity allow fewer phonons to travel. Thermal barrier coatings operate at such high temperatures that phonons travel at the nano scale, thus any scattering mechanisms must be of the atomic level.

In this study, effects of ion exchange on thermal conductivity are examined. In the past, the mixture of two ions resulted in observable change of thermal conductivity. Following this lead, for the study, the two ions, hafnia and zirconia, were chosen. While possessing equivalence in size, atomic charge, radius, and bonding, the mass of hafnia near doubles that of zirconia. Although thermal conductivity cannot be directly measured, thermal diffusivity and other values

can be related. The effects of the ion exchange between the two were examined through measuring the thermal conductivity of samples with increased hafnia content.

**Procedure:**

Thermal conductivity is not directly measured; rather determined with use of thermal diffusivity, heat capacity, and density values. Ten pellets (zirconia to hafnia ratios: 1:8, 1:3, 1:1, 3:1, and 8:1) were batched, pressed, and sintered to theoretical density. Removing all pores ensures that any phonon scattering stems from the ion exchange. The effect of yttria content was also examined with the first set of five pellets having low yttria content and the second set having higher yttria content. This low and high yttria pairing allowed for further examination of the yttria content’s effect on thermal properties. Pellets were then tested for thermal diffusivity in the Flashline 3000 with a pyroceram reference.

**Results and Conclusions:**

Testing produced several sets of thermograms for each sample at various temperatures. The highest, 1000°C, was of primary concern due to the high operating temperatures of gas turbine engines. The thermograms were analyzed with the Clark and Taylor method to produce thermal diffusivity values ( $\alpha$ ), indicated in Figure 2. Along with the density ( $\rho$ ) and heat capacity ( $C_p$ ), the relationship,  $\kappa = \alpha * \rho * C_p$ , produces a thermal conductivity of ( $\kappa$ ).

The thermal diffusivity and density values have been determined. Coupled with the pyroceram reference and specimen densities, and pyroceram heat capacities, the heat capacity and resulting thermal conductivity of the specimen can be calculated.

Finding a thermal barrier coating with lower thermal conductivity than yttria-stabilized zirconia is yet to be fulfilled. Illustrated in Figure 3, the comparison of the thermal diffusivity values with increasing hafnia content at 1000°C describes issues for further investigation. Although the thermal diffusivity values do not correlate directly with thermal conductivity, compositions with 1:3 and 3:1 zirconia to hafnia ratio exhibit an interesting increase. Also noted, is that the thermal diffusivity values are comparable to the diffusivity values for yttria-stabilized zirconia, roughly  $0.6 \text{ mm}^2\text{s}^{-1}$ . This, however, does not eliminate the hafnia zirconia ion exchanged mixtures as a potential future coating, as the heat capacity values are yet to be determined.

**Future Work:**

With the collected thermal diffusivity values, the specific heat and thermal conductivity values are remaining to be calculated. Along with more testing, the thermal conductivity values would be ready for comparison to yttria-stabilized zirconia with the goal of creating a potential new thermal barrier coating.

**Acknowledgments:**

I would like to thank my mentor, Michael Winter, for providing the opportunity to study under his tutelage. I would also like to thank Professor David Clarke, NNIN and NSF for their generosity in providing me with the rare opportunity to my expand my horizons.

**References:**

- [1] Clarke, D. R. and Levi, C. G. “Materials Design for the Next Generation Thermal Barrier Coatings.” Annual Reviews of Materials Research: Vol. 33, 383-417 (2003).

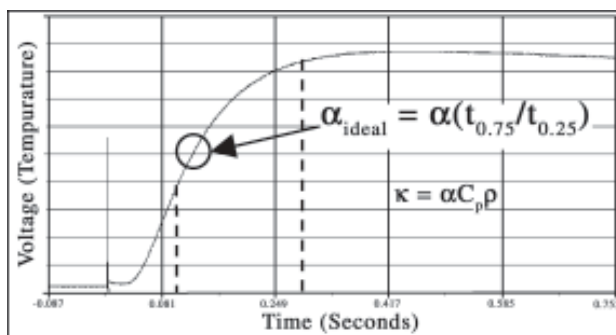
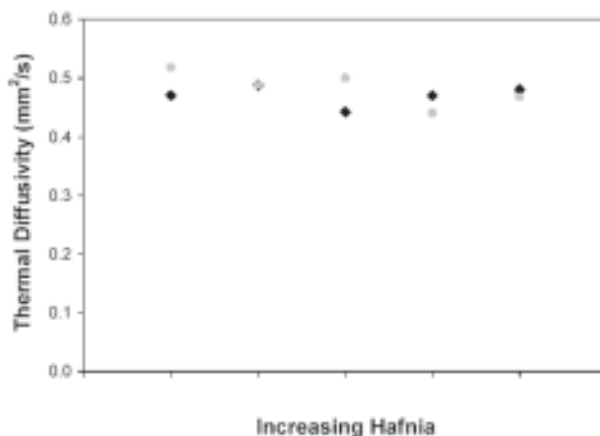


Figure 2, above: Thermal diffusivity calculation and thermogram.

Figure 3, below: Thermal diffusivity values with increasing hafnia at 1000°C.



# Resolution Enhancement Techniques for Optical Lithography

Kabongo Ngandu, Electrical Engineering & Physics, Virginia Commonwealth University

NNIN REU Site: Penn State Center for Nanotechnology Education and Utilization, Pennsylvania State University  
Principal Investigator & Mentor: Dr. Mark Horn, Engineering Science and Mechanics, Pennsylvania State University  
Contact: udnagn@aol.com, mhorn@engr.psu.edu

## Abstract:

The increasing demands for smaller device structures have pushed Optical Lithography (OL) to its resolution limit. Several techniques have been developed to extend the use of optical lithography. Phase Shifting Lithography (PSL) and Immersion Lithography (IM) are two of these techniques.

The focus of this paper is to report the results of using PSL with a broadband UV light exposure and then coupling it with IM. This was done to produce features with a high aspect ratio and high resolution.

## Introduction:

PSL has extended optical lithography by allowing the fabrication of sub-wavelength features without much modification of the OL process. The phase shifting is done by taking a regular chrome-on-quartz mask and reactive ion etching it to a pre-determined depth in certain regions. Next, the chrome is striped off, leaving a chromeless phase shifting mask. Then, the mask is exposed to broadband irradiation. Due to the fact that these adjacent regions have different depths, the transmitted light will undergo a phase shift. Normally, for monochromatic light, the relationship between the phase and etch depth is given by the Equation 1 [1].

$$\Theta = \frac{2\pi d(n-1)}{\lambda}$$

Equation 1: Determines the resultant phase shift

In this equation  $\Theta$  is the phase,  $\lambda$  is the wavelength of the exposing light,  $d$  is the etch depth, and  $n$  is the index of refraction at this wavelength. Ideally it is desired to have a phase shift of  $180^\circ$ . This will allow the transmitted light from the etched and non-etched regions to form a dark field on the photoresist due to destructive interference.

Due to the fact that a broadband exposure was used, the exact shifter depth to produce the phase shift was not known. Therefore, four phase shifting masks, with

different shifter depth gradients across each mask were used to determine which shifter depth produced the higher resolution features.

Recently IM has been accepted by the integrated circuit industry as a new technique that will extend the use of OL. The resolution (minimum feature size) is determined by the Raleigh equation listed in Equation 2 [2].

$$R = k_1 \frac{\lambda}{NA}$$

Equation 2: Determines resolution (min. feature size).

In this equation  $R$  is the resolution,  $\lambda$  represents the wavelength of the exposing light,  $k_1$  is the resolution factor, and  $NA$  is the numerical aperture. IM focuses on increasing  $NA$ , which is proportional to the index of refraction of the medium between the wafer and the lens of the contact aligner. Traditionally the medium was air, which has an index of refraction of 1. In IM, the air is replaced with water, which has an index of refraction of 1.33. This allows for a higher  $NA$  and leads to a higher resolution.

The focus of this project was to use broadband irradiation with PSL to fabricate high aspect ratio sub 200 nm features. Then IM would be used to produce even higher resolution features. This project used bare silicon wafers, MF-CD-26 developer, four pre-fabricated phase shifting masks, and SPR 3012 photoresist. The exposure tool used was a Karl Suss MA-6 Contact Aligner with a broadband UV light exposure.

## Experimental Procedure:

The experimental procedure can be divided into three parts: First, a lithography process was developed. This was done using a chrome-on-quartz mask. This process consisted of learning how to optimize different parameters using OL. The steps included application, exposure, and development of the photoresist. Figure 1 illustrates this process.

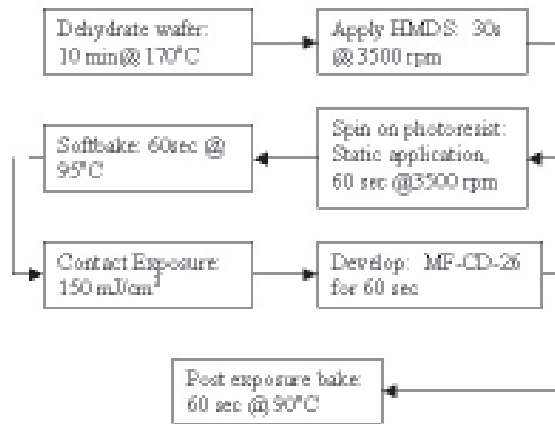


Figure 1: Optical lithography process.

The second part involved using four pre-fabricated chromeless phase-shifting-masks to produce sub-wavelength features. Each mask had a different shifter depth gradient. This gradient allowed for an investigation of which shifter depth produced the highest resolution features, while keeping all other parameters constant.

In the final step, the phase shifting process was coupled with immersion lithography to decrease the minimum feature size even further. This was done using the same phase shifting mask that produced the highest resolution feature, and placing a drop of water between the mask and the wafer.

### Results and Conclusion:

After optimizing the parameters in the PSL process, a sub-200 nm feature was fabricated. Mask 3 produced the 193 nm feature at a shifter depth of 3820 Å. This is shown in Figure 2. The image was taken using a LEO 1530 Field-Emission Scanning Electron Microscope. This shows that a PSL can produce sub-wavelength features when broadband exposure is used.

The result of coupling IM with the PSL was not as successful. The first experiment was done with the same 150 mJ/cm<sup>2</sup> exposure dose used in the PSL, but that was too strong. As soon as the wafer was placed in the developer, all the features were developed away.

The dose was then decreased to 72 mJ/cm<sup>2</sup>. This produced features that had a lower resolution than the features produced using PSL. The result was not consistent with what was conjectured to be the outcome. Unfortunately, due to time constraints the goal to produce higher resolution features was not reached.

### Acknowledgements:

I would like to thank the NSF and NNIN for allowing me to participate in this program. I would also like to thank my advisor Dr. Mark Horn. Last but not least I would like to thank the entire staff at the Penn State Center for Nanotechnology Education and Utilization. They always took the time to answer my questions and assist me when I had problems.

### References:

- [1] H. Dang, J. Tan, "Sub-150nm, High-Aspect-Ratio Features Using Near-Field Phase-shifting Contact Lithography." American Vacuum Society (May/June 2003), 1143-1147.
- [2] Y.Fan, N. Lafferty, A. Bourov, L. Zavyalova, B.W. Smith, "Study of Air Bubble Induced Light Scattering Effect On Image Quality in 193 nm Immersion Lithography", Proc. SPIE 5377, (2004).

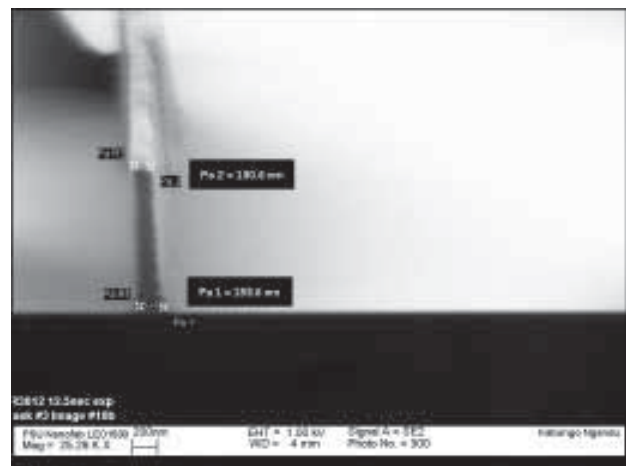


Figure 2: Resultant 193 nm feature using a broadband exposure and Phase Shifting Lithography.

# Fabrication and Characterization of a Nanonozzle

Khiem Nguyen (aka Leo Trong), Electrical & Computer Engr., Illinois Institute of Technology

NNIN REU Site: Microelectronics Research Center, Georgia Institute of Technology

Principal Investigator: Mark Allen, Electrical and Computer Engineering, Georgia Institute of Technology

Mentor: Nisarga Naik, Electrical and Computer Engineering, Georgia Institute of Technology

Contact: nguykhi2@iit.edu, mark.allen@ece.gatech.edu, gtg493p@mail.gatech.edu

## Abstract:

A new fabrication process proposed by the Nanotechnology and Interdisciplinary Research Team (NIRT) uses a nanonozzle as the mechanical interface with liquid applied at high pressure through a mechanical pump. This process has the potential application in direct substrate surface modification. This paper introduces the prototype nozzle design and experimentation of the nanonozzle.

The initial orifice of the nanonozzle was designed with a feature size in a few microns range. The orifice feature size was reduced by growing an oxide layer covering the inside of the silicon nanonozzle. Cross-sections of the nanonozzle at various distances from the original orifice were examined with a scanning electron microscope (SEM). The data from the SEM were analyzed to characterize the oxide growth layer inside the nozzle.

## Introduction:

The new era of nanotechnology demands both mechanical and electronic devices to be made with parts in the nanometer scale. NIRT has proposed a new fabrication process in which a nanonozzle modifies or prints nano-device parts directly onto a surface. One of the many challenges lies in the proper design of an applicable nanonozzle.

Several nozzle fabrication approaches have been considered, including conformal electrodeposition of silicon microneedles, micromachined reconfigurable shadow masks, and photolithography patterning with silicon etching and oxidation. The third approach seems most viable in the context of controllable shape and appropriate characteristics to withstand high pressure. Hence, it is the chosen process for the NIRT project.

The approach of photolithography patterning creates nozzles with orifice feature sizes, or diameters, in the micron range. Hence, oxidation of the silicon inside the nozzle orifice is necessary to reduce the feature size to nanometer scale. There are two types

of oxidation processes: wet oxidation and dry oxidation. Dry oxidation uses oxygen gas to oxidize silicon as depicted by the following chemical reaction equation:



Wet oxidation uses steam to oxidize silicon as shown in the following equation:



The major advantage of wet oxidation over dry oxidation is the faster oxide growth rate. Wet oxidation grows  $\text{SiO}_2$  up to 5 times faster than dry oxidation. For instance, after 10 hours of oxidation on the flat surface of a silicon wafer, wet oxidation process grows 2.2  $\mu\text{m}$  of  $\text{SiO}_2$ , while dry oxidation process grows only 0.4  $\mu\text{m}$  of  $\text{SiO}_2$ .

These oxidation rates reflect oxidation on a flat plane. However, the process NIRT proposes involves oxidation inside an open-ended, tunnel-shaped nozzle. Consistency of the oxidation growth rate for these two different geometries may diverge. Hence, it is also required to determine the oxidation rate inside the nozzle's orifice neck.

## Procedure:

The fabrication process of the nanonozzles involved photolithography. After proper mask design and successful translation of the top view nozzle patterns (Figure 1) onto a silicon wafer, wet chemical etching of silicon (KOH) was used to etch the depth dimension of the nozzles. Due to the crystal orientation of the silicon wafer, hot concentrated KOH etched the (100) crystal plane several hundred times faster than the (111) plane. Hence, the initial nozzle's edges were slanted. A second plain wafer was fusion bonded with the first wafer in order to seal the top opening of the nozzles.

The fabricated nozzle structures' orifices with feature sizes ranging from 3  $\mu\text{m}$  to 20  $\mu\text{m}$  were too large for direct nanojet applications. As a result, wet oxidation was used to grow an oxide layer, ranging

from 1-3  $\mu\text{m}$  of thickness, inside the orifice. Three different nozzle batches were oxidized for 5, 12, and 15 hours independently in a Lindberg furnace at 1100°C.

After completing the fabrication process of the nozzles, the Hitachi scanning electron microscope (SEM) was used to examine and measure the orifice dimensions and the oxide thickness. To better characterize the tunnel oxidation, cross-sections of the orifice neck were needed every other few micrometers apart. A polishing machine with slurry sizes of 1  $\mu\text{m}$ , 0.3  $\mu\text{m}$ , and 0.05  $\mu\text{m}$  was used to polish the nozzles.

### Results and Conclusions:

Wide ranges of oxide growth thickness were obtained for all three oxidation cases (5, 12, and 15 hours). Both of the 5-hour and 12-hour experiments produced oxide thickness ranges (0.7  $\mu\text{m}$  to 1.5  $\mu\text{m}$  and 1.5  $\mu\text{m}$  to 2.2  $\mu\text{m}$ , respectively) less than the theoretical flat surface oxide thickness (2.4  $\mu\text{m}$ ). Only the 15-hour experiment produced an oxide thickness range (2.0  $\mu\text{m}$  to 2.8  $\mu\text{m}$ ) that included the respective theoretical oxide thickness (2.7  $\mu\text{m}$ ). However, these ranges of growth thickness measurements were insufficient to support any conclusive analysis. Accurate examinations and measurements of the nozzle orifice's dimensions were limited by the capacity of the SEM (i.e. degree of visibility at high magnification) and the ability to visually distinguish the boundary of oxide layer and silicon layer. Part of the explanation for the deviated oxide thicknesses measurements could be attributed to inconsistent performance (i.e. low visibility at high magnification) and settings (i.e. the orientation of the specimen in the vacuum chamber) of the SEM.

As a result, more future work with controlled experiments and refined measurement tools (i.e. SEM) would be needed to further explore this nozzle design challenge.

### Acknowledgements:

Dr. Mark Allen, principal investigator. Dr. Frazier, for the Lindberg Furnace. Christophe Courcimault, mentor. Nisarga Naik, mentor. Jennifer Tatham, GA Tech REU program coordinator. Microelectronics Research Center (MiRC), NSF & NNIN.

### References:

- [1] Campbell, Stephen. The Science & Engineering of Microelectronic Fabrication. Oxford University Press, 2001.
- [2] Deal, B. E., et al. J. Appl. Phys. Vol. 36, No. 12, pp. 3770-3778, 1965.
- [3] "KOH Etching and Decontamination Procedures." <http://snf.stanford.edu/Equipment/wbgeneral/KOHEtch.html>.

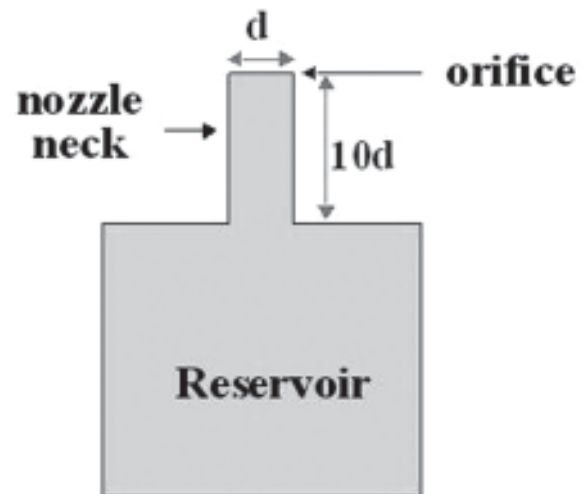


Figure 1: View of nozzle.

# Fabrication of a Discriminating Gas Sensor

Alex O'Day, Physics, Cornell University

NNIN REU Site: Nanofabrication Center, University of Minnesota, Twin Cities

Principal Investigator & Mentor: Stephen Campbell, Electrical Engineering, University of Minnesota

Contact: [campbell@ece.umn.edu](mailto:campbell@ece.umn.edu)

## **Abstract:**

Gas sensors have been used for many years for equipment control and environmental monitoring. A basic problem is that they typically are unable to discriminate between gasses that are chemically similar. This generic problem is the source of considerable research, typically involving the creation of arrays of sensors that are slightly different and then developing an empirical signature for different gasses.

In this project we designed and fabricated a new type of gas sensor. The gas must diffuse down a nano sized cavity to reach the sensing elements. By spacing the elements along the cavity one can determine the diffusion coefficient and from that infer the size of the diffusing species.

We laid out the test chip and developed several critical processing steps needed to build the device. Next the necessary materials were deposited and patterned. Finally, we intend to package the device and test its response.



# Characterization and Optimization of ZEP520A Electron Beam Lithography Resist

Nathan Olds, Physics and Electrical Engineering, University of Washington

NNIN REU Site: Microelectronics Research Center, Georgia Institute of Technology

Principal Investigator: Kevin Martin, Microelectronics Research Center, Georgia Institute of Technology

Mentor: Devin Brown, Microelectronics Research Center, Georgia Institute of Technology

Contact: nolds@u.washington.edu, kevin.martin@mirc.gatech.edu, devin.brown@mirc.gatech.edu

## Abstract:

The goal of this project was to determine the ultimate nanometer pattern resolution in ZEP-520A electron beam resist. E-beam lithography was done using a JEOL JBX 9300FS system. Thickness measurements of ZEP-520A were taken using a Woollam Ellipsometer, Tencor KLA Profilometer, and a Veeco Atomic Force Microscope (AFM). Line edge and surface roughness were compared across a range of E-beam doses using the AFM. E-beam dose was compared to the depth and clarity of trenches of varying dimensions drawn in AutoCAD and written in ZEP-520A. Exposed resist was developed using ZED-N50. Trenches of 18 nm were demonstrated previously. Resolving 10 nm trenches was the specific goal in achieving the maximum resolution of ZEP-520A.

## Introduction:

Electron Beam Lithography (EBL) is a method to create nanoscale patterns in resist-coated wafers. A positive resist undergoes chain-scission and becomes soluble. A negative resist reacts to electrons by crosslinking or becoming insoluble. A solvent is used to dissolve away exposed soluble areas of a positive resist or leave behind the exposed insoluble areas on a negative resist. ZEP-520A is a positive electron beam resist suspended in Anisole, hence the A.

Characterization of ZEP-520A involved determining what thicknesses of ZEP-520A were coated onto 3" silicon wafers given a certain dilution and RPM. The optimization of ZEP-520A involved choosing a spin speed, thickness, e-beam parameters, and dilution corresponding to the clearest and most properly resolved features.

## Procedure:

This project involved gathering thickness and trench-width data of a 4 to 1 dilution and a 3 to 1 dilution of ZEP-520A after writing features in the resist. Several different tools were used for resist measurements and comparisons made. Thicknesses were measured via KLA Profilometer, Woollam Ellipsometer, and Veeco AFM. Widths of features were also measured using an AFM and Scanning Electron Microscope (SEM).

The first part of this project involved collecting data on thickness variation as two dilutions of ZEP-520A were spun at 2000 to 6000 RPM. Two vials of 3 and 4 parts Anisole to 1 part bottled ZEP-520A were diluted using an electronic

scale. These dilutions were dropped onto 3" silicon wafers using a 0.2  $\mu\text{m}$  filter. Wafers were individually coated and then spun at different speeds. Immediately after being spun, wafers were placed on a hot plate, set to 180°C, for 90 seconds. They were then removed and cooled by the ambient cleanroom temperature. Resist thickness was first measured on the Woollam Ellipsometer. Each wafer was then scratched to reveal the silicon substrate for a KLA Profilometer second measurement. Once measured, the data was compiled into a Microsoft Excel spreadsheet with the resultant graphs shown in Figures 1 and 2.

AFM measurements were taken after writing and developing trenches with the e-beam and ZEP-520A developer respectively. Only the 3:1 dilution of resist spun at 3000 RPM was used in the AFM thickness measurement.

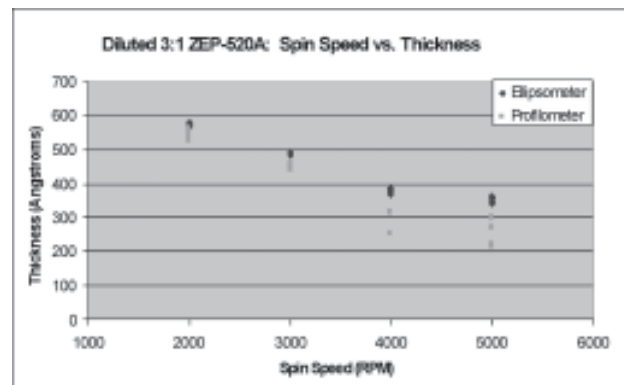
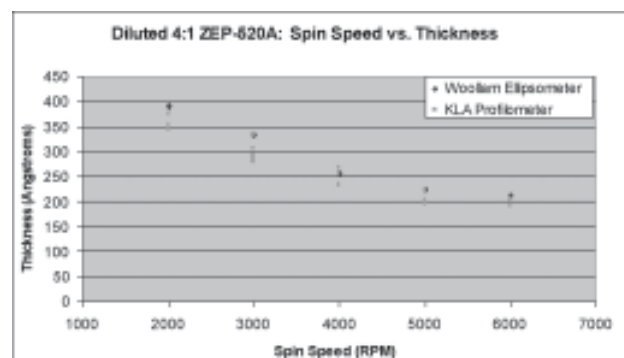


Figure 1, above: Speed vs. thickness for 3:1 dilution of ZEP-520A.

Figure 2, below: Spin speed vs. thickness for 4:1 dilution of ZEP-520A.



An AutoCAD drawing, consisting of several lines per dose and line width, was converted to GDSII format by a program called LinkCAD. Dose vs. depth for ZEP-520A is shown in Figure 3.

SEM imaging was also done on a line patterned in AutoCAD to be 10 nm. This was written by programming the JEOL JBX 9300FS with a 10 nanoamp beam current for a relatively fast exposure. This fast exposure resulted in the data shown Figure 4.

### Results and Conclusions:

For EBL it is important to understand how spin speed affects the thickness of ZEP-520A resist layers. Spin speeds were compared, for a 3:1 dilution and a 4:1 dilution, to their resulting thicknesses as shown in Figures 1 and 2. These data were used to determine which spin speed corresponds to which thickness of resist in order to optimize the development process.

Measuring resulting trench depth across several doses compared the clarity of developed lines or trenches. AFM measurements of how resist depth compared to electron beam dose are compared in Figure 3. Assuming the 10-20 nm AFM tip was significantly narrower than the trench width, this data would show the dose at which features start to resolve. The 30 nm data or dark blue data in Figure 3 shows this resolution of trench depth to occur around 700  $\mu\text{C}/\text{cm}^2$ .

The project goal was to resolve features smaller than 20 nm. An attempt to make a 10 nm line using very fast settings and a 10 nanoamp beam current resulted in a line about 52 nm wide as shown in Figure 4.

### Future Work:

Future work could involve optimizing exposure of the e-beam or using dose correction software. Setting up the e-beam to run more precisely involves narrowing the beam to a minimum spot size of 4 nm or possibly using dose correction software. Several parameters are bundled up into the term “dose”. Varying many of these can result in the same dose and possibly a different line width. Further optimization could involve working more directly with 9300FS software to modify these parameters. Different dilutions of resists could also be used, maybe 5:1, although 4:1 dilution at 6000 RPM left areas of uncoated wafer.

### Acknowledgements:

Special thanks goes to Devin Brown, my mentor, and Raghu Murali, a helpful graduate student, Jennifer Tatham, Kevin Martin, my PI, all of the cleanroom staff, the Microelectronics Research Center (MiRC) for its resources and helpful staff, the National Nanotechnology Infrastructure Network (NNIN.org) and the National Science Foundation for funding, and the Georgia Institute of Technology for hosting us.

### References:

- [1] Cornell NanoScale Science & Technology Facility, “SPIE Handbook of Microlithography, Micromachining and Microfabrication”, <http://www.cnf.cornell.edu/SPIEBook/toc.htm>
- [2] ZEON Corporation, EP520 Ver.1.02 Mar.2001, “Technical Report, ZEONREX Electronic Chemicals, ZEP520 High Resolution Positive Electron Beam Resist”, <http://www.zeon.co.jp/>
- [3] D. M. Tanenbaum et. all, 16 August 1996 “High resolution electron beam lithography using ZEP-520 and KRS resists at low voltage.”
- [4] W. Chen et. all, 21 June 1999, “Very uniform and high aspect ratio anisotropy SiO<sub>2</sub> etching process in magnetic neutral loop discharge plasma.”

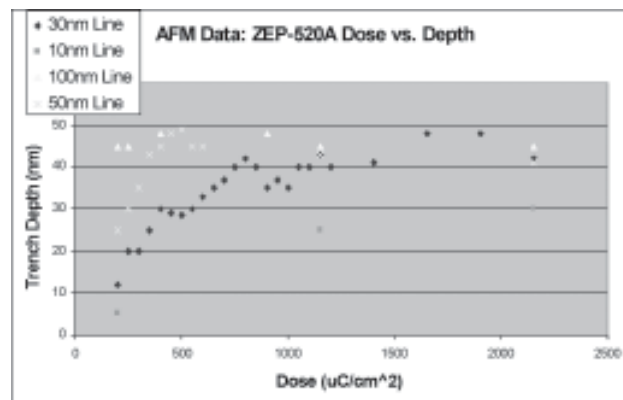
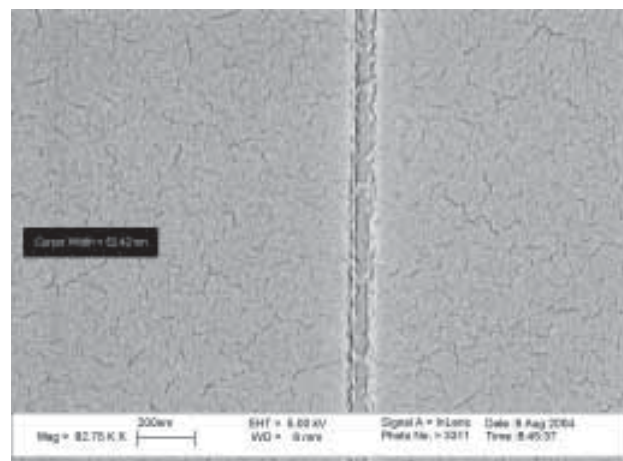


Figure 3, above: Veeco AFM trench depth variability with several incremented doses by 50 $\mu\text{C}/\text{cm}^2$ .

Figure 4, below: 3:1 dilution of ZEP-520A trench width measurement using SEM of 10 nm line attempt as 52.42 nm measured.



# Thermal Effects in Silicon Based Resonant Cavity Devices

Vaidehee Padgaonkar, Electrical Engineering, University of Michigan, Ann Arbor

NNIN REU Site: Cornell NanoScale Science & Technology Facility, Cornell University

Principal Investigator: Professor Michal Lipson, Nanophotonics, Cornell University

Mentor: Dr. Sameer Pradhan, Nanophotonics, Cornell University

Contact: vpadgaon@umich.edu, ml292@cornell.edu, ssp29@cornell.edu

## Abstract:

CMOS process-compatible silicon photonic devices provide the possibility of monolithic integration with standard CMOS chips. They are, however, very sensitive to changes in temperature. In this project, we fabricated high-index contrast ring resonators on a silicon-on-insulator (SOI) platform and characterized the changes in resonance of these devices due to changes in temperature.

## Introduction:

Silicon based photonic devices and circuits are attractive due to their fabrication compatibility with the CMOS process and possibility of monolithic integration on CMOS chips [1, 2]. Various photonic devices including micro-ring resonators [3] and high-Q cavities [4] have been demonstrated on SOI substrates.

Silicon-based ring resonators, such as the one shown in Figure 1, can act as ultra-compact add-drop switching devices [5]. The resonance condition of the ring resonator is given by the following equation.

$$C\lambda = 2\pi r$$
$$\lambda = \lambda_0/n$$

where  $C$  is an integer,  $\lambda_0$  is the wavelength of light in free-space,  $n$  is the refractive index of the medium, and  $r$  is the radius of the ring. At the resonant wavelength, the light circulates in the ring and is either scattered out or absorbed, resulting in less light transmitted at the output. This drop

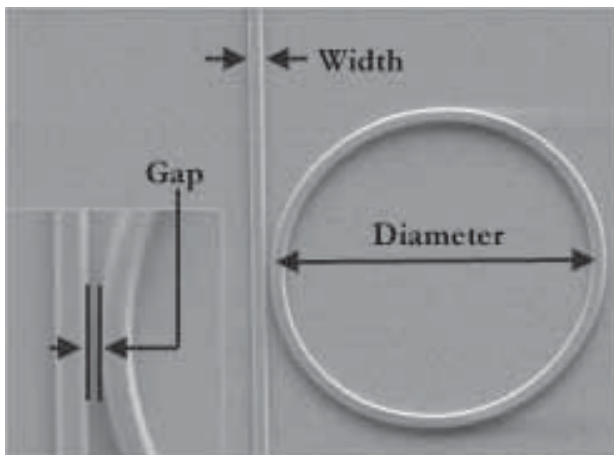


Figure 1: Ring resonator fabricated on silicon, with a ring radius of 12  $\mu\text{m}$  and gap of 250 nm.

in transmission at the resonant wavelength, as displayed in Figure 2, can be used to make optical modulators on Si [6].

The refractive index ( $n$ ) of silicon changes with temperature ( $T$ ), as represented by the thermo-optic effect in silicon:

$$\Delta n/\Delta T = +1.8 \times 10^{-4} \text{ K}^{-1}$$
$$\Delta n/\Delta T = +1.8 \times 10^{-4} \text{ K}^{-1}$$

Moreover, the resonant wavelength  $\lambda$  is a function of the refractive index  $n$  ( $\lambda = \lambda_0 / n$ ).

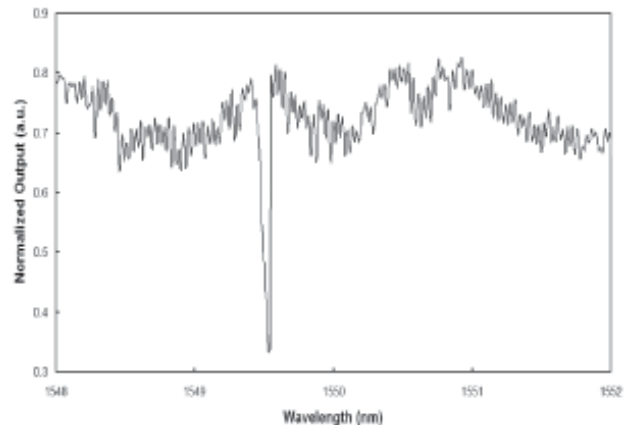


Figure 2: Transmission spectrum at room temperature using TE mode.

## Fabrication Process:

We fabricated an Si ring resonator closely spaced from a waveguide with two bends to distinguish light coupled with the input and light transmitted to the output. There were 32 of these devices on the chip. All the waveguides were approximately 300 nm tall and 450 nm wide. The ring diameter was varied from 12  $\mu\text{m}$  to 40  $\mu\text{m}$  and was spaced 200 nm to 300 nm from the waveguide. The SEM of a fabricated ring resonator on a SOI platform is shown in Figure 1.

For the fabrication process, negative e-beam resist called FOX-12 was spun on a Silicon On-Insulator (SOI) wafer. The pattern was exposed using e-beam lithography with a 2 nA current and pixel step of 3. After developing in 300MIF, an Inductively Coupled Plasma (ICP) etcher was used to etch through the silicon layer.

The potential challenge with using a positive resist was large area exposure and high exposure time. The challenge

encountered with using negative resist was slanted side walls, later found to be the cause of noisy output and subsequently undistinguishable resonances. The slanted side walls were mixing the TE and TM polarizations at the bends of our single-mode waveguides. Increasing the etch-chamber pressure from 22 mTorr to 30 mTorr and ICP power from 800 W to 850 W on the ICP etcher reduced the side wall slant.

In order to examine thermal effects on resonances, the input wavelength was swept from 1548 nm to 1552 nm using a tunable laser. A polarization controller was used to select TE or TM polarization of the input light. The light from the fiber was coupled with the waveguide. A lens was placed between the output end of the device and a power meter, in order to focus the output light into the detector. The device rested on a temperature controller used to heat the device. Furthermore, resonance shifts for 5°C increments between 25°C and 45°C were observed.

### Results and Conclusions:

It is evident from Figure 2 that a resonance occurs at 1549.782 nm at room temperature (~ 25°C). Figure 3 illustrates how the resonances shift with a temperature increase. Based on this data, a linear relationship between the temperature and resonant wavelength was established, as represented in Figure 4. In conclusion, a 0.1 nm ( $\pm 0.01$  nm) shift of the resonance wavelength occurs for every 1°C ( $\pm 0.05^\circ\text{C}$ ) change of the chip.

### Future:

Now that the thermal effect on resonances has been characterized, the next step is to reduce and perhaps even eliminate these thermal effects. One suggested method is to add strain to the optical medium, with the ideal relationship being  $\Delta n/\Delta T + \Delta n/\Delta P = 0$ .

Using either tensile or compressive strain within the optical waveguides, the change in refractive index due to strain can be made to compensate for the change in refractive index due to temperature changes [7].

### Acknowledgements:

Professor Michal Lipson and Dr. Sameer Pradhan, Nanophotonics, Cornell University. Members of the Nanophotonics Group at Cornell University. Melanie-Claire Mallison, NNIN REU coordinator. Cornell NanoScale Facility. National Science Foundation.

### References:

[1] P. Daniesi, A. Kung et.al., "CMOS compatible fully-integrated Mach-Zehnder interferometer in SOI technology", IEEE Photon. Technol. Lett., vol. 12, #6, June 2000, p. 660-2.  
 [2] S. M. Csutak, J. D. Schaub, W. E. Wu, and J. C. Campbell, "High-speed monolithically integrated silicon optical receiver fabricated in 130-nm CMOS technology", IEEE Photon. Technol. Lett., vol. 14, no. 4, April 2002, p. 516-18.

[3] W. Guo, H. Ma, Z. Jin, Y. Tang and Y. Wang, "Novel structure of passive ring waveguide resonator on silicon substrate", MEMS/MOEMS Technologies and Applications (Shanghai, China), Proc. SPIE - Int. Soc. Opt. Eng., 17-18 Oct. 2002, p. 297-300.  
 [4] M. K. Emsley, O. Dosunmu and M. S. Unlu, "Silicon substrates with buried distributed Bragg reflectors for resonant cavity-enhanced optoelectronics", IEEE J. Sel. Top. Quantum Electron., vol. 8, no. 4, July-Aug. 2002, p. 948-55.  
 [5] B. E. Little, J. S. Foresi et. al., "Ultra-compact Si-SiO<sub>2</sub> microring resonator optical channel dropping filters", IEEE Photon. Technol. Lett., vol. 10, no. 4, April 1998, p. 549-51.  
 [6] C. A. Barrios, V.R. Almeida, R. Panepucci, M. Lipson, "Electrooptic Modulation of Silicon-on-Insulator Submicrometer-Size Waveguide Devices", Journal of Lightwave Technology, vol. 21, no. 10, Oct 2000, p. 2332-39.  
 [7] S.M Weiss, M. Molinari, P.M. Fauchet, "Temperature Stability for Silicon-based Photonic Band-gap Structures", App.Phys.Lets, vol. 83, no.10, September 2003, p. 1980-82.

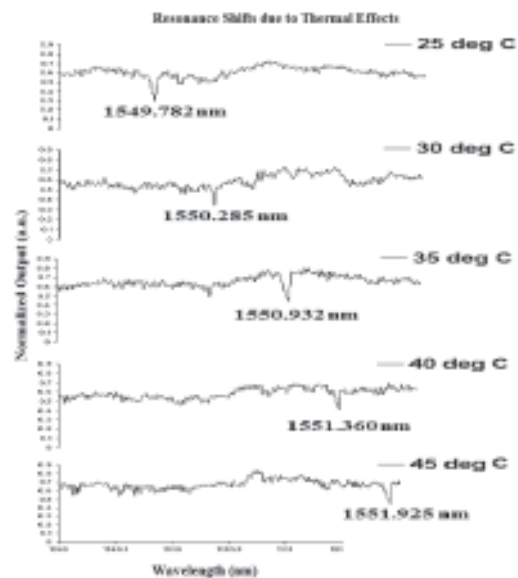
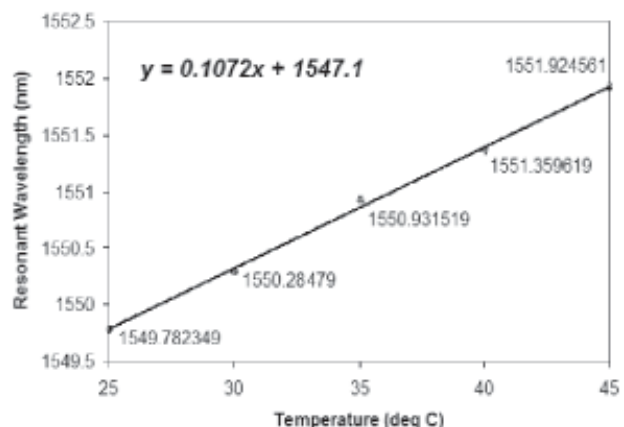


Figure 3, above: Transmission spectra with increasing temperature.

Figure 4, below: Linear relationship between temperature and resonant wavelength.



# Nano-Excision of Thin Diamond Membranes for a High Brightness Electron Source

Heyjin Park, Biomedical Engineering, Northwestern University

NNIN REU Site: Stanford Nanofabrication Facility, Stanford University

Principal Investigator: Prof. R.F.W. Pease, Electrical Engineering, Stanford University

Mentor: Daniel S. Pickard, Electrical Engineering, Stanford University

Contact: h-park2@northwestern.edu, pease@cis.stanford.edu, pickard@stanford.edu

## Abstract:

Diamond is potentially attractive as an electron source because it can be activated to a condition of negative electron affinity (NEA) by hydrogen termination. To excite high-energy electrons into the conduction band, we bombard the back surface of a diamond membrane with high-energy ( $> 1$  KeV) electrons. Excited electrons can then transport through the film and be emitted from the front surface.

This device requires a fabrication technique for thinning single crystal diamond membranes ( $< 0.5 \mu\text{m}$ ) and mounting them for subsequent transport and emission measurements. We have developed a milling and polishing technique for the membranes with a 30 kV  $\text{Ga}^+$  focused ion beam. We have fabricated thin single crystal p-type diamond membranes with thicknesses ranging from 0.2 to 2  $\mu\text{m}$  along a chosen crystal orientation and have mounted them onto a macroscopic sample holder.

## Introduction:

Electron sources are a crucial component in many instruments. Electron sources based on negative electron affinity (NEA) can exhibit high brightness. When the condition of NEA is met, low-energy electrons within the conduction band find no energy barrier to the vacuum and are emitted freely. Usually, these photocathodes use materials such as GaAs and are activated to NEA by a single layer of cesium and oxygen. Unfortunately, the  $\text{Cs}/\text{O}_2$  activation leaves the surface highly sensitive to contamination. Diamond can be activated to NEA by hydrogen termination, which also passivates the surface, minimizing its sensitivity to other forms of contamination.

The challenge to exploiting diamond for a high brightness electron source is that there are no continuous wave light sources available that can produce photons of sufficient energy to excite bound electrons across diamond's wide bandgap of 5.47 eV. Since diamond cannot be used as a photocathode, it is necessary to inject electrons directly into diamond's

conduction band with a high-energy electron beam. The high-energy electrons bombard the back surface of a diamond membrane, exciting a cascade of secondary electrons. Theoretically, these electrons fully thermalize during their transport from the back surface to the diamond's hydrogen activated NEA front surface when they are freely emitted into vacuum (Figure 1).

Choosing the thickness of the diamond membrane is a tradeoff between high gain and low energy spread. It must be thick enough to fully absorb the high-energy incident beam as well as allow complete thermalization of electrons before reaching the NEA surface. The membrane must also be thin enough so energy losses from scattering and recombination do not significantly reduce the emission current density. The best thickness for 3 kV electrons is approximately 0.5  $\mu\text{m}$ .

Since such thin single crystal diamond membranes are not commercially manufactured, we developed a

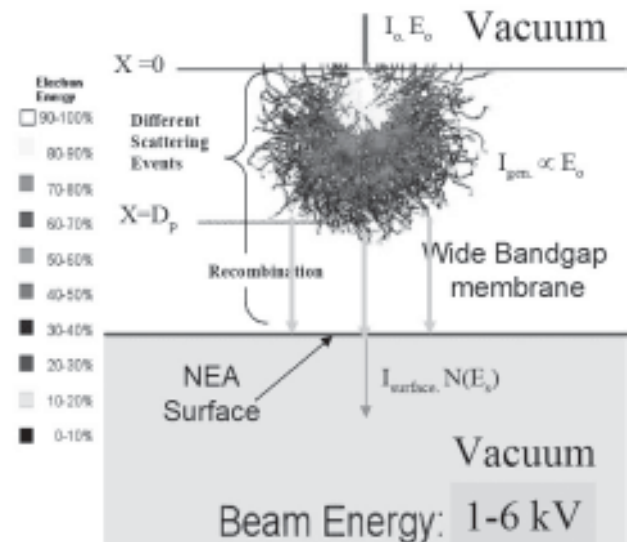


Figure 1: This Monte Carlo simulation predicts the trajectory of electrons excited by the bombardment of a high energy electron beam on the back surface of a NEA membrane. Thickness range for optimal emission depends on incident beam energy.

procedure utilizing a system featuring both a scanning electron beam and a focused ion beam (FIB).

### Fabrication Technique:

The dual beam FIB incorporates a scanning electron beam column for imaging with minimal sample damage, and an ion beam column, which uses  $\text{Ga}^+$  ions for imaging and milling samples with submicron precision. The FIB also comprises several accessories such as a capillary needle to bleed in a Pt precursor gas, and a remotely controlled micromanipulator (omniprobe) facilitating sample transfer.

The diamond membrane is extracted from a single crystal substrate by milling two adjacent trenches with a 30 kV, 30,000 pA  $\text{Ga}^+$  focused ion beam (Figure 2a). The trenches are each 20  $\mu\text{m}$  in width and length with a depth of 20  $\mu\text{m}$ . The thickness of the wall remaining between the two adjacent trenches forms a single crystal diamond membrane 20  $\mu\text{m}$  square with a thickness controlled by the separation between the trenches and subsequent polishing steps with lower current. The thickness of the membrane can be trimmed as thin as 200 nm.

The sides of the membrane are cut with the FIB leaving a small segment on each side of the sample, and the omniprobe needle is remotely manipulated over the top edge of the membrane. A capillary is then inserted that bleeds a platinum precursor gas in the vicinity of the sample. The ion beam is focused locally to crack the precursor gas and deposit metallic

platinum where the ions impinge to weld the omniprobe needle to the membrane. Once the omniprobe is securely connected to the membrane, the remaining segments holding the membrane are severed by the ion beam.

The omniprobe is used to lift and transfer the diamond membrane to a Pt aperture, 5  $\mu\text{m}$  in diameter located at the center of a 3.04 mm Pt disk (Figure 2b). The diamond sample is positioned over the aperture, and then securely welded onto the wafer by Pt deposition (Figure 2c). The omniprobe is then cut free from the membrane. The pending device (Figure 2d) is ready for cleaning, activation, and testing.

### Summary and Results:

Diamond membranes of thicknesses in the range of 0.2 to 2  $\mu\text{m}$  have been fabricated and subsequently mounted onto sample holders. The next phase in demonstrating this new electron device is to measure the gain, energy spread, and brightness of the diamond electron bombardment source as a function of the incident beam energy, thickness of the membranes, crystal orientation, and doping concentration.

### Acknowledgments:

Thanks to SRC and DARPA ALP, the NSF and the NNIN REU Program, Stanford University Center for Integrated Systems, P.I. Professor Fabian Pease, and Mentor Dan Pickard, for all their help and support.

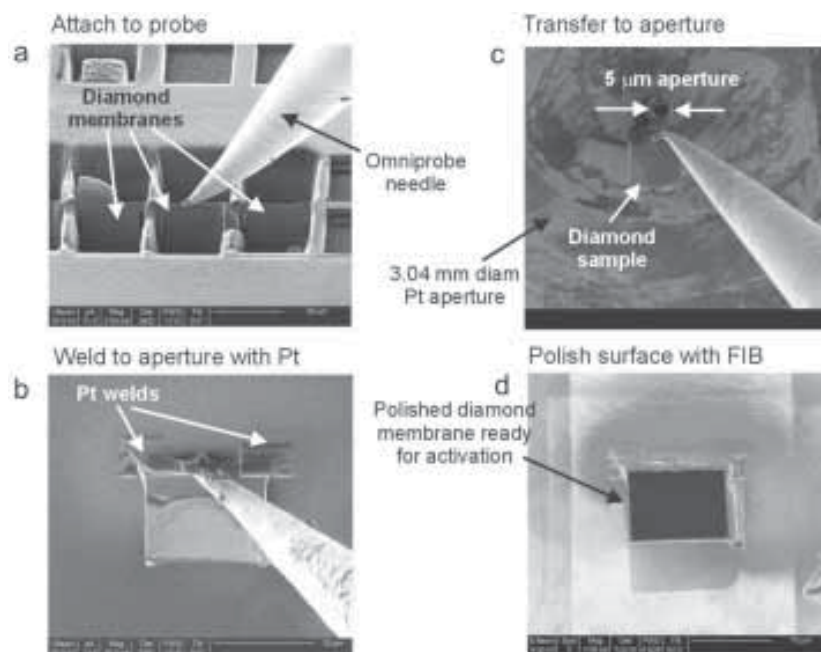


Figure 2: Slow scan images taken by electron and ion beams during diamond membrane fabrication. a) Remaining wall between two trenches forms a 15 by 15  $\mu\text{m}$  diamond membrane. b) Omniprobe needle used to transfer diamond over a 5  $\mu\text{m}$  aperture within a Pt wafer sample holder. c) Membrane is secured with Pt welds. d) Final polish is performed by milling from the top of the membrane at grazing incidence.

# Simulations of Simplified Cell Membranes

Peter Philips, Computer Science & Biochemistry, CUNY - Baruch College

NNIN REU Site: Nanotech at UCSB, University of California Santa Barbara

Principal Investigator: Frank Brown, Chemistry, University of California at Santa Barbara

Mentor: Grace Brannigan, Physics, University of California at Santa Barbara

Contact: flbrown@chem.ucsb.edu

## Abstract:

Macroscopic properties of cell membranes can be simulated using a simple, flexible, solvent-free model. Each amphiphilic lipid composing the membrane is represented as a chain of five beads governed by four potential energy parameters. The simulations are conducted according to Metropolis Monte Carlo algorithms, effectively minimizing the free energy of the system. Obtaining the proper parameters such that the membrane remains structurally intact has been a challenge, as pores have developed in many of the simulated membranes. The bending rigidity falls within ranges similar to biological systems. Also, when simulated with a large bending parameter, the molecules in the membrane assumed a tilted structure seen in gel membranes.

## Introduction:

Cell membranes are composed of amphiphilic lipids, which self assemble into a flexible bilayer arrangement. The cell membrane is involved in many important cell processes that occur on scales greater than 100 nm<sup>2</sup>, although cell size is much larger. Some of these processes include but are not limited to protein aggregation and trafficking, cell motility, endo- and exocytosis, and cell division. Alzheimer's Disease has been linked to aggregation of proteins in the cell membrane. Undulations

in the membrane are important in influencing these processes, and thus, the flexibility of the membrane, or bending rigidity, is an important area of study.

Experimental testing of cell membranes can often be too expensive, difficult, or even impossible to perform under certain conditions. Computer simulations of membranes can alleviate some of these obstacles. However, they present their own set when faced with decisions on how to begin modeling the membrane. Precise atomistic simulations, although useful for small systems, cannot be used in larger systems because of the computationally expensive calculations required. Alternatively, models that are too coarse grained have had certain properties outside of biological ranges. For example, the rigid, solvent free model proposed by Brannigan was found to have a bending rigidity off by an order of magnitude [1].

An acceptable model will be computationally efficient, yet still exhibit cell processes that occur on length scales greater than 100 nm<sup>2</sup>. Also, the model should be equipped to account for multiple types of lipids, and inclusions such as cholesterol and proteins, all of which are found in real membranes. Finally, the model should be tunable to simulation parameters such as molecular flexibility and intermolecular attractions.

The purpose of this project was to check the newly developed flexible, solvent free model against experimental data by examining the flexibility of the simulated membranes. The quantification of the flexibility of a membrane is the bending rigidity ( $K_b$ ), which is defined by how much energy is required to bend the membrane. Real membranes have a bending rigidity that lies between 10-80 $\epsilon$ , where  $\epsilon = 4 \cdot 10^{-21}$  J [2].

## Procedure:

The model examined in this paper represents each lipid as a chain of five beads. The second bead is special, accounting for a membrane's amphiphilicity with implicit solvent. The chains in this model are flexible, but don't stretch. Lipid interactions are governed by four potential energy parameters: an excluded volume interaction ( $c_{core}$ ) enforces shape and prevents overlap of lipids; a long range attraction ( $c_{long}$ ) is calculated for the 2nd bead giving the bilayer a skin; a short range attraction ( $c_{tail}$ ) governs the hydrophobic tail attraction; and a molecular bending interaction ( $c_{bend}$ ) discourages the beads from overlapping

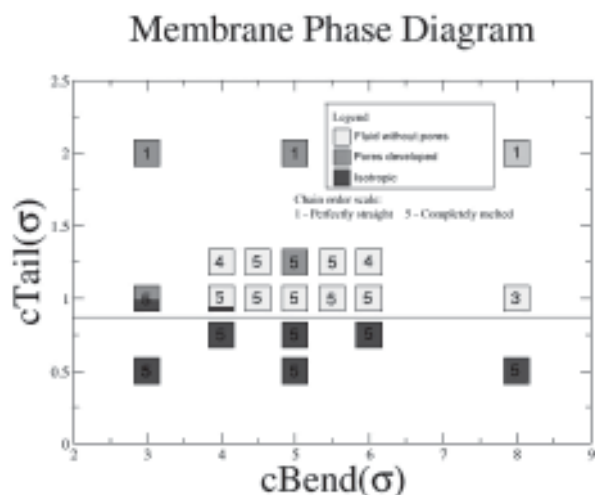


Figure 1: Pores develop unpredictably in this parameter space search.

because the energy is at a minimum when the chain is perfectly straight. This model has the capacity to accommodate different types of lipids, as well as accommodate inclusions such as proteins and cholesterol.

The simulations were conducted using between 392 and 800 molecules. The simulations were run at constant tension as opposed to constant area, where the dimensions of the bounding box of the membrane can fluctuate, more accurately simulating a real membrane. The long range and excluded volume interaction parameters were held constant, while the effect of a variable tail attraction and bending parameter on the membrane were studied to identify a parameter space.

The flexibility of the membrane was studied by investigating the effect of the molecular bending parameter,  $C_{bend}$ , on  $K_c$ . To do this, the discrete points comprising the membrane were turned into a mesh surface using Delaunay Triangulation, and then were interpolated such that  $K_c$  can be found by fitting the Fourier mode of this surface according to:

$$F(x) = \frac{1}{K_c * x^2}$$

### Results:

In the parameter space search, three basic phases were found (see Figure 1): the membrane fell apart and became isotropic; the membrane developed pores; and the membrane remained stable and fluid. As intramolecular bending is discouraged (a higher  $C_{bend}$ ), average box length decreases continuously (see Figure 2b). This is logical because stiffer chains can pack more closely. However, the bending rigidity is not continuous with increasing  $C_{bend}$  (see Figure 2a). The reasons for this are not readily apparent, although data must be collected at greater resolution before any conclusions can be made. When large values for  $C_{bend}$  were used, the membrane formed a tilted, yet highly ordered gel phase (see Figure 3). This is significant because this ordering has been seen experimentally [2] and is an indicator the flexible, solvent free model is behaving appropriately.

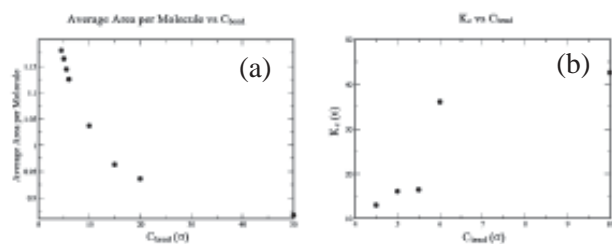


Figure 2: The average area decreases continuously with increases of  $C_{bend}$ . However,  $K_c$  exhibits a large increase with  $C_{bend} = \sim 6.0$ .

### Conclusions:

This project verified that the bending rigidity for the flexible model is within appropriate biological ranges, as well as the effect of molecular flexibility on total membrane flexibility.  $K_c$  increases with an increase in the molecular bending parameter, which is consistent with theory: it should be harder to bend the membrane when each molecule is stiffer. Also, further parameter searches should be conducted, possibly at different temperatures, to see if other phases of lipid membranes can be simulated, i.e., a vesicle.

### Acknowledgments:

Grace Brannigan, Frank Brown, Lawrence Lin, Howard Wong, NSF

### References:

- [1] G. Brannigan and F. L. H. Brown, 2004, "Solvent-free simulation of fluid membrane bilayers," Journal Of Chemical Physics, vol. 120, p. 1059
- [2] U. Seifert and R. Lipowsky, Structure and Dynamics of Membranes, ed. R. Lipowsky and E. Sackmann (Elsevier Science, 1995), vol. 1.

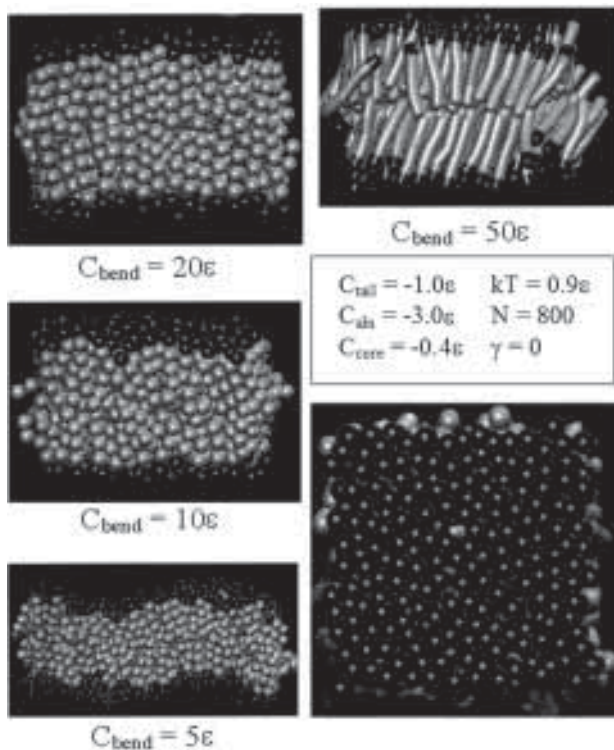


Figure 3: As molecular bending is increased (lowering  $C_{bend}$ ), the entire membrane gets more flexible. The bottom membrane,  $C_{bend} = 5\epsilon$  exhibits clear undulations. The top membrane,  $C_{bend} = 50\epsilon$ , formed a tilted gel phase that has been seen experimentally.

# Investigating the Formation of Polymeric Sculptured Thin Films as a Functional Template for Collagen Growth and Attachment

Sean Pursel, Engineering Science and Mechanics, The Pennsylvania State University

NNIN REU Site: Penn State Center for Nanotechnology Education and Utilization, Pennsylvania State University  
Principal Investigators: Drs. Mark Horn and Melik Demirel, Engr. Science and Mechanics, The Pennsylvania State University  
Mentors: Paul Sunal and Obi Ezekoye, Engineering Science and Mechanics, The Pennsylvania State University  
Contact: smp296@psu.edu, mhorn@enr.psu.edu, mcd18@psu.edu

## Abstract:

The primary focus of this project was to form polymeric Sculptured Thin Films (STFs). The vaporization of parylene or poly-para-xylylene and the radio frequency (rf) sputtering of Teflon® or polytetrafluoroethylene (PTFE) were explored. A motion control system was designed to provide two axis control of the substrate. Chiral parylene STFs were successfully deposited. PTFE films were unsuccessfully deposited.

## Introduction:

Sculptured Thin Films (STFs) are deposited by glancing angle deposition, typically at 75° or more. Directional flux introduces shadowing effects that force growth in a highly oriented manner. The film grows in the direction of the flux and can be manipulated into columnar, chiral, chevron, or other engineered growth patterns. STFs have been shown to have an abundance of properties that can be engineered to precise specifications.

The goal of this project was to produce polymeric STFs to be used to enhance the attachment of collagen. However, polymeric STF deposition has not been found in the literature. Polymer evaporation and sputtering techniques require some form of polymerization to occur before the vapor species' mobility is lost. Hence, the structure of some polymers will not allow vapor deposition. STFs have a controllable porosity that gives a large surface area for attachment. Larger surface area has been shown to enhance cell attachment [1]. Collagen attached to these films would provide a biocompatible material for medical implants and biological sensors. Teflon® or polytetrafluoroethylene (PTFE) has been successfully sputtered [2] and was chosen as a STF candidate. Parylene was chosen because a deposition system was already available for use and parylene has been shown to be good bio-active material.

## Experimental Procedures:

A motion control device was built to enable

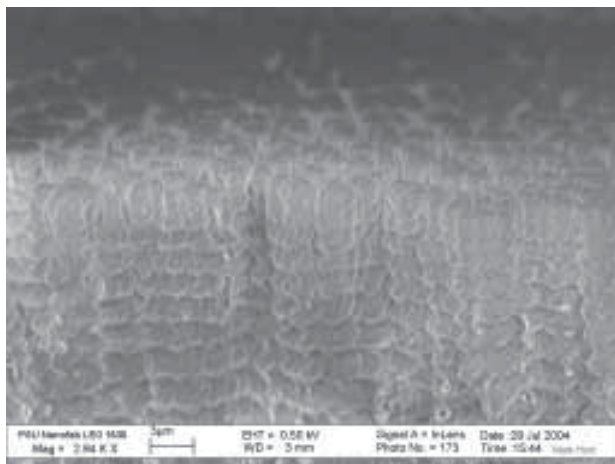


Figure 1: Chiral parylene sculptured thin film (0.025 rps).

deposition at various angles with substrate rotation. The stage assembly was designed to be used inside any vacuum system and controlled in real time with a windows interface. The system can operate at  $10^{-7}$  torr and 155°C internal temperature. Conventional parylene deposition systems use non-directional flux to achieve conformal coatings. For STF deposition, a nozzle was constructed to provide directional flux. Deposition time was measured from when the vaporization temperature reached 150°C to when the system was manually shut-down. Parylene depositions were done for five, ten, and fifteen minutes with rotation speeds of 0.167 and 0.025 rotations per second at 80° from the normal of the flux. Two depositions were done perpendicular to the vapor flux as control samples. Depositions were done on Corning Glass and also on silicon for SEM microscopy. In an attempt to maintain the same vapor pressure during each deposition, five grams of the parylene C dimer were inserted into the vaporizer for each deposition.

Sputtering PTFE was attempted during the end of the project. A PTFE target, one eighth inch thick, was constructed for a two inch sputtering gun. Five depositions were done at varying pressures and powers in order to find a deposition rate.

## Results:

The parylene depositions that were done at a glancing angle turned a frosted white color to the naked eye. The depositions done at normal incidence were transparent. Deposition thickness varied from 15-30  $\mu\text{m}$  showing no apparent dependence on deposition time. The microscopy results showed a chiral structure for a ten minute deposition on a silicon substrate rotating at 0.025 rotations per second, as seen in Figure 1. The results show fifteen turns at a thickness of about 30  $\mu\text{m}$ . This gives the chiral columns a period of  $\sim 2 \mu\text{m}$  per turn. An interesting result was seen on the same sample. A section of the film had delaminated from the substrate revealing a pin-hole free bottom surface, as seen in Figure 2. The results for substrates rotating at 0.167 rps showed a more complex structure, as can be seen in Figure 3.

PTFE rf sputtering did not give any film as measured by profilometry. A bright argon plasma was formed and upon removing the target a faint erosion track was seen.

## Discussion:

The parylene deposition system did not allow enough user control to form the engineered films that were sought. The pressure could not be controlled. Residual vapor in the system was deposited after the vaporizer was shutdown. This may explain the discrepancy in the deposition rate. The results show that polymeric STF's can be formed from PVD processes. The chiral films that were formed showed a continuous under layer. This layer would provide the same barrier from gas and moisture that a conventional parylene film would and could be

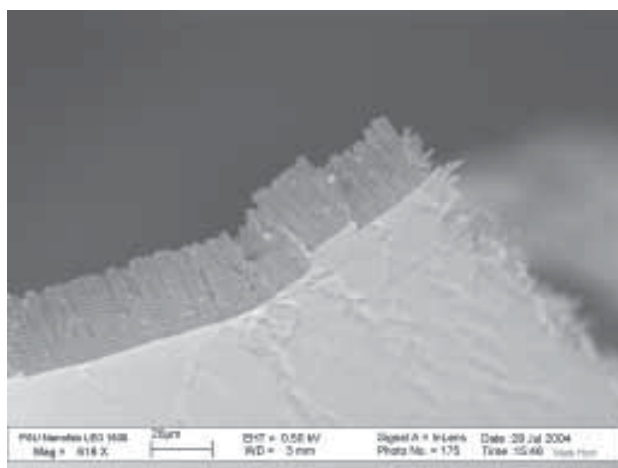


Figure 2: Continuous under layer of parylene STF (0.025 rps).

important in implantable device applications. The films deposited at 0.167 rps showed a structure containing a weaving of parylene strands underneath columns, seen in Figure 2. These films were unexpected but may provide an increased surface area for collagen attachment. PTFE sputtered films were too thin to measure with profilometry. However, the erosion track suggests that PTFE was sputtered and a longer deposition time was needed. No other PTFE depositions were attempted and experiments evaluating collagen attachment were not done due to time constraints.

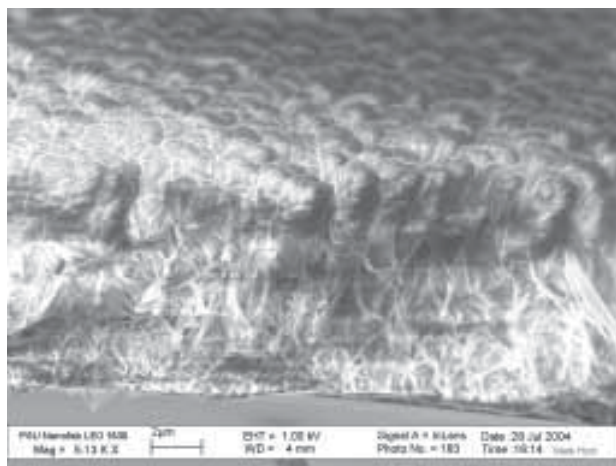


Figure 3: Parylene strands underneath columns (0.167 rps).

## Conclusions:

1. Polymeric STF's can be made from PVD processes and more polymers need to be investigated to determine the films usefulness.
2. Parylene can form STF's but a system made to produce a controlled directional flux needs to be used to attain the engineering control necessary for more in depth investigations.
3. Current parylene films need to be tested for collagen attachment and growth.
4. Attempts to form sputtered PTFE STF's will need to be done with longer deposition times or by increasing deposition rates by increasing rf power or target size.

## References:

- [1] T.A. Desai, J. Deutsch, D. Motlagh, W. Tan, and B Russell, *Biomedical Microdevices* 2:2, 123-129, 1999.
- [2] G.A. Hishmeh, T.L. Barr, A. Aklyarov, and S. Hardcastle, *J. Vac. Sci. Technol. A*, Vol. 14, No. 3, 1330-1338 May/June 1996.

# Mechanical Properties of Human Stratum Corneum: Influence of pH-Treatment

Rena Rudavsky, Mechanical Engineering, Columbia University

NNIN REU Site: Stanford Nanofabrication Facility, Stanford University

Principal Investigator: Reinhold Dauskardt, Materials Science, Stanford University

Mentor: Kenneth Wu, Mechanical Engineering, Stanford University

Contact: rmr2003@columbia.edu, Dauskardt@stanford.edu

## Abstract:

The stratum corneum (SC), the outermost layer of the skin, is the body's first barrier against the external environment. As such, the underlying microstructure and mechanical properties of the SC are of fundamental and practical interest.

While pH treatments have been shown to influence the lipid lamellar matrix, alterations to the mechanical properties have not been examined thoroughly. Since many topically applied substances like surfactants, creams, and adhesives for transdermal technologies possess varying pH levels, it is important to understand resultant property changes of the SC.

In particular, we looked at pH-induced changes to physical relaxation time and strain-recovery of human SC. We completed time-dependent creep-recovery tests in ambient conditions on pH-treated SC specimens using a dynamic mechanical and thermal analysis (DMTA) device. While various pH levels affected the strain-recovery, they did not appear to significantly alter the physical relaxation time.

## Introduction:

The skin has three distinct layers—the epidermis, dermis, and subcutaneous fat. The stratum corneum (SC), the top layer of the epidermis, has a thickness of 10-20  $\mu\text{m}$ . Following a 14-day cycle, cells from lower epidermal layers flatten, rise and fill with the protein keratin to form SC. While a cross-section of the SC reveals inter-digitated cell layers surrounded by a lipid lamellar matrix, similar to bricks and mortar, a top-view reveals complete surface coverage resembling a soccer ball. Keratin, the main component of SC, is the same metabolically inactive protein in hair and fingernails, making it easy to study *in vitro*.

The SC is the body's primary chemical, diffusional, and mechanical barrier. Changes in the biophysical characteristics of this outer layer could greatly influence its mechanical properties and thus its biophysical functions as well. Yet, there is still necessary work needed to fully characterize SC

physical properties. Particularly, we focused on the mechanical effects of pH on SC.

Even though healthy SC has a pH of 5.5-7, common skin therapies tend to vary greatly along the pH scale. With anti-wrinkle fighting treatments like pH 3.5 alpha-hydroxy acid and many daily-use soaps of pH 9-10, it is important to identify specific changing mechanisms in this essential barrier. Additionally, with new advances in transdermal technology, it is essential to understand adhesive-induced changes to SC physical properties. Alterations to the barrier could inhibit diffusion or increase tearing during patch removal. Lastly, diseases like eczema and diabetes tend to raise skin pH, thus affecting possible transdermal drug delivery.

## Procedure:

We tested human SC separated from full thickness cadaver skin using a trypsin treatment. Specimens were treated for 18 hours with buffered solutions of pH 4.2, 6.7 or 9.9 of constant 0.006 M ionic strength. Other specimens were delipidized with a chloroform-methanol (2:1) soak for 2 hours. All specimens were

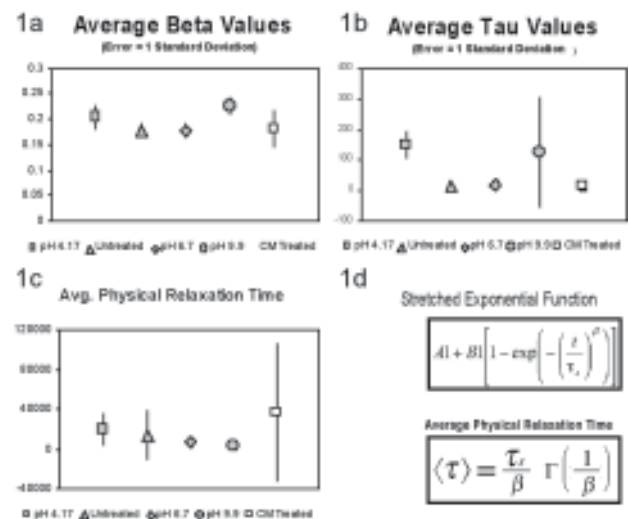


Figure 1: a, b, c) Stretched exponential values/functions; d) Physical relaxation time.

then dried in ambient conditions (~ 25°C; 50% RH).

To study physical relaxation time and strain-recovery of SC, we completed in-plane creep-recovery testing using a Rheometric Scientific Dynamic Mechanical and Thermal Analysis (DMTA V) device. Because SC exhibits viscoelastic and viscous components in addition to elastic properties, response strain to applied stress is time dependent. So, we applied a constant 1 MPa stress for 21020 seconds then lowered the applied stress to 1 kPa for 21020 seconds while measuring the resultant strain (2).

To isolate the elastic modulus of pH-treated specimens, tensile tests were completed at a strain rate of 0.002. Values were used from earlier tests for untreated and chloroform methanol treated specimens.

In preparation for scanning electron microscope imaging, specimens were coated for 45 seconds with gold palladium. SEM images were taken to qualify SC damage.

### Results:

We can see a distinct strain-recovery change in treated specimens in Figure 1c. By comparing the creep strain to the equivalent time interval recovery strain for each treatment, we can see that recovery ranges from 76% for the untreated specimens to as low as 31% for pH 9.9 treated specimens.

Using the stretched exponential equation in Figure 1d, we calculated the viscoelastic response of SC. The viscous component was subtracted from the raw data and the elastic component was isolated using tensile test data- leaving the viscoelastic component to fit with the stretched exponential equation. A  $\beta$  value less than 1 creates a curve stretched from a regular exponential function while  $\tau_s$  values characterize the physical relaxation time ( $\tau_s$ ) seen in Figure 1d. Figures 1a,b show little statistical difference between the averaged  $\beta$  and  $\tau_s$  values for each treatment.

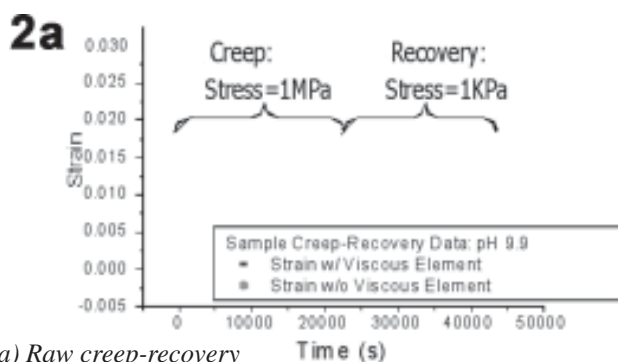


Figure 2: a) Raw creep-recovery data; b) Strain-recovery analysis.

### Discussion:

A clear trend indicates that strain-recovery decreases as pH moves farther away from the normal ~ 5.5 pH of SC, increasing plastic deformation and greater tendency of the material to remain deformed after reduction of applied stress. This may be attributed to the isoelectric point (IEP) of ~ pH 5 of keratin and the pKa of ~ pH 7 of lipid fatty acids. As charge in the keratin increases so does swelling and damage [1]. The downward concavity of the strain-recovery data shown in Figure 2b with the lowest point at pH 9.9-, the largest deviation from both the keratin IEP and the lipid pKa- suggests that pH affects both lipids and keratin synergistically. The delipidized specimen, however, suggests that lipid removal does not significantly influence strain-recovery. It appears as though SC alterations are primarily caused by damaged keratin, although more verification is needed.

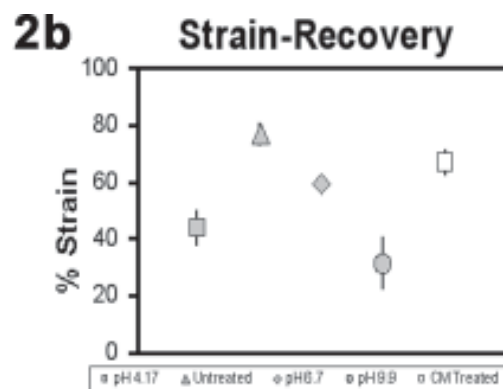
Harsher treatments, like surfactants, will be analyzed to compare effects on keratin. Interestingly, the physical relaxation times do not vary appreciably in the current data set, but more intensive study is needed for verification.

### Acknowledgments:

Thanks to Kenneth Wu, Reinhold Dauskardt, Michael Deal, and the National Science Foundation for giving me this opportunity.

### References:

- [1] Ananthapadmanabhan, K. P., et al. pH-Induced Alterations in Stratum Corneum Properties. *Journal of Cosmetic Sciences*, 25, 103-112.
- [2] Menard, Kevin P. *Dynamic Mechanical Analysis: A Practical Introduction*. CRC: Boca Raton, 1999.



# Ordered Growth on Nanostructured Glass Surfaces

Marjan Saboktakin, Electrical Engineering/Engineering Physics, Lehigh University

NNIN REU Site: Cornell NanoScale Science & Technology Facility, Cornell University

Principal Investigator & Mentor: Prof. Christopher Umbach, Materials Science and Engineering, Cornell University

Contact: mjs7@lehigh.edu, umbach@ccmr.cornell.edu

## Abstract:

This project investigated the possibility of creating ordered structures on corrugated glass substrates. The process involved creating corrugations with amplitude of  $\sim 1.5$  nm and wavelength of  $\sim 50$  nm by bombarding the surface of the glass with 0.45 keV  $\text{Ar}^+$  ions at  $45^\circ$  from the normal angle. Then small amounts of gold, with thicknesses ranging from 5-15 Å, were deposited onto the corrugated glass surfaces through thermal and E-gun evaporation at various angles. We investigated the changes in the positions of the deposited gold particles through a series of annealing processes and characterization utilizing atomic force microscopy (AFM).

We also studied various ways to create higher amplitude corrugations through depositing  $\text{SiO}_2$  in an off-angle geometry at various thicknesses ranging from 5 to 30 Å. These surfaces were also characterized by AFM.

## Introduction:

The process of creating sputter-induced corrugated surfaces on amorphous, crystalline and metal surfaces

is an established process which can be controlled in order to create surface corrugations with a desired wavelength and amplitude.

These corrugated surfaces can potentially be used as a method of self-organization and self-orientation of various deposited thin molecular films. Therefore, studying the formation of nano-particles after deposition and their response to the curvature of corrugated surfaces is an essential part of developing a method to control the size and distribution of the nano-particles formed.

The size and position of formed nano-particles is depended on the thickness of deposited material as well as the curvature of the surface. Figure 1 compares different thicknesses of material deposited on corrugations with the same amplitude and wavelength. The particles' response to the surface morphology was studied. As the deposited thickness increases, the particles tend to form bigger particles and their response to the surface curvature becomes minimal.

The annealing process provides enough energy for these formed nano-particles to respond to surface curvature. In Figure 2, the annealing processes for

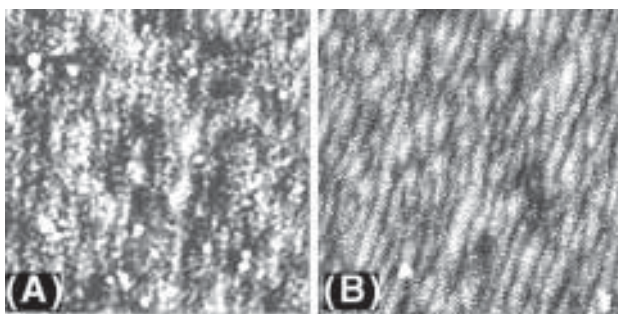


Figure 1: AFM images of  
A) 3nm gold deposited  
sample, B) 1nm gold  
deposited sample,  
C) 0.5nm gold  
deposited sample.

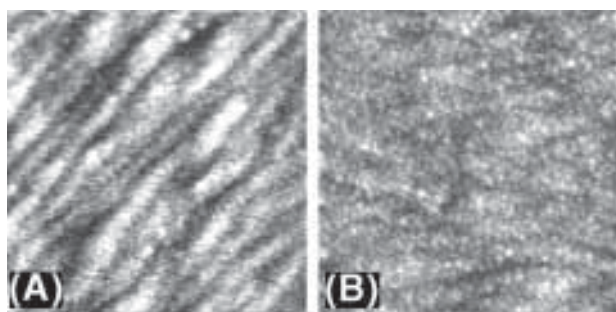


Figure 2: AFM images of  
0.5 nm gold dep. with  
A) no annealing time,  
B) 20 sec annealing time,  
C) 60 sec annealing time.

5 Å deposited gold is compared as the annealing time increased from 10 to 60 seconds. Increase in the anneal time results in increase in the size of the particles as is apparent in the figures.

### Procedure:

Corning code 1737, boroaluminosilicate glass pieces were washed with acetone and isopropyl alcohol and blown dry with dry nitrogen. The pieces then were placed in a Veeco Ion Mill with an incoming ion angle of 45° where they were bombarded at 450 V and 80 mA for 20 minutes. The resulting corrugations had a wavelength of approximately 50 nm, and amplitude of 1.5 nm.

The corrugated samples were then placed in CVC 4500 evaporator where small amounts of gold with thicknesses ranging from 5 to 15 Å were thermally deposited onto the corrugated glass surface at normal incident angles. A series of annealing processes and characterization was then performed. Samples were placed in an RTA (Rapid Thermal Anneal) oven for various times ranging from 10-60 seconds at 450°C. Characterization was performed after each annealing time utilizing AFM.

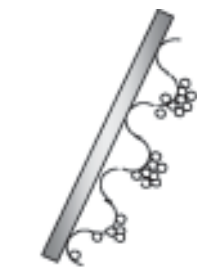


Figure 3: Off-normal angle geometry used for SiO<sub>2</sub> deposition.

In another set of samples, after the corrugations were made utilizing the same set up as described above, the samples were placed in CVC 4500 where small amounts of SiO<sub>2</sub> ranging from 5 to 30 Å were deposited on the corrugated surface in off-angle geometry. Figure 3 shows the set up used for this deposition. Samples were placed at 11° away from normal which corresponds to the maximum curvature of the corrugated glass surface, and is required for the shadowing effect to be apparent. The samples were placed away from the center of the deposition chamber to which angle we added.

### Results and Conclusions:

The effect of thickness variation in the deposition process has been investigated and studied. Also, providing thermal energy for the formed gold particles, their response to the curvature of the surface has been investigated.

In off-angle geometry deposition, the shadowing-

effect in deposition SiO<sub>2</sub> on corrugated glass surface has been successfully observed and studied, and an asymmetrical structure, and height increase in the deposited corrugated glass has been identified.

### Future Work:

More control over the off-angle geometry deposition is favorable since small changes in the deposition angle can cause the shadowing effect to be less effective.

Also, deposition while the sample is being heated can provide enough energy for the particles to respond to the curvature of the surface during formation. Through this process we might be able to avoid the annealing process.

### Acknowledgements:

I would like to thank Dr. Christopher Umbach whose insight and support guided me through this project. Also I thank the CNF staff and Ms. Melanie-Claire Mallison for their support. I also thank NSF for providing the funding for this project.

### References:

- [1] C.Allen, M.Daniels, C.Umbach, and J.Blakely. NanoMeter, Vol.14, 130-131 (2003).
- [2] C.Lee, Z.Liu, E.Kan. MatResSocSymp. Proc. Vol. 737 2003.
- [3] Z. Liu, C.Lee, V.Narayanan, G.Pei, and E.Kan. IEEE Transaction on Electron Devices, Vol.49, No.9, September 2002.

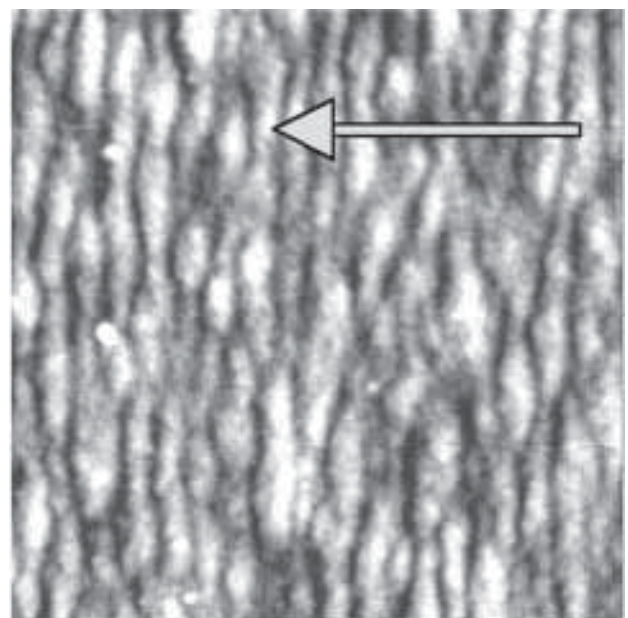


Figure 4: AFM image of the sample with 5 Å SiO<sub>2</sub> deposited in an off-angle geometry. The arrow shows the direction of SiO<sub>2</sub> deposition.

# Silicide Contacts to Ultra-Thin Silicon Films for Nano-Scale Devices

Ludwig Salomon, Electrical and Computer Engineering, Carnegie Mellon University

NNIN REU Site: Cornell NanoScale Science & Technology Facility, Cornell University

Principal Investigator: Dr. Sandip Tiwari, Electrical and Computer Engineering, Cornell University

Mentors: Uygur Avci, Applied and Engineering Physics; Arvind Kumar, ECE; Cornell University

Contact: lsalomon@andrew.cmu.edu, st222@cornell.edu

## Abstract:

The goal of this project was to develop and understand techniques to produce ohmic contacts using cobalt silicide, and to use this method to achieve a silicide thickness of 10 to 15 nm. Test structures were fabricated with varying thicknesses of N<sup>+</sup> polysilicon, and factors contributing to polysilicon loss and poor silicidation were determined, as well as optimal annealing temperatures. Electrical and film thickness measurements taken on the finished wafers showed the presence of cobalt silicide on a 17 nm film of polysilicon.

## Introduction:

Techniques have been developed to build nano-scale devices on single-crystal silicon films as thin as tens of nanometers, such as transistors and memories with 30 nm gates built on 15 nm silicon films. However, at this size it is difficult to make low-resistance, device-quality ohmic contacts to the silicon, since interface reactions are often on the same order of thickness as the silicon film itself.

A solution to this problem is silicidation, an annealing process that results in the formation of a silicon-metal alloy. The advantages of using silicide include: less parasitic resistance, lower thin-film resistivity than polysilicon, higher thermal stability, and protection of the contact interface from surface effects. Since its resistivity is approximately 1/5 that of doped polysilicon, cobalt silicide serves well as an ohmic contact and significantly improves the performance of devices that use it [1].

Cobalt was chosen specifically for this project because it consumes less polysilicon in the process and produces more silicide than the other available metals. Also, its thin-film resistivity of 14-20  $\mu\Omega$ -cm is one of the lowest among common silicides [2].

## Procedure:

Three fundamental test devices, as shown in Fig.1, were designed. The first, a transmission line structure,

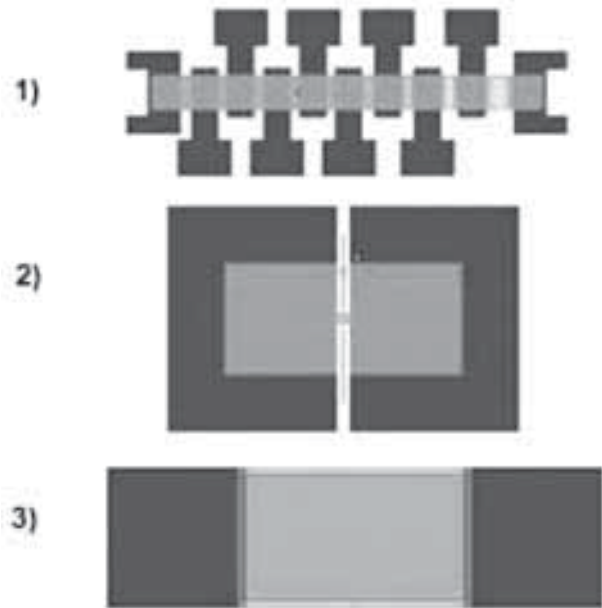


Figure 1: Test structure layouts.

tests contact resistance. The second, consisting of two contacts, monitors the formation of silicide around a thin strip of silicon dioxide that imitates the gate of a transistor. The third, a single via with varying separation between the metal interconnect pads, tests the resistance of the metal to the silicide. These designs were also modified to make devices to monitor effects on silicidation from via size, active region width, and slanted sidewalls.

Masks were made for the final layout, and pseudo-SOI wafers were prepared for device fabrication. The wafers were divided into groups, each having 18, 41, 47, or 71 nm of N<sup>+</sup> polysilicon on top of 500 nm of SiO<sub>2</sub>. After a thin sacrificial oxide growth and deposition of 50 nm of low stress nitride, the polysilicon active regions were lithographically defined and plasma etched. A local oxidation step grew additional oxide around the active regions, and then a hot phosphoric acid bath removed the remaining nitride.

Next, 100 nm of low temperature oxide was deposited, and the contacts were patterned and etched through the LTO onto the active regions. Cobalt was

then sputtered onto the wafers, followed by titanium to protect the cobalt from oxidation. The first rapid thermal anneal, just to start the silicidation reaction, was performed at 550°C on one group of wafers and at 450°C on the next. A Nanostrip dip selectively etched the non-silicided metal. Finally, the second anneal was performed at 700°C to ensure that the cobalt silicide was in the correct phase, CoSi<sub>2</sub> rather than CoSi or Co<sub>2</sub>Si.

### Results:

After the etch that opened the contact regions, film measurements showed that negligible amounts of polysilicon remained within active regions on all of the wafers except for the group with the greatest polysilicon thickness. This loss was due to the lateral etching of polysilicon during the oxide etching process, and also to oxide's property of consuming polysilicon during growth.

Several bare N-type wafers and wafers with 100 nm of LTO that were used during the metal sputtering were also annealed in order to experiment with annealing temperatures. Originally, the first rapid thermal anneal was planned to be at 550°C, but the test wafers exhibited a flaky, non-conducting surface. Other wafers that underwent the fabrication process up to the first anneal exhibited a brittle, non-conducting layer that had to be scratched through in order to get contact between the probe tips and the vias. Annealing at 450°C gave consistently better results; Figure 2 shows the difference in appearance before and after the anneal.

Ultimately, wafers from the 71 nm polysilicon group exhibited silicide formation between 17 nm of

polysilicon and a metal layer consisting of 20 nm of cobalt and 7 nm of titanium. The silicide thickness was not determined, but preliminary electrical measurements after the first anneal showed resistances between 465 Ω and 535 Ω on contacts in the silicided areas of the wafer, resistance on the order of 10<sup>3</sup>Ω over contacts in non-silicided areas, and resistance on the order of 10<sup>11</sup> Ω (essentially zero current) over field oxide. The phenomenon of silicidation at relatively low temperatures, below 600°C, was also observed. Figure 3 shows a sample that had 20 nm of cobalt and 7 nm of titanium over a bare wafer grew approximately 20 Å of cobalt silicide after undergoing transmission electron microscopy (TEM).

Future work includes determining the thickness of the silicide grown on the samples that underwent the full fabrication process, and applying this process toward fabricating transistors.

### Acknowledgements:

My sincerest thanks to Dr. Tiwari and the Tiwari group for all their help, Michael Guillorn for the TEM work, Melanie-Claire Mallison, and the CNF staff. I also thank the NNIN and National Science Foundation for making this experience possible.

### References:

- [1] G. T. Sarcona, M. Stewart, and M. K. Hatalis, "Polysilicon Thin\_Film Transistors Using Self-Aligned Cobalt and Nickel Silicide Source and Drain Contacts," IEEE Electron Device Lett., vol. 20, 1999.
- [2] J. D. Plummer, M. D. Deal, and P. B. Griffin, "Silicon VLSI Technology: Fundamentals, Practice, and Models," Prentice Hall, 2000.

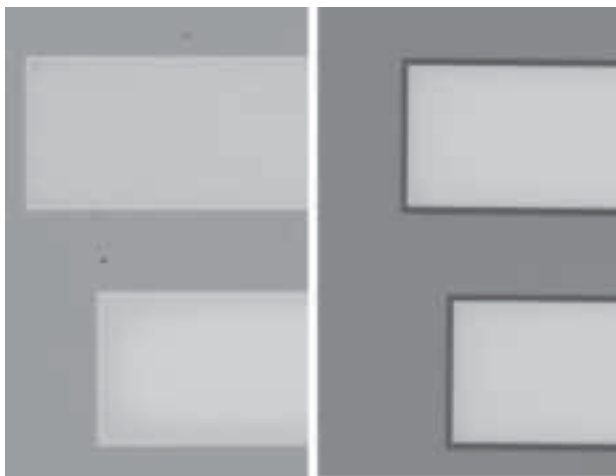


Figure 2: Left: before anneal. Right: after anneal.

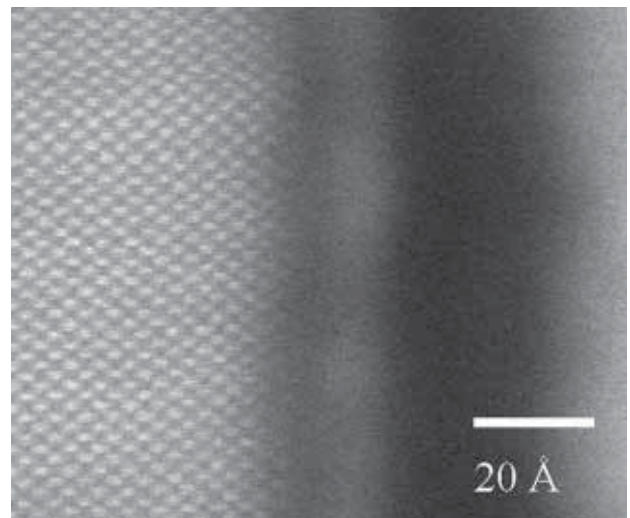


Figure 3: TEM of silicide (center) at Si-Co interface.

# The Growth of GaN Nanowires using Ni Nano Particles as Catalyst

Francis Sammy, Electrical Engineering, Howard University

NNIN REU Site: Materials Science Research Center of Excellence, Howard University

Principal Investigator: Dr. Gary Harris, MSRCE, Howard University

Mentor: Dr. Moaqi He, MSRCE, Howard University

Contact: Fsammy@howard.edu, gharris@msrce.howard.edu, mqhe@msrce.howard.edu

## Abstract:

In this work, photolithography is used to create nickel disks on a silicon substrate. These disks aid the growth of uniform wires. Half of the samples are  $N_2$  plasma etched, creating a rough surface for the wires to grow from. Rough and smooth surfaces were then compared in their ability to grow wires more uniformly. After the samples were properly prepared, they were placed into a furnace and heated to  $1000^\circ\text{C}$  in a gallium and ammonia environment for 20 minutes. This process resulted in the growth of nanowires in the range of  $5\text{-}7\ \mu\text{m}$  in length and approximately  $50\text{-}90\ \text{nm}$  in diameter.

## Introduction:

Gallium Nitride (GaN) nanowires are semiconductor wires that are grown through chemical-vapor deposition. These wires have many different uses and applications including lasers and diodes. GaN is a wide bandgap semiconductor material and this allows for the emission of blue and ultra-violet light. Due to its ability to emit light, GaN can be used in data storage, because of its high frequency and short wavelength. This makes it far superior to modern technology and thus an interesting option in the development of new technology.

To aid in the growth of our wires, a Nickel (Ni) catalyst was chosen to increase the rate of reaction. The Ni catalyst typically decreased the time taken to grow by 2 hours. GaN nanowire growth has been achieved in the past but in a matrix form. A pattern of Ni disks was chosen to control both the size and location of the nanowires. This was to ensure a sample that contained uniform nanowire growth.

## Experimental Procedure:

The first thing that was done was to create the Ni disks for the GaN to grow on. We started out by cleaning and preparing three different substrates: sapphire, quartz and silicon. These three substrates were washed with soap, and then doused with acetone

and methanol to ensure a clean surface. After cleaning, through the process of photolithography, a pattern was placed on top of each of the substrates. The pattern contained  $2\ \mu\text{m}$  disks spaced  $2\ \mu\text{m}$  apart from each other. We had hoped for the nanowires to grow perpendicular to the surface of the substrate. We had also hoped for growth parallel to the surface from one disk to another. A bridge-like structure connecting the disks was wanted to regulate nanowire growth.

In the past nanowire growth has been in the form of a matrix. The matrix is a shapeless array of random nanowire growth. The precise size and direction of these wires cannot be predicted.

After the pattern is placed on the substrate, the sample is then put into the electron beam evaporator so the Ni can be deposited on the surface of the substrate. The desired thicknesses of the Ni disks were  $35\ \text{nm}$ . After deposition, liftoff was used. In liftoff, acetone is sprayed on the substrates and the excess Ni is shed away. The samples now have the Ni disks deposited on them (Figure 1).

Half of the samples are then placed into the plasma

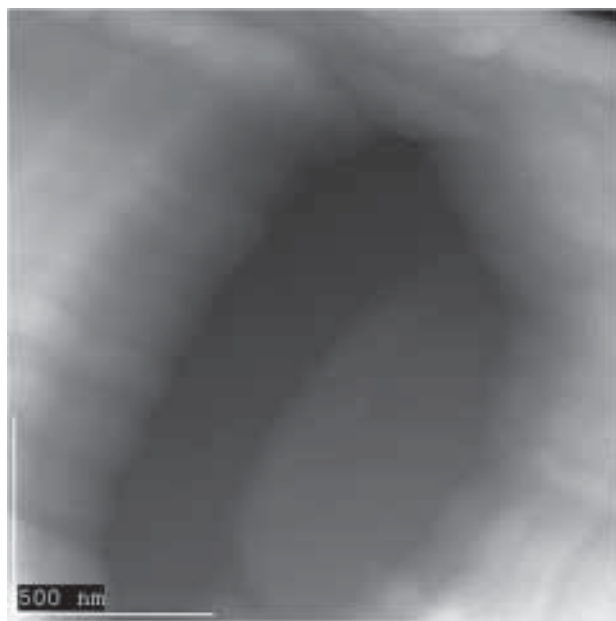


Figure 1: An unetched nickel disk before growth.

etch chamber to guarantee a rough surface for the nanowires to grow from. The samples were to undergo  $N_2$  plasma etching for a period of 3 minutes and then we measured the surface profile by AFM. This process resulted in a rough, bumpy surface, like nano particles, for nanowire growth (Figure 2). The next step was the growth process.

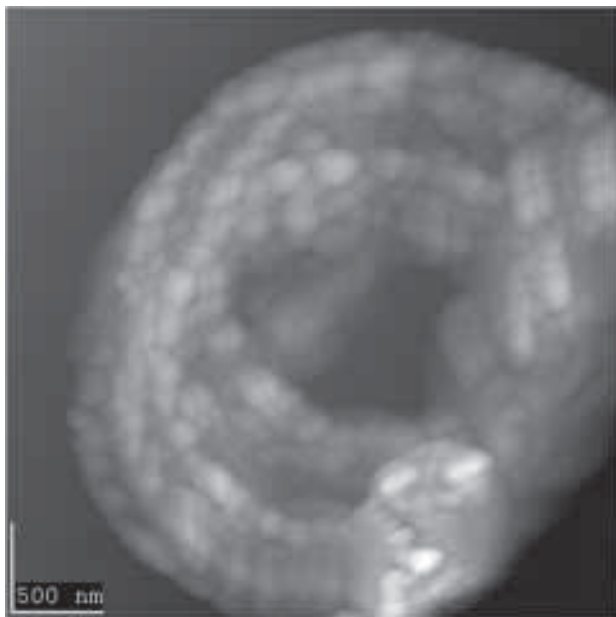


Figure 2: An etched Ni disk before growth.

The samples were placed into a quartz tube of a furnace behind gallium. The samples were then heated to  $1000^{\circ}C$  for 20 min while ammonia was flowed through the tube at a rate of 10 sccm and kept pressure at 10 torr. At the end of the growth process, the samples were measured by Scanning Electron Microscope (SEM) to observe their profile.

The Ni disks on the sapphire and quartz substrates did not become nano particles after  $N_2$  plasma etch, so we did not use them for growing wires.

### Results:

The etched Si substrate with Ni on it was able to produce nanowires in the 50-90 nm diameter range (Figure 4). These wires grew nearly perpendicular to the surface and had a sort of plant-like growth. The unetched silicon substrate was able to produce wires in the 200-300 nm diameter range (Figure 3). These were not nanowires; these are called whiskers. The etched sample did not contain nanosized particles.

### Conclusion and Future Works:

From these experiments, we conclude that nanowire

growth is largely based on nanoparticles. In the sample that contained nanosized dots on the disk, nanowires grew. If no nanoparticles were present either large wires or big crystalline structures would grow. In the future, if nanodisks were available, then individual wires may be able to grow. These nanodisks may be achieved through a process called self-assembly.

### Acknowledgements:

I would like to thank the entire MSRCE staff including Dr. Zhou, Mr. William Rose, Mr. Crawford Taylor, Mr. James Griffin, Dr. White and Dr. Harris for their support. I would like to especially thank Dr. He for helping me and mentoring me in this project. Thank you to the National Science Foundation for their funding. I also thank the REU program for giving me an opportunity to work in such a prestigious lab.

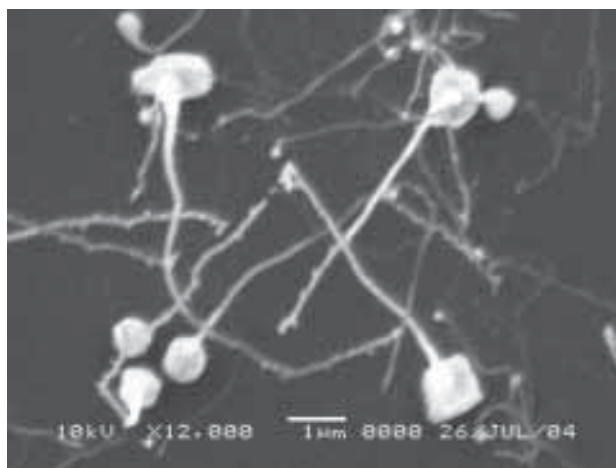
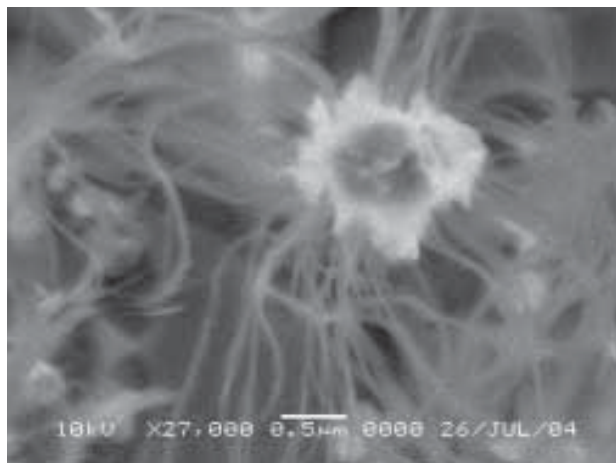


Figure 3, above: Unetched Ni disk after growth, size ~ 200-300 nm in diameter.

Figure 4, below: Etched Ni disk after growth, size ~ 50-90 nm in diameter.





experiment. Colloidal processing then allowed any expelled  $\text{Co}^{2+}$ , now complexed by additional TOPO, to be separated from the nanorods by their markedly different solubilities.

**C) Physical Methods:** A Phillips 1830 powder diffractometer was used to determine crystallinity. Electronic absorption spectra were collected on a Cary 5E (Varian) spectrophotometer using 1 cm path-length quartz cuvette. Dopant ion concentrations were determined using an inductively coupled plasma emissions spectroscopy (ICP-AES, Jarrel-Ash model 955). Magnetic susceptibility measurements were performed on powder samples using a Quantum Design MPMS SQUID magnetometer.

### Results and Conclusions:

The data in Figure 2 show that no  $\text{Co}^{2+}$  migration out of the lattice was observed at any temperature within the error of the experiment. Room temperature magnetic saturation data were collected on a ligand-exchanged control sample and the 36 hour annealed samples from each time dependent annealing experiment. Though all the samples proved to be weakly ferromagnetic, the annealing steps show no increase on the ferromagnetic moment. On the contrary, a three fold higher magnetic moment per cobalt was observed in the un-annealed samples (Figure 3a).

One possibility for this decrease may be that the TOPO itself is withdrawing electron density from the nanorod, thereby reducing the ferromagnetic moment in a carrier mediated exchange model. An alternative explanation lies in the volume percentage of passivating ligand per sample. Thermal gravimetric analysis experiments (TGA) show less ligand for the 180°C ligand exchanged sample (19 wt%) than the annealed samples (36 wt%). A smaller fraction of capping ligand provides an opportunity for sintering in the dried powder used for magnetic measurements.

Figure 4 shows the paramagnetic component of the magnetic susceptibility data as a function of temperature. Though no increase in ferromagnetic component was observed, the paramagnetic moment decreases monotonically with increasing annealing temperature. Such a reduction would be expected if a portion of the

paramagnetic  $\text{Co}^{2+}$  were being converted into an exchange coupled antiferromagnetic species reducing the total paramagnetic moment.  $\text{Co}^{2+}$  ( $d^7$ ) may also be undergoing a spin-crossover from high spin ( $S=3/2$ ,  $\mu_{\text{eff}}=4.2 \mu_B$ ) to a low spin ( $S=1/2$ ,  $\mu_{\text{eff}}=1.8 \mu_B$ ) state, thus decreasing the overall paramagnetic moment.

Figure 4 also shows  $\mu_{\text{eff}}/\text{Co}^{2+}$  for  $\text{Co}^{2+}$  decreasing from 4.2 to  $\sim 2.1$  in agreement with a spin-crossover type event. Further experiments would be necessary to differentiate these two possibilities.

In conclusion, no thermal activation to ferromagnetism or  $\text{Co}^{2+}$  expulsion was observed under our experimental conditions. The results of this study support the idea that nanoparticles sintering and/or aggregation is essential to activation of ferromagnetism. Further studies focusing on the observed paramagnetic reduction are of great interest to the magnetic semiconductor community.

### Acknowledgements:

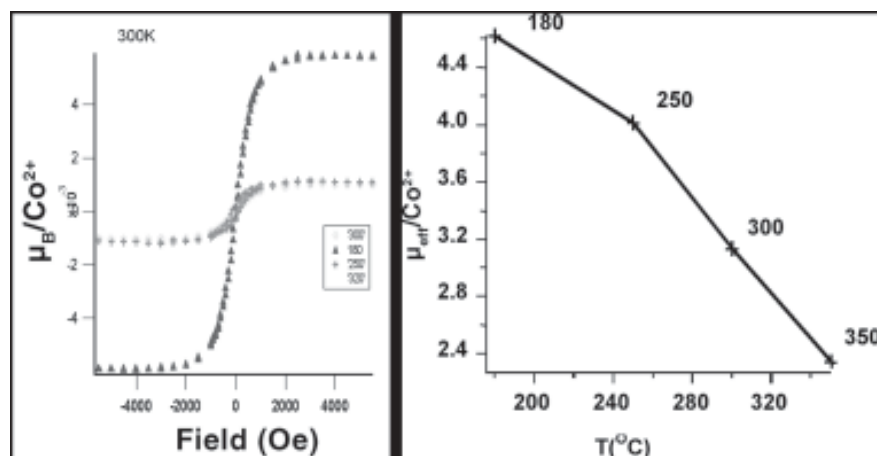
I would like to foremost thank my mentor J. Daniel Bryan Ph.D. Without Dr. Bryan's guidance, expertise, and most importantly, patience, no work would have been possible. Thank you to Professor Daniel Gamelin for the enriching opportunity presented to me. I would also like to thank everyone in the Gamelin group for fielding any question that arose. I would also like to thank NNIN/NSF for organizing and funding this program.

### References:

- [1] Bryan, J. Daniel, Hearld, Steve M., Chambers, Scott A. Gamelin, Daniel R. J. Am. Chem. Soc. 2004. in press.
- [2] Majetich, S. A.; Scott, J. H.; Kirkpatrick, E. M.; Chowdary, K.; Gallagher, K.; McHenry, M. E. Nanostructured Materials. 1997. 9(1-8), 291-300.
- [3] Cozzoli, P. Davide; Kornowski, Andreas; Weller, Horst. J. Am. Chem. Soc. 2003. 125(47), 14539-14548.
- [4] Bryan, J. Daniel, Santangelo, Steven, Keveren, Sean, Gamelin, Daniel R., manuscript in preparation, 2004.
- [5] Knauth, P., Tuller, H. L. Solid State Ionics. 2000. 136-137, 1215-1224.

Figure 3, left: Ferromagnetic data of each annealed sample and the unannealed sample.

Figure 4, right: Effective magnetic moment per  $\text{Co}^{2+}$ .



# Scaling Up Catalytic Nanomotors

John Sarik, Electrical Engineering & Physics, University of Texas at Austin

NNIN REU Site: Penn State Center for Nanotechnology Education and Utilization, Pennsylvania State University

Principal Investigator: Ayusman Sen, Department of Chemistry, Pennsylvania State University

Mentor: Tim Kline, Department of Chemistry, Pennsylvania State University

Contact: sarik@ece.utexas.edu, asen@chem.psu.edu

## Abstract:

To gain insight into the mechanism of motion of platinum/gold rods in hydrogen peroxide solution, a process was developed to fabricate micron diameter platinum/gold rods with aspect ratios similar to previously studied nanometer diameter rods. The micron diameter rods were fabricated in a sacrificial template formed using high-aspect-ratio photolithography. SJR 5740 was patterned on a silver-coated silicon wafer to form the template. The template was then connected to a standard three-electrode cell and a voltage was applied to electroplate gold, then platinum, into the template features. Once the platinum/gold rods were fabricated, the photoresist and the silver seed layer were removed, and the rods were collected and studied.

## Introduction:

In previous studies done by Dr. Sen's group at the Pennsylvania State University, platinum/gold nanorods approximately 370 nm in diameter and 2  $\mu\text{m}$  in length were grown electrochemically in alumina membranes. When placed in water, the rods exhibited random Brownian motion. However, when placed in a hydrogen peroxide solution, the rods catalyzed the spontaneous decomposition of hydrogen peroxide and exhibited autonomous, non-Brownian movement.

The purpose of this project was to fabricate larger platinum/gold rods with aspect ratios similar to the previous nanorods (6:1) and study their movement in hydrogen peroxide solution.

## Procedure:

**Fabricating the Mold:** To fabricate the electroplating mold, 50 nm of silver (a conductive seed layer for electroplating) and 10 nm of chromium (an adhesion layer between the silver and silicon) were evaporated onto a silicon wafer. SJR 5740, a positive photoresist that produces high-aspect-ratio features with vertical sidewalls and resists degradation during

electroplating, was dynamically spun onto the wafer at 3000 RPM for 50 seconds. The wafer was then soft-baked at 105°C for 13 minutes. A second application of SJR 5740 was spun onto the wafer. This double coat allows for greater photoresist thickness with better uniformity than a single coat at a lower spin speed. The average thickness of the photoresist was 18-20  $\mu\text{m}$ . During the coating process, the photoresist beaded along the edge of the wafer. This edge-bead was removed by applying acetone to the wafer's edge at 3000 RPM. The wafer was then soft-baked a second time at 105°C for 13 minutes. The wafer was held at clean-room temperature and humidity for 24 hours to allow the photoresist to rehydrate before exposure. Finally, the wafer was exposed with a Karl Suss MA6 Contact Aligner at an intensity of 12 mW/cm<sup>2</sup> at 365 nm and developed in AZ400K diluted in DI Water (1:4). Exposure and development times were systematically varied to find the times that produced the best features [1].

The first attempt to fabricate the mold used a photolithography mask with densely packed square and rectangular features ranging in size from 1  $\mu\text{m}$  to

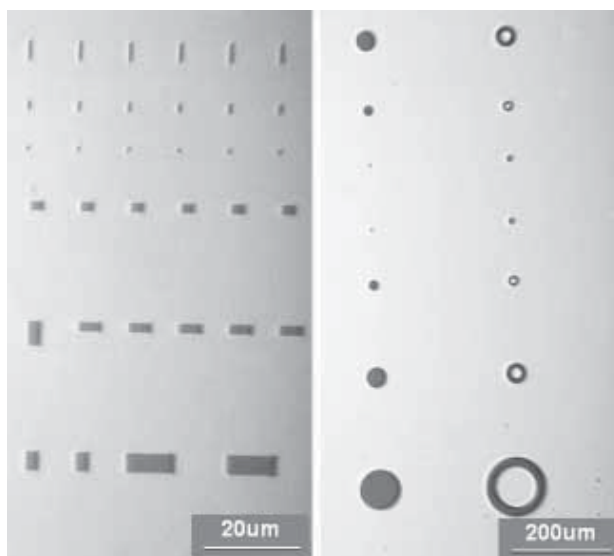


Figure 1: Photolithography masks.

50  $\mu\text{m}$  (Figure 1a). Exposures with this mask produced features that did not extend down to the wafer surface. Increased exposure time created poor resolution of the smaller features, while increased development time created non-vertical sidewalls. This is believed to be due to the dense spacing of the features and the large amount of surface area being exposed.

A second attempt to fabricate the mold used a mask with loosely packed circle and ring features ranging in size from 6  $\mu\text{m}$  to 60  $\mu\text{m}$  (Figure 1b). With this mask, an exposure time of 150s and development time of 14m produced features with good resolution that extended down to the wafer. However, the smallest feature was 6  $\mu\text{m}$  in diameter, which means with an 18  $\mu\text{m}$  thick photoresist, the aspect ratio was 3:1, and not the desired 6:1. Due to time constraints, wafers with this 3:1 ratio were used to continue the work.

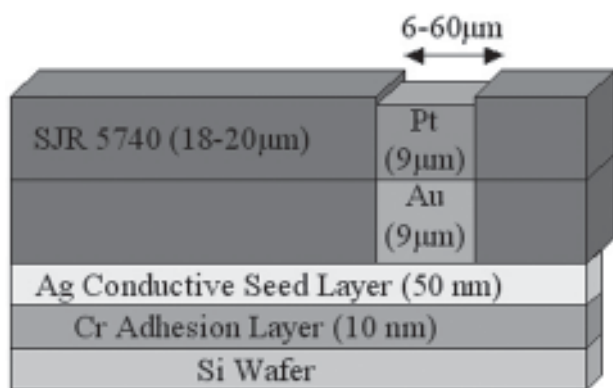


Figure 2: Overview of the fabrication process.

**Fabricating the Rods:** The electroplating was done in a standard three-electrode cell containing a titanium counter electrode, a silver/silver chloride reference electrode, and the electroplating mold as the working electrode. Techni Gold 25 ES, a slightly alkaline cyanide-free solution, and Techni Platinum AP, a neutral solution, were used.

Through cyclic voltammetry it was determined that the deposition potential of the gold and platinum plating solutions are -900 mV and -800 mV, respectively. The deposition rate for gold was determined to be approximately linear with a rate of 1  $\mu\text{m}/10$  min, but platinum's deposition rate was found to be non-linear.

During the platinum plating process, oxygen bubbles formed in the features of the mold. These bubbles blocked ion-transport and limited the amount of platinum that could be plated to  $\sim 1$   $\mu\text{m}$ .

Once the features had been fabricated, the silver

seed layer was dissolved in 5M nitric acid leaving the rods in a photoresist "pancake". This "pancake" was removed from the nitric acid and dissolved in acetone. Finally, the rods were collected, rinsed in DI water, and ready for study in hydrogen peroxide solution.

### Results and Conclusions:

The features fabricated through this process were approximately 9  $\mu\text{m}$  (8  $\mu\text{m}$  Au / 1  $\mu\text{m}$  Pt) tall and ranged in diameter from 6-60  $\mu\text{m}$ . These features did not have the desired aspect ratio and a majority of the features were discs, not rods. It was not surprising that these features did not exhibit motion (Brownian or non-Brownian) in water or hydrogen peroxide solution. Instead, the features settled to the bottom of the solution. Although rods with the desired dimensions and aspect ratio were not fabricated, a process to create a mold for electroplating micron diameter rods was successfully developed.

Further study is warranted into using this process with a different mask having loosely packed, smaller features to produce a mold that would yield rods with the desired geometry.

### Acknowledgments:

I would like to thank my principal investigator Dr. Ayusman Sen, my graduate student mentor Tim Kline, Wally Paxton, Shakuntala Sundararajan, and the Penn State Nanofabrication staff for their assistance this summer. This project was made possible by funding from the National Science Foundation.

### References:

- [1] Li, X.; Diss. UCLA, 1999.

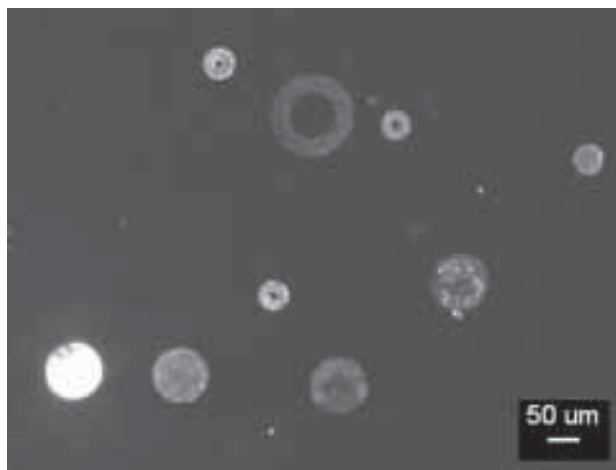


Figure 3: Free features in DI water. Dark field microscopy 50x.

# Self-Assembly of Sub-Micron Channels for Nanofluidic Applications using Interferometric Lithography and Spin-Coating

Cortland M. Setlow, Physics, Swarthmore College

NNIN REU Site: Center for High Technology Materials, University of New Mexico

Principal Investigator: S.R.J. Brueck, Director, Center for High Technology Materials, University of New Mexico

Mentor: Deying Xia, Electrical & Computer Engineering, University of New Mexico

Contact: csetlow1@swarthmore.edu, brueck@chtm.unm.edu

## Abstract:

Nanoscale channels offer an experimental apparatus for validating theoretical predictions of fluid flow in the nanometer regime, as well as practical applications in biology, chemistry, and engineering. In nanochannels, the electrical double layer becomes large compared to the dimensions of the channel, and flow is strongly dependent on the electrical properties of the channel and the fluid. The focus of this project is to fabricate nanochannels using a faster, cheaper method.

Interferometric lithography is used to create a template in Shipley 510A photoresist and a wet-i ARC layer, on which silica beads self-assemble during spin-coating. The sample is then calcinated, burning off the photoresist and wet-i ARC template and leaving the beads. Nanochannels as narrow as 300 nm have been fabricated. These devices will provide a good basis for further investigation of nanofluidic flow.

## Introduction:

Currently, microfluidic technology offers intriguing possibilities for biological, chemical, and engineering applications. Microfluidics allow heatsinks to be integrated into microchips, make possible on-chip gene sequencing, and enable advanced propulsion technologies. Future applications will include automated chemical and biological synthesis at the nanoliter scale.

Nanofluidic technology, although further into the future, offers even more exotic promise. Nanochannels are on the length scale of large molecules and so can shape them somewhat directly. They allow assays to be performed on picoliter and smaller samples. As channels narrow, electrical effects from the walls spread into the bulk of the fluid. This allows efficient electrical manipulation of fluid flow and other properties.

Nanochannels are the pipes of a nanofluidic plumbing system. No more than voids in some material, they are the simplest nanofluidic device.

Valves, joints, basins, reactors, and all other devices require more complex design; as such, nanochannels are the obvious first thing to try to design.

## Procedure:

Our fabrication process begins with a 6 inch diameter silicon wafer. Before it can be processed, it must be clean of all organic residues. This is accomplished by dipping it first into a hot solution of 3/4 sulfuric acid (70% aqueous  $H_2SO_4$ ) and 1/4 hydrogen peroxide (30% aqueous  $H_2O_2$ ). This caustic mixture, called piranha, cleans away all organic traces from the wafer, but leaves it with a coating of hydrophilic silica. Hydrofluoric acid (50% aqueous HF) is then used to remove this layer of silica, leaving a clean and hydrophobic surface.

The clean wafer is spin-coated with two chemicals. Spin-coating, similar to the spin-art process beloved by children, involves applying a few drops of chemical to a quickly spinning (~3k rpm) silicon wafer. The chemical forms a thin, even layer across the surface and quickly dries.

The two chemicals here are a wet-i back antireflective coating, which prevents reflections off the shiny wafer from interfering with the exposure, and Shipley 510A photoresist, the light-sensitive

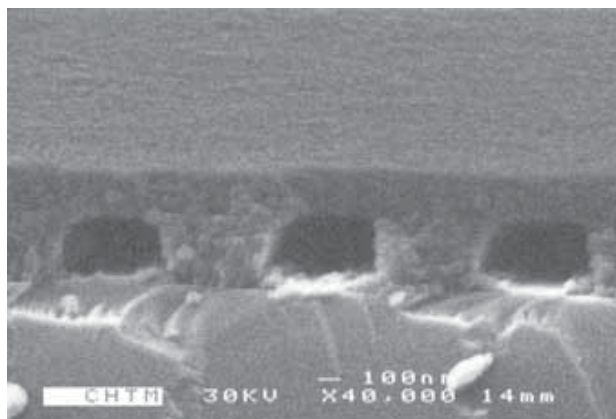


Figure 1: Nanochannels of silica nanospheres on a silicon substrate.

chemical that can be developed into our template.

The wafer is exposed to laser light in the desired pattern, gently baked, and developed. Areas exposed to light either etch away or are retained, depending on whether a positive or negative photoresist was chosen. We exposed a series of regular vertical bars, seen in Figure 1 end-on. Typical channel widths are in the low hundreds of nanometers.

The developed wafer is spin-coated with a 5% by weight solution of approximately 60 nm silica spheres. This concentration was chosen so that a single spin-coating would yield roughly a single layer of spheres. The spheres fill the grooves in the photoresist first.

After 3 or 4 coatings, the grooves are filled. The silica spheres are not hydrophobic, so one can see from the behavior of the aqueous sphere solution that the grooves have been filled.

Having filled the grooves, one may now calcine (bake) the sample for 2 hours in an 800°C oven. This will form hard, open grooves of silica spheres. Hydrolytic bonding is believed to occur between the spheres; longer bakes yield little difference. Higher temperatures cause cracking as the spheres deform too much; lower temperatures do not allow the spheres to bond.

Irregular and even arbitrary patterns of nanochannels can be easily fabricated; the simplicity of this pattern results from limitations in our interferometric lithography setup, and not the general process.

### Results and Conclusions:

Nanochannels have been successfully fabricated using self-assembly and interferometric lithography.

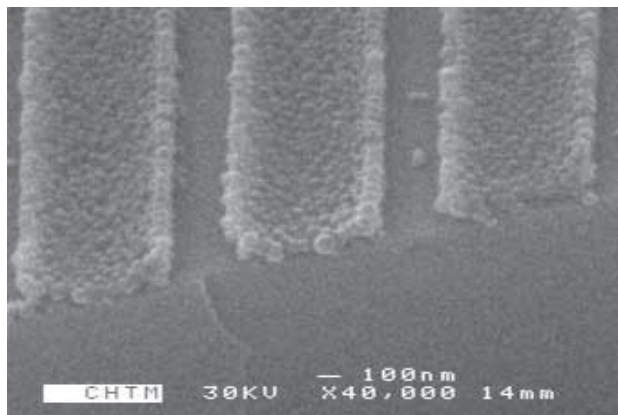


Figure 2: A single layer of silica nanospheres on a silicon substrate.

Representative nanochannels are shown in the two electron micrographs. The methods presented here are fast, comparatively environmentally friendly, and require less equipment than many others. The nanochannels we fabricated are useful; they offer an experimental system in which to verify currently-untested theoretical predictions of molecular dynamics and electrokinetic flow. They could be an important component in biological or chemical sensing or synthesis systems.

### Future Work:

Future work includes further characterization of this process and analysis of fluid flow within the channels. Long-term future work includes fabrication of arbitrary patterns of nanochannels, nanochannels with different surface properties, and nanofluidic devices.

### Acknowledgments:

Dr. S.R.J. Brueck, my P.I.; Deying Xia, my mentor; Michael O'Brien; Abani Biswas; Andrew Frauenglass, lab supervisor; Alex Raub, backup mentor.

### References:

- [1] J.Phys.Chem (69) 4017.
- [2] Phys.Fluids (14) 1146.
- [3] Appl.Phys.Lett. (81) 174.
- [4] Anal.Chem. (74) 394.
- [5] J.Appl.Phys (80) 6997.

# Reactive Ion Etching Process Development and Characterization

Shahid Shaikh, Chemical Engineering, University of California, Santa Barbara

NNIN REU Site: Center for Imaging & Mesoscale Structures, Harvard University

Principal Investigator: Dr. Erli Chen, Department of Engineering and Applied Sciences, Harvard University

Mentor: Dr. Ling Xie, Center for Imaging and Mesoscale Structures, Harvard University

Contact: shahid\_shaikh@uemail.ucsb.edu, erlichen@deas.harvard.edu

## Abstract:

Reactive Ion Etching (RIE) is a major process in the fabrication of semiconductor devices for transferring patterns from masks to semiconductor substrates. From neutral gases and glow discharge utilization, chemically reactive species are generated to react with materials being etched to form volatile by-products.

This research focuses on etching process developments for SiO<sub>2</sub>, Si<sub>3</sub>N<sub>4</sub>, GaAs, and InAs, and studies etch depth, etch rate, surface roughness, and wall angle. Approximately 1.5 μm photoresist is coated on the materials and patterned prior to etching. After etching, the samples are analyzed using a Dektak profilometer, Scanning Electron Microscope (SEM), Ellipsometer, and Atomic Force Microscope (AFM).

## Introduction:

There is increasing interest in nanotechnology and its general framework, nanofabrication; specifically in the semiconductor industry. A primary process for semiconductor nanofabrication is RIE, which uses chemical and physical processes to etch away desired materials. Compared to wet etching, RIE has higher anisotropy, better uniformity and control, and better etch selectivity [1].

This paper reports the preliminary results of RIE process developments of SiO<sub>2</sub>, Si<sub>3</sub>N<sub>4</sub>, GaAs, and InAs substrate materials. Etch depths and etch rates versus etch time have been measured. GaAs studies for surface roughness and wall angle have also been conducted.

## Experimental Procedure:

All materials are prepared using the same photolithographic process. Shipley S1813 photo resist is spin coated onto all samples, forming ~ 1.5 μm layer. Then the samples are soft baked at 110°C for 3.5 minutes. Karl Suss MJB-3 mask aligner is used to expose the samples. Shipley CD-30 developer is used to develop the photoresist. Finally, the samples are hard baked at 120°C for 10 minutes.

Table 1 shows the RIE process conditions for each material. All etches are carried out in a Nexx Cirrus-150RIE at room temperature. After etching, the photoresist is removed using an O<sub>2</sub> plasma. A Dektak profilometer is used to measure the etch depth. AFM is used to measure the surface roughness and LEO982 SEM is used to measure the wall angle.

## Process Conditions

Film	Pressure	Etching Gases	Microwave Power	RF Power
SiO <sub>2</sub>	15 mTorr	15 sccm CF <sub>4</sub>	200 W	200 W
Si <sub>3</sub> N <sub>4</sub>	10 mTorr	10 sccm Ar 15 sccm CF <sub>4</sub>	600 W	100 W
GaAs	10 mTorr	10 sccm Ar 5 sccm CH <sub>4</sub> 15 sccm H <sub>2</sub>	250 W	70 W
InAs	10 mTorr	10 sccm Ar 5 sccm CH <sub>4</sub> 15 sccm H <sub>2</sub>	250 W	70 W

Table 1: RIE process conditions (at RT).

## Results and Discussion:

For semiconductor applications, minimizing surface roughness is essential; the less surface roughness, the better the device's performance. Surface roughness is correlated with etch time: the longer etch time, the more surface roughness. Therefore, it is essential to find high etch rates to optimize device performance.

**Etch Depth versus Etch Time:** Figure 1 shows etch depths versus etch times. All points were repeated several times to ensure accuracy and repeatability. The standard deviations are low, indicating the etch processes are repeatable and consistent. All lines have a linear trend, showing that the materials' etch rates are consistent and independent of time.

Etch rate is calculated by finding the best fit slope, setting the etch depth intercept to 0. The results for calculation show that the etch rates for SiO<sub>2</sub>, Si<sub>3</sub>N<sub>4</sub>, GaAs, and InAs are: 17.14 Å/s, 31.20 Å/s, 4.16 Å/s, and 6.67 Å/s, respectively, with R<sup>2</sup>, or correlation values, 0.9999, 0.979, 0.841, and 0.9864 respectively.

**Etch Rate:** Figure 2 shows point division calculated etch rates versus etch time. Again, the standard deviation bars are low, showing repeatability and consistency. All materials exhibit a 1/Log trend, converging to a finite number. However, due to the graph's scale, it is not easily seen for SiO<sub>2</sub>, GaAs, and InAs. The curves have a 1/Log trend because of chamber conditioning. However, Si<sub>3</sub>N<sub>4</sub> causes concern because of the much higher initial etch rate compared to its converging etch rate. Further investigations need to be conducted on Si<sub>3</sub>N<sub>4</sub>.

Point division etch rate calculations show that  $\text{SiO}_2$ ,  $\text{Si}_3\text{N}_4$ , GaAs, and InAs etch rates converge to  $17.07 \text{ \AA/s}$ ,  $31.17 \text{ \AA/s}$ ,  $4.66 \text{ \AA/s}$ , and  $6.81 \text{ \AA/s}$ , respectively. These values are within  $0.5 \text{ \AA/s}$  of their best fit slope etch rate calculations, showing consistency.

**Surface Roughness:** A preliminary GaAs surface roughness study after etch has been conducted using AFM. The etching conditions are listed in Table 1, with an etch time of 200s. The average surface roughness measured was  $1.73 \text{ \AA}$ , which is promising. Further investigations must be done to try and reproduce this result.

**Wall Angle:** Wall angle for GaAs has been investigated, though only preliminarily. Figure 3 shows a GaAs wafer SEM picture etched for 200s at the same process conditions listed in Table 1. A vertical wall is desired, however, the wall angle measured is between  $75^\circ$  and  $80^\circ$ . Further experiments need to be conducted to improve the wall angle.

### Conclusions and Future Work:

Several properties were characterized for  $\text{SiO}_2$ ,  $\text{Si}_3\text{N}_4$ , GaAs, and InAs in this project. The first was etch depth versus etch time. This showed a linear trend for all materials, with low standard deviation bars. Best fit slope calculations showed that all materials had high etch rates. The second property characterized was etch rate versus etch time. Etch rate was calculated using point division. Results showed that the materials exhibited a  $1/\text{Log}$  trend, converging to a finite number, with low standard deviation bars. The  $1/\text{Log}$  trend is due to chamber conditioning.  $\text{Si}_3\text{N}_4$  etch rate needs to be further investigated due to the higher starting etch rate value in comparison to its converging value.

Preliminary surface roughness and wall angle studies for GaAs were reported. Surface roughness was low at the process conditions studied. Further experiments need to be done to reproduce this result. Wall angle was not as vertical as desired. Process conditions need to be changed to get a vertical wall etch.

### Acknowledgements:

Thanks to Dr. Erli Chen (PI), Dr. Ling Xie (mentor), Mr. John Tsakirgis and the CIMS staff for their mentorship; Dr. Kathryn Hollar, Dr. Robert Graham, Mr. James Reynolds, the program directors and coordinators at Harvard University; the NNIN, REU, NSF, and Harvard University for this opportunity.

### References:

- [1] Rahman, M.; Deng, L.; Wilkinson, C.; van den Berg, J.; J. Appl. Phys. 89, 5 (Feb. 2001).
- [2] Coburn, J.: Plasma Etching and RIE: Fundamentals and Applications.
- [3] Fleming, D.; Geil, R.; Dhar, S.; Han, K.: Plasma Etching (Dec 2000).
- [4] Wolf, S.; Tauber, R.N.: Silicon Processing for the VLSI Era. 1986.

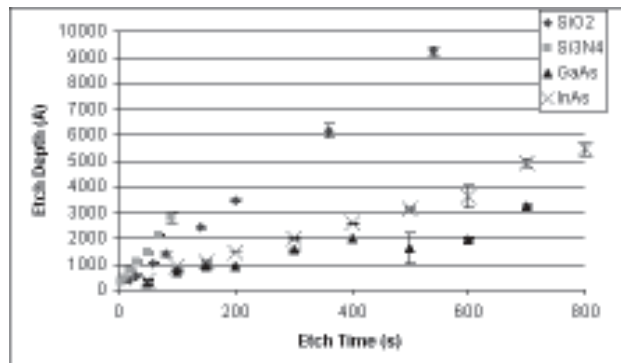


Figure 1: Etch depth versus etch time.

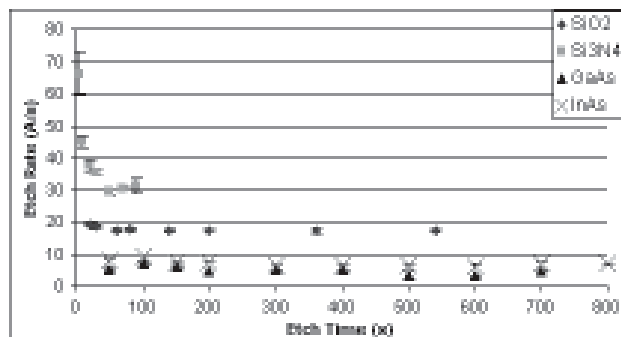


Figure 2: Etch rate versus etch time.

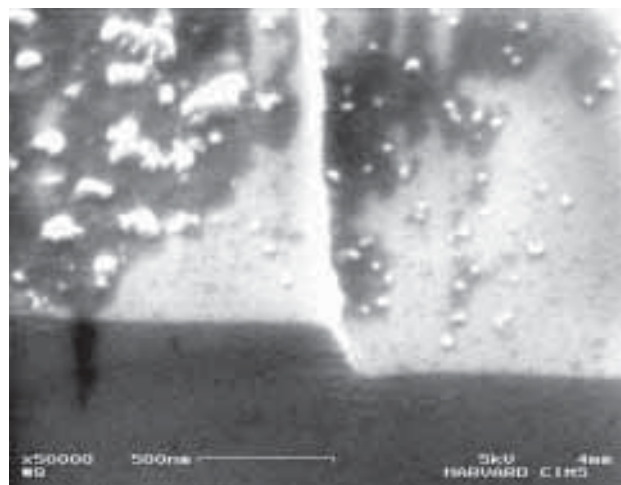


Figure 3: GaAs SEM picture.

# The Novel Formation of Photodefinable Porosity to Fabricate Direct-Write Waveguides for Optoelectronic Applications

Marshall Silver, Chemical Engineering, University of Texas at Austin

NNIN REU Site: Microelectronics Research Center, Georgia Institute of Technology

Principal Investigator: Paul Kohl, School of Chemical and Biomolecular Engineering, Georgia Institute of Technology

Mentor: Jassem Abdallah, School of Chemical and Biomolecular Engineering, Georgia Institute of Technology

Contact: Marshall.Silver@mail.utexas.edu, paul.kohl@chbe.gatech.edu

## Introduction:

As the microelectronics industry continues to follow Moore's law, interconnects have become an obstacle to improving integrated circuit (IC) performance. Optoelectronics solutions are being considered for improving interconnect efficiency. As illustrated in Figure 1, a direct-write waveguide can be fabricated by the creation of microporosity in a rigid spin-on-glass (SOG) matrix via selective decomposition of a templated photodefinable sacrificial material (porogen). The porous regions are less optically dense due to refractive index mixing of the matrix and air.

## Experimental Procedure:

Photoacid molecules can catalyze the decomposition of photodefinable sacrificial polymers by attacking the linkages between the repeating units releasing volatile products [1]. By templating the polymer in a matrix, porosity is formed as air replaces the decomposition products escaping from the matrix. To study the photoacid-catalyzed decomposition behavior of the porogen and determine appropriate processing conditions for the novel direct-write system, thermogravimetric analyses (TGA) were performed on mixtures of sacrificial polymer and photoacid generators (PAGs). As shown in Figure 2, UV-exposed PAG/porogen mixtures were less stable than the unexposed PAG/porogen mixtures, thus indicating that sacrificial polymer in a direct-write system could be selectively decomposed via UV radiation.

However, it was found that all PAGs tested were unstable

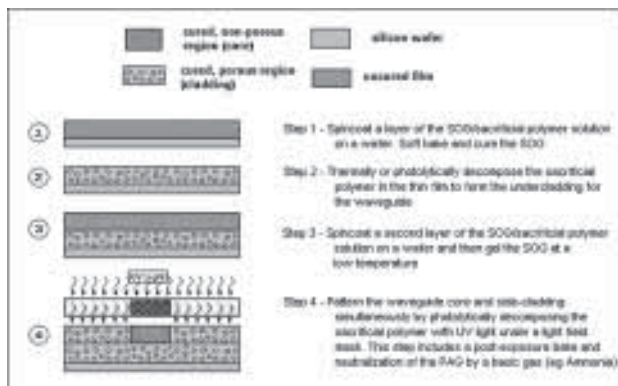


Figure 1: Basic sequence of the direct-write process based on photodefinable porosity.

at the glass transition temperature ( $T_g$ ) of the SOG, meaning that thermally curing the SOG to achieve rigidity would activate the PAG, uniformly decomposing the porogen and precluding selective creation of porosity. To avoid blanket decomposition of the sacrificial polymer, the matrix was hardened below the  $T_g$  of the SOG. This was achieved by the use of bases, which catalyzed the hydrolysis of silane bonds into highly reactive silanol bonds. The silanol groups condensed to form crosslinked siloxane bonds, hence increasing the film rigidity [2].

FTIR spectroscopy was used to track the formation of network siloxane bonds in 0.7-1.2  $\mu\text{m}$  thick gelled films. In the FTIR spectrum of the SOG matrix, two separate stretch peaks centered at  $1130\text{ cm}^{-1}$  and  $1070\text{ cm}^{-1}$  correspond to the Si-O caged and Si-O networked bond energies respectively [3]. As the extent of gelation increased, the network siloxane stretch peak grew larger and the extent of gelation was evaluated by comparing the relative area of the siloxane peaks (the Si-O cage/network ratio) [4].

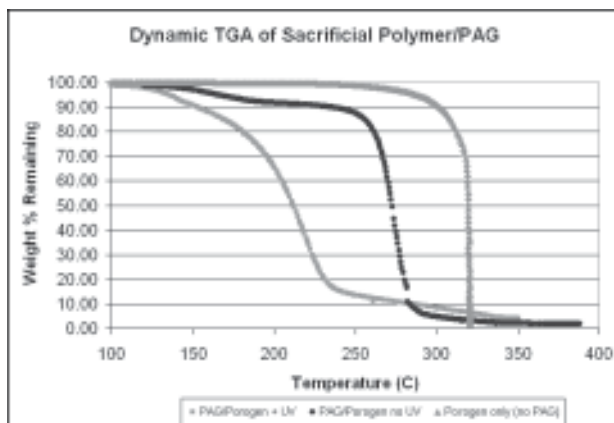


Figure 2: Dynamic TGA for determining PAG compatibility.

Nanoindentation tests were performed after the FTIR study in order to confirm the rigidity of the SOG matrix after different gelation treatments. The results of both studies, shown in Figure 2, showed that the reduced modulus ( $E_r$ ) of gelled films increased as the cage/network peak area ratio decreased. This confirmed that as the relative amount of networked siloxane bonds increased during gelation, the SOG matrix did indeed become more rigid.

Two processes using two different photobase generators

were developed to gel the SOG in a direct-write system without the activation of any PAG. For the first process, PBG 1 was mixed into solutions with the SOG matrix and spin-coated to form films. The PBG1 species in these films were thermally activated to release free base by heating films at 160-170°C for 30 minutes. TGA results showed that at 170°C, only trace amounts of the PAG were activated, indicating that PBG1 could be activated without activating the PAG.

In the second process, PBG 2 and a photosensitizer were mixed into solutions with the SOG matrix and spin-coated to form films. The films were exposed to 5 J/cm<sup>2</sup> of filtered 365 nm radiation, followed by a 30 minute post-exposure bake (PEB) at 120°C and then a 30 minute bake at 170°C to volatilize residual photobase. The PAG used is very weakly sensitized at 365 nm [5], hence in principle a compatible direct-write process involving mid-UV initiated gelation followed by 248 nm (DUV) initiated acid-catalyzed decomposition of sacrificial polymer is possible.

### Results and Conclusions:

To test if porosity could be selectively produced, the films were exposed to 5 J/cm<sup>2</sup> of DUV radiation after gelation and then post-baked at 170°C for 1 hour in order to decompose the sacrificial polymer. Half of the wafer was covered during the exposure step so that the exposed and unexposed regions could be compared. The remaining PAG was deactivated by exposing the entire wafer to 1 J/cm<sup>2</sup> DUV radiation and immediate neutralization with a basic vapor. Finally, a 30 minute bake at 250°C was used to volatilize the residual reactants that might degrade the optical properties of the film over long periods of time. An ellipsometer was used to determine the refractive index (RI) of the film after each processing step. As shown in Figure 4, there was a refractive index difference of 0.0583 between the exposed and unexposed parts of the wafer for a dual-tone system with PBG 1.

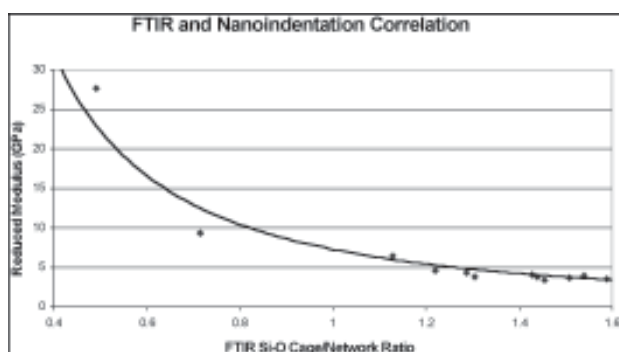


Figure 3: Comparison of FTIR and nanoindentation experimental results.

For a dual-tone film with PBG 2, the RI difference between the exposed and unexposed sides was only about 0.0153. This suggests that not all of the porogen was decomposed. Processing conditions for films containing PBG2 must be modified to increase their final RI difference.

The ability to selectively lower the refractive index of the SOG films suggests that, in principle, a direct-write waveguide can be made using a photomask to define waveguide patterns in a dual-tone process. Greater RI differences between core and cladding regions could be achieved by increasing porogen loading, which will require optimization of process conditions.

Future testing of the resolution limitations of photo-defined patterns must be done to ensure that features can be patterned at sizes useful to waveguide fabrication. The optical and mechanical properties of porous SOG waveguides must be thoroughly tested to determine the viability of this system as an alternative to current direct-write waveguides.

### References:

- [1] Joseph Paul Jayachandran et al, J. Microelectromechanical Systems (2003), vol. 12, No.2, 147-159.
- [2] Leo Sommer, "Stereochemistry, Mechanism and Silicon," McGraw-Hill. New York (1965).
- [3] Wei-Chih Liu, "The structural transformation and properties of spin-on poly(silsesquioxane) films by thermal curing," J. Non-crystalline Solids (2002), vol. 311, 233-240.
- [4] F. Iocopi et al, "Studies on XLK film characterization and integration in copper damascene process," Materials Research Society: Advanced Metallization Conference (2000), 287-293.
- [5] S. Peter Papas et al, Polymer Photochem. (1984), v.5, 1-22.

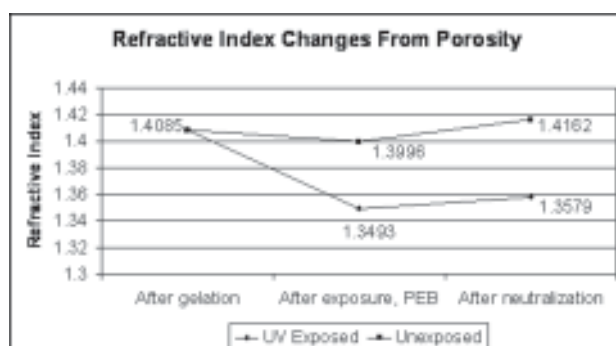


Figure 4: Refractive index values for two halves of a wafer of the PBG 1 dual-tone system.

# Applications of Nanofluidic Devices in Chemistry

Gregory J. Slavik, Chemistry, Valparaiso University

NNIN REU Site: Solid State Electronics Laboratory, University of Michigan, Ann Arbor

Principal Investigator: L. Jay Guo, Electrical Engr. & Computer Science, University of Michigan Ann Arbor

Mentor: Li-Jing (Larry) Cheng, Electrical Engr. & Computer Science, University of Michigan Ann Arbor

Contact: guo@eecs.umich.edu

## Abstract:

Nanofluidic channels have many uses in the chemical field, including site specific combinatorial synthesis, macro- and bio-molecular analysis, and other “lab on a chip” applications. The objective of this research is to fabricate arrays of nanochannels designed to facilitate the transport of aqueous ionic solutions by adapting a form of the nanoimprinting technique. Nanoimprinting relies on deforming the resist material under elevated pressure and, typically, temperature to replicate a mold surface.

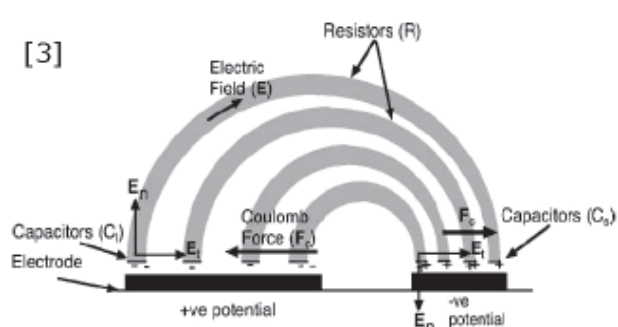
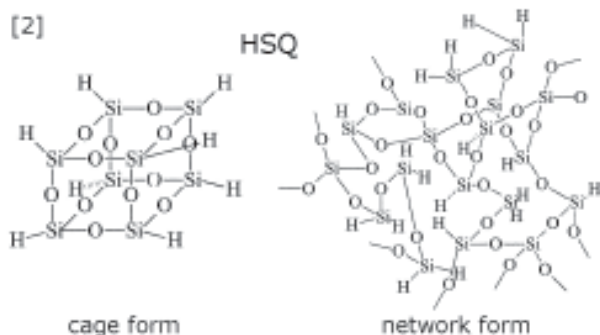
Since the contribution of capillary force is insufficient for extended channel lengths, the device is designed to employ the principle of asymmetric AC-field electroosmosis to drive fluid flow. The fabrication also incorporates the non-traditional resist of hydrogen silsesquioxane (HSQ). This material was selected due to its resulting hydrophilic surface property and unique ability to be imprinted at room temperature. This work is dedicated to developing and optimizing the processing conditions for fabricating arrays of nanochannels in HSQ capable of active pumping.

## Introduction:

Scaling down of fluidic channel dimensions and the ability to construct fluidic devices in quantity can lead to new types of analyses and applications. Many of their exclusive uses stem from the high amount of surface interaction per unit volume of the mobile medium. In some cases confinement on the molecular level can be achieved. The challenge of this study lies in the fabrication and adaptation of established processes to an actively pumped device consisting of a regular array of nanofluidic channels. The resulting design and process employs two key principles: nanoimprint lithography (NIL) and asymmetric AC-field electroosmosis.

Although embossing has been around for ages, the practice of nanoimprinting is regarded as a promising technique for reproducing designs on the nanometer level. The primary motivation for NIL is the creation of smaller feature sizes on semiconductor chips. Much like traditional photolithography, it is a high throughput method of replicating structures once an initial pattern is established. Nanoimprint lithography is, however, a mechanical means of patterning. This gives it several distinct advantages: it can be accomplished without highly specialized, expensive equipment in a relatively short amount of time and it can overcome the limitations of light wavelengths to reproduce extremely small features [1]. NIL methods are applied to creating the channel structures from resist material in this project.

Though highly unconventional for this fabrication method, hydrogen silsesquioxane (HSQ) was selected as the deformed resist for properties favorable to this particular application. Hydrogen silsesquioxane is an inorganic polymer with a repeating unit of  $[\text{HSiO}_3/2]$ , primarily used for its low dielectric constant and, more recently, advantageous behavior as a resist for electron beam lithography. The main issue with following traditional NIL procedures with polymeric materials as the resist material is that the resulting surfaces are often hydrophobic. Structures in HSQ resemble hydrophilic silica surfaces on the molecular level. Lab observations suggest the retention of solvent in HSQ solid is responsible for its ability to be imprinted during a temporary viscous state. As it turns out, this permits replication to be achieved at room temperature, a very unusual trait for the nanoimprint technique. This material is also capable of redistributing and cross-linking from primarily the cage form to the more mechanically stable network form at elevated temperature [2].



Since the device is intended to transport aqueous solutions, it can be designed to take advantage of electro-osmosis to implement active pumping. First experimentally demonstrated by Brown, Smith, and Rennie on the micron level in the configuration applied here, asymmetric AC-field electro-osmosis induces a double layer of ionic charges to form along the electrode surfaces and relies on Coulombic forces on ions to move the bulk of water [3]. The prevention of gas formation from the electrolysis of water necessitates applying low AC potential of fairly high frequency, and electrode size asymmetry accounts for net fluid flow. Fabrication procedures were developed to make use of established processes, including electron beam lithography, for patterning interdigitated parallel electrode arrays on silica substrates.

**Procedure:**

Approximately 300 nm of HSQ was spin-coated on a substrate, the preparation of which will be described later in this section, using a 12% by weight solution in methyl isobutyl ketone (MIBK). This film could be verified with the following metrology tools available in the lab, used during spin characterization: DekTak 6M stylus profiler, AutoEL ellipsometer, and Nanospec 6100 optical instrument.

The sample was immediately imprinted on an in house apparatus with a uniform gas pressure of 1000 psi at 25°C for 1 minute against a surfactant coated silicon mold and later heated slightly at 80°C to expel any remaining solvent. An anisotropic CHF<sub>3</sub> / CF<sub>4</sub> reactive ion etch (RIE) may be used to remove residuals. Replication was evaluated by scanning electron microscopy on a FEI Nova Nanolab.

Sealing of the channels can be accomplished with a slight modification of the nanoimprint process. The replicated diffraction grating in HSQ acts as a mold for a low imprint depth into about 200 nm of HSQ deposited on a surfactant coated silicon wafer under a pressure of 600 psi.

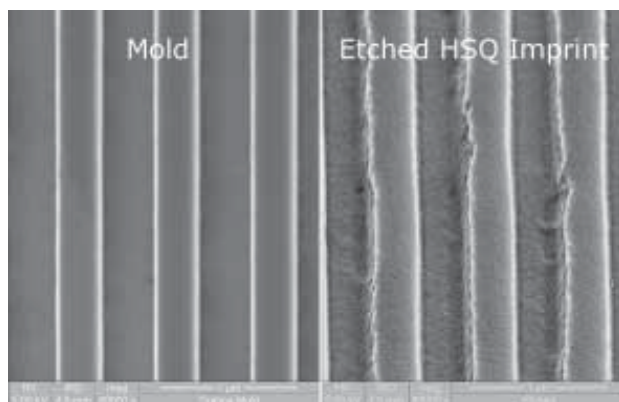


Figure 3

The initial substrate would be prepared by evaporating 50 Å Ti / 2000 Å Au over a resist on silica substrate that would have undergone electron beam lithography of the CAD electrode design shown in Figure 4 and chemically lifting off the unexposed regions.

**Results and Conclusion:**

The fabrication proceeded despite forgoing the substrate preparation with electrodes described in the previous section due to an extended e-beam equipment outage.

Unfortunately, the nanochannels were not tested due to time constraints and other factors, mainly involving the development of a procedure by which HSQ could be reliably imprinted, which in itself was a valuable accomplishment. However, realization of the total design would likely be relatively fault tolerant and efficient, considering the choices made.

**Future Work:**

Agreement among the literature studied regarding electroosmosis in microfluidics provides evidence that fluid velocity and, thus, effectiveness of such devices increases as channel dimensions decrease. The progress of work done here, therefore, has much promise in future applications.

**Acknowledgements:**

I would like to express my appreciation for the direction of Dr. L. Jay Guo, the contributions of Li-Jing (Larry) Cheng, Phillip Choi, and Xing Cheng, and funding from NNIN and the NSF.

**References:**

- [1] S. Y. Chou, P. R. Krauss, W. Zhang, L. Guo, and L. Zuang: J. Vac. Sci. Technol. B 15(6), 2897 (1997).
- [2] C. Yang and W. Chen: J. Mater. Chem. 12, 1138 (2002).
- [3] A. B. D. Brown, C. G. Smith, and A. R. Rennie: Phys. Rev. E 63, 4129 (1996).

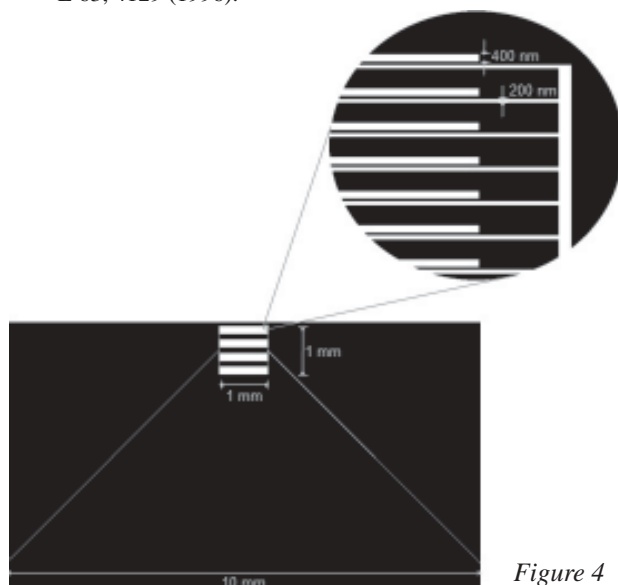


Figure 4

# Controlled Neuron Growth By Patterned Protein Gradients

Margo Smith, Biology, Emphasis in Exercise Physiology, Chapman University

NNIN REU Site: Nanofabrication Center, University of Minnesota, Twin Cities

Principal Investigator: Dr. David Pui, Department of Mechanical Engineering, University of Minnesota

Mentors: Drs. Christopher Stipe and Seong-Chan Kim, Mechanical Engineering, University of Minnesota

Contact: smith178@chapman.edu, dyhpui@tc.umn.edu

## Abstract:

Neuron guidance is mainly controlled by the growth cone, located at the end of an axon. Extra-cellular components, including proteins, control the directional growth of these neurons; this allows for the possibility to manipulate extra-cellular factors to aide in the accurate rewiring of damaged neurons.

The objective of this project is to create a standard platform on which to study neuron guidance by protein gradients using an electrospray system. The electrospray system is first studied using polystyrene latex (PSL) particles. This method deposits a uniform distribution of particles on a substrate and can be controlled to spray at constant velocities or accelerations. Neuron cells from extracted dorsal root ganglia (DRG) of fetal chickens are used to observe growth patterns under varying conditions, including various protein gradients and the presence of different proteins.

## Introduction:

In the United States, there are approximately 200,000 people with spinal cord injuries, with another 11,000 new injuries each year. The majority of injuries occur between the ages of 16 and 30; therefore the preponderance of patients live many years paralyzed. Currently, there are no treatments for such injuries, resulting in a push to find a regeneration technique.

Control of immature neuron growth is instigated at the end of the axon in a region known as the growth cone. Within the growth cone are two sensory structures: filopodia, finger-like projections, and

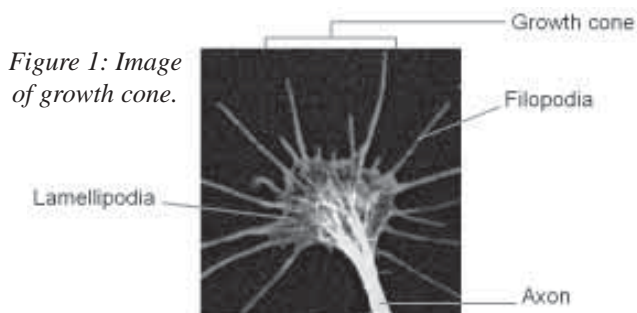


Figure 1: Image of growth cone.

lamellipodia, web-like structures (Figure 1). These structures sense the presence of various extracellular components, such as proteins. These proteins either repel or attract axon growth, in processes known as chemorepulsion and chemoattraction, respectively. By controlling the location, concentration, and gradient of the guidance proteins, the directional growth of the neurons can be controlled also.

An electrospray system is one method by which particle location can be controlled. A minute amount of solute is sprayed and deposited onto a surface with the aid of a strong electric field present under the surface. The repelling charges of the particles prevent agglomeration on the substrate surface. Guidance proteins are electrosprayed onto a pattern of extra cellular matrix molecules that are micro-contact printed onto the substrate. Combining these two techniques creates a guided pathway on which the neurons grow. The objective of this project is to use the attraction properties of certain proteins deposited by the electrospray system to guide neuron growth.

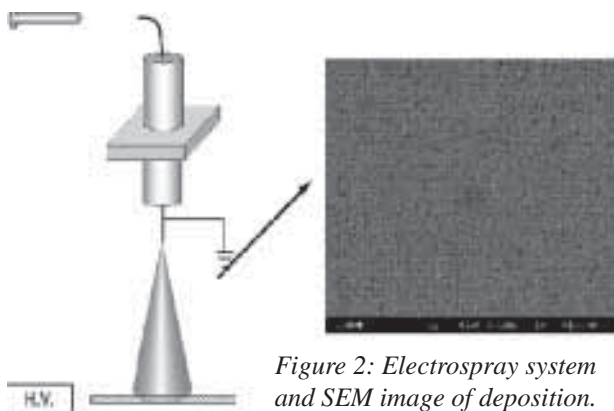


Figure 2: Electrospray system and SEM image of deposition.

## Methods:

The electrospray system was first tested using a 57 nm PSL particle solution at a concentration of 10 drops PSL/10 mL deionized water. The solution was pumped from a syringe into a capillary with a constant flow rate. Under the capillary, a stencil taped

to a silicon wafer was placed on a plate with a charge of 5-7 kV, producing a uniform distribution of particles. This plate was then placed on a computer-controlled stage, with the capability of moving the substrate at either a constant velocity or constant acceleration (Figure 2). The stage was moved at constant velocities of 25  $\mu\text{m/s}$ , 50  $\mu\text{m/s}$ , and 75  $\mu\text{m/s}$ , and constant accelerations of 1.20  $\mu\text{m/s}^2$ , 1.98  $\mu\text{m/s}^2$ , and 2.75  $\mu\text{m/s}^2$ .

Dorsal root ganglia (DRG) were harvested from embryonic stage nine chicken fetuses. Half of the DRGs were chemically dissociated into individual neurons. Both the DRGs and dissociated neurons were placed on a silicon wafer stamped with lines of laminin 1  $\mu\text{m}$  wide. The neurons grew for 2 days in an incubator.

### Results:

Electron microscope analysis of the electro sprayed silicon wafers showed that the distribution of particles was uniform with little agglomeration (Figure 2). The deposited concentration of the PSL particles was determined by converting the images to black and white and analyzing the fraction of each color with an intensity histogram software program. The samples were also analyzed using a fluorescent microscope. The fluorescent intensity was measured for each sample to determine the concentration gradient qualitatively. The samples generated by moving the stage at a constant acceleration created a non-linear gradient described by Equation 1, which determines the surface concentration at any point  $x$  on the line (Figure 3).

Analysis of the directed neuron growth showed no neuron growth for either the DRGs or dissociated neurons.

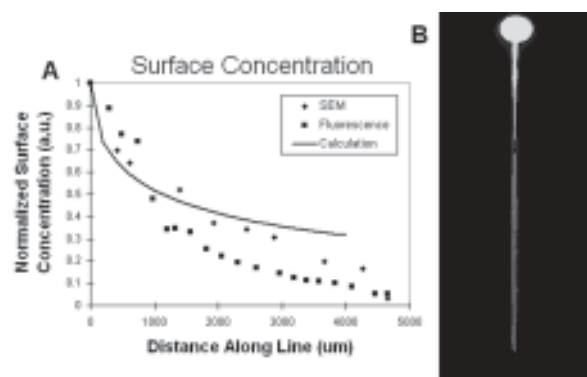


Figure 3: (A) Comparison of SEM and Fluorescent samples with calculation; (B) Fluorescent image of sprayed line.

$$\# / \mu\text{m}^2 = \frac{C \cdot Q}{A} \left( \frac{\sqrt{V_0^2 + 2ax + 2ad} - \sqrt{V_0^2 + 2ax}}{a} \right)$$

Equation 1:  $C$ =concentration of solution,  $a$ =acceleration rate,  $Q$ =flow rate of solution,  $d$ =diameter of sprayer,  $A$ = spray area,  $x$ =distance along line,  $V_0$ =initial velocity of stage.

### Conclusions:

The electro spray system has the capability to create uniform concentration patterns or nonlinear concentration gradients; however, a method to create a linear gradient is still needed. These gradients all contain a uniform deposition with little agglomeration of particles.

Directed neuron growth was not successful; however, we believe this was due to contamination of the sample, which allowed for the growth of a fungus. Previous experiments show that neurons are able to grow on stamped lines of the extracellular matrix molecule laminin, as seen in Figure 4.

Future work on this project includes the development of a method to spray a linear concentration gradient as well as the ability to spray proteins. As of now, the spraying of proteins has been unsuccessful, possibly due to the proteins being denatured by the strong electric field. Once these technical difficulties are solved, this approach will be useful for studying the guided growth of neurons.

### References:

- [1] Mueller, Bernhard K. "Growth Cone Guidance: First Steps Towards a Deeper Understanding." *Annu. Rev. Neurosci.*, 22:351-388. (1999)
- [2] Rosentreter, S.M.; Davenport, R.W.; Loschinger, J.; Huf, J.; Jung, J.; Bonhoeffer, F. "Response of Retinal Ganglion Cell Axons to Striped Linear Gradients of Repellent Guidance Molecules." *J Neurobiol.* 1998 Dec;37(4):541-62. (1998)
- [3] Rangappa, N.; Romero, A.; Nelson, K.D.; Eberhart, R.C.; Smith, G.M. "Laminin-Coated Poly(L-lactide) Filaments Induce Robust Neurite Growth While Providing Directional Orientation." *J. Biomed. Mater. Res.* 51:625-634, 2000.

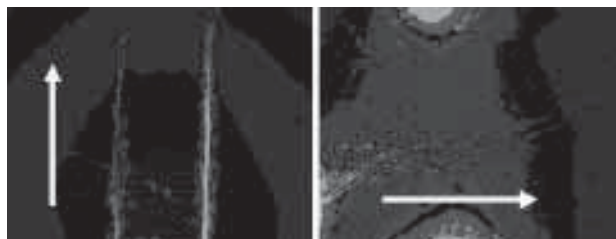


Figure 4: Neuron growth along laminin lines.

# Surface-Enhanced Raman Scattering Substrates: Highly Sensitive Sensors for the Detection of Adsorbate Molecules

Tina Soumahoro, Bio-Chemistry, Rosemont College

NNIN REU Site: Penn State Center for Nanotechnology Education and Utilization, Pennsylvania State University

Principal Investigator: David Allara, Department of Chemistry, The Pennsylvania State University

Mentor: Gregory S. McCarty, Engineering Science and Mechanics, The Pennsylvania State University

Contact: Tina868@excite.com, dla3@psu.edu, gmccarty@enr.psu.edu

## Abstract:

Surface-enhanced Raman spectroscopy (SERS) is one of the most sensitive tools for the detection of adsorbate molecules on roughened metal surfaces. The roughened metal surface produces a large enhancement to the Raman scattering signal. Here, SERS substrates consisting of Au features on  $\text{SiO}_2/\text{Si}$  wafers were manufactured using electron-beam lithography in combination with self-assembled multilayered resists. The initial Au posts ( $\sim 100$  nm in diameter with 300 nm spacing) were defined by thermal deposition of a Cr/Au layer onto developed e-beam samples, followed by a lift-off process. Subsequent daughter structures were defined by alternating self-assembled monolayers of an alkanethiol and coordinated metal ions to produce features with  $\sim 20$  nm spacing.

To test the substrates, a monolayer of 4-nanobenzenethiol (4-NBT) molecules were adsorbed on the nanofabricated Au Raman substrates. Then a confocal Raman optical microscope with an incident  $\text{Ar}^+$  laser of 514 nm was utilized to collect the spectral data on the 4-NBT adsorbed on the SERS substrates.

## Introduction:

The SERS techniques augment Raman signals through both electromagnetic enhancement (EM), associated with

the roughened metal surface and a chemical (CHEM) factor, due to the electronic coupling of molecules adsorbed on the roughened metal surfaces. Here a combination of electron-beam lithography, capable of producing patterns of features at 100 nm or less, and molecular lithography, which allows for precise control of the spacing between the features by selective placement and controlled thickness of self-assembled monolayers (SAMs), are used to nanofabricate Raman substrates. The gap spacing between the features can be estimated by the number of SAMs deposited on the parent structures.

Reported here are the Raman peaks of the 4-NBT adsorbed in the nanoscale hierarchical features.

## Procedure:

The initial parent structures were formed using electron-beam lithography: 3"  $\text{SiO}_2/\text{Si}$  wafers were coated with  $\sim 200$  nm of polymethyl methacrylate (PMMA) resist.

Four quadrants of the coated wafer underwent electron-beam exposure with a dose-array of 8 to 9 patterns. Single quadrant-samples were developed one at a time in a 1:3 (MIBK:IPA) PMMA development solution for 1.5 minutes for the lift-off process. The quadrant-sample underwent reactive ion etching with oxygen plasma, for ten seconds, to remove any access exposed PMMA resist. A layer of Cr

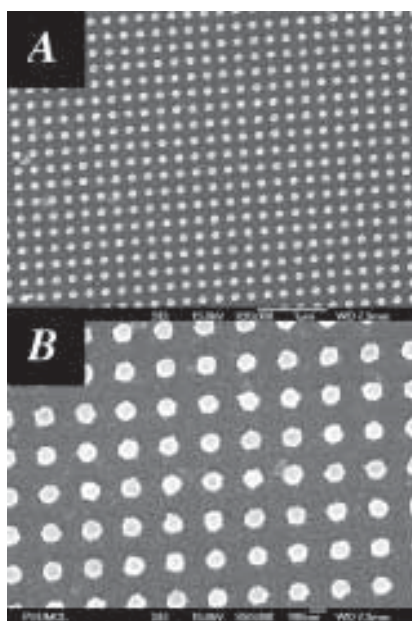


Figure 1: FESEM of nanofabricated SERS-substrate. A) Series of posts fabricated using e-beam lithography. B) The substrate after fabrication. The  $\sim 20$  nm gaps around the posts are apparent.

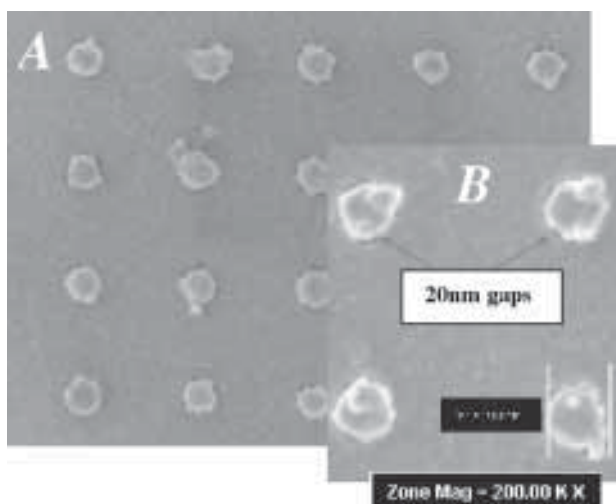


Figure 2: FESEM images of a nanofabricated SERS-substrate. The features seen here are 116 nm in diameter with 250 nm period. A small separation around the posts is apparent.

(5 nm) was electron-gun evaporated onto the developed samples as an adhesion layer prior to the direct-vapor deposition of a Au (55 nm) layer. The unexposed PMMA resist, with the unwanted Au areas, were dissolved in methylene chloride. The lift-off reaction was between 40 minutes to an hour at 200°C with 15 minutes of ultrasonic agitation to quicken the development time and improve the resolution of the features [2]. The nanoscale features were examined under a FESEM to ensure a successful lift-off and take measurements of the Cr/Au posts (~ 100 nm).

Once the parent features were obtained, subsequent daughter structures were defined by molecular lithography. The Si substrates, with the parent structures, were immersed in a 1 mM solution of 16-mercaptohexadecanoic acid in 95% ethanol for 40 minutes to form a self-limiting monolayer exclusively on the Cr/Au features, and not on the SiO<sub>2</sub>/Si substrate. The samples were removed from the C16 solution, rinsed with acetone, then ethanol. Next, the substrates were immersed into a 1 mM solution of copper perchlorate in ethanol for 10 minutes to allow the coordination of the Cu<sup>+</sup> ions with the carboxylate terminal of the alkanethiol.

Ten layers of SAMs of C16 (~ 2 nm long) were deposited onto the initial parent structures. Then a 2nd layer of Cr/Au (5 nm and 15 nm, respectively) was deposited onto the SAMs resist. The ACT935 chemical-striper removed the SAMs resist film to yield SERS-substrates with ~ 20 nm gaps. To evaluate the enhancement factor (EF), the SERS-substrates were incubated in a 1 mM solution of 4-nitrobenzenethiol in 95% ethanol for 24-hours and characterized by a confocal Raman optical microscope with a 514 nm Ar<sup>+</sup> laser.

### Results and Conclusion:

Figure 1 shows two FESEM images of a nanofabricated SERS-substrate. Figure 1A shows a series of posts fabricated using e-beam lithography. The Cr/Au posts are ~ 116 nm in diameter with a 250 nm periods. Figure 1B shows the substrate after fabrication. The ~ 20 nm gaps around the posts are apparent.

Figure 2 shows high resolution FESEM images of a nanofabricated SERS-substrate. The features seen here are 116 nm in diameter with 250 nm period. A small separation around the posts is apparent.

Figure 3 shows a Raman spectrum collected from bare gold with adsorbed 4 NBT and a Raman spectrum collected from a SERS substrate with no chemical modification. The bare gold with our surface-enhancement shows high fluorescence with adsorbed 4-NBT. The second spectrum is the SERS-substrate without 4-NBT.

Figure 4 shows a spectrum collected from the nanofabricated SERS-substrate with adsorbed 4-NBT. A number of peaks are apparent including a silicon peak at

540 cm<sup>-1</sup>, and peaks at 1140 cm<sup>-1</sup>, 1330 cm<sup>-1</sup>, and 1570 cm<sup>-1</sup> from the 4-NBT.

### Acknowledgements:

The National Science Foundation; David Allara; Group members Gregory McCarty, David Dwight, Edward Basgal, An Cheng; Penn State Nano-fabrication Center staff.

### References:

- [1] M. E Anderson, L. P. Tan, H. Tanaka, M. Mihok, H. Lee, M. W. Horn, P. S Weiss. *J. Vac. Sci. Technol B* 21( Nov/Dec 2003): 3116-3119.
- [2] L.Gunnarsson, E.J.Bjorneld, H.Xu, S.Peronis, B.Kasemo, and M. Kall. *Applied Physics Letters* 78, #6 (2001): 802-804.
- [3] McCarty, Gregory S., *Nano Letters*.

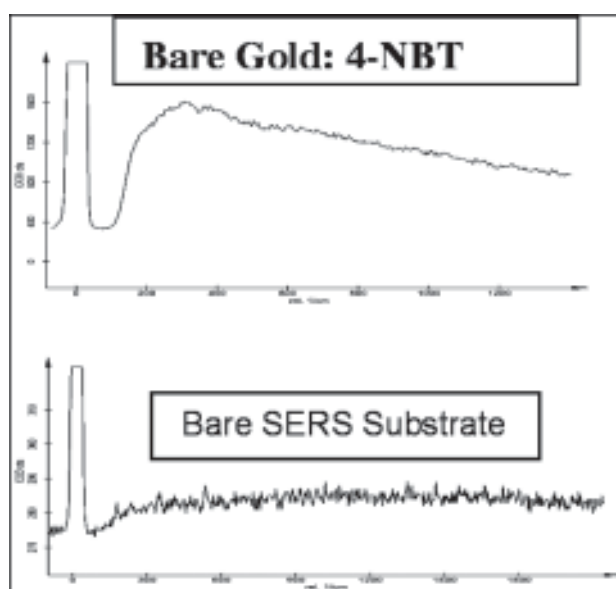
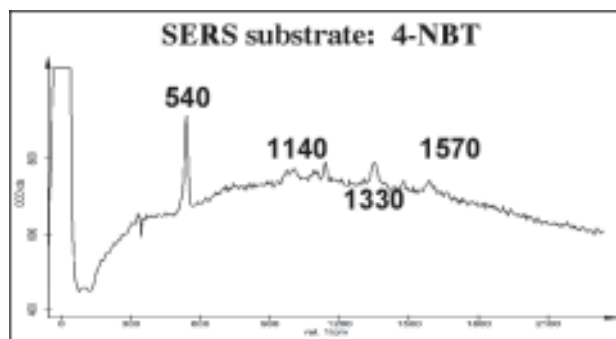


Figure 3, above: A Raman spectrum collected from bare gold with adsorbed 4 NBT and a Raman spectrum collected from a SERS substrate with no chemical modification.

Figure 4, below: A Raman spectrum collected from the nanofabricated SERS-substrate with adsorbed 4-NBT.



# MEMS Based Real-Time Non-Invasive Biological Cell Diagnostics

Tabitha Staniszewski, Biomedical Engineering, North Carolina State University

NNIN REU Site: Penn State Center for Nanotechnology Education and Utilization, Pennsylvania State University

Principal Investigator: Aman Haque, Mechanical Engineering, Pennsylvania State University

Mentor: Amit Desai, Mechanical Engineering, Pennsylvania State University

Contact: tastanis@ncsu.edu, mah37@psu.edu

## Introduction:

Scientists have been trying for years to learn about the inner functioning and mechanisms of cells, and why cells behave the way they do. One major area of research is the reaction of cells to mechanical forces. However, scientists often come across the problem of knowing for certain when a cell is actually reacting to the applied force.

Many scientists have explored the use of impedance measurement technology to characterize normal cell growth and function in culture [1, 2]. We propose that the use of this same technology can be used in tandem with the experimental loading of the cell to tell us whether or not the cell is reacting to the applied forces and the extent of its reaction. These data will prove useful in future research involving *in vitro* chondrocyte formation as well as a better understanding of how sudden impact on cells affects the functioning of those cells.

## Fabrication Process:

A silicon wafer coated with silicon dioxide was obtained. Using the thermal evaporation process of a Kurt Lesker E-Gun/Thermal Evaporator, a thickness of 1000Å of Aluminum was then evaporated onto the wafer to provide electrical contact pads with the oxide as the insulating layer.

Photolithography was then performed using a mask specifically designed for our needs with various electrodes patterned to our specifications. A Shipley 3012 photoresist was used to coat the wafer with 1.5 μm of resist. The wafer was exposed in a Karl Suss MA6 contact aligner for 6.3s. It was then placed in CD-26 developer solution for 50s. The wafer was then hard baked for two minutes at 110°C to preserve the patterned resist. The wafer was then etched using ACT 935 Aluminum etch for approximately 5 min or until the oxide layer became visible.

## Experimental Setup:

Mouse myeloma cells were cultured in Delbeco's

Modified Eagle Medium until they reached confluency. Approximately 1 mL cell-media solution was then placed on the electrodes of the MEMS device and, using micromanipulators, a cell was positioned between two electrode tips. The electrodes were then placed in a parallel circuit to a variable capacitor (between 2 and 6 pF). An AC power source (variable but maximum voltage of 0.4V), an impedance monitor, a resistor (330 Ω) and inductor (100 μH) were connected in series to the electrodes and capacitor (see Figure 1). One of the micromanipulators (sharp probe tip) was positioned to contact the cell and the other was positioned to contact an electrode.

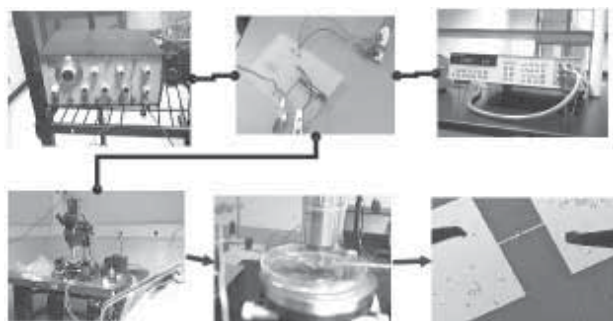
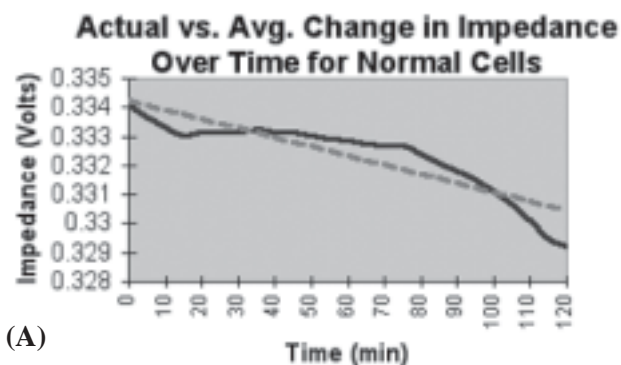


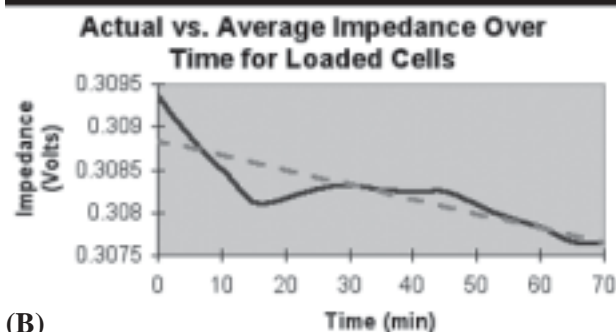
Figure 1: Experimental setup and images as seen through microscope (lower right).

The AC power source in the circuit is then adjusted to match the resonance frequency of the cell. The system was allowed to equilibrate for approximately ten minutes. The cell was then placed under load using the sharp probe tip. The impedance values for the cell were then recorded every five minutes for a two hour time span (see Figure 2). A sample of only media was also run to ensure that the media was electrically stable and that the devices were running properly.

Graph (A) shows the data collected from the cell under control conditions. This was done to rule out any ambient conditions that might have affected the cell and to compare the loaded cell's electrical behavior to that of the control. Graph (B) shows the loaded cell. The data collected from the loaded cell



(A)



(B)

Figure 2: A) Data for cells in control conditions.  
B) The loaded cell.

and the control cell is compared not only using the average impedance changes (the dotted line in the graphs) but the initial change as well.

### Results and Conclusions:

We found that the cells do in fact react internally to mechanical loading. The impedance values in both the average calculations and actual data points were dramatically different. Data we collected led us to the conclusion that the cell reacts initially to the load and then over time becomes accustomed to the load and approaches normal cell function. This is consistent with data found in previous studies (see Figure 3) [3]. These data show that in order for mechanical loading to effectively change a cell's behavior, the length of the loading and how often the cell is loaded must be carefully monitored and adjusted to achieve the desired results. While we did not have time to further study how the length or frequency of load and rest times affect the cells longevity and health, these results were encouraging.

Future work might include a refining of the fabrication process of our electrodes and possibly successful fabrication of cantilevers of various

specifications in order to determine whether different types of loading affect the cell in different ways. We would also like to study a dynamic loading situation as well as various displacement levels of the cell. Long term goals include applying this technology to stem cell work and hopefully learning more about why stem cells differentiate the way they do.

### Acknowledgements:

This work was performed in part at the Penn State Nanofabrication Facility, a member of the NSF's National Nanofabrication Infrastructure Network. Special thanks to: Amit Desai, Jennifer Looi, Benedict Samuel, Aman Haque, Ph.D., M.B.A.

### References:

- [1] DC Walker, BH Brown, DR Hose, RH Smallwood. Modelling the electrical impedivity of normal and premalignant cervical tissue. *Electronics Letters Online* 36(19). 2000.
- [2] J Wegener, CR Keese, I Giavier. Electric Cell-Substrate Impedance Sensing (ECIS) as a Noninvasive Means to Monitor the Kinetics of Cell Spreading to Artificial Surfaces. *Experimental Cell Research* 259:158-66. 2000.
- [3] AG Robling, DB Burr, CH Turner. Recovery periods restore mechanosensitivity to dynamically loaded bone. *The Journal of Experimental Biology* 204:3389-99. 2001.

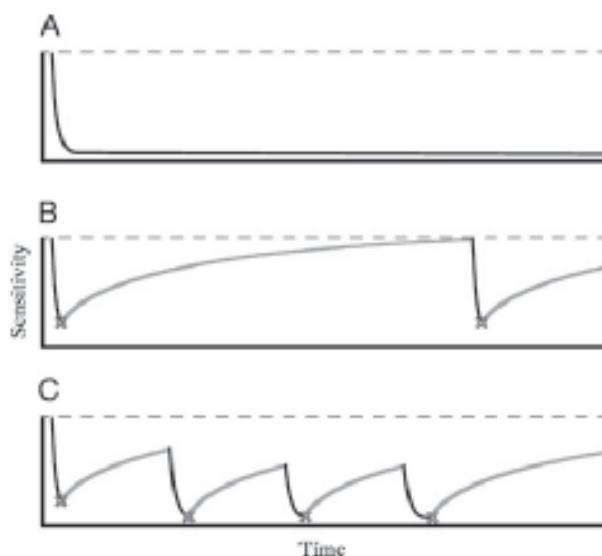


Figure 3: Data from previous study [3].  
Graph is the comparable load regimen.

# Synthesis and Characteristics of ZnO Nanowires

Nicole Staszkievicz, Electrical Engineering, University of Florida

NNIN REU Site: Solid State Electronics Laboratory, University of Michigan, Ann Arbor

Principal Investigator & Mentor: Dr. Jamie D. Phillips,

Electrical Engineering and Computer Science, University of Michigan Ann Arbor

Contact: stasz24@yahoo.com, jphilli@eecs.umich.edu

## Abstract:

Zinc Oxide (ZnO) nanowires hold a promising key to the world of nanotechnology. With its wide-band gap (3.37 eV), high breakdown strength, and large excitonic binding energy, ZnO possesses several advantages for use in electronic and photonic devices. Nanowires hold promise for future electronic devices and novel sensing devices. Pulsed laser deposition (PLD) has been used to deposit thin films, but its use in growing nanowires has been largely unexplored. This paper discusses the growth possibilities of ZnO nanowires using the PLD system.

In this work, ZnO materials obtained by pulsed laser deposition were studied to determine the potential for nanowire formation. ZnO was deposited (26 kV, 6 Hz, 350 mJ) on a variety of substrates including glass and sapphire. Depositions at 500 and 600°C were performed to examine the effects of temperature on growth. The effects of pressure were tested through depositions at 3.2 mTorr and 31.8 mTorr, at 500°C. The use of nanoscale metal clusters obtained by annealing thin films enabled us to study possible formations of nucleation sites for ZnO nanowires. Scanning electron microscopy (SEM) was used to gain knowledge of growth structure.

## Introduction:

ZnO is a promising material for the realization and future of nanotechnology. With its wide band-gap (3.37 eV), high excitonic binding energy, and high breakdown strength, ZnO can be utilized for electronic and photonic devices, as well as for high-frequency applications. The availability of a native substrate and the potential for room-temperature operations opens the door to ZnO applications including chemical sensors and subscale electronic circuits.

Currently, pulsed laser deposition (PLD) is used to deposit thin films on a variety of substrates. PLD consists of a vacuum chamber containing a target material and substrate, mounted approximately 5 cm from the target. A KrF Excimer laser ( $\lambda = 248$  nm) ablates the target material at high energy (350 mJ) and repetition (6 Hz) in the presence of ambient oxygen to form a plasma. The target material is then deposited on the substrate.

Stoichiometric control with the pulsed laser deposition system allows for careful control over the ratio of atomic molecules deposited. The presence of ambient oxygen in the PLD chamber aids in depositing oxides. The focus of many PLD systems has been on the deposition of thin films. This experiment attempts to use the PLD system in a novel way: to grow ZnO nanowires. Nanowires are tiny components of nanotechnology ( $10^{-9}$  meter range) that

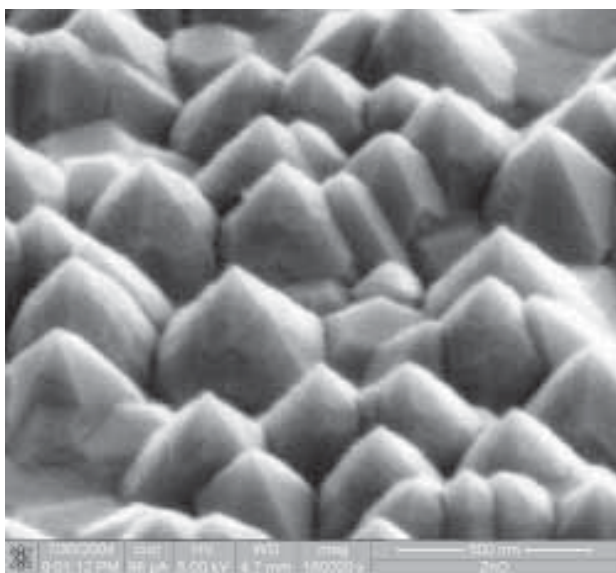


Figure 1: Low temperature and high pressure effects.

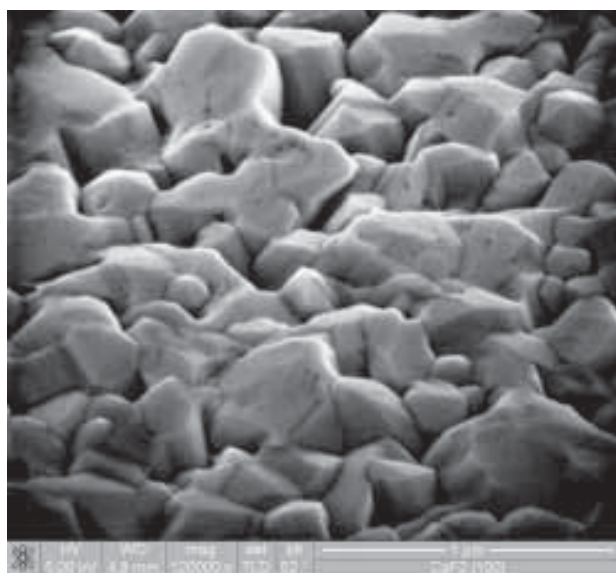


Figure 2: High temperature and high pressure effects.

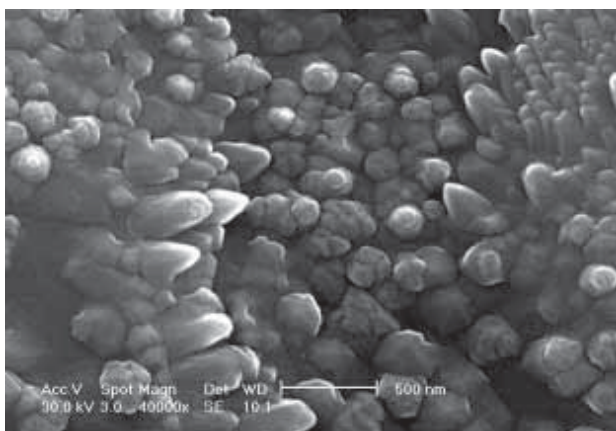


Figure 3: Low pressure and low temperature effects.

comprise the building blocks used to create electrical circuits. Attention is focused on developing methods of growth and control, leaving the future to develop applications of the nanowires.

ZnO holds promise for nanowire growth because of the chemistry of its growth method. ZnO grows preferentially along the C axis of a substrate, regardless of the specific composite of that substrate. This property of ZnO facilitates the construction of ZnO nanowires.

#### Procedure:

ZnO thin films were deposited with a pulsed laser deposition system using a KrF Excimer Laser ( $\lambda=248$  nm) at a pulsed repetition rate of 6 Hz. [pulse width=20 ns]. ZnO targets were made from zinc oxide powder (purity 99.99%). The target to substrate distance was  $\sim 5$  cm.

Three main experiments were performed involving the deposition of ZnO on sapphire ( $\text{Al}_2\text{O}_3$ ), quartz glass, and gold ( $\sim 80$  Å) on glass (Au/Glass). The gold had been deposited previously using electron beam evaporation. The depositions were done in ambient oxygen at  $500^\circ\text{C}$  for 2 hours at a pressure of 31.0 mTorr,  $500^\circ\text{C}$  for 2 hours at 3.1 mTorr, and  $600^\circ\text{C}$  for 2 hours at 32.8 mTorr. In each experiment, the samples were held at deposition temperature for a thermal clean of 10 min.

The samples were examined using scanning electron microscopy.

#### Results and Discussion:

Comparisons at deposition temperatures of 500 and  $600^\circ\text{C}$  at 31.8 mTorr show that lower temperature results in consistent surface morphology. Structures are hexagonally faceted with pointed tips and are uniform in growth. At higher temperature, there is rough, non-uniform growth morphology (see Figure 1).

Comparisons at deposition pressures of 32.1 and 3.1 mTorr at  $500^\circ\text{C}$  show that low-pressure morphology is hilly and follows the contours of the underlying substrate. High pressure results in a flat underlying morphology on

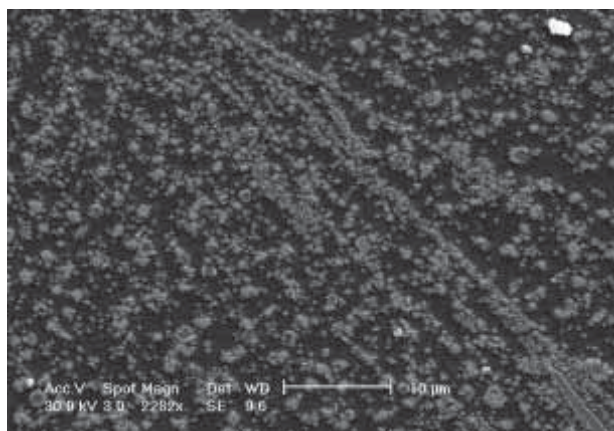


Figure 4: Clustering deposition over annealed thin film.

which the hexagonally faceted structures grow (see Figure 2).

Thin gold films (80 Å) were annealed upon which the ZnO was deposited and the results show the adhesion properties of gold did produce clusters of growth. Nucleation sites formed and the resulting structures are hexagonal and oriented in the c-axis (see Figure 3).

The results of the research indicate that low temperature and high pressure allow for better deposition of ZnO, and annealing gold thin films does affect the location of growth. However, it is not believed that nanowires were grown due to the pointed nature of the structures. Further analysis must be done.

#### Future Work:

A wider range of deposition conditions should be explored, in particular, growth at  $400^\circ\text{C}$  at 30.0 mTorr and 3.0 mTorr pressure. All experiments should be repeated as well to extract exact relationships between growth and deposition conditions. Optical reflectance measurements would be taken to characterize the ZnO growth further. The possibilities of glass substrates would be further examined.

#### Acknowledgments:

Support was received through the National Nanotechnology Infrastructure Network Research Experience for Undergraduates (NNIN REU) Program. The research was conducted at the University of Michigan, Ann Arbor. Assistance was provided by: Dingyuan Chen on the pulsed laser deposition system and scanning electron microscope (SEM), Greg Slavik and Steven Froelich and Tim Brock on the SEM. Support from the Rackham Graduate School of the University of Michigan.

#### References:

- [1] <http://encyclopedia.thefreedictionary.com/Nanowire>.
- [2] P. Yang, UC Berkeley, CVD <http://www.cchem.berkeley.edu/pdygrp/main.html>.

# Surface Functionalization of Barium Titanate Nanoparticles

Blake Stevens, Materials Science and Engineering, Cornell University

NNIN REU Site: Nanotech at UCSB, University of California Santa Barbara

Principal Investigator: Professor David R. Clarke, Materials Department, University of California, Santa Barbara

Mentor: Jennifer Andrew, Materials Department, University of California, Santa Barbara

Contact: bls32@cornell.edu, clarke@engineering.ucsb.edu

## Abstract:

Barium titanate nanoparticles were synthesized using an aqueous coprecipitation reaction with barium hydroxide and titanium n-propoxide at a temperature of 90°C. A surfactant was added to cap the particles in order to inhibit particle growth and agglomeration. A variety of surfactants were used: anionic, cationic, and non-ionic. The samples were then analyzed using a series of techniques including x-ray diffraction (XRD), Fourier Transform Infrared Spectroscopy (FT-IR), scanning electron microscopy (SEM), dielectric measurements, and secondary harmonic generation. Based on XRD, the particles were cubic in nature with average size varying from 25-50 nm. FT-IR spectroscopy was used to measure the effectiveness of the capping agents. The influence of these capping agents on size, structure, and dielectric properties of the BaTiO<sub>3</sub> powder is discussed.

## Introduction:

High dielectric nanoparticles have caught the attention of researchers due to their higher efficiency and other unique properties that could be obtained at this size scale. Ferroelectric materials exhibit very high dielectric constants, due to their noncentrosymmetric unit cells. However, there seems to exist a critical size below which the particles take on a cubic system [1]. Despite the lack of ferroelectric properties, the materials still retain high permittivity. This project focuses on the creation of BaTiO<sub>3</sub> nanoparticles. BaTiO<sub>3</sub> was chosen because it is a well studied ferroelectric material in bulk form.

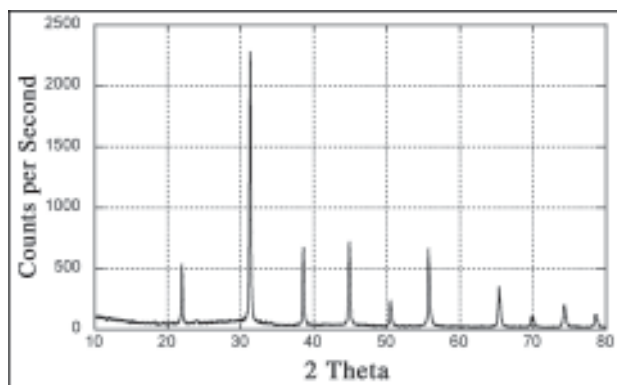


Figure 1:  $\theta$ - $\theta$  x-ray scan of BaTiO<sub>3</sub> sample. All peaks coincide with BaTiO<sub>3</sub> except small peak located at 23.9°.

## Procedure:

BaTiO<sub>3</sub> was synthesized using an aqueous coprecipitation reaction based on the LaMer method [2], using Barium Hydroxide and Titanium n-propoxide as the reactants. Nitrogen gas was bubbled through the solution in order to hinder the formation of BaCO<sub>3</sub>, an unwanted impurity. The pH of the solution is controlled using NaOH. A basic solution is required for both the formation of BaTiO<sub>3</sub>, and to increase the effectiveness of the surfactant. The reaction occurs over 24 hours at 90°C. After this time the surfactant is added. The suspended powder is rinsed and dried in a vacuum for 12 hours.

## Results and Conclusions:

Each sample yielded a white powder, which was then analyzed using the theta-theta technique for powder x-ray diffraction. As can be seen in Figure 1, the scans conclusively showed that the samples were cubic BaTiO<sub>3</sub>, and that there were traces of BaCO<sub>3</sub>. The BaCO<sub>3</sub> forms in rod-shaped particles [3], unlike BaTiO<sub>3</sub> which forms sphere-like particles. This was supported with the SEM images which showed rod-shaped particles amongst the BaTiO<sub>3</sub> particles.

Average particle size measurements were obtained from the x-ray data using Scherrer's formula [4]. The full width half max of the largest peak was measured using a Reitveld refinement technique. This calculation gave particle sizes in the range of 30 to 50 nm, with no significant difference between the types of surfactants used.

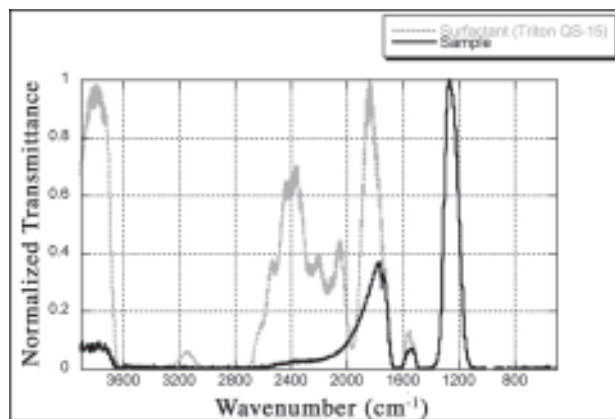


Figure 2: FT-IR comparison of a sample and surfactant. The scans were normalized to one.

Fourier Transform Infrared Spectroscopy (FT-IR) was used in order to determine if the surfactant remained on the particles. These scans were used to compare the sample absorption spectra to pure surfactant absorption spectra to qualitatively determine if the capping agent remained on the sample. An example of the data comparison can be seen in Figure 2. There is a large amount of matching in the range from  $1900\text{ cm}^{-1}$  to  $1400\text{ cm}^{-1}$ , which implies that the surfactant is present in the end sample.

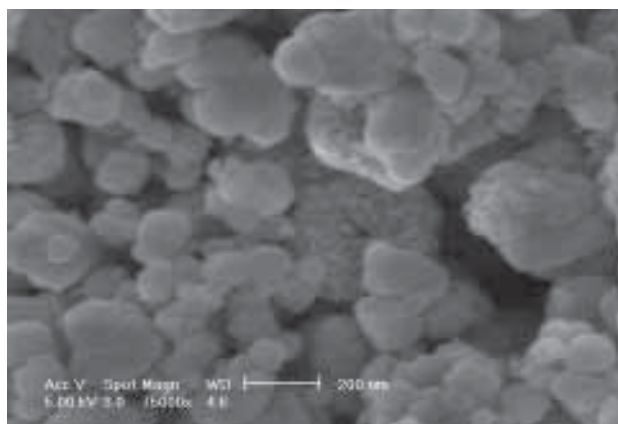


Figure 3: SEM scan of  $\text{BaTiO}_3$  sample. Notice the different particle sizes and agglomeration.

To get a closer look at the particles SEM and TEM were performed. The SEM pictures, as seen in Figure 3, show particles of different sizes and possible agglomerations. Some of the particles appear to be much larger than originally thought by the x-ray scans. This observation is probably due to the upper limit of Scherrer's formula, about 100 nm [4]. In order to determine if the particles agglomerate post growth, or grew in the raspberry-like formations, TEM was used. The TEM scans showed that they were most likely agglomerations. Also, the scans showed that the samples were not 100% crystalline. Once again the type of surfactant used showed no difference in the electron microscopy scans.

Dielectric measurements of the samples were taken using pellets of various densities with a dielectric test fixture on an Agilent Impedance analyzer. The experimental dielectric constants ranged from 20 to 50. These numbers are much lower than the theoretical value of 80. A comparison of dielectric constant to density was plotted along with a simple model based on the rule of mixtures using  $\text{BaTiO}_3$  and air for the components. These plots, Figure 4, do coincide, which implies that density, not surfactant type, accounts for most of change from theoretical values.

Overall no significant differences were seen in the types of surfactants used. This could be due to the fact that all, or none, of the surfactants partially bonded to the surface. Another reason could be the interference of the alcohol groups associated with the Ti n-propoxide. The particles did show small particle size, though perhaps not in the nanometer range. Furthermore, based on the FT-IR scans some type of surfactant was present on the samples.

#### Future Work:

Work that needs to be completed on this project in the future includes further FT-IR scans, dielectric scans at lower frequencies, and quantitative analysis of the substance remaining on the particles. FT-IR scans can be used to help quantify the material left on the particles. Lower frequency dielectric scans would be better suited for these particles, and allow more data to be collected.

#### Acknowledgements:

The author would like to acknowledge Jennifer Andrew for providing guidance, support, and being an amazing mentor. Also Prof. David Clark and his research group for their guidance and ideas, the National Science Foundation for funding, and the NNIN REU program for a great experience.

#### References:

- [1] W. Shih, et. al.. Phys. Rev. B., 50, 21 15575.
- [2] V. K. LaMer and R. H. Dinegar, J. Am. Chem. Soc. 72, 4847 (1950).
- [3] M. del Carmen Blanco Lopez, et. al.. J. Am. Ceram. Soc. 82, 1777 (1999).
- [4] B. D. Cullity and S. R. Stock, Elements of X-Ray Diffraction p. 170, Prentice Hall.

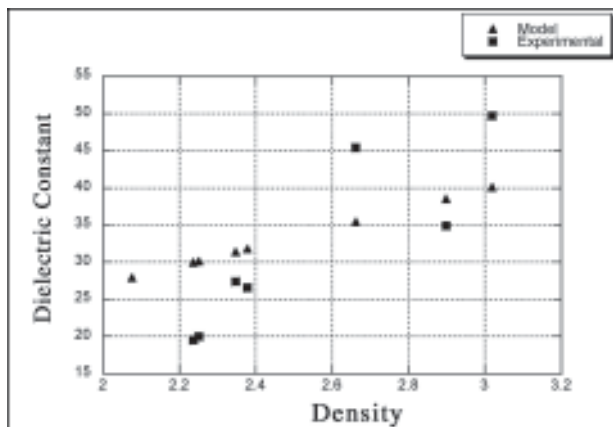


Figure 4: Comparison of experimental dielectric constants & a model based on a mixture of  $\text{BaTiO}_3$  & air.

# Spectroscopic Imaging of Single-Walled Carbon Nanotubes by Resonant Raman Scattering

Alexander Stolyarov, Physics, The University of Texas at Dallas

NNIN REU Site: Center for Imaging & Mesoscale Structures, Harvard University

Principal Investigator: Prof. Michael Tinkham, Physics, Harvard University

Mentor: Stephen Cronin, Postdoc. Physics, Harvard University

Contact: sashastolyarov@comcast.net, tinkham@physics.harvard.edu

## Abstract:

Resonant Raman Scattering from single-walled carbon nanotubes (SWNTs) provides an effective and nondestructive means to characterize electronic and vibrational properties on a single nanotube level. In this work, SWNTs are grown by chemical vapor deposition over lithographically patterned trenches etched in quartz. A tunable Ti:Sapphire laser is employed to locate individual nanotubes in resonance with the laser energy. The Raman radial breathing mode (RBM) from these resonant nanotubes is spectroscopically mapped versus spatial coordinates with submicron precision.

## Introduction:

A SWNT can be envisioned as a honeycombed graphite sheet rolled into a tube of nanometer scale diameter. Among the many characteristics that carbon nanotubes possess, their strong absorption and emission of light render them potential candidates for use in future optical devices [1]. As with any nanoscale device, a substrate support is necessary, therefore, understanding effects of nanotube / substrate interaction is of crucial importance.

The presented research project focuses on utilizing resonant Raman scattering to study the optical effect of this interaction on two particular nanotubes.

## Fabrication Process:

To isolate an individual nanotube for analysis, a multi-step fabrication process was developed, yielding

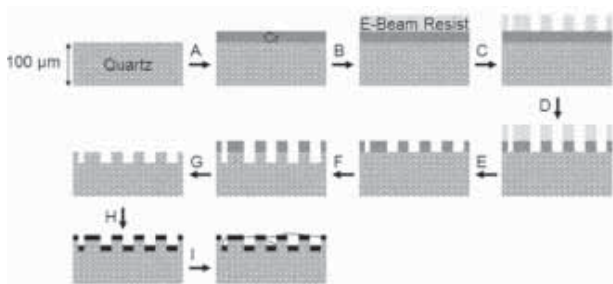


Figure 1: Fabrication process schematic.

SWNTs suspended over trenches. To mask the quartz substrate from subsequent reactive ion trench etching, ~ 40 nm of chromium are thermally evaporated on its surface (Figure 1A). Electron beam resist is spun on top of the Cr (1B), and subsequent electron beam lithography (1C) yields the desired CAD patterned trenches in the resist. Cr etchant is used to etch the exposed Cr down to the quartz level (1D). The resist is removed with acetone (1E) and the sample is subjected to a  $CF_4$  reactive ion etch (1F). The exposed quartz is etched downward, while the Cr masks the rest of the substrate. After the etch, the mask is removed with Cr etchant, leaving a substrate with trenches 700 nm deep and widths ranging from 20 nm-2 μm (1G). To catalyze the formation of SWNTs by chemical vapor deposition, ~ 1 nm of iron particles are evaporated on the substrate prior to nanotube synthesis (1H). Growth of nanotubes occurs within minutes in a furnace supplied with methane and hydrogen gas at 900°C (1I).

## Experimental Procedures:

Unlike bulk sample measurements, optical

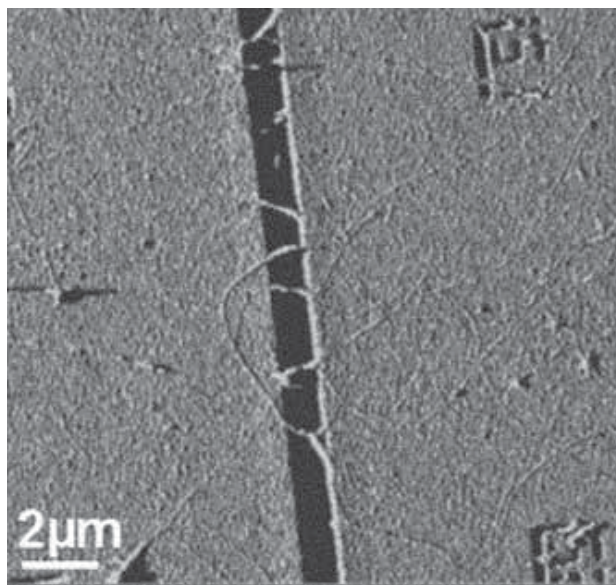


Figure 2: AFM of nanotubes grown over a trench.

absorption and emission in a single nanotube is strongly resonance enhanced [1]. The laser energy that matches a nanotube's electronic band transition is determined by tuning the laser through a maximum in RBM intensity. In our experiments, a 100x objective is used to focus a 2 mW laser beam onto a  $\sim 1 \mu\text{m}$  spot on the sample. The emitted light is collected and a single grating spectrometer diffracts the light into a CCD camera. The determined resonant wavelength is used to perform an area scan of the nanotube and its surroundings. Submicron control of the microscope stage allows for precise spatial mapping of RBM intensity.

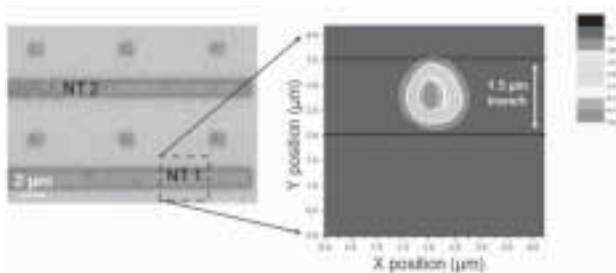


Figure 3: Spectroscopic map of NT1. ( $4 \times 4 \mu\text{m}$  scan,  $0.2 \mu\text{m}$  steps, 30 seconds at each step,  $E_{\text{laser}} = 770 \text{ nm}$ .)

### Results and Discussion:

As is evidenced by atomic force microscopy in Figure 2, we have successfully fabricated nanostructures with SWNTs suspended over trenches. Individual nanotubes are selected for analysis based on the above described resonance requirements. Two distinct nanotubes (NT1 and NT2) are analyzed in this report. Figure 3 plots the intensity of NT1's RBM ( $206 \text{ cm}^{-1}$ ) in a  $4 \times 4 \mu\text{m}$  area confined to the dashed square outlined on the optical image. The resonant wavelength of NT1 was determined to be 770 nm. A clear maximum in the RBM intensity is observed directly in the center of the trench, suggesting a strong optical enhancement from the suspended portion of the nanotube.

The trench position on the spectroscopic map (marked by solid lines), was determined by analyzing before and after scan optical images. The RBM signal from the substrate area was below noise level, indicating that a longer collection time is needed to observe the signal, or perhaps the nanotube is confined in the trench, thereby not in the vicinity of the laser spot away from the trench. NT2 (RBM =  $256 \text{ cm}^{-1}$ ), imaged in Figure 4 was resonant at  $E_{\text{laser}} = 786 \text{ nm}$ . Two maxima in intensity are evident, both on and off the trench. This suggests that the strong signal from

the substrate area arises from nanotube suspension over a local micro trench introduced during the highly reactive ion etching process. These micro trenches, however, are too small to observe with light microscopy.

Clearly, two data sets are not enough evidence to claim suspension enhanced signals. However, this possibility is supported by line scans performed independently on multiple trenches and on the substrate, with the latter exhibiting no RBM features between 100 and  $300 \text{ cm}^{-1}$ , while the former displays tens of resonant nanotubes per trench. Since all the nanotube atoms are on its surface, we hypothesize that the fading of the RBM intensity on the substrate possibly arises from the nanotube's shift in resonant frequency as an effect of nanotube / substrate interactions occurring at the atomic level. This can be tested by spectroscopically mapping the same area at different laser energies.

### Conclusions:

We have developed a technique of spectroscopically imaging individual resonant nanotubes using Raman scattering. The RBM intensities of two distinct nanotubes were mapped versus their spatial positions over trenches etched in quartz. This method probes locally sensitive electronic and vibrational features of nanotubes, and can be a powerful tool in characterization of nanotube / substrate phenomena.

### Acknowledgments:

Research made possible by National Science Foundation, National Nanotechnology Infrastructure Network, and Center for Imaging and Mesoscale Structures at Harvard University.

### References:

- [1] M.S. Dresselhaus, G. Dresselhaus, Ph. Avouris, Carbon Nanotubes: Synthesis, Structure, Properties, and Applications (Springer, Berlin, 2000).

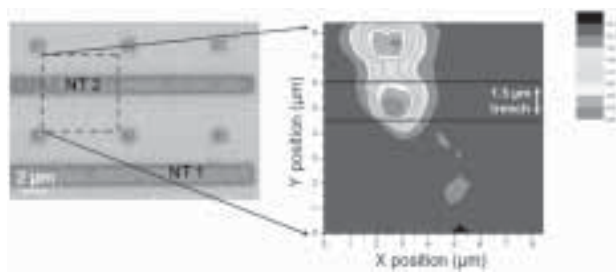


Figure 4: Spectroscopic map of NT2. ( $8 \times 8 \mu\text{m}$  scan,  $0.4 \mu\text{m}$  steps, 120 seconds at each step,  $E_{\text{laser}} = 786 \text{ nm}$ .)

# Effect of Solution pH on the Retention & Flux of Aqueous Solutions of G<sub>3</sub>-NH<sub>2</sub> PAMAM Dendrimer by Regenerated Cellulose Ultrafiltration Membranes

Lynette Tally, Biology, Tennessee State University

NNIN REU Site: Materials Science Research Center of Excellence, Howard University  
Principal Investigator: Dr. Mamadou Diallo, Environmental Engineering, Howard University  
Mentor: Dr. Piraba Swaminathan, Environmental Engineering, Howard University

Contact: ltally@yahoo.com, mdiallo@howard.edu

## Abstract:

A PAMAM dendrimer (from Greek dendra for tree) is an artificially manufactured or synthesized molecule built up from branched units called monomers and can be used to remove ions from water systems. It is removed through polymer enhanced ultrafiltration (PEUF), which uses partially permeable membranes to separate fluids or ions. Experiments with dendrimer to remove metal ions have been performed; however, this paper will discuss how an aqueous solution, with dendrimer alone, filters through an ultrafiltration membrane.

The focus of the project is to filter the dendrimer solution through regenerated cellulose (RC) membranes, so that we can; (a) observe the concentration of dendrimer using ultra-violet visible spectrophotometer (UV-Vis), and (b) study flux with time. The pH of solution is adjusted before being filtered through the RC membrane (3k Dalton). During the ultrafiltration process, the solution filters through a RC membrane. Filtered samples are collected in ten minute increments to record the weight while combining the samples after thirty minutes to observe the concentration. The expected results of the project should be that the concentration of dendrimer and flux of the samples should decrease as time increases.

## Introduction:

Polyamidoamine (PAMAM) dendrimer is a polymer made of subunits called monomers and has a configuration similar to a branched tree (Figure 1). The PAMAM dendrimer has various generations according to the number of active sites. Generation three PAMAM dendrimer has 32 active sites and is also the dendrimer used for this research project. The PAMAM dendrimer can be used to remove toxic ions from waste water systems.

This project focuses on the preliminary work before experimenting to observe how PAMAM dendrimer removes toxic ions from water systems. The research focuses on how pH levels effect an aqueous solution

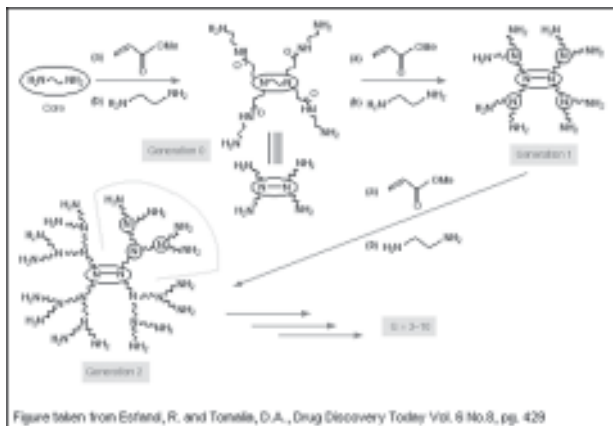


Figure taken from Estlund, R. and Tonello, D.A., Drug Discovery Today Vol. 9 No.8, pp. 429

Figure 1: Dendrimer synthesis.

with dendrimer alone while filtering through a regenerated cellulose (RC) membrane by; (a) determining the retention of dendrimer using UV-Vis, and (b) measuring the dendrimer flux across the membrane with time. The retention is the percentage of dendrimer retained by the RC membrane while the permeate flux is the amount of dendrimer that pass through the RC membrane.



## Procedure:

To prepare the aqueous dendrimer solution, 135 parts per million (ppm = 135 mg) of Generation 3 PAMAM dendrimer is added to one liter of dionized water. The pH of the aqueous solution is adjusted to the desired level using HNO<sub>3</sub> or NaOH while the RC membrane is soaked in dionized water for one hour. After the membrane has finished soaking, the membrane is then attached to the stirred cell (Figure 2, above). The control sample of the solution is collected before pouring the rest of the solution into the reservoir.

The stirred cell is attached to the reservoir and the nitrogen is turned on with the pressure being set to 450 pounds per square inch (psi). Once the solution had begun filtering through the RC membrane, samples are collected every 10 minutes for a total of 4 hours to determine the retention of dendrimer using UV-Visible Spectrometer and also measure the dendrimer flux across the membrane with time.

**Results and Conclusions:**

Retention is the percent of dendrimer retained by the RC membrane where as the permeate flux is the amount of dendrimer that was able to pass through the membrane. In Figure 3a, we see that the percentage of dendrimer retained by the RC membrane is higher for pH 7 than the percent retained for pH 9. We also see that the permeate flux of dendrimer is lower for pH 7 than the permeate flux for pH 9 according to Figure 3b. The two figures show that there is a relationship between the retention and permeate flux. When the percent of dendrimer retained by the membrane is high, it is clogging the pores of the membrane and therefore not allowing dendrimer to pass through the membrane. As a result, the permeate flux will be relatively low. On the other hand, when the percent of dendrimer retained by the membrane is low, the permeate flux will be high meaning that more dendrimer will pass through the RC membrane.

There is a theory, not proven, that when the pH level is adjusted to 7, the dendrimer becomes protonated. That can result in the dendrimer molecule becoming larger and therefore making the dendrimer molecules too large to pass through the pores of the membrane so more dendrimer is retained by the membrane. However, when the pH level of the aqueous dendrimer solution is adjusted to pH 9, the dendrimer molecules are not as protonated and more dendrimer molecules are able to pass through the RC membrane.

**Future Work:**

For future work, repeating of the experimental procedure with pH levels 7 and 9 will be necessary to check for consistency. Once there is consistency with pH levels 7 and 9, experimental procedures using different dendrimer generations (ex. Generations 4 and 5) will be performed.

The experimental procedures should also be observed at various pH levels including 4 and 11. Once the preliminary work has been finished, the experiment will be performed with metal ions (such as Copper) to study ultrafiltration of water systems.

**Acknowledgements:**

I would like to thank the following for their help and support this summer: Dr. Mamadou Diallo, Dr. Piraba Swaminathan, Dr. Gary Harris, Mr. James Griffin, MSRCE staff, and NNIN co-workers. Special thanks go to The National Science Foundation and National Nanotechnology Infrastructure Network for making the summer program possible and great experience for undergraduate students.

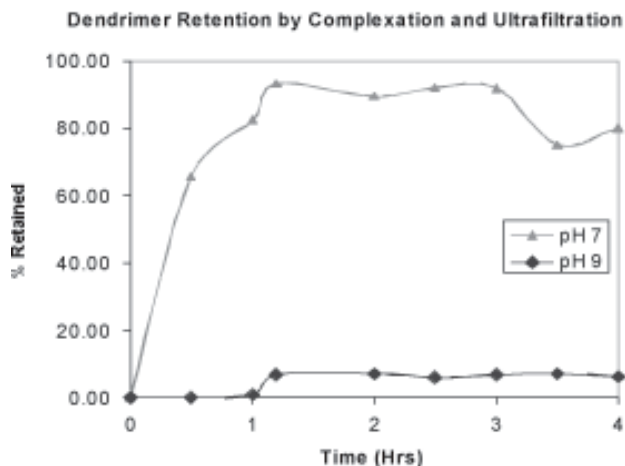
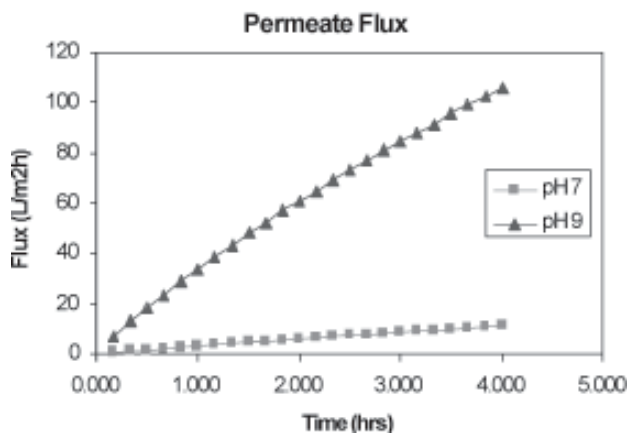


Figure 3a, above: Dendrimer retention.

Figure 3b, below: Permeate flux of dendrimer.



# Stability of Silver Nanoparticles in Aqueous and Organic Media

Patricia Tillmann, Chemistry, Western Washington University

NNIN REU Site: Materials Science Research Center of Excellence, Howard University

Principal Investigator: Dr. James Mitchell, Chemical Engineering, Howard University

Mentor: Dr. Jude Abanulo, Chemical Engineering, Howard University

Contact: jwm@msrce.howard.edu

## Abstract:

Several chemicals have been used to research the stability of silver nanoparticles in aqueous and organic media for use in electrophoretic deposition and, ultimately, the fabrication of an infrared detector. Every chemical component in the electrophoretic medium must be compatible with the ultrapure reaction conditions required for the fabrication of the semiconductor infrared detector. Appropriate reagents must introduce no detrimental impurities and be easily removed by decomposition or volatilization. Moreover, the silver nanoparticles must be ultrapure.

In this experiment, silver nanoparticles are obtained commercially and an electrochemical synthesis is attempted [2]. To ensure the silver nanoparticles are the appropriate 10 nm size, particle-size distributions of some samples are obtained using the Zetasizer 3000. In addition, the relative abilities of ethylene glycol, water, sodium dodecyl sulfate, methanesulfonic acid, formic acid, and 1,1,1-trifluoro-2,4-pentanedione to stabilize silver nanoparticles are compared using UV-Vis spectrophotometry. These results, plotted in an absorbance vs. time graph, indicate that ethylene glycol and sodium dodecyl sulfate are the best stabilizing agents.

## Introduction:

Silver is a versatile element with applications in the clothing [4], appliance [3], and semiconductor industries. It can be used to destroy bacteria [3, 4] or fabricate a nanocomposite IR detector. For the latter application, this paper reports the results of a ten week exploratory investigation to optimize conditions for preparing an electrophoretic deposition medium containing 5-10 nm silver particles.

Following deposition of silver onto a silicon substrate, a nanocomposite silver-silicon matrix is processed into an IR detector. Prior to deposition, using a stabilizing agent compatible with electrophoretic deposition and subsequent semi-conductor processing prevents the agglomeration of silver nanoparticles in the processing medium. The relative effectiveness of ethylene glycol, sodium dodecyl sulfate, methanesulfonic acid, formic acid, and 1,1,1-trifluoro-2,4-pentanedione to stabilize silver nanoparticles are compared.

## Experimental Procedures:

Silver nanoparticle suspensions containing six stabilizing

reagents and varying pHs were prepared. Samples containing the same initial loading of silver (%) were prepared from an original 10% w/v stock suspension (commercially obtained). Each sample contained an amount of stabilizer that produced an initial absorbance of 0.7 to 1.0. The stabilizing reagents include: formic acid, methanesulfonic acid, sodium dodecyl sulfate, 1,1,1-trifluoro-2,4-pentanedione, ammonium hydroxide (for a sample of pH 11), acetic acid (for a sample of pH 3), and ethylene glycol as the control.

To prepare the samples, an Eppendorff pipette was used to measure the appropriate amount of silver nanoparticle suspension. This amount was then added to the solution of water or ethylene glycol and a stabilizing agent to total 15 mL of suspension. Once prepared, 2-3 mL of a sample were transferred into a quartz cuvette using a polyethylene transfer pipette and tested using the UV-Vis. Following measurement of the initial absorbance, each suspension was periodically measured over a 1-2 week period.

Ten measurements were averaged to obtain results for a single day. During the measurement cycle, samples were stored in sealed vials and kept in a cool, dry, dark place until the next series of tests.

## Results and Conclusion:

Particle-size distributions of several nanoparticle suspensions, determined by electrophoretic light scattering with a Zetasizer 3000, are shown in Figure 1. A slightly narrower distribution of particles over the same size range

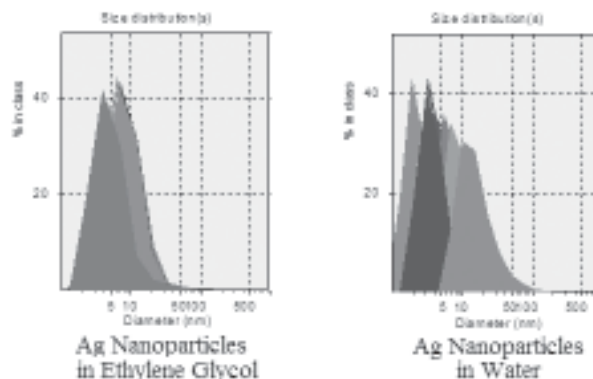


Figure 1: Size distributions of silver nanoparticles. Most silver nanoparticles are 5-10 nm in diameter.

exists in ethylene glycol. To determine the relative stability of the various silver nanoparticle media, a comparison of absorbance versus time at a constant wavelength was used. In the absence of the stabilizer chemically transforming silver metal particles into ionic forms or neutral absorbing chromophores, the decrease of the absorbance with time is dominated by the agglomeration and/or settling of silver nanoclusters from solution. Silver precipitates formed easily on the walls of vessels containing the least effective stabilizers. This provides a relative comparison of the stabilizing effect of various reagents.

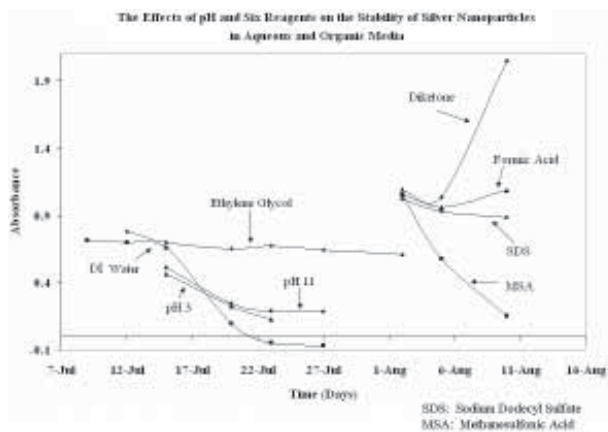


Figure 2: Ethylene glycol and SDS show the smallest decreases in absorbance over time and are the best stabilizers.

After 1-2 weeks of testing, Figure 2 shows ethylene glycol and sodium dodecyl sulfate are the most obvious and effective stabilizers of silver nanoparticles in aqueous and organic media. It is possible that ethylene glycol, the control, performed so well because another stabilizing agent is present in the solution. However, proprietary issues preclude analyses to document this.

Sodium dodecyl sulfate has previously been used to stabilize silver nanoparticles in aqueous solutions successfully [1] and these results are confirmed here. Unfortunately, the reagent does not meet our requirements. Results for the diketone (1,1,1-trifluoro-2,4-pentanedione) and formic acid require further investigation to verify or refute their validity. Within a few days, in the presence of methanesulfonic acid, absorbance decreases rapidly and silver particles precipitate. Other experiments can determine if the isoelectric point is reached, causing the destruction of electrostatic stabilization or if another explanation for this result is valid.

#### Future Work:

AFM images, as seen in Figure 3, are but one form of characterization necessary to validate or refute the above hypotheses. It is ideal to prepare silver nanoparticles in the lab to achieve complete control over the fabrication process. To efficiently perform the electrophoretic deposition, the pH at the isoelectric point of silver should be found. To make the fabrication process easier and purer, electrophoretic co-deposition of silver and silicon is ideal.

#### Acknowledgements:

I would like to thank Dr. James Mitchell, Dr. Jude Abanulo, Dr. Vilma Gultneh, Mr. Uche Nwodo, Mr. James Griffin, Dr. Otto Wilson, and my co-workers for their assistance and support. Finally, thank you to the NNIN and NSF for funding.

#### References:

- [1] Mafune, F.; Kohno, J.K.; Takeda, Y.; Kondow, T. J. Phys. Chem. B, 2000, 104 (35), 8333-8337.
- [2] Kortenaar, M.V. ten; Kolar, Z.I.; Tichelaar, F.D. J. Phys. Chem. B, 1999, 103, 2054-2060.
- [3] [http://www.samsung.com/ph/presscenter/samsunginthephilippines/productnews\\_20040608\\_0000058342.asp#](http://www.samsung.com/ph/presscenter/samsunginthephilippines/productnews_20040608_0000058342.asp#)
- [4] <http://www.essentialapparel.com/shopping/product/detailmain.jsp?itemID=1564&itemType=PRODUCT&iProductID=1564>

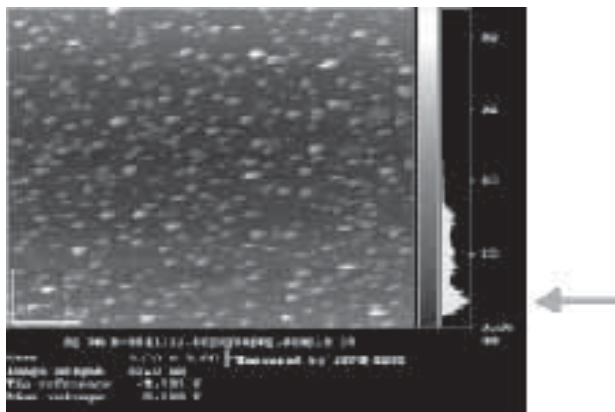


Figure 3: Silver nanoparticles are about 10 nm across and monodispersed.

# The Effect of Organic Compounds on the Synthesis of Nanophase Materials

Paul Vallett, Chemistry & Math, University of Vermont

NNIN REU Site: Center for High Technology Materials, University of New Mexico  
Principal Investigator: Dr. Huifang Xu, Earth and Planetary Sciences, University of New Mexico  
Mentor: Dr. Adrian Brearley, Earth and Planetary Sciences, University of New Mexico  
Contact: pvallett@uvm.edu, hfxu@unm.edu

## Abstract:

In this study, we investigated the effect of the organic molecules glycine and ethylamine on the synthesis of ZnS nanocrystals. The organic molecules were introduced during a low temperature (180°C) hydrothermal synthesis of ZnS. High resolution transmission electron microscope (HRTEM) images show that the morphology and structure of the ZnS crystals formed in the experiments were affected by the ethylamine, but not by the glycine.

Using ethylamine as the organic molecule, the morphology of the nanocrystals changed from spherical, to lamellar, to rod-like aggregates as the concentration of ethylamine was increased. The crystals were mostly in the stable cubic form. The thermodynamically-unstable hexagonal phase of ZnS was also observed in nanorods and stacking faults within the cubic phase in experiments run with intermediate concentrations of ethylamine.

## Introduction:

The study of nanocrystals is important for their future use in possible nanoscale optical or electronic devices. Their unique properties are usually highly dependent on their crystallographic structure. Therefore size and shape are very important factors to consider when trying to synthesize nanocrystals

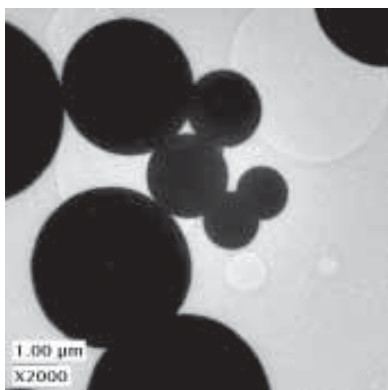


Figure 1: ZnS in sphere morphology synthesized in 0.5M glycine.

with a specific property. ZnS is a good group II-IV semiconductor, and emits light in the blue part of the spectrum. ZnS is a naturally occurring metal that has two polymorphs at room temperature. The stable cubic sphalerite form and the meta-stable hexagonal wurtzite form. The wurtzite is rarer in nature, as it more unstable by about 13 kJ/mole at room temperature and is only stable at higher temperatures.

The purpose of this research is to determine how organic molecules can affect the shape and morphology of ZnS nanocrystals, using a hydrothermal synthesis method. The crystallographic structure will be characterized using HRTEM imaging.

## Procedure:

**Synthesis:** Thiourea ( $\text{SC}(\text{NH}_2)_2$ ) was used as the sulfur source in this experiment because it dissolves and releases  $\text{S}^{2-}$  ions only at higher temperatures. Zinc acetate ( $\text{Zn}(\text{CH}_3\text{COO})_2$ ) was used as the Zinc source. The samples were prepared with 0.8M and 0.4M of thiourea and zinc acetate, respectively, in water or a solution of water and either ethylamine or glycine with concentrations of organics ranging from 0.5M to 2.0M. These solutions were created in 30 mL - Teflon<sup>®</sup> cups, sealed, and placed in an autoclave. They were kept at 180°C for 2 hours, removed and allowed to cool to room temperature naturally. The solutions containing product were then centrifuged, had the supernatant poured off, washed with distilled water, which was repeated ten times to remove impurities in the sample.

Ethylamine was chosen as an organic to use because of its similarity in structure to ethylenediamine, a molecule that has been used previously to synthesize pure wurtzite ZnS [1]. Glycine was chosen because it is the most basic amino acid, and has a similar functional amine group to ethylamine.

**Characterization:** Samples were characterized using a JEOL 2010 transmission electron microscope (TEM) and a Oxford Energy Dispersion Spectroscopy (EDS) system. Samples were prepared for character-

ization by placing them in an ultrasonic bath for 60 seconds and dispersing the sample from a suspension directly onto holey carbon-coated copper grids.

### Results and Conclusions:

**Glycine:** The TEM images for glycine showed that the organic molecule had little to no effect on the structure and morphology of the ZnS nanocrystals. Figure 1 shows the overall shape of the crystals to be spherical and ranging from 1-5  $\mu\text{m}$  in diameter. As the concentration of glycine in reaction medium increased from 0.5 to 2.0M, general morphology of the crystals remained in this spherical shape. HRTEM revealed that the ZnS was in the cubic sphalerite form.

Some of the crystals observed with about 1.0M glycine were destroyed when placed under the high energy electron beam of the TEM. It is possible that glycine was incorporated into the ZnS crystal structure. When exposed to the high energy of the electron beam, the glycine molecules could be destroyed and the rest of the ZnS structure then appears to fall apart as seen in Figure 2.

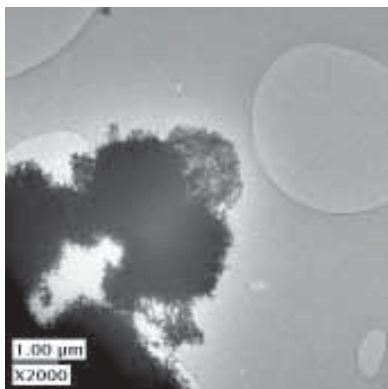


Figure 2: ZnS spheres after being exposed to high energy electron beam.

**Ethylamine:** Ethylamine had a large influence on the structure of the ZnS crystals. As the concentration of ethylamine in reaction medium increased from 0.5 to 2.0M, there was a wide range of structures seen. Starting at a spherical morphology, the crystals changed to an aggregate of lamellar plates, to nanorods, to clusters of small crystals. HRTEM images of medium concentrations of ethylamine (1.25-1.75M) revealed increasing sections of wurtzite ZnS plates forming as seen in Figure 3. At 1.50M of

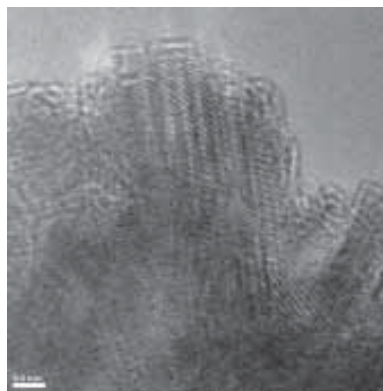


Figure 3: HRTEM image of wurtzite plates forming in 1.25M ethylamine.

ethylamine, interesting wurtzite nanorods were observed. These nanorods were growing along an unusual axis of growth. Wurtzite nanorods observed in previous experiments involving ZnS showed growth along the C axis, while these nanorods showed wurtzite growth along the A axis as seen in Figure 4. To our knowledge these structures have not been previously found in synthesis of ZnS nanocrystals.

### Acknowledgements:

I would like to thank the University of New Mexico, the NNIN REU program, Dr. Xu, Hiromi Konishi, and Zimin Nie for all their help during my internship.

### References:

- [1] X. Chen, H. Xu, N. Xu, F. Zhao, W. Lin, G. Lin, Y. Fu, Z. Huang, H. Wang, M. Wu, "Kinetically Controlled Synthesis of Wurtzite ZnS Nanorods through Mild Thermolysis of Covalent Organic-Inorganic Network", *Inorg. Chem.* 2003, Vol. 42, pp. 3100-3106.

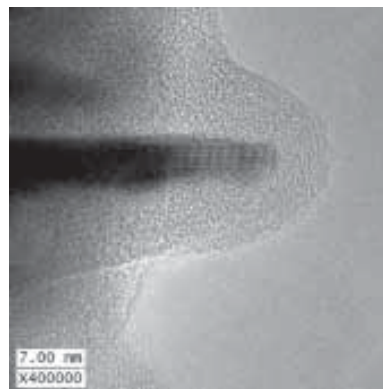


Figure 4: HRTEM image of wurtzite nanorod growing in unusual direction.

# Silicon Carbide Light Emitting Diode Fabrication and Characterization

Damian J. Vaughan, Electronic Computer Tech., North Carolina A&T State University

NNIN REU Site: Materials Science Research Center of Excellence, Howard University

Principal Investigator: Dr. Gary Harris, MSRCE, Howard University

Mentor: Mr. Crawford Taylor, MSRCE, Howard University

Contact: dv005121@ncat.edu, gharris@msrce.howard.edu

## Abstract:

Light emitting diodes or LEDs are the next level of technology when it comes to a light bulb. LED technology is about finding a semiconducting material that emits different color light. This project focused on what a LED is and how it works. We also discuss silicon carbide (SiC) LED fabrication and characterization.

Talking about LED briefly, it is a semiconductor diode that emits incoherent monochromatic light when electrically biased in the forward direction. This report will explain in detail how this device emits light and how it emits multi-color light by using different semiconductor material. To understand this, there will be a brief explanation of what a semiconductor and a diode are. We will be explaining silicon carbide which is the semiconductor material that we used to fabricate the LED while working in the lab.

Also, we will explain in this paper the fabrication technique that we followed in processing this device. Pictures and photos of this device will be included. In the results and conclusion, we will give opinions on LED performance, and compare and contrast the LED bulb to the incandescent bulb of today.

## Introduction:

What is a light emitting diode? LEDs are special types of semiconductor diodes that emit incoherent monochromatic light when electrically biased in the forward direction. Like a normal diode, the LED consists of a chip of semiconductor material impregnated or doped with impurities to create a structure called a pn junction. The junction consists of a p-type and n-type semiconductor regions. The p-type semiconductor has an excess of conducting holes which are created by adding trace amounts of other elements to the original pure semiconductor crystal. The n-type semiconductor has an excess of conduction electrons which can be made n-type by adding trace amounts of another element to the semiconductor crystal.

Before any light is emitted, another region is formed in the middle of the diode called the depletion region. The depletion region is formed because the negative charges attract with the positive charges along the junction. This creates a neutral charge in the junction where the electrons and holes can't move.

To fix this problem, an electric field has to be applied and when sufficient voltage is applied to the chip across the leads of the LED, electrons can move easily in only one direction across the junction between the p and n regions. In the p region, there are more positive charges than negative. In the n region, there are more negative charges than positive. As current passes thru the junction, the electrons combine with the holes and this recombination gives off energy in the form of light which can be called photons. When all free holes and electrons combine, they produce enough light to be emitted through the bulb. We can see this process in Figure 1.

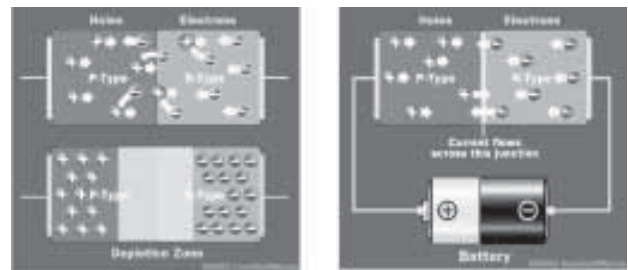


Figure 1: PN junction diagram of how the LED works.

To produce different color light, you use different kinds of semiconductors. Silicon carbide (SiC), indium gallium nitride (InGaN), and zinc selenide (ZnSe) produce blue LED's. Gallium phosphide (GaP), and gallium nitride (GaN) produce green LED's. Gallium arsenide/phosphide (GaAsP) produce red, orange and yellow LED's. Aluminum gallium arsenide (AlGaAs) produces red and infrared. When blue, red, and green are combine, they can produce white LED's, and the white light is the most expensive diode to make.

## Procedure:

For fabricating the device, we used photolithography. The following are the procedures to follow when fabricating the SiC substrate:

**Cleaning Process** (To be done at wet bench): Apply soap solution with brush in one direction. Rinse in DI water and blow dry with nitrogen gas. Ultrasound with trichloroethylene, acetone, and methanol for three minutes without exposing to the air. Rinse in DI water and blow dry with nitrogen gas. Place sample in pre-bake oven for 5 minutes to dry off any residual moisture on the surface.

**Lithography Process** (To be done under yellow light): Turn on spinner and place sample. Turn on vacuum pump, then apply a few drops of photoresist (Shipley 1818 "4:1") to sample surface. Cover spinner and spin sample on a 1.4  $\mu\text{m}$  thick layer in 30 sec. at 6000 rpm. Remove sample from spinner and place in the pre-bake oven for 30 min. at 105°C. Turn on mask-aligner lamp and main power. Remove sample from pre-bake, let cool, then expose to UV light for 18 sec. Use fume hood to develop. Dip sample in toluene for 60 sec. (this hardens the surface), rinse & dry with nitrogen. Dip sample in developer (gently agitating) for 60 sec, rinse & dry with nitrogen gas. Repeat process for each layer.

**Electron Beam Evaporator:** Turn on power. Deposit 100 Å Aluminum to create p-type region on substrate, then anneal at 650°C for 60 sec. Ohmic contact of (50Å/400Å/1500Å) chrome, nickel, gold, respectively, for probing n-type region, then anneal at 650°C for sec. Transparent layer of (50Å/100Å) chrome, gold for p-type region. Metallization contact of (50Å/400Å/1500Å) chrome, nickel, gold for probing p-type. See Figure 2.

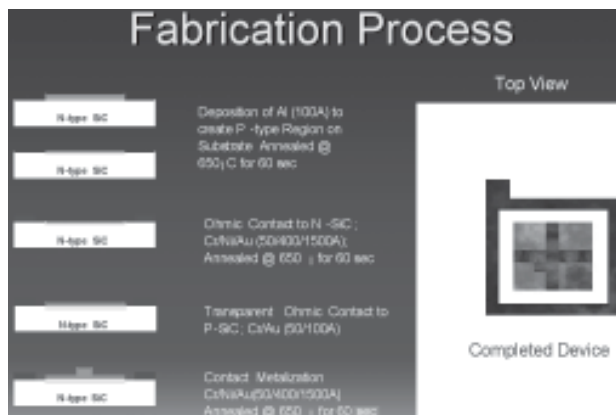


Figure 2: Procedure for using the e-beam evaporator.

## Results and Conclusion:

After fabricating and probing the device, results were obtained showing that the diode had a characteristic curve (current vs. voltage) with a turn-on voltage that was greater than 0.7 V with a doping concentration of  $10^{18} \text{ cm}^{-3}$ . Also, the light that was produced had very low light intensity and low light efficiency. Refer to Figure 3.

In conclusion, we have fabricated a preliminary light emitting diode (LED) with a fair characteristic curve (current vs. voltage) that had low levels of light intensity. In future work, we intend to work more on changing the device structure and then measuring the intensity and spectrum of the light. Also, we can characterize the parameters by the doping concentration, the junction depth, and the mobility of the p- and n-type regions. Last, we can then package the device in the bulb.

## Acknowledgements:

I would like to thank the NNIN for allowing me to participate in the REU program. Also, I would like to give my sincere thanks to the staff at the Howard Nanoscale Science and Engineering Facility (HNF), especially: Dr. Gary Harris, Mr. Crawford Taylor, Mr. James Griffin, the graduate students for their assistance, and The National Science Foundation.

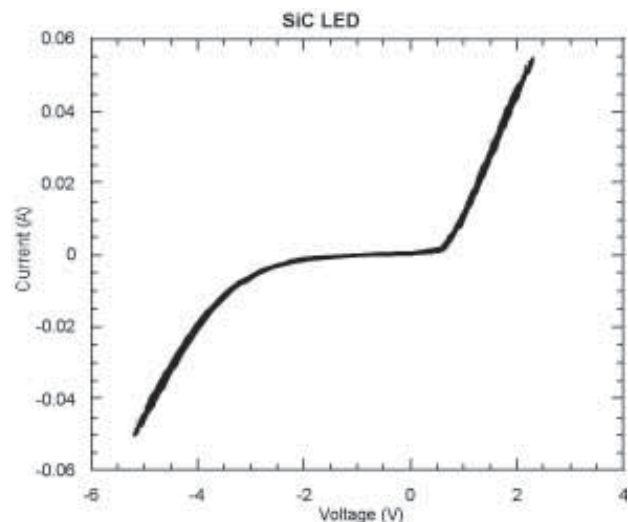


Figure 3: Characteristic curve showing current vs. voltage.

# Micro-Scale Two Phase Flow Device Fabrication

Steven Virost, Mechanical Engineering, Tennessee Technological University

NNIN REU Site: Cornell NanoScale Science & Technology Facility, Cornell University

Principal Investigator: Dr. Yoav Peles, Mechanical, Aerospace & Nuclear Engr., Rensselaer Polytechnic Institute

Mentor: Chih-jung Kuo, Mechanical, Aerospace & Nuclear Engineering, Rensselaer Polytechnic Institute

Contact: smvirost21@tntech.edu, pelesy@rpi.edu

## Abstract:

As computer chips get smaller and faster, there rises a need for new innovative ways to keep them cool without making the computer chip bulky. This study investigated the possible heat transfer abilities of micro-scale two-phase flows, primarily in water. The devices used varied in surface roughness, temperature, flow regime, length, and methods of two-phase heat exchange. They were fabricated with three main components: micro-channels, a heater, and a thermistor. The micro-channels were etched into silicon substrates and then bonded to glass. An external pump created the flow through the channels. On the bottom sides of the substrates, in order to model an application such as a hot computer chip, Aluminum heaters were installed. Also, for temperature measurement accuracy, polysilicon thermistors were introduced underneath the heaters (in close proximity to the channels). Preliminary testing has begun, but no results have been measured currently.

## Introduction:

The present methods of heat dissipation could pose a problem in the near future for the miniaturization of the electronic world. The heat transfer capabilities of two-phase flow on the micro-level demonstrate an effective response to this problem. Unlike the common heat transfer of single-phase flow available today on the macro-scale, in radiators for example, two-phase micro flow offers two exceptional advantages. Though both single- and two-phase flows can occur at the micro-scale, the convective heat transfer coefficients of two-phase flows are predicted to be higher than those of single-phase flows, which will allow energy to be removed at a higher rate. Also, the energy exchange involved with phase change from liquid to vapor will facilitate more heat dissipation than that of single-phase flow. Our study works primarily with water but the idea of two-phase flow heat transfer is applicable to any substance.

## Procedure:

The devices were devised of three major components: A thermistor, a heater, and the micro-channels. The thermistor and heater were both located on the bottom side and the micro-channels on the top side.

**Thermistor:** Using a standard silicon wafer, a 0.5  $\mu\text{m}$  layer of thermal oxide was grown on both sides with a MOS furnace. Then, on the top side, another 1  $\mu\text{m}$  layer of oxide was deposited using PECVD which served as the hard mask for the micro-channel deep etch in a later step. This step designated the 'top side' of the wafer. A 2  $\mu\text{m}$  layer of polysilicon was deposited next using a LPCVD MOS furnace. Then, on the bottom side of wafer, a thermistor was etched into the polysilicon using  $\text{CF}_4$  reactive ion etch in a PT 72 after the necessary photolithography. This was followed by the metallization of the thermistor vias with 150 $\text{\AA}$  of Ti for adhesion and 0.3  $\mu\text{m}$  of Al+1%Si+4%Cu in the CVC sputtering machine. Following photolithography of the vias, the Al+1%Si+4%Cu was etched into the thermistor vias using Type A Aluminum Etchant. The Ti was etched using 10:1 HF. In order to isolate the thermistor and vias, a protective layer of 1  $\mu\text{m}$  oxide was deposited using PECVD.

**Heater:** On the bottom side, over the isolated thermistor component, the metallization of the heater and its vias was achieved with the CVC sputtering machine. A 150  $\text{\AA}$  Ti adhesion layer, a 0.5  $\mu\text{m}$  Al+1%Si+4%Cu layer for the heater, and a 1  $\mu\text{m}$  Cu layer for the vias of the heater were respectively deposited. Basic photolithography was used to pattern the heater's vias into the Cu layer and then the Cu was etched using Copper Etchant. Next, the pattern for the heater was imposed over the existing vias with contact photolithography and the heater itself was etched with Aluminum Etchant Type A. The remaining adhesion layer of Ti was etched using a 10:1 HF dip. Another isolating protective layer of 1  $\mu\text{m}$  oxide was deposited over the heater and its vias using PECVD.

**Micro-Channels:** On the top side, after the photolithography of the micro-channels was completed, the hard mask for the subsequent deep etch, or Bosch etch, of the micro-channels was made by etching the polysilicon and oxide layers in a PT 72 with a  $\text{CHF}_3$  plasma etch. The Unaxis 770 was used to etch the actual channels 100  $\mu\text{m}$  initially, with a pause when the photoresist was removed, and then was continued 150  $\mu\text{m}$  more. A protective 1  $\mu\text{m}$  oxide layer was then deposited with PECVD. The micro-channels are shown in Figures 1 and 2. Figure 1 illustrates micro-channels with re-entrant cavities and Figure 2 shows a close-up of the actual micro-channels.

**Access to Channels:** On the bottom side, the photolithography for the access to channels was performed and then followed by the etching of the 2.5  $\mu\text{m}$  of oxide layers in the PT 72 with a  $\text{CHF}_3$  plasma etch. The first 100  $\mu\text{m}$  of the through-etch was realized with the Unaxis 770, only stopping briefly to remove the photoresist. Then the through-etch for access to the channels was completed in the Unaxis 770.

**Sealing of Channels:** First, the bottom side was coated with photoresist. Then, the oxide layer on the top side was removed with BOE 6:1. The wafer was then anodically bonded to a Pyrex<sup>®</sup> glass wafer using an EV501 wafer bonder.

**Access to Heater/Thermistor:** A window photolithography was done on the bottom side and succeeded by an oxide etch in the PT 72 with a  $\text{CHF}_3$  plasma etch allowing contacts to be made with the heater and thermistor. Finally, the wafer was cut into singular devices with a wafer saw making them ready for the fixture used in experimentation. Experiments are currently being carried out with results pending.

**Acknowledgements:**

I would like to thank Dr. Yoav Peles for his support and guidance in this project as well as Chih-jung Kuo for his help and knowledge. I would also like to thank Cornell NanoScale Facility for allowing us to use their facility, and the National Science Foundation for their financial support.

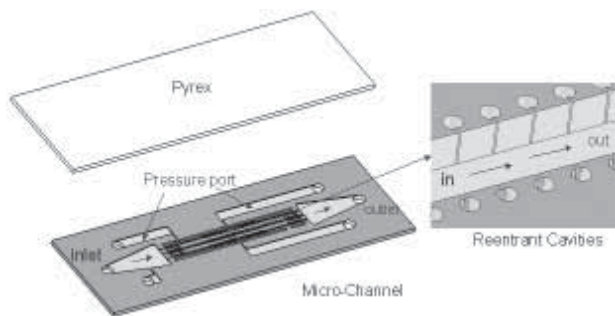
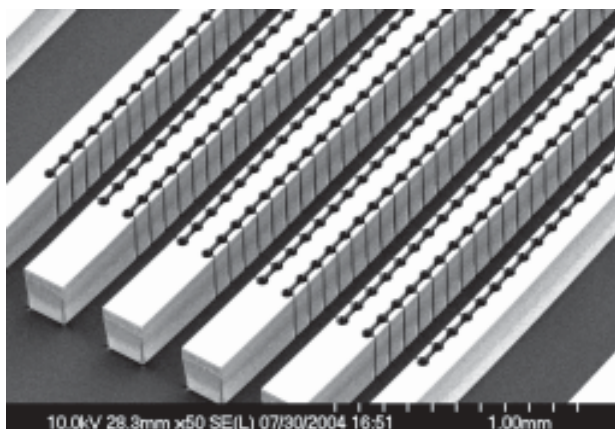


Figure 1, above: Sample micro-channel features.

Figure 2, below: Micro-channels with re-entrant cavities to facilitate phase change.



# Quantum Computing via Single Charges in Self-Assembled Coupled Quantum Dots

Rogers Whitlock Jr., Electrical Engineering, Southern University

NNIN REU Site: Nanotech at UCSB, University of California Santa Barbara  
Principal Investigator: Mark Sherwin, Physics, University of California at Santa Barbara  
Mentor: Kohl Gill, Physics, University of California at Santa Barbara  
Contact: rog\_81@yahoo.com, sherwin@physics.ucsb.edu

## Abstract:

Quantum computers take advantage of the phenomenon known as quantum mechanics. The quantum bits, or 'qubits' that comprise these computers have the capability of existing in two states simultaneously, allowing them to provide more bit representation than the conventional transistor. As a result, quantum computers will be faster, contain more memory and possess superior encrypting capability than today's traditional computers.

The purpose of this research is to define the independent control of both the loading and tuning of charges in quantum dots using applied voltage as opposed to sample doping. The tunnel splitting of the coupled electronic states is in the terahertz regime but they are only split at specific applied electric fields. The quantum dot sample being used is comprised mainly of InAs and GaAs. That is, InAs layers deposited between GaAs layers, which are deposited on top of a AlGaAs sample.

## Introduction:

Quantum dots are defined as anything that can contain and confine one or more electrons in all three dimensions. As a result, they are commonly referred to as "artificial atoms." One exciting characteristic of quantum dots is that they can actually be manipulated with respect to the number of these electrons. This phenomenon is known as loading and unloading, and can be accomplished utilizing an applied voltage in conjunction with light pulses to create the free electrons then fill the quantum dots. The sample is comprised of three materials (AlGaAs, InAs and GaAs,

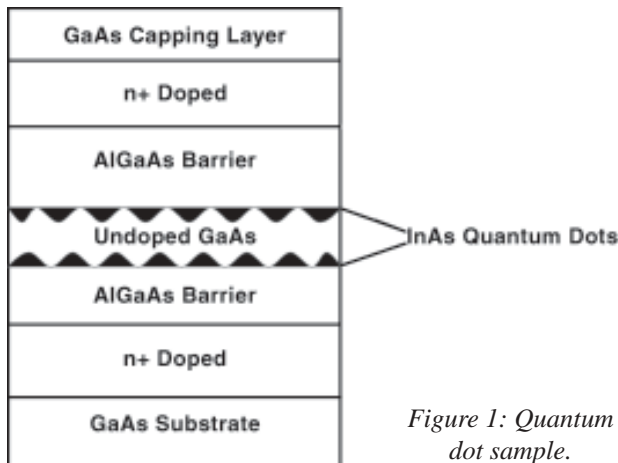


Figure 1: Quantum dot sample.

Figure 1) each having a different band gap energy. This band gap energy level is important because it specifies the level at which electrons are excited and "freed" within the material. The light pulse (from a laser diode) is tuned to a certain frequency or energy that when applied to the sample, will excite and generate electron/hole pairs in only one of the present materials. Once the free electrons are present within the sample, loading the quantum dots is only a matter of manipulating them. This is where the voltage differential comes into play. This applied voltage shifts the band gap diagram as shown in Figure 2. This shift then fills the quantum dots due to their tendency to flow to the level of lowest energy.

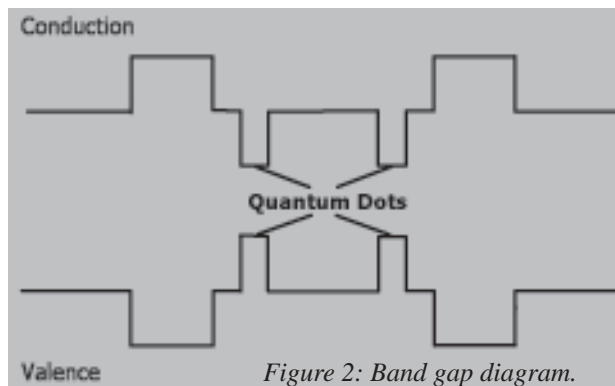


Figure 2: Band gap diagram.

The next area of concern is the tuning of coupled quantum dots. Tuning essentially involves the discrete control of two quantum dots constructed in a way that their band gap energy states are superimposed as far as the electrons are concerned. This provides the stability necessary to create the eventual quantum bit. The technique involved with tuning is a little more complex but it is important to note that the process of doping the sample is involved.

We now arrive at our present challenge. Both loading/unloading and tuning have been accomplished but we aim to do both simultaneously, without involving the complexities of doping, controlling them only with light pulses and applied voltages.

## Procedure:

The investigation of coupled quantum dots involves many procedures done at different levels of experimentation. The different levels are single quantum dots and

coupled quantum dots and the procedures can be classified as diagnostic, inquisitional then experimental. We begin performing diagnostic research at the single quantum dot stage (on single quantum dot layers). The tests include taking capacitance readings as a function of applied voltage (C-V) and current readings as a function of voltage (I-V). As implied, these tests serve the main purpose of validating our test sample. These tests allow us to determine whether or not our sample is constructed properly. By looking at the conductivity of the sample, we can tell if the sample, including the voltage leads, are positioned properly. If misplaced, the C-V curve will indicate the sample is acting more like a short or open circuit. Finally, the I-V curve reveals the proper range in which our experiments can be conducted.

Once sufficient data has been analyzed to confirm the sample's validity, we move to the more inquisitional tests. These include photoluminescence (PL) tests and sample responses as a function of temperature, voltage, light intensity, and period (to name a few). The purpose of these tests is to further define the behavior of our quantum dots. The PL test is set up to allow us to view the intensity signature as electrons and holes are created and recombine within the sample. The sample responses as a function of temperature, voltage and light intensity allow us to study and determine various characteristics of the sample. These include charge lifetime, unloading dependency and frequency reaction. Upon completion, the actual experimental procedure of loading and unloading the dots using voltage pulses is performed.

**Results:**

There are many charts, tables and graphs in which to show various characteristics and responses of our sample as a function of frequency, voltage, light intensity, temperature and so forth. Due to our restriction in space, we now discuss only a couple of our results taken in the

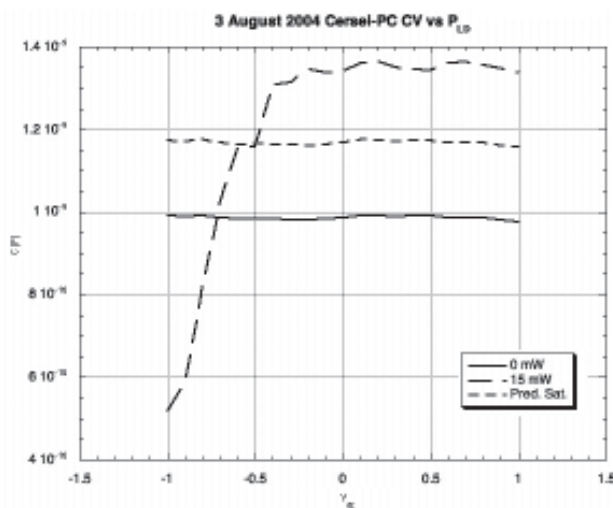


Figure 3: C-V plot.

experiment. First, we show a C-V plot of our sample in Figure 3. As stated earlier, this graphically represents the capacitance of the sample. In our construction, the sample acts like a small capacitor due to the fact that it is comprised of two metal plates (the voltage leads) with a dielectric contained between (the semiconductor material). Depending on the graphical output, we can determine the validity of our sample. If constructed incorrectly, the graph will show the response of a more open circuited object where there is no current charge. If the leads actually touch (also improper construction), the graph will show the response of a more short circuited object.

The next set of data is loading and unloading pulse height as a function of period. From this plot in Figure 4, we calculate the line function whose inverse exponent component reveals the lifetime of our charge (the electrons) within the sample. This lifetime turned out to be roughly one second.

**Future Work:**

As stated earlier, this project involves more than one stage. To this point, we have embarked on researching the first stage (that of single quantum dot systems). Once sufficient leeway is made on single quantum dots, the next step is to research coupled, quantum dot systems. In this stage, many of the same tests and procedures will be carried out. In addition, determining the proper setup to accomplish independent loading/unloading and tuning using only light pulses and voltage biases will be studied.

**Acknowledgements:**

To begin, I would like to thank my mentor, Kohl Gill, for giving me the opportunity to study under his tutelage and (attempt to) contribute to his work in the wonderful field of physics. Then I would also like to thank Mark Sherwin, the entire Sherwin quantum computing research group, UCSB, NNIN and NSF.

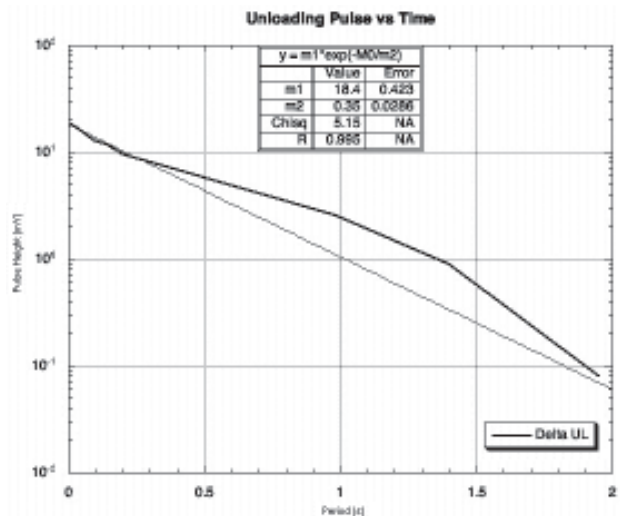


Figure 4: Pulse vs Period (time).

# Scanning Hall Probe Fabrication

James Willett, Physics Major, University of Montana

NNIN REU Site: Stanford Nanofabrication Facility, Stanford University

Principal Investigator: Kathryn Moler, Applied Physics, Stanford University

Mentors: Hendrik Bluhm and Clifford Hicks, Applied Physics, Stanford University

Contact: jamwill80@yahoo.com, kmoler@stanford.edu

## Abstract:

Scanning Hall probes can be used to measure and image magnetic fields in a non-invasive manner. Magnetic field imaging is a very useful way to study the properties of superconducting materials. Improvements to the Hall probe design have been made to decrease the size and shorten the processing time of the probes. In this work, the new design was implemented and the Hall probe recipe was altered to optimize the fabrication process.

## Background:

Scanning Hall probes utilize the Hall effect to make magnetic field measurements. Consequently, Scanning Hall probe microscopy is a very useful approach to studying superconducting materials. High temperature superconductivity has been a major technological advancement of recent history, yet there is still much to be learned about the fundamental physics behind the superconducting phenomenon. Using Hall probes to study the magnetic properties of superconducting materials can help to elucidate the physical mechanisms behind superconductivity.

Smaller Hall probes are desirable for improved magnetic field measurements. The Hall probe design has been enhanced to create 100 nm probes. The Hall probe design has also been changed so more of the probe can be defined optically. E-beam lithography is a slow and tedious process, using optical photolithography to define larger features of the probes can greatly decrease the processing time. Other changes to the probe design include the addition of an extra lead to enable gate defined probes, and more alignment marks.

## Process:

The first step in Hall probe fabrication is the chip preparation. The probe mask design requires a chip that is approximately 7 mm x 9 mm, which must be cleaved from a gallium arsenide wafer. The chip then must be cleaned with a three solvent clean of acetone,

methanol, and isopropyl alcohol. To improve the cleanliness of the chip, we added a hydrofluoric acid dip, which removed an additional 25%-35% of the particles on the chip. The chip is then baked and coated with HMDS to promote adhesion.

The next step is to coat the chip with Shipley's 3612 photoresist. Spinning on the resist at 3500 rpm's for 35s creates a 1.6  $\mu\text{m}$  layer of resist. The spin coating is followed by a 60 second bake at 90°C. The next step is to define the Hall probe design using photolithography. A Karl Suss aligner was used to expose the chip. Before exposing the probe design, it is helpful to expose the edges of the chip to remove the edge bead created during the spin coating. Any additional edge bead must be removed with acetone and a clean room wipe.

Frequently the chuck range of the aligner and the size of the chip made it difficult to align the probe design on the chip. One way of getting around this problem was to mount the chip on a piece of silicon. In the future, the mask design will be changed to accommodate this problem.

After exposure, the piece is developed for 35s in LDD-26W developer. After another HF dip and oxygen plasma clean, the chip is ready for the deposition of the metal contacts. The metal deposition is done in an evaporator and consists of nickel, germanium, and gold layers. After deposition the unwanted metal is lifted off in acetone. Generally an ultrasonic bath is needed to aid the liftoff. The first attempt at liftoff produced less than desirable results, consequently, we began using an undercutting technique to improve the liftoff results.

Before spinning on the photoresist, we coated the chip with LOL 2000. The LOL 2000 was spun on at 3000 rpm's for 60s and then baked at 170°C for 5 minutes. It was found that the bake time for the LOL 2000 is very sensitive. Baking for 7-8 minutes seemed to cause problems with the development of the resist. Figure 1 shows the results of an incomplete development of the resist on a non-scan probe pattern.



*Figure 1: Residue left after incomplete development of resist.*

After the bake, the chip is then coated with Shipley's 3612 photoresist. After liftoff, the piece is annealed in the Rapid Thermal Annealer. Annealing creates an electrical connection between the ohmic contacts and the 2-dimensional electron gas below the surface of the chip. The ohmic contacts must now be electrically isolated from one another. This is done using a deep mesa wet etch.

The mesa etch is defined using optical photolithography as before. Test samples were etched using both sulfuric acid and citric acid to help determine the ideal etching solution. The citric acid had an average etch rate of 2.6 nm/s, making it preferable for the mesa etch. The 100 nm active area of the probe must be defined using e-beam lithography. Unfortunately the e-beam machine was down and we were unable to complete the probes before the end of the program.

### **Results/Conclusions:**

The Hall probe fabrication process was optimized by incorporating optical photolithography into the design where it was possible to do so. This saved considerable time and effort, which would otherwise be spent in the e-beam processing. The metal liftoff was improved by spinning a layer of LOL 2000 beneath the photoresist. This led to more a complete liftoff of the metal. The etch rates of sulphuric and citric acid were tested to determine the best choice for the wet mesa etch. The citric acid was determined to be the most ideal with an etch rate of 2.6 nm/s. The above improvements to the Hall probe recipe were used to fabricate chips with scanning Hall probes, non-scanning test probes, and Hall bars.

### **Future Work:**

The active areas of the probes still need to be written using e-beam lithography. This will be done when the machine is up and running. After completion, the probes will then be ready for characterization and testing.

### **Acknowledgements**

I would like to thank Clifford Hicks, Hendrik Bluhm, and Rafael Dinner of the Moler group for allowing me to participate in their research for the summer. In addition I would like to acknowledge the NSF and NNIN for funding, and Stanford University for the use of their labs and equipment.

# Miniaturizing DNA Sequencing Technology: Designing Microfluidic Channels for Performing Chemistry on Beads

Alyssa Wu, Biology and Chemistry, Cornell University

NNIN REU Site: Stanford Nanofabrication Facility, Stanford University

Principal Investigator: Peter Griffin, Electrical Engineering, Stanford University

Mentor: Ali Agah, Electrical Engineering, Stanford University

Contact: axw2@cornell.edu, griffin@stanford.edu

## Abstract:

The availability of several complete organismal genomic sequences, made possible by drastic reductions in sequencing cost in concert with advances in sequencing technology, has revolutionized the nature of biological and biomedical research. Yet for this rapid progress to continue, and to enable the genomes of countless more organisms to be sequenced cheaply and efficiently, a new approach to DNA sequencing that exponentially decreases its current costs must be developed.

Pyrosequencing is one such novel approach that is based on the detection of visible light generated via an enzymatic reaction cascade occurring in response to the successful incorporation of nucleotides during DNA elongation. In this project, we design, fabricate and package a miniaturized microfluidic version of the pyrosequencing process as a prototype of a potentially more cost-effective and rapid method of DNA sequencing.

The progression of microfluidic channels is etched in a silicon wafer; the wafer is then bonded to a glass wafer with holes drilled at positions corresponding to the channel inlet/outlet ports; finally, the enclosed channels are connected to the macroscopic world of reagent supplies and tested for successful microfluidic capabilities. A successful prototype will demonstrate the potential for miniaturizing DNA sequencing to a lab-on-a-chip scale.

## Introduction:

In February of 2004, the National Human Genome Research Institute issued a request for grant applications "to develop novel technologies that will enable extremely low-cost genomic DNA sequencing." [1] Presently, a mammalian-sized genome can be sequenced for \$10 to \$50 million. The ultimate goal of the NHGRI is to reduce costs by at least four orders of magnitude, to produce the \$1000 mammalian genome. Substantial fundamental research is needed for such a major advance, and it is anticipated that the realization of this goal may take up to a decade to achieve [1].

Of the many alternative approaches to the dideoxy chain termination technology most commonly employed to sequence DNA today, pyrosequencing is a particularly promising method [2]. The pyrosequencing process (Figure 1) begins with the release of pyrophosphate when polymerase successfully adds a correct nucleotide to a

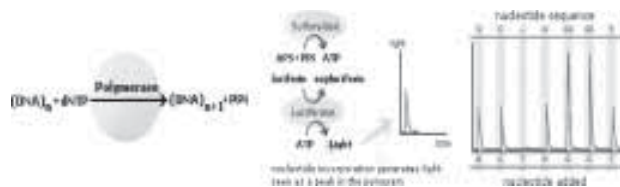


Figure 1: The pyrosequencing process miniaturized in this work [3].

growing primer strand hybridized to a template DNA molecule. This pyrophosphate is then converted to ATP by ATP sulfurylase. ATP then provides the energy for luciferase to oxidize luciferin, a reaction that generates light and occurs naturally in fireflies.

The pyrosequencing technique, then, is based on the detection of light released when the correct nucleotide is incorporated into each successive position on the growing DNA strand. As the four types of nucleotides are added to the reaction mixture one type at a time, the sequence of the template can be determined.

In this project, we develop a prototype for a miniaturized pyrosequencer by designing a series of microfluidic channels etched in silicon and sealed with a glass cover. These microfluidic channels must secure in a stationary location certain beads with attached single-stranded DNA templates, permit all of the requisite enzymes and nucleotides to flow, allow one type of nucleotide to be washed away before the introduction of another, enable detection of generated light, and facilitate connections to the macroscopic world.

## Procedure:

We designed a series of microfluidic channels consisting of a main channel with a protruding pillar to contain the 30  $\mu\text{m}$ -diameter DNA beads in single file at a downstream point, and six separate inlet channels into the main channel for flow of enzymes, wash, and the four types of nucleotides (Figure 2). The channel inlets were widely separated in anticipation of the macroscopic size of capillary connections to the microfluidic channels. We created a mask with four motifs of the design that varied the diameter of the main channel from 30-60  $\mu\text{m}$  and the pillar from 10-40  $\mu\text{m}$  in order to test the effectiveness of flow through channels of different widths. We transferred the mask design to silicon test wafers using standard photolithographic methods and

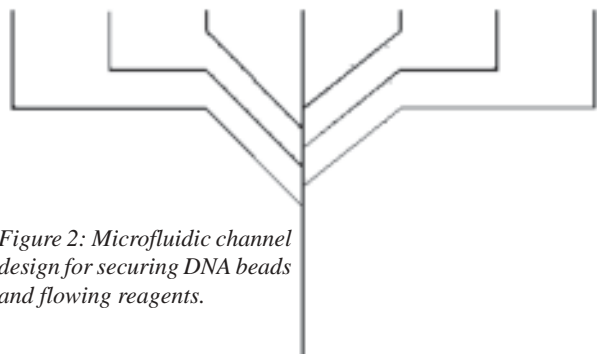


Figure 2: Microfluidic channel design for securing DNA beads and flowing reagents.

etched the design using plasma etching. Inlet and outlet holes were manually drilled into glass wafers using a drill press with a 1.1 mm diamond tip, and then these cover glass wafers were anodically bonded to the etched silicon wafers. Using Upchurch microfluidic-to-capillary connections, we packaged the wafers for reagent flow and prototype testing.

#### Results and Discussion:

SEM and optical microscope pictures of key elements of the microfluidic pyrosequencing prototype show their successful fabrication (Figures 3-4). When the channels were connected to macroscopic connections, deionized water could be flowed through the channels smoothly, with little back-pressure and minimal obstruction by particles or bubbles, even through the narrowest pillar region of the main channel. A significant amount of fluid, however, is diverted up the side channels if pressure is not applied at their inlet ports. If a light signal can be detected when pyrosequencing reagents are flowed through the channels, this will be the first prototype for a miniaturized pyrosequencer.

#### Future Work:

The next steps will be to run colored fluid through the channels for better flow visualization, then DNA beads and the rest of the pyrosequencing reagents to test the prototype's pyrosequencing capabilities. Further work on this project includes trying different types of microfluidic-to-macroscopic connections based on other connector prototypes in the literature, designing inlet channels that will prevent contamination of one type of nucleotide by another, and automating enzyme distribution methods.

#### Acknowledgments:

This work has been supported by the NSF through a NNIN REU program site at Stanford Nanofabrication Facility and by Stanford's Center for Integrated Systems.

I thank Peter Griffin and Ali Agah for valuable discussions and guidance, and Michael Deal and the rest of the staff at SNF.

#### References:

- [1] <http://grants.nih.gov/grants/guide/rfa-files/RFA-HG-04-003.html>.
- [2] Ronaghi, M. 2001. Pyrosequencing sheds light on DNA sequencing. Cold Spring Harbor Laboratory Press. [www.genome.org/cgi/doi/10.1101/gr.150601](http://www.genome.org/cgi/doi/10.1101/gr.150601).
- [3] Graphic adapted from <http://www.pyrosequencing.com/pages/technology.html>.

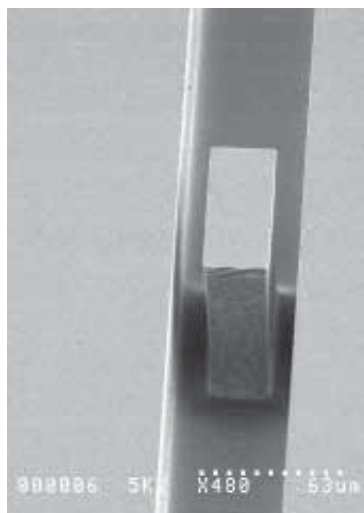


Figure 3: SEM picture of pillar region of main channel.



Figure 4: Optical microscope picture of inlet hole over etched silicon channel.

# Fabrication and Stabilization of Non-Spherical Colloids for Self-Assembly

Allen Yang, Chemical Engineering, Carnegie Mellon University

NNIN REU Site: Cornell NanoScale Science & Technology Facility, Cornell University

Principal Investigator: Dr. Abraham Stroock, Chemical Engineering, Cornell University

Mentors: Joseph Woody and Dr. Cecil Cottin-Bizonne, Chemical Engineering, Cornell University

Contact: alleny@andrew.cmu.edu, ads10@cornell.edu

## Abstract:

Currently, there are no general purpose methods of selectively assembling non-spherical colloidal particles into large ordered structures. One proposed solution to this dilemma is the depletion interaction, an entropy driven ordering effect, which can be manipulated through the shape of the particles.

The challenge is two-fold: the fabrication of non-spherical objects at the limit of micron-scale technology, and manipulating specific interactions to force the ordered assembly of said objects. Our work focused on this first challenge, to experimentally produce these non-spherical particles. We utilized photolithography techniques to fabricate releasable cylindrical particles on a silicon wafer. We employed an interferometer to test the average height of the particles; the variation across a wafer was  $1.2 \mu\text{m} \pm 3\%$ . Examination under SEM showed that the cylindrical particles were approximately  $1 \mu\text{m}$  in diameter and mono-dispersed in both shape and size. The particles displayed Brownian motion when suspended in an aqueous solution.

Our work also studied the possibility of fabricating particles that could compliment each other, introducing structures comprised of particles with different shapes. For this, we produced mono-dispersed particles with a negative curvature of radius  $\sim 1 \mu\text{m}$ ; these particles are predicted to assemble specifically with the cylinders.

## Introduction:

The science of colloids, Brownian particles in solution, has been greatly advanced during the last century. Through the study of colloidal materials and the interactions between them, scientists will be able to develop novel applications to solve the problems currently facing the world. However, previous studies have mostly focused on spherical colloid particles [1]. But to truly understand the phenomena, we need to study the interactions between increasingly complex colloidal structures.

It is for this reason that we look towards the depletion interaction to serve as an assembling force for colloidal particles and to understand the interactions of non-spherical colloidal objects. Dispersed colloidal particles exclude a small volume outside their actual size, preventing other non-adsorbing polymers from entering the excluded region. The entropy of this system is maximized through the assembly of the colloidal particles. The shape dependency of the

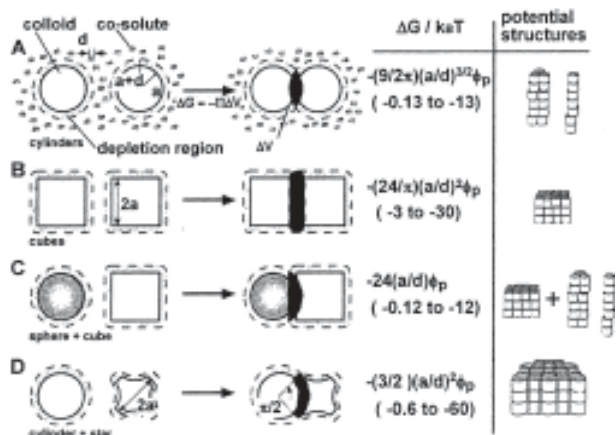


Figure 1: Shape dependency of the depletion interaction.

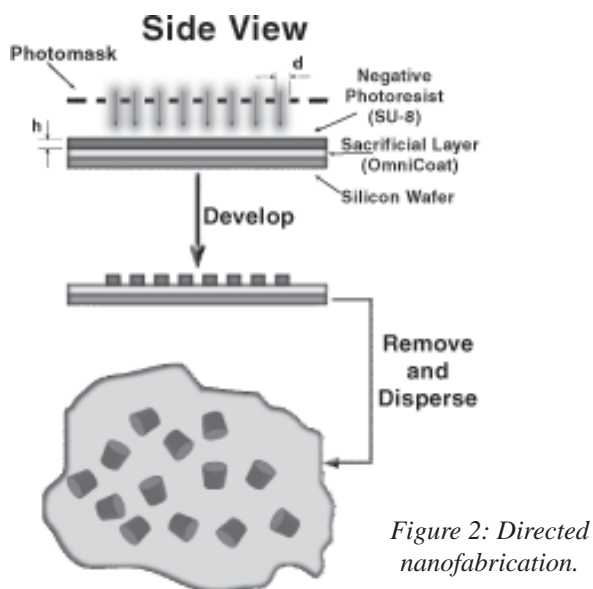
interaction, illustrated in Figure 1, suggests that a complementary surface would induce a stronger interaction than a non-complimentary surface, such as a sphere [1]. Therefore, developing methods of fabricating non-spherical particles at this level becomes critically necessary to understanding the depletion interaction.

## Procedure:

Our experiment had three main goals; (1) fabrication, (2) stabilization, and (3) assembly. The process developed to create our particles is directed nanofabrication. This method involved spinning a layer of SU-8 negative photoresist (MicroChem) on top of a sacrificial layer of OmniCoat (MicroChem), which is spun on a silicon wafer. The SU-8 was spun at speeds of 6000 RPM to produce a layer as thin as possible.

The mask used for the photolithography step was comprised of an array of  $2000 \times 2000$  circles,  $1 \mu\text{m}$  in diameter with a  $2 \mu\text{m}$  pitch which, once processed, would become cylinders. Alternate masks were used as well to test more complex shapes than cylinders. The GCA Autostep allowed us to repeat this array 450+ times across the wafer, fitting approximately 1.5 billion circles on a single wafer. SU-8 polymerizes during the photolithography process, making it possible for us to use the resist as our colloidal particle. Figure 2 illustrates each step of the process.

Once fabricated, the layer of OmniCoat is dissolved by submerging the processed wafer in RemoverPG



(MicroChem) for 30 minutes. Afterwards, we sonicated the wafer in a minimal solution of isopropyl alcohol to facilitate the removal from the silicon wafer.

The next step was to suspend and stabilize our particles in a surfactant solution. We centrifuged the particle/IPA solution at 13,000 RPM in a microcentrifuge and then redispersed the particles in a Water/Triton X-100/NaCl solution. The concentrations of Triton and sodium chloride were 0.15 mM and 5 mM respectively. Once stabilized, a solution of varying molecular weight poly(ethylene oxide) (PEO, Fisher) was added to initiate the depletion interaction.

### Results:

The directed nanofabrication process proved to be successful in fabricating and assembling colloidal cylinders. Interferometer testing showed that the average thickness of SU-8 on the wafers was  $1.2 \mu\text{m} \pm 3\%$ , a relatively small deviation considering most manufactured colloids have much higher deviation in size. Also, from run to run, we were able to produce a high yield of cylinders with little to no defects. We believe that using highly automated equipment such as the GCA Autostep will reduce the amount of error introduced during the photolithography step.

During the release process, we determined that given enough time and amount of IPA, 99% of the cylinders were released into solution. However, because of the volume limitations of a microcentrifuge tube, our average yield per wafer was 85-90%. Figure 3a is an SEM picture of released cylinders on aluminum foil. When PEO was added to the solution, we found small columnar phases forming, shown in Figure 3b. However, at most these columns were comprised of 8-10 cylinders, which we compared to a zero PEO solution, where we found no columnar phases.

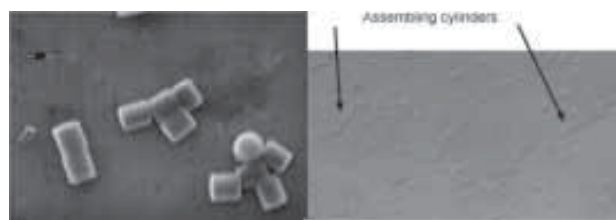


*Figure 3: (a) Released particles on aluminum foil. (b) Initial assembly of colloidal cylinders.*

We also investigated irregular particles, structures based upon groupings of smaller “cylinders”, and given enough exposure time, we are able to create unique shapes that have the potential of assembling complementarily with the cylinders. Figure 4 shows the structure of one of these complimentary structures.

### Future Work:

Future work in this area will involve further investigation of the relation between the aspect ratio of our cylinders versus their ability to form columnar phases. Also, we will explore more thoroughly colloids made from other materials, and of different shapes and sizes.

### Acknowledgements:

I would like to acknowledge Professor Abraham Stroock for supporting this project, my mentors Joe Woody and Dr. Cottin-Bizonne for showing me the right direction, and making my work fun and interesting, the CNF for providing the facility and training, and the NSF for funding.

### References:

- [1] Ilett S M, Orrock A, Poon C K, Pusey P N. Phase behavior of a model colloid-polymer mixture. *Phys. Rev. E*, Volume 51, No 2, 1995, pp. 1344-1352.

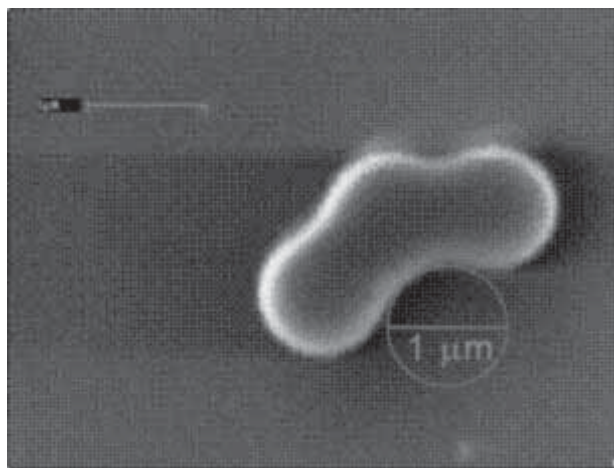


*Figure 4: Complimentary shapes.*

# Biosensors on Surface Acoustic Wave Phononic Band Gap Structures

Yan Zheng, Electrical Engineering, University of California, San Diego

NNIN REU Site: Microelectronics Research Center, Georgia Institute of Technology  
Principal Investigator & Mentor: Dr. William D. Hunt, Electrical Engineering, Georgia Institute of Technology  
Contact: Bill.hunt@ee.gatech.edu

## Abstract:

Already proven in a wide array of industrial applications, surface acoustic wave devices (SAWs) also have been demonstrated to hold substantial potential in the biosensor arena. Currently, SAW resonators coated with a biolayer can distinguish specific biomolecules in both liquid and vapor phases. By incorporating periodic perturbations in the design of SAW delay line, we were able to introduce a phononic band gap in the propagation of surface waves. With the coating of a specific biolayer on these band gap structures, we looked at how the phononic crystal affected the detection of molecules. Finally, we will discuss our results and compare them with current acoustic wave biosensors.

## Introduction:

In current SAW designs, the delay line is one of the most simple. They consist of a piezoelectric layer and finger link projections called interdigitated transducers (IDT) on top separated by a gap. Because acoustic waves follow the relations,  $t = d/v$ , by varying the width of the gap and the velocity of the acoustic wave through fabrication and material selection respectively, we can affect the delay line response. The central operating frequency of the device can also be altered by changing the distance between the fingers.

A more important parameter, though is the overall transfer function characterized by  $H = T_{emitter} * Aexp(i\omega t) * T_{receiver}$  [1]. Currently groups have developed complex transfer functions in both the

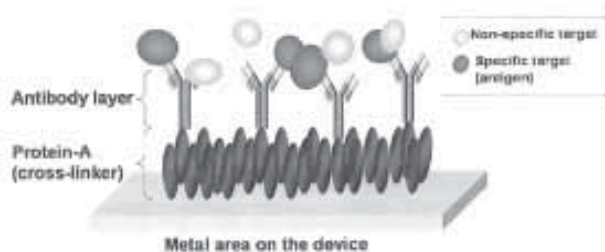


Figure 1: Immobilized layer showing binding.

emitter and receiver ends by incorporating intricate designs on IDTs called apodizations. The next stage of design is the creation of 1-3-dimensional structures that will allow for nonlinear transfer functions in the SAW propagation phase. These structures, called phononic crystals, are analogous to photonic crystals in their ability to manipulate acoustic waves. Besides easing the pressure on complex IDT designs, we can exploit acoustic properties, like tunneling, to view new phenomena [3].

Of these new phenomena, we hoped to find a correlation between the complex transfer functions of these structures with that of the device's ability to act as a biosensor. Previous work has shown that a SAW delay line sensor exhibits a frequency shift when an immobilized layer of antibodies is coated on the device [2]. The coating is designed to capture specific antigens onto the SAW metal surface thus increasing mass. The increase in mass can be quantified by observing shifts in center frequency. This phenomenon is illustrated in Figure 2. We aimed to compare the response of normal SAW delay lines to SAW delay lines with phononic crystals both of which were coated with an immobilized antibody layer.



Figure 2: SAW device.

## Fabrication:

Our SAW devices were made using ST-cut quartz. This ensures that our acoustic waves (Rayleigh waves) travel in a known direction perpendicular to the wafer flat. The wafer is first washed and coated with a negative photoresist, then soft baked for 60 seconds. The wafer then is brought to the mask aligner and has the device mapped onto the photoresist. After this process, the wafer is treated in chlorobenzene, to aid in liftoff, and developed.

The resultant wafer is then placed in the e-beam evaporator in order to deposit 300  $\mu\text{m}$  of Cr as an adhesion layer and 1200  $\mu\text{m}$  of Al for the pads and phononic crystal towers. The towers were 5  $\mu\text{m}$  diameter cylinders spaced 19  $\mu\text{m}$  apart in a square array between IDTs. The same process was used to create the devices with phononic crystals except a different mask containing the crystal was used instead. Each wafer contained devices of different operating frequencies, allowing us to observe a gamut of responses. Figure 2 shows an overview of a SAW device with a phononic crystal.

### Experimental Procedure:

An immobilized antibody gel was coated on select devices with and without phononic crystals. The devices were then allowed to sit refrigerated overnight. S21 measurements were taken using a network analyzer and were recorded and graphed. A drop of water was placed in between IDTs for selected delay lines in order to check for Rayleigh waves. The water droplet is expected to dampen Rayleigh waves yielding no delay line response for a given center frequency.

### Discussion/Results:

When comparing the phononic crystal device to non-crystal devices we saw no difference in magnitude. Figure 3 illustrates lack of differentiation between the two waveforms. We suspect that the size of the crystal towers was too small to affect the acoustic waves. Larger, heavier towers would have a bigger impact on altering wave propagation.

In Figure 4, we see two plots of responses for the coated device versus the uncoated one. There is a prominent down shift in the frequency for the coated device. This result tells us that Rayleigh waves are being altered as mass is increased on the metallic surface (mass loading effect).

The next stage of research is to redesign the phononic crystal and expose the immobilized layer to specific antigens and measure the frequency shift. By comparing the results of normal SAWs to ones with phononic crystals, we can better gauge the efficacy of the phononic crystals.

### Acknowledgements:

I would like to thank Dr. William D. Hunt and the micro acoustics group for all their support when times were hard. In addition, the Georgia Tech faculty and

staff were of immense help as well. Lastly, thanks to the National Science Foundation for its financial support.

### References:

- [1] Lafond E, Zhang X, Deymier P. Executive Summary Phononic Crystal for Acoustic Applications in Telecoms. <http://www.ipst.gatech.edu/.../lafond/Executive%20Summary%20on%20Phononic%20Crystals%20for%20Telecom%20Appl.pdf>. 2004 June 27.
- [2] D.D.Stubbs, S. Lee, W.D. Hunt. "Molecular Recognition for Electronic Noses Using Surface Acoustic Wave Immunoassay Sensors." IEEE Sensors Journal, vol. 2, pp.294-300, August 2002.
- [3] S. Yang, J.H. Page, Z. Liu, M.L. Cowan, C.T. Chan, P. Sheng. "Ultrasound Tunneling through 3D Phononic Crystals". Physical Review Letters. vol. 88, pp. 104301-1-104301-4, March 2002.
- [4] R.S. Penciu. "Phononic Crystals". 2002 International Conference on Transparent Optical Networks, Poland. pp. 11.

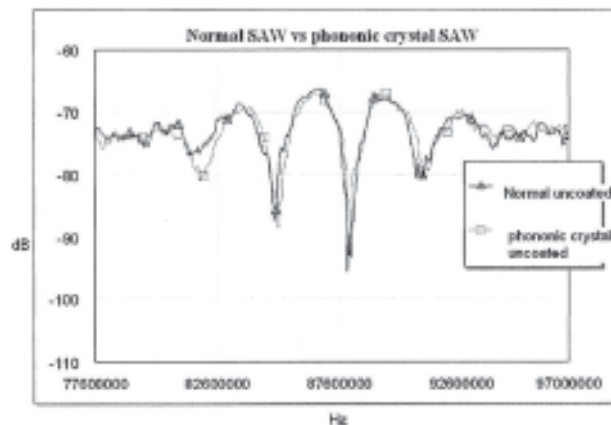
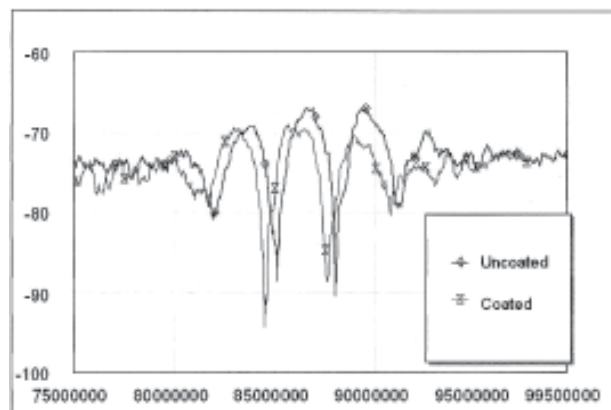


Figure 3, above: Response showing no difference between two devices.

Figure 4, below: Response frequency shift.



The 2004 National Nanotechnology Infrastructure Network  
Research Experience for Undergraduates Program Research Accomplishments

## Index

(*NNIN REU Interns are in BOLD*)

### REU Reports by NNIN Site

Cornell University .....	
6, 18, 30, 40, 42, 52, 56, 78, 98, 108, 110, 146, 154	
Georgia Institute of Technology .....	
6, 44, 68, 92, 96, 122, 156	
Harvard University .....	7, 84, 120, 136
Howard University .....	
7, 32, 64, 112, 138, 140, 144	
The Pennsylvania State University .....	
8, 24, 54, 82, 90, 104, 116, 128, 130	
Stanford University .....	
8, 14, 16, 22, 26, 28, 38, 58, 80, 100, 106, 150, 152	
University of California Santa Barbara .....	
9, 34, 46, 60, 66, 76, 88, 102, 134, 148	
University of Michigan .....	9, 50, 124, 132
University of Minnesota .....	10, 48, 94, 126
University of New Mexico .....	10, 118, 142
University of Texas at Austin ...	11, 20, 62, 70
University of Washington .....	11, 74, 86, 114

### A

Abanulo, Jude .....	140
Abdallah, Jassem .....	122
Agah, Ali .....	26, 152
Allara, David .....	128
Allen, Mark .....	92
<b>Alley, R. Louis</b> .....	<b>8, 14</b>
Andrew, Jennifer .....	134
<b>Anito, Mary E.</b> .....	<b>8, 16</b>
Ardanuc, Serhan .....	52
<b>Arias, Ana Isabel</b> .....	<b>6, 18</b>
Avci, Uygur .....	110

### B

<b>Bagga, Neha</b> .....	<b>11, 20</b>
<b>Bastianon, Nick</b> .....	<b>8, 22</b>
Bates, Jr., Clayton W. ....	64
Berenstein, Angela .....	9
<b>Bhatia, Priya</b> .....	<b>8, 24</b>
Bluhm, Hendrik .....	150
Bowers, John .....	76
<b>Brady, Kevin</b> .....	<b>8, 26</b>
Brannigan, Grace .....	102
Brearley, Adrian .....	142
Brown, Devin .....	96
Brown, Frank .....	102
Brueck, S.R.J. ....	118
Bryan, J. Daniel .....	114
<b>Burt, Nathaniel</b> .....	<b>8, 28</b>

### C

Campbell, Stephen .....	94
<b>Carroll, Heather</b> .....	<b>6, 30</b>
<b>Chalumo, Kovner</b> .....	<b>7, 32</b>
Chao, Joseph .....	72
Chen, Erli .....	120
Cheng, Li-Jing (Larry) .....	124
Choi, Philip .....	50
Clarke, David R. ....	88, 134
<b>Cochran, Peter</b> .....	<b>9, 34</b>
Cottin-Bizonne, Cecil .....	154
Cronin, Stephen .....	136

## D

Dai, Hongjie .....	14, 22
Dauskardt, Reinhold H. ....	58, 106
Deal, Michael .....	8
Demirel, Melik .....	104
<b>DeRosa, Diana .....</b>	<b>9, 36</b>
Desai, Amit .....	130
Desai, Shahyaan .....	56
Diallo, Mamadou .....	138
<b>Dietz, Carl .....</b>	<b>8, 38</b>
<b>Domenech Garcia, Maribella .....</b>	<b>6, 40</b>
Dube, Abhishek .....	78

## E

Edwards, Jane .....	8
El-Sayed, Mostafa .....	68
Engstrom, James R. ....	78
Eustis, Susie .....	68
Ezekoye, Obi .....	104

## F

Felix, Nelson .....	30
<b>Fields, Diane .....</b>	<b>6, 42</b>
<b>Finger, Isaac .....</b>	<b>6, 44</b>
Flickinger, Michael C. ....	48
<b>Fraser, Eric M. ....</b>	<b>9, 46</b>
<b>Freeman, Elizabeth .....</b>	<b>10, 48</b>
<b>Froelich, Steven .....</b>	<b>9, 50</b>
<b>Fu, Yenyun .....</b>	<b>6, 52</b>

## G

<b>Gainor, Danielle .....</b>	<b>8, 54</b>
Gamelin, Daniel .....	114
<b>Gannon, John .....</b>	<b>6, 56</b>
<b>Gantz, Jay .....</b>	<b>8, 58</b>
Gill, Kohl .....	148
<b>Gliem, Jill L. ....</b>	<b>9, 60</b>
<b>Goodfellow, Brian .....</b>	<b>11, 62</b>

Gowrishankar, Vignesh .....	80
Griffin, James .....	7
Griffin, Peter .....	26, 152
Guo, L. Jay .....	50, 124
Guyer, Eric P. ....	58

## H

<b>Hammond, William .....</b>	<b>7, 64</b>
Hanrath, Tobias .....	70
Haque, Aman .....	130
Harris, Gary L. ....	7, 32, 112, 144
Harris, James S. ....	28, 38
He, Moaqi .....	112
Henderson, Clifford .....	44
Hicks, Clifford .....	150
Holmes, Jr., Archie L. ....	20
<b>Horgan, Briony .....</b>	<b>9, 66</b>
Horn, Mark .....	90, 104
<b>Hsu, Hsan-yin .....</b>	<b>6, 68</b>
Hu, Evelyn .....	34
<b>Huang, Jessica .....</b>	<b>11, 70</b>
Hunt, Tom .....	84
Hunt, William D. ....	156

## I

Irudayaraj, Joseph .....	54
--------------------------	----

## J

Javey, Ali .....	22
Jindal, Raja .....	76

## K

Kaburaki, Tadahiro .....	42
Kaeding, John .....	46
Kangas, Miikka .....	66
<b>Karlsqodt, Brandon E. ....</b>	<b>11, 72</b>
Khuri-Yakub, Pierre .....	16
Kim, Sae-Hoon .....	82

## K, continued

Kim, Seong H. ....	82
Kim, Seong-Chan .....	126
Kline, Tim .....	116
Kohl, Paul .....	122
Korgel, Brian A. ....	70
<b>Krueger, Lisa</b> .....	<b>11, 74</b>
Kumar, Arvind .....	110
<b>Kung, Edward Chih Yuen</b> .....	<b>9, 76</b>
Kuo, Chih-jung .....	146
Kurland, Adam .....	24

## L

LaFleur, Lisa .....	74
Lal, Amit .....	52
Lee, Doh C. ....	70
<b>Lee, William</b> .....	<b>6, 78</b>
Lepak, Lori .....	40
Lewenstein, Bruce .....	18
Liechti, Kenneth M. ....	62
Lipson, Michal .....	98
Lowrimore, Melissa .....	6
Lubin, Philip .....	66

## M

MacDonald, Noel .....	36
Mallison, Melanie-Claire .....	6
Martin, Kevin .....	96
McCarty, Gregory S. ....	54, 128
McGehee, Michael .....	80
Meldrum, Deirdre .....	72
<b>Miller, Nate</b> .....	<b>8, 80</b>
Mitchell, James .....	140
Moler, Kathryn .....	150
Moore, Amanda .....	24
<b>Moore, Eric</b> .....	<b>8, 82</b>
<b>Moss, William</b> .....	<b>7, 84</b>
Motayed, Abhishek .....	32

## N

Naik, Nisarga .....	92
Nakamura, Shuji .....	46
<b>Newsome, Brad</b> .....	<b>11, 86</b>
<b>Ng, Mai</b> .....	<b>9, 88</b>
<b>Ngandu, Kabongo</b> .....	<b>8, 90</b>
<b>Nguyen, Khiem</b> .....	<b>6, 92</b>

## O

Ober, Christopher .....	30
<b>O'Day, Alexander</b> .....	<b>10, 94</b>
<b>Olds, Nathan</b> .....	<b>6, 96</b>

## P

<b>Padgaonkar, Vaidehee</b> .....	<b>6, 98</b>
<b>Park, Heyjin</b> .....	<b>8, 100</b>
Parviz, Babak .....	74
Pease, R.F.W. ....	100
Peles, Yoav .....	146
<b>Philips, Peter</b> .....	<b>9, 102</b>
Phillips, Jamie D. ....	132
Pickard, Daniel S. ....	100
Pradhan, Sameer .....	98
Pui, David .....	126
<b>Pursel, Sean</b> .....	<b>8, 104</b>

## R

<b>Rudavsky, Rena</b> .....	<b>8, 106</b>
-----------------------------	---------------

## S

<b>Saboktakin, Marjan</b> .....	<b>6, 108</b>
Sahin, Deniz .....	86
<b>Salomon, Ludwig</b> .....	<b>6, 110</b>
Samah, Zuruzi Abu .....	36
<b>Sammy, Francis</b> .....	<b>7, 112</b>
<b>Santangelo, Steven</b> .....	<b>11, 114</b>
<b>Sarik, John</b> .....	<b>8, 116</b>
Sarikaya, Mehmet .....	86

## **S, continued**

Scaccabarozzi, Luigi .....	28
Sen, Ayusman .....	116
<b>Setlow, Cortland M.</b> .....	<b>10, 118</b>
<b>Shaikh, Shahid</b> .....	<b>7, 120</b>
Sharma, Manish .....	78
Sherwin, Mark .....	148
<b>Silver, Marshall</b> .....	<b>6, 122</b>
Sinha, Ashwini .....	44
<b>Slavik, Gregory J.</b> .....	<b>9, 124</b>
<b>Smith, Margo</b> .....	<b>10, 126</b>
<b>Soumahoro, Tina</b> .....	<b>8, 128</b>
Spencer, Michael .....	40, 42
<b>Staniszewski, Tabitha</b> .....	<b>8, 130</b>
<b>Staszkiwicz, Nicole</b> .....	<b>9, 132</b>
<b>Stevens, Blake</b> .....	<b>9, 134</b>
Stipe, Christopher .....	126
<b>Stolyarov, Alexander</b> .....	<b>7, 136</b>
Stroock, Abraham .....	154
Stroumpoulis, Dimitris .....	60
Sunal, Paul .....	104
Swaminathan, Piraba .....	138

## **T**

<b>Tally, Lynette</b> .....	<b>7, 138</b>
Tatham, Jennifer .....	6
Taylor, Crawford .....	144
Thibeault, Brian .....	34
Thompson, Michael .....	56
<b>Tillmann, Patricia</b> .....	<b>7, 140</b>
Tinkham, Michael .....	136
Tirrell, Matthew .....	60
Tiwari, Sandip .....	5, 110

## **U**

Umbach, Christopher .....	108
---------------------------	-----

## **V**

<b>Vallett, Paul</b> .....	<b>10, 142</b>
<b>Vaughan, Damian J.</b> .....	<b>7, 144</b>
<b>Virost, Steven</b> .....	<b>6, 146</b>

## **W**

Waldrab, Peter .....	54
Wang, Ke .....	38
Wang, Qian .....	14, 22
Weiss, Paul S. ....	24
Westervelt, Robert .....	84
White, Juan .....	64
<b>Whitlock, Jr., Rogers</b> .....	<b>9, 148</b>
<b>Willett, James</b> .....	<b>8, 150</b>
Winter, Michael .....	88
Woody, Joseph .....	154
<b>Wu, Alyssa Xia</b> .....	<b>8, 152</b>
Wu, Kenneth .....	106

## **X**

Xia, Deying .....	118
Xie, Ling .....	120
Xu, Huifang .....	142

## **Y**

<b>Yang, Allen</b> .....	<b>6, 154</b>
Yaralioglu, Goksen .....	16

## **Z**

<b>Zheng, Yan</b> .....	<b>6, 156</b>
-------------------------	---------------

**Thank you all for a great summer!**

(Find the 2004 NNIN REU Research Accomplishments on the web in PDF at: <http://www.nnin.org>)